

Durham E-Theses

Study of strongly interacting particle in the cosmic radiation at sea level using a flash tube chamber

Saleh, A. J.

How to cite:

Saleh, A. J. (1975) *Study of strongly interacting particle in the cosmic radiation at sea level using a flash tube chamber*, Durham theses, Durham University. Available at Durham E-Theses Online: <http://etheses.dur.ac.uk/8216/>

Use policy

The full-text may be used and/or reproduced, and given to third parties in any format or medium, without prior permission or charge, for personal research or study, educational, or not-for-profit purposes provided that:

- a full bibliographic reference is made to the original source
- a [link](#) is made to the metadata record in Durham E-Theses
- the full-text is not changed in any way

The full-text must not be sold in any format or medium without the formal permission of the copyright holders.

Please consult the [full Durham E-Theses policy](#) for further details.

PLATE 1

FRONT VIEW OF THE FLASH TUBE CHAMBER



"TO MY MOTHER"

STUDY OF STRONGLY INTERACTING PARTICLES
IN THE COSMIC RADIATION AT SEA LEVEL USING
A FLASH TUBE CHAMBER

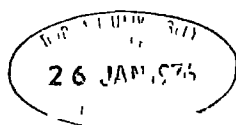
by

A.J. SALEH, B.Sc. (Basrah); M.Sc. (Durham)

The copyright of this thesis rests with the author
No quotation from it should be published without
his prior written consent and information derived
from it should be acknowledged

A thesis submitted to the
University of Durham
for the Degree of Doctor of Philosophy

December 1975



CONTENTS

	<u>Page</u>
ABSTRACT	1
PREFACE	ii
CHAPTER 1 INTRODUCTION	1
1.1 Basic developments in the study of cosmic rays	1
1.2 The primary cosmic ray spectrum	4
1.3 The secondary cosmic ray particles	4
1.4 Hadron energy spectra	5
1.5 Search for quarks	5
CHAPTER 2 REVIEW OF MEASUREMENTS OF SINGLE HADRON SPECTRA AT SEA LEVEL AND HIGH ALTITUDE	7
2.1 Introduction	7
2.2 Experimental methods of measuring particle intensities.	7
2.2.1 The direct measurement method	7
2.2.2 The nuclear interaction method	8
2.2.3 The ionization calorimeter method	9
2.2.4 The burst method	9
2.3 Measurements at sea level	10
2.3.1 Brooke and Wolfendale (1964)	10
2.3.2 Brooke et al. (1964)	11
2.3.3 Diggory et al. (1974)	11
2.3.4 F. Ashton (1973)	12
2.3.5 Cowan and Matthews (1971)	12
2.3.6 Siohan et al. (1973a)	13
2.3.7 Dmitriev et al. (1960)	14
2.3.8 Babecki et al. (1961)	14
2.3.9 Baruch et al. (1973)	15
2.3.10 G. Yodh (1974)	16

	<u>Page</u>	
2.4	Measurements at high altitude	17
2.4.1	Kaneko et al. (1971)	17
2.4.2	Grigorov et al. (1965)	17
2.4.3	Jones et al. (1970)	18
2.4.4	Siohan et al. (1973b)	18
2.5	Discussion	19
CHAPTER 3	THEORY OF THE PRODUCTION OF BURSTS IN THICK IRON AND LEAD ABSORBERS	21
3.1	Introduction	21
3.2	Outline of the cascade process	21
3.3	One-dimensional electron-photon shower development	23
3.3.1	Basic equations	23
3.3.2	The analytic solution using Approximations A and B	24
3.3.3	Method of moments	25
3.3.4	Monte Carlo method	26
3.3.5	A comparison between calculations and experiments	26
3.4	Simulation of nuclear interactions in a thick absorber	27
3.4.1	General remarks	27
3.4.2	Model of nuclear interactions	28
3.5	Result of the calculation	31
3.5.1	Energy-burst size relation	31
3.5.2	Burst size distribution	32
3.6	Discussion	34
CHAPTER 4	THE FLASH TUBE CHAMBER AND THE VERTICAL BURST EXPERIMENT	35
4.1	Introduction	35
4.2	The flash tube chamber	35

	<u>Page</u>
4.2.1 Construction of the chamber	35
4.2.2 The high voltage pulsing system	37
4.2.3 Characteristics of the flash tubes	37
4.2.4 The efficiency-time delay measurement	39
4.3 The arrangement for the vertical burst experiment	40
4.3.1 Introduction	40
4.3.2 Modification of the flash tube chamber	41
4.3.3 Calibration of the scintillators	41
4.3.4 Setting up the experiment	43
4.4 The experimental data	44
4.4.1 The procedure of analysing the data	44
4.4.2 Lateral spread of bursts	45
4.4.3 Extension to higher energies	47
CHAPTER 5 THE ENERGY SPECTRUM OF HADRONS AT SEA LEVEL	49
5.1 Introduction	49
5.2 The basic results	49
5.3 Photography rate	51
5.4 The chamber acceptance functions	51
5.5 Angular distribution	55
5.6 The attenuation length	57
5.7 Estimate of the hadron energy spectrum	57
5.7.1 The measured spectrum	57
5.7.2 Comparison with other results and discussion	58
5.8 Fluctuations	59
5.9 Accompanied events	61
5.10 Conclusion	62

	<u>Page</u>
CHAPTER 6 THE HIGH ENERGY SPECTRUM OF NEUTRONS AND PIONS AT SEA LEVEL	64
6.1 The neutron spectrum	64
6.1.1 General remarks	64
6.1.2 The measured spectrum	64
6.1.3 Comparison with previous measurements	65
6.2 Predicted muon burst spectrum in iron and lead	66
6.2.1 Introduction	66
6.2.2 Theoretical considerations	66
(a) Knock-on electron	66
(b) Bremsstrahlung	67
(c) Direct electron pair production	68
6.2.3 Muon burst spectrum	68
6.3 The pion spectrum	70
6.3.1 Introduction	70
6.3.2 The measured pion spectrum	71
6.4 Charge to neutral ratio	73
6.5 Conclusion	74
CHAPTER 7 QUARK THEORY AND REVIEW OF THE QUARK SEARCHES	76
7.1 Origin of the concept of quark theory	76
7.2 The predicted properties of free quarks	78
7.3 Some successes and difficulties arising in the quark model	80
7.4 Other quark models	82
7.5 Review of quark searches	83
7.5.1 Introduction	83
7.5.2 Search at accelerators	84
7.5.3 Search in cosmic rays	85
(a) Search for relativistic quarks in unaccompanied cosmic rays	86

	<u>Page</u>
(b) Search for non-relativistic heavy mass particles	86
(c) Search for quark accompanied by EAS	87
(d) Delayed particles in EAS	88
7.5.4 Other quark searches	89
CHAPTER 8 SEARCH FOR $e/3$ QUARKS IN EXTENSIVE AIR SHOWERS	90
8.1 Introduction	90
8.2 Distribution of the core distance and shower size of EAS given by a local electron density trigger	92
8.3 The EAS experiment	93
8.3.1 Calibration of the chamber	93
8.3.2 Setting up the trigger	94
8.3.3 Running the experiment	94
8.4 Analysis of the data	94
8.4.1 The procedure of the analysis	94
8.4.2 Basic quark data	95
8.4.3 Details of the two quark candidates	97
8.5 The background effects	97
8.5.1 The expected number of background muon tracks	97
8.5.2 The expected number of knock-on electrons	98
8.6 Quark flux limit	100
8.7 Summary of the flash tube chamber results	100
8.8 Conclusion	101
CHAPTER 9 THE ENERGY SPECTRA OF HADRONS IN EXTENSIVE AIR SHOWERS	103
9.1 Introduction	103
9.2 Analysis of the data	103
9.2.1 Scanning technique	103
9.2.2 Basic data	104

	<u>Page</u>
9.3 The energy spectra	105
9.4 Study of the muon contamination	106
9.4.1 General remarks	106
9.4.2 Ratio of rate of bursts produced in lead and iron absorber	106
9.4.3 Bursts produced in the flash tubes	106
9.4.4 Predicted muon burst spectrum	107
9.5 Characteristics of hadrons in EAS	109
9.6 Comparison between the measured and predicted hadron number	111
9.7 Conclusion	114
CHAPTER 10 SUMMARY	115
APPENDIX A DERIVATION OF A HADRON BURST SPECTRUM IN 15 CM OF LEAD	118
APPENDIX B SEARCH FOR THE MAGNETIC MONOPOLE	120
B.1 Introduction	120
B.2 Previous monopole searches	121
B.3 Present search	122
B.4 Discussion	123
ACKNOWLEDGMENTS	125
REFERENCES	126

ABSTRACT

A measurement of the energy spectrum of hadrons at sea level in the energy range 10 GeV to 10 TeV has been performed. The hadrons interacted in a thick iron or lead absorber and the burst size produced was detected by a scintillation counter placed under each absorber. The burst sizes were used to estimate the energy of hadrons. The result on the hadron energy spectrum shows a constant slope of the form $E^{-2.7 \pm 0.1}$ over the whole energy range from 10 GeV to 10 TeV. There is no change or step in the slope between 2 - 8 TeV as has been suggested by Baruch et al. (1973).

A measurement of the energy spectrum of neutrons at sea level in the energy range 50 - 1,000 GeV has been made and the experimental result represented as a differential energy spectrum in the form $N(E) = K E^{-2.9 \pm 0.1}$ in the same energy range. This result agrees with previous Durham neutron spectrum measurements.

A statistical method has been used to derive the high energy pion flux at sea level from the total measured hadron spectrum. The results show an increase in the π/P ratio as the energy increases and over the energy range 40 GeV to 7 TeV the differential vertical flux decreases with increasing energy as $E^{-2.55 \pm 0.10}$.

A search for $e/3$ charged particles (quarks) close to the core of air showers of median size $6.5 \cdot 10^5$ particles has been carried out. The search was conducted at sea level using a flash tube chamber technique as a visible detector. Air showers were selected in this experiment by requiring a local electron density above the chamber to be greater than 250 m^{-2} . In 7,009 hours two quark candidates were observed and both were explained as due to background incoherent muons. With no definite quark tracks having been observed, the upper limit on the $e/3$ quark flux is $< 4.3 \cdot 10^{-11} \text{ cm}^{-2} \text{ sec}^{-1} \text{ st}^{-1}$

at 90% confidence level.

The energy spectrum of hadrons in EAS of median shower size $6.5 \cdot 10^5$ particles has been measured in the energy range $10 < E < 1,000$ GeV. A slope of $\gamma = 1.07 \pm 0.09$ has been found for the integral spectrum for energies > 200 GeV.

PREFACE

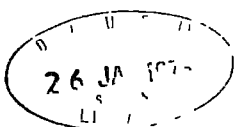
This thesis describes the work performed by the author in the Physics Department of University of Durham while he was a research student under the supervision of Dr. F. Ashton.

An experiment to study the energy spectrum of strongly interacting particles in the cosmic radiation at sea level has been performed using a flash tube chamber. The chamber has been used also to study the particles close to the core of extensive air showers, in particular to search for quarks and study the characteristics of hadrons.

The construction of the experiment, running of the chamber, analysis and interpretation of the data have been the responsibility of the author with the assistance in some of the early work from Dr. D.A. Cooper. The results described in this thesis on the energy spectrum of hadrons at sea level, the energy spectrum of charged pions at sea level and the quark search have been reported earlier by Ashton and Saleh (1975a, b and c).

CHAPTER 1INTRODUCTION1.1 Basic developments in the study of cosmic rays

The discovery of the existence of the cosmic radiation was a consequence of certain experiments undertaken at the end of the last century and the beginning of the present century on the conductivity of gases. This work showed that the conductivity of a gas was increased when it was exposed to high energy radiation, for example, that produced by radioactive materials. In attempts to test this hypothesis a number of workers flew ionisation chambers in balloons and studied the variation of conductivity with height. The early experiments were inconclusive due to technical difficulties but in 1912 Gockel, Hess and Kolhorster, sent suitable ionisation chambers up with balloons and measured the variation of conductivity of the contained gas as a function of altitude. They showed that the radiation, and hence the ionisation produced in the gas, first dropped to a minimum and then increased considerably with height. From the experimental result it was clear that the whole of the residual ionisation observed at sea level could not be due to the radioactivity of the earth, nor can it be a property of the gas with which the ionisation chamber is filled. Thus, Hess put forward the hypothesis that the increase was due to the existence of a penetrating ionising radiation which enters the earth's atmosphere from outer space. He concluded that the radiation must be extremely penetrating for it is able to penetrate the whole of the earth's atmosphere. He also deduced further that the radiation was not of solar origin from the absence of any significant difference in



ionisation between day and night experiments, so the phenomenon came eventually to be called cosmic radiation. At that time the most penetrating radiation explained as γ - radiation was thought to come from the radioactive elements. Kolhorester (1914) working at 9,200 metres above sea level found that the ionisation increased up to ten times its value at sea level.

He found that the absorption coefficient λ derived from $I = I_0 e^{-\lambda d}$ where d is the thickness of the atmosphere had the value 10^{-5} per cm of air which was much less than for γ - radiation from naturally occurring radioactive materials. The conclusions of Hess and Kolhörster were not immediately accepted and in fact a great deal of controversy took place between 1912 - 1926. In the meantime, however, a number of different types of radiation detectors had been developed within the field of nuclear physics such as the Geiger - Muller counter. This counter was capable of being discharged by the passage of a single charge particle or γ - ray quantum. Thus, for charged particle discharges the counter operates by means of the ionisation which the charged particle produces directly, while the γ - ray quantum does so by virtue of the ionisation produced by secondary electrons to which it loses part of its energy in Compton scatters.

Therefore it is possible to detect γ - rays which have a detection efficiency less than charged particles.

In 1929 Bothe and Kilhörster used the Geiger counter to study cosmic rays and by using counters in coincidence to insure that the radiation was due to single charge particles passing through the successive counters. This proved the existence of charged particles.

The other instruments introduced into cosmic ray physics at the end of the twenties was the Wilson cloud chamber, which was not only capable of detecting individual charged particles but also of giving much more detailed

information on their trajectories and interactions. However, with a cloud chamber operated in a strong magnetic field Anderson discovered the positive electron (positron) in 1932, and this was confirmed soon afterwards by Blackett and Occhialini using a cloud chamber controlled by Geiger counters.

In 1929 a cloud chamber photograph showed a case where many particles crossed the chamber simultaneously. This was defined as a 'shower' and later, Blackett and Occhialini showed the existence of positive and negative electrons in these showers.

Rossi in 1932 made measurements on the absorption properties of cosmic radiation showing the existence of two main components, the hard (penetrating) component and the soft (absorbed) component.

Direct determination of the mass from cloud chamber observations has been made using a combination of magnetic and multiplate chambers.

Range - momentum methods were used by Anderson and Neddermeyer and independently by Street and Stevenson in the period 1936 - 1938 to evaluate the mass of the particles. The particles were found to have a mass of about $200 M_e$ (M_e is the mass of the electron) and were later named μ - mesons.

Yukawa in (1935) had predicted the existence in the nucleus of a particle of mass about $200 M_e$ which would act as a link between the neutrons and protons in the nucleus. This particle according to Yukawa should interact strongly with matter. It was suggested that the μ - mesons should not be identified with the Yukawa particle. However, with the development of the nuclear emulsion technique such a suggestion was shown to be correct and another heavy particle was discovered which fitted Yukawa's prediction better. So in 1947 the π - meson was identified by Lattes, Muirhead, Occhialini and Powell and experimentally it was shown that these particles were produced directly in interactions and decay to μ - mesons.

Rochester and Butler (1947) reported the existence of even heavier mesons called 'strange' particles. However, this discovery was followed up by an intensive search for other new particles in cosmic rays and accelerators, table 1.1 shows a summary of the discovery of the so called elementary particles given by Hillas (1972). By this time the general picture of the cosmic radiation was becoming clear and the interactions involving the primary cosmic rays (proton) with air nuclei also became clear.

1.2 The primary cosmic ray spectrum

The primary particles arriving at the top of the atmosphere have come in a small proportion from the sun but the majority have come from more distant sources.

In the primary cosmic radiation nucleons are known as a single proton; and when the protons and neutrons are together they form the heavier nuclei. The spectra for various primary components are shown in figure 1.1. This figure can be expressed in a variety of ways, the choice being usually determined by the method of measurement. At the highest energies, where extensive air showers are examined, the information is usually in terms of primary energy per nucleus. Below 10^{14} eV the ordinate refers to the number of nuclei per unit kinetic energy per nucleus. Figure 1.2 also shows this composition in more detail where the primary cosmic radiation protons represent about 85% of the particles and the remainder are heavier nuclei.

1.3 The secondary cosmic ray particles

The primary particles (protons) interact with air nuclei when they pass through the atmosphere producing secondary particles. The heavier nuclei in their collisions fragment into nuclei of lower atomic number so that after a few interactions they have completely split into their

Date	Particle	Source of radiation	Instrument used	Specific observation made
1900				
1930				
1931				
1932	$\bar{\nu}_e (\nu_e)$	nuclear reactor	liquid scintillator	Capture by proton
1933	ν_μ	accelerator	spark chamber	Production of μ and not e
1934				
1935	e^-	discharge tube	fluorescent screen	Ratio e/m
1936	e^-	cosmic rays	cloud chamber	Charge mass
1937	μ^+, μ^-	cosmic rays	cloud chamber	Absence of radiation loss in Pb, decay at rest, mass
1938				
1939	τ^-	cosmic rays	nuclear emulsion	$\tau - \mu$ decay at rest
1940	τ^-	cosmic rays	nuclear emulsion	Nuclear interaction at rest
1941				
1942	τ^0	accelerator	counters	Decay into γ -rays
1943	k^-	cosmic rays	nuclear emulsion	$K_{\gamma 1}$ decay
1944	K^-	cosmic rays	nuclear emulsion	Nuclear interaction at rest
1945				
1946	K^0	cosmic rays	cloud chamber	Decay into $\tau^+ \tau^-$ in flight
1947				
1948	η	accelerator	bubble chamber	Total mass of decay products
1949				
1950	p	discharge tube	spectroscopes, mass spectrometers	Charges and masses of ions
1951				
1952	\bar{p}	accelerator	Cerenkov counter	e/m measured, annihilation
1953				
1954	n	radioactivity	ionization chamber	Mass from elastic collisions
1955				
1956	\bar{n}	accelerator	counters	Annihilation
1957	Λ^-	cosmic rays	cloud chamber	Decay to $p \tau^-$ in flight
1958	Λ^0	accelerator	nuclear emulsion	Decay to $p \tau^-$ in flight
1959	Σ^-	cosmic rays	nuclear emulsion	Decay at rest
1960	Σ^-	accelerator	diffusion chamber	Decay to $n \tau^-$ in flight
1961	Σ^0	accelerator	bubble chamber	Decay to Λ^0 in flight
1962	Ξ^-	cosmic rays	cloud chamber	Decay to $\Lambda^0 \tau^-$ in flight
1963	Ξ^0	accelerator	bubble chamber	Decay to Λ^0 in flight
1964	Ω^-	accelerator	bubble chamber	Decay to $\Xi^0 \tau^-$ in flight
1965	Very many 'resonance particles with lifetimes $\sim 10^{-23}$ to 10^{-19} s	accelerator	bubble chambers	Total mass of decay products
1966				
1967	"Fireball"	cosmic rays	nuclear emulsion	Angles of meson emission

Table 1.1

Summary of the discovery of the elementary particles. After Hillas, 1972.

Figure 1.1

Summary of measurements on the primary spectrum of protons and nuclei in the cosmic radiation, corrected for geomagnetic effects.

The groupings of nuclei are as follows:

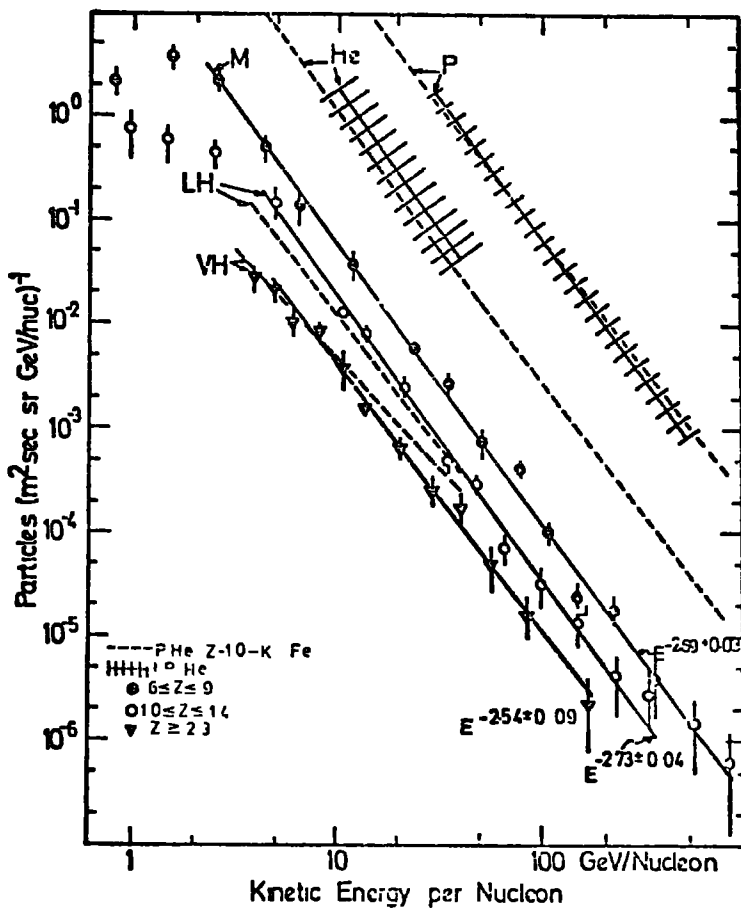
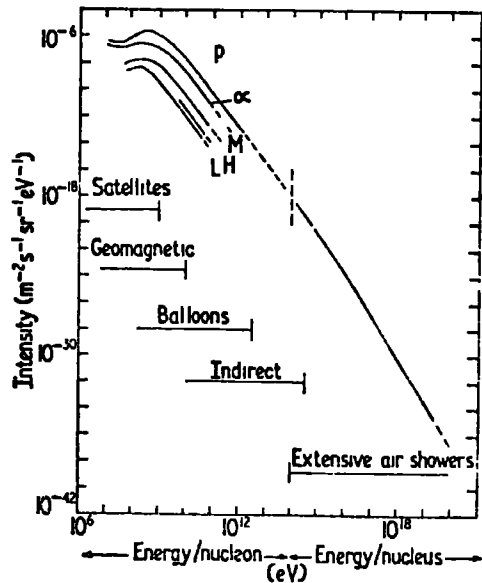
L : $3 \leq Z \leq 5$; M: $6 \leq Z \leq 9$ and H: $10 \leq Z$.

After Wolfendale, (1973).

Figure 1.2

Differential energy spectra of various groups of nuclei obtained by the Max Planck⁶ Institute group and the Goddard group. Both of these experiments use total energy calorimeters.

After Webber, (1973).



constituent nucleons. In each interaction the nucleons emerge with a certain fraction of their initial energy and the remaining energy is used into the production of pions.

At sea level neutrons, pions, kaons and muons must be secondaries produced in nuclear interactions while protons and neutrons may be surviving primaries.

1.4 Hadron energy spectra

The energy spectra of hadrons or nuclear active particles (protons - neutrons and pions) have been studied in detail using the flash tube chamber. A technique has been adopted for measuring the energy of these particles interacting in lead and iron absorber.

In chapter 3 the theory of these cascades is developed and the relation between the burst size (number of particles measured in a detector below an absorber) and the energy of the primary particle has been given. Chapter 5 describes the experimental results on the hadron energy spectrum at sea level and chapter 6 summarises the results on the neutron and pion energy spectra.

The energy spectra and the characteristics of hadrons in an extensive air shower of median shower size $6.5 \cdot 10^5$ has been studied. The results of this study are given in chapter 9.

The full experimental arrangement of the present work has been discussed in chapter 4.

1.5 Search for quarks

Since the theory of quarks was first postulated to explain the structure of elementary particles many experiments have been performed to search for these particles.

The basic developments of quark theory and a review on the quark

searches has been given in chapter 7.

Chapter 8 explains the experiment carried out to search for these particles in the secondary cosmic radiation. In this chapter the search was carried out close to the core of EAS, assuming the quarks, if they exist, to be produced in very high energy interactions of the primary cosmic rays with the atmospheric nuclei.

CHAPTER 2

REVIEW OF MEASUREMENTS OF SINGLE HADRON SPECTRA

AT SEA LEVEL AND HIGH ALTITUDE

2.1 Introduction

In this chapter measurements of the hadron (nuclear active particles) spectrum at various depths in the atmosphere are summarised and compared.

The majority of experiments to study the interactions of hadrons in the atmosphere have been performed at mountain altitudes, although some measurements have been performed at sea level. The main reason for the mountain altitude experiments is that for the higher altitude of the apparatus the greater flux of high energy particles one can get.

In the primary cosmic radiation protons contribute about 85% of the particles the remainder being heavier nuclei, see figure 1.2, so that the neutrons, pions and kaons must be secondaries produced in the nuclear interaction of the primaries. By studying the energy spectra of all the different components at different depths in the atmosphere it is possible to obtain information about the nature of their interaction.

2.2 Experimental methods of measuring particle intensities

It is convenient to discuss the experimental methods according to the techniques used, and one can classify the techniques used into four categories, with each of them restricted to a fairly well defined energy range.

2.2.1 The direct measurement method

The direct measurement method used to measure the particles momenta

were determined from (a) a comparison of their rates of ionization loss and their ranges. The rate of ionization loss by a singly charged particle in any given medium is a function only of the velocity of the particle. At non relativistic energies this loss is inversely proportional to the square of the velocity so that the difference in ionization ranges of protons and the other types of particles present in the cosmic radiation is large. By observing the rates of particles stopped by an absorber of suitable thickness as a function of energy, the low energy protons spectrum can be derived. (b) Another technique in this energy range uses a magnetic spectrometer, which gives a particularly reliable estimate of the particle momentum. A charge particle shows a curvature of its trajectory in a magnetic field. However, it should be possible with higher fields to measure the higher energies.

These techniques are therefore suitable only for measuring the charged particles, and if the momentum spectrum of positive particles (protons, pions and muons) were determined from either magnetically or from a comparison of their rates of ionization loss and their ranges and also if the negative particles (pions, muons) were determined in the same way, then the proton momentum spectrum can be evaluated. This method covers the energy range up to ~ 200 GeV.

2.2.2 The nuclear interaction method

This method has been used with conjunction with a magnetic spectrograph and in the region of energies $\geq 10^{10}$ eV. After deflecting the charge particle by a magnetic field a nuclear interaction occurs in a thick absorber and either the pions produce in this interaction or evaporation neutrons from the 'target' nuclei can be detected. Nuclear active

particles were recognized by their production of evaporation neutrons. The proton spectrum has been derived from the difference between the positively and negatively charged particle spectra, and after subtracting the muon contribution from the spectrum of negative interacting particles a pion spectrum can be derived.

2.2.3 The ionization calorimeter method

The ionization calorimeter was originally developed by Grigorov et al. (1958) and initially it was intended for use in measuring the energy of individual particles, either charged or neutral in the energy range above 10^{11} eV. Usually in the top of the calorimeter a large block of absorber, several interaction lengths in thickness, in which the hadrons (nuclear active particles) interacts with it. The calorimeter used as an object of absorbing the whole of the energy of incident hadrons, most of the energy goes into the electron-photon cascades which develop from the neutral pions (π^0) produced either in the interactions of the incident hadrons or from the secondary charged pions which interact inside the calorimeter. From the shower (electron-photon) development curves measured at a series of depths inside the calorimeter the incident energies of the primary particles can be calculated. The calibration for the absolute energy is difficult and systematic errors may be significant, but it can measure the energy of an individual particle to an accuracy of approximately 30%. This device has been employed in several experiments with spark chambers and different target materials at sea level and high altitude to study the characteristic of high energy nuclear interactions.

2.2.4 The burst method

From the electron-photon showers or 'bursts' which eventually develop

from the neutral pions as the result of a high energy interaction of incident hadrons in a thick target, incident hadron energies can be estimated. Usually the apparatus used consists of a single layer of a target material above a detector which is capable of measuring the total number of electrons emerging from the absorber. By using a simple model one can calculate the number of electrons as a function of the primary energy. This type of technique is thus not very reliable for determining the energy for individual particles but it can be employed more usefully in the measurement of a spectrum where a large number of events are being taken. This method has been used in the present work and it will be discussed further in chapter 3.

2.3 Measurements at sea level

2.3.1 Brooke and Wolfendale (1964)

A magnetic spectrograph was used to measure the sea level momentum spectrum of cosmic ray protons in the range 0.6 to 150 GeV/c. The spectrograph used four measuring levels, two above and two below the magnet and the deflections, and therefore the momenta of the triggering particles are determined from the intersection of their trajectories with the four levels. Protons were detected by two methods (a) by their absorption, either through ionization loss or interaction, in a local absorber, or (b) through their production of evaporation neutrons using a neutron monitor. Both methods can be used in the low energy region but at high energies where the probability of secondaries emerging from the absorber is high, then the evaporation neutron method becomes more reliable to use.

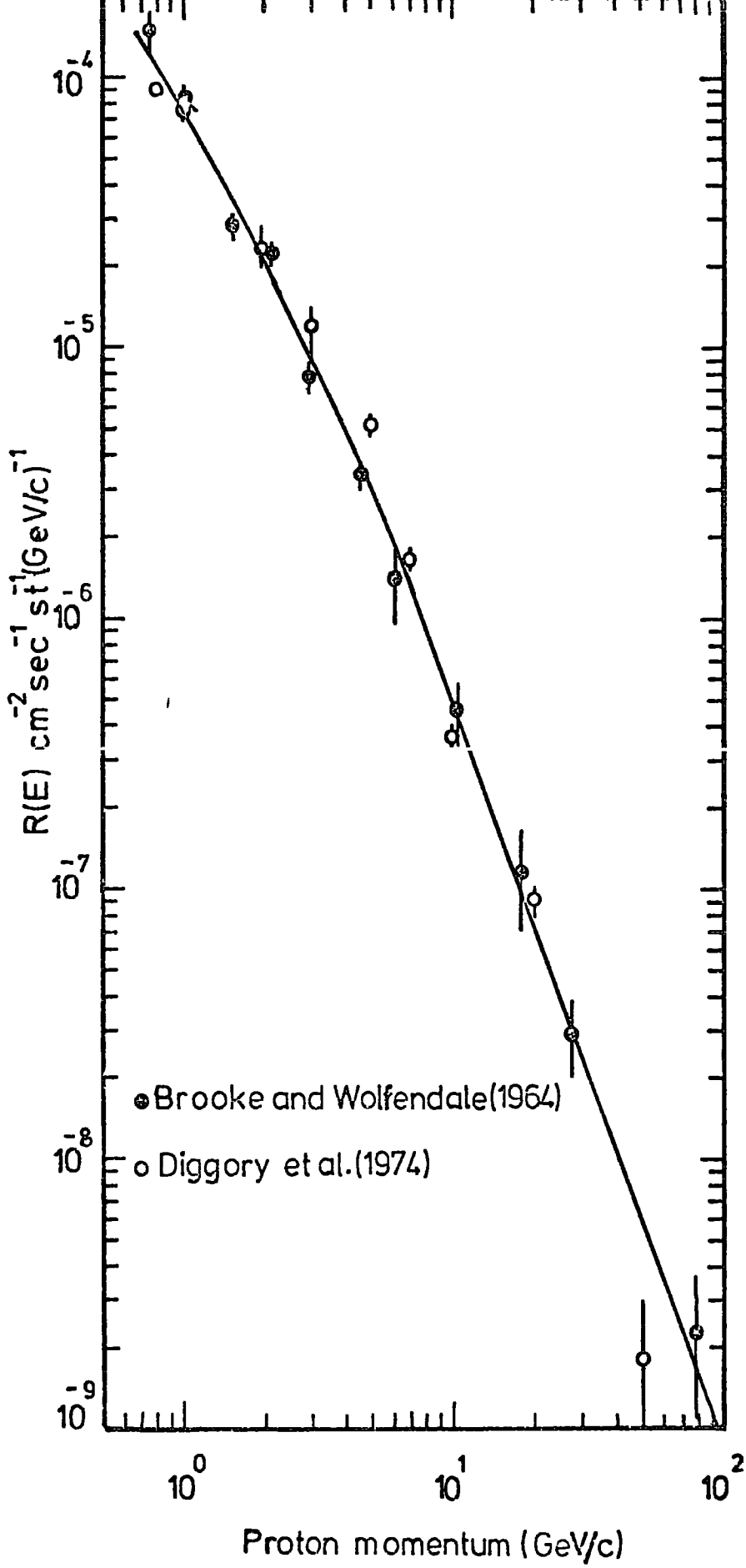


Figure 2.1

The vertical momentum spectrum of single protons at sea level.

Figure 2.1 shows the measured differential vertical momentum spectrum of protons at sea level by Brooke and Wolfendale. Mylori^{et al.} and Wilson (1951) have measured the proton spectrum at sea level in the range 0.6 - 12 GeV/c using the absorption method, the measurements agree with the measurements of Brooke and Wolfendale up to 2GeV/c, but above this the intensities of Mylori and Wilson become lower.

Also an estimate of the proton to muon ratio has been made. The result found is that this ratio falls as the momentum increases, the ratio being 6% at 0.7 GeV/c and about 0.4% over the momentum range 50 - 150 GeV/c.

2.3.2 Brooke et al. (1964)

The momentum spectrum of negative pions in the vertical direction was measured using the same spectrograph discussed in Section 2.3.1 in conjunction with a neutron monitor. Pions were detected by means of their interaction and subsequent neutron production in the monitor. The ratio between positive and negative pions is taken to be unity as calculations show that even for momenta of about 100 GeV/c at sea level the majority of the surviving pions come from interactions at low altitudes, where the proton to neutron ratio is unity. Figure 2.2 shows the measured vertical differential energy spectrum of pions at sea level.

2.3.3 Diggory et al. (1974)

A magnetic spectrograph similar in principle to that used by Brooke and Wolfendale, which included a large air gap magnet and neutron monitor. The method adopted to derive the absolute flux of protons and pions was similar to the one discussed in section 2.3.1. The data of Diggory et al.

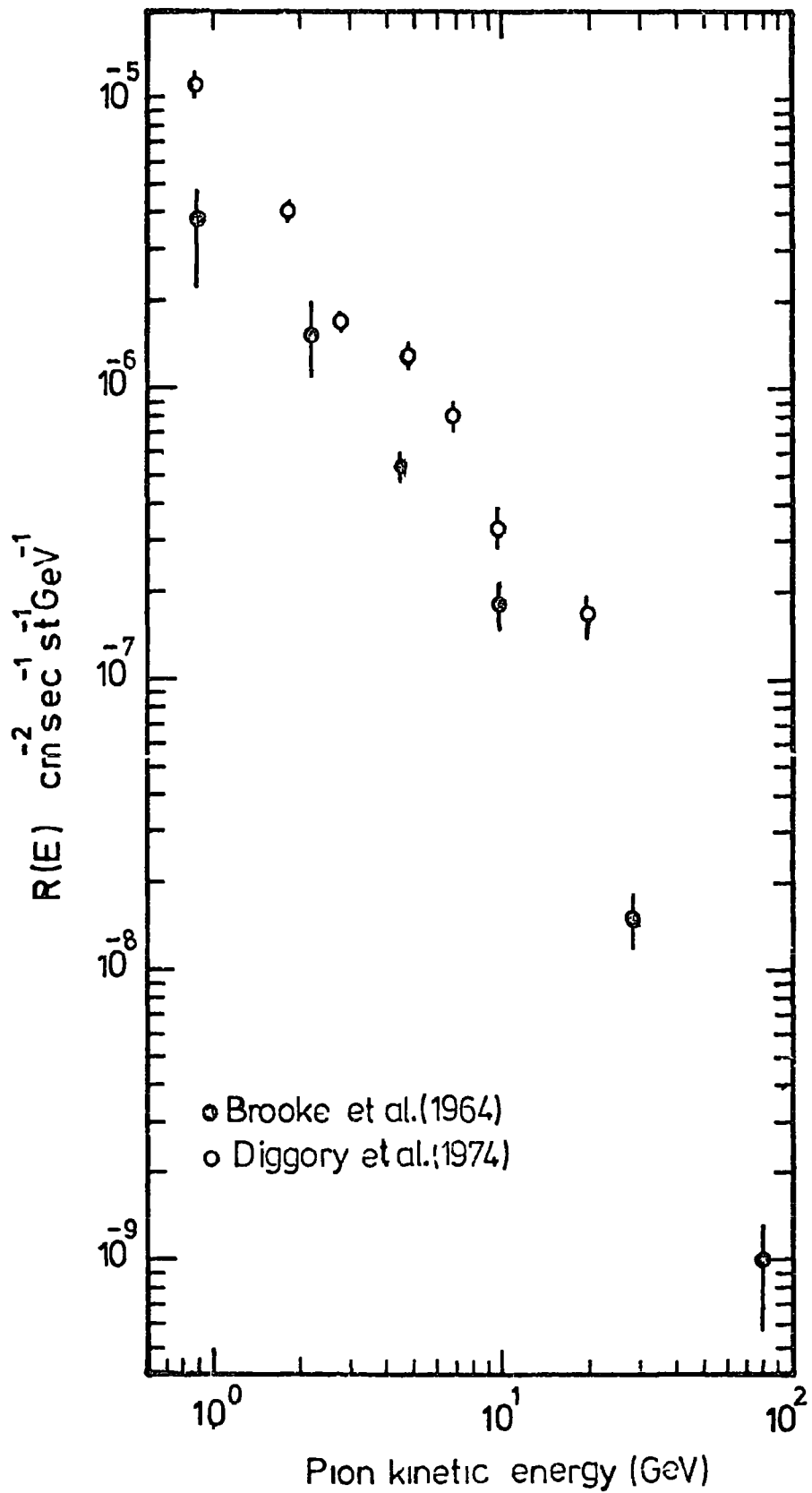


Figure 2.2

The vertical differential energy spectrum of pions (π^\pm) at sea level.

may be usefully compared with results of Brooke and Wolfendale. It appears from figure 2.1 that the spectra are in reasonable agreement. The data of the negative pion momentum spectrum has been corrected for positive pions assuming the ratio π^+/π^- is unity and the final result is shown in figure 2.2 as the pion energy spectrum at sea level. This result is compared with the result of Brooke et al. in the same figure.

2.3.4 F. Ashton (1973)

The low and the high energy spectra of neutrons are summarised as the best estimate for the neutron energy spectrum at sea level, Ashton (1973). The direct measurement of the low energy spectrum has been made in the region 0.4 - 1.2 GeV Ashton et al. (1971a) using the charge exchange reaction $n + p \longrightarrow p + n$. Figure 2.3 shows the result of the low energy neutron spectrum compared with other works. From this figure it can be seen that ionization loss can be neglected in considering the propagation of nucleons of energy greater than 5 GeV through the atmosphere. At higher energies (> 20 GeV) the neutron spectrum has been obtained from the burst spectrum produced by neutral primary particles in a thick steel target Ashton et al. (1970). Figure 2.4 shows the vertical differential energy spectrum. Over the energy range 50 - 1,000 GeV the spectrum $N(E) = A E^{-\gamma}$ shows $\gamma = 2.95 \pm 0.1$.

2.3.5 Cowan and Matthews (1971)

Cowan and Matthews (1971) used an ionization calorimeter together with nine cloud chambers principally to study hadron interactions and also to measure the energy spectrum of unaccompanied incident hadrons.

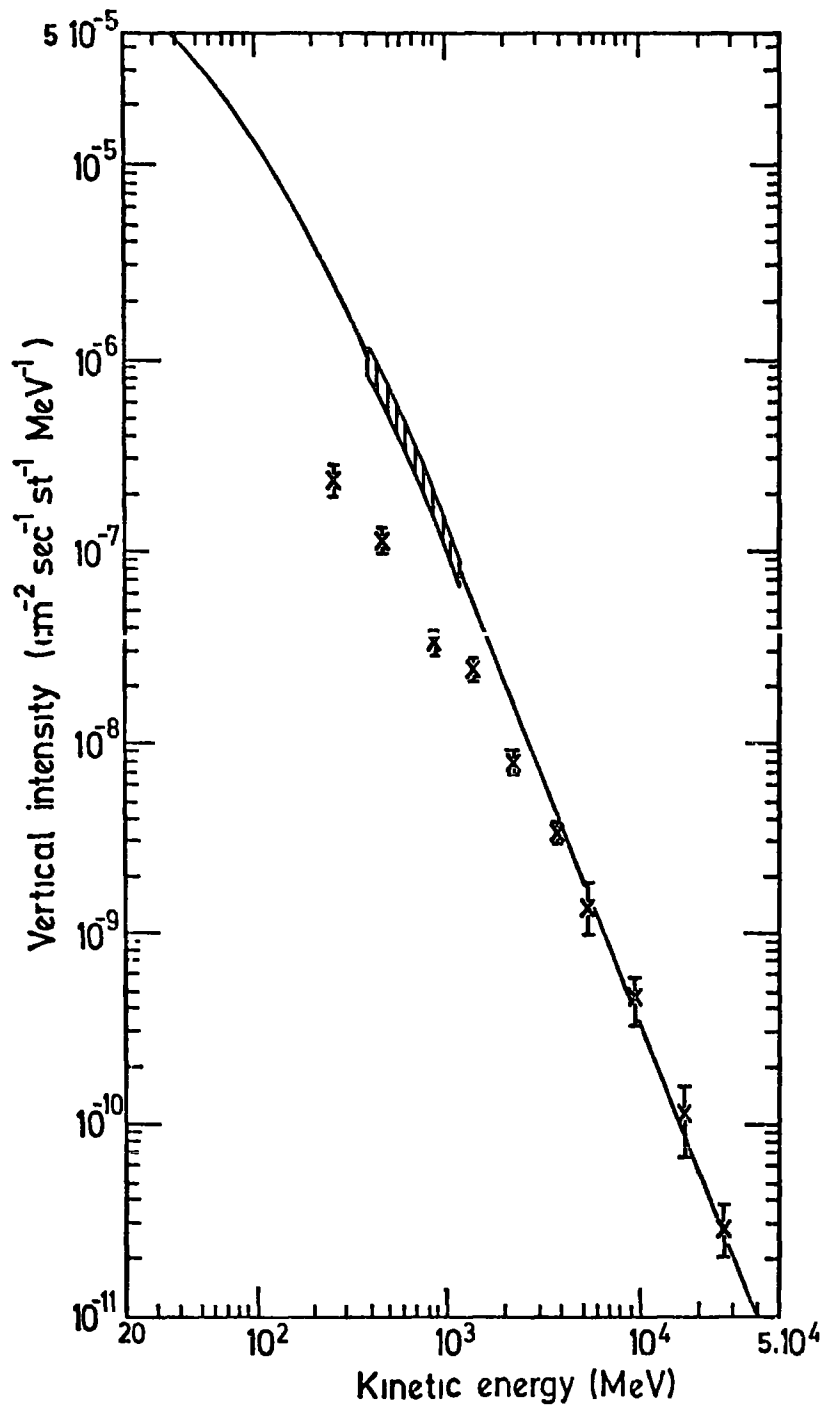


Figure 2.3

Summary of the sea level vertical neutron and proton spectra. The full line is the vertical neutron spectrum calculated from global spectrum given by Hughes and Marsden (1966). The crosses are proton measurements of Brooke and Wolfendale (1964) and the hatched area is the vertical neutron spectrum given by Ashton et al. (1971b). After Ashton (1973).

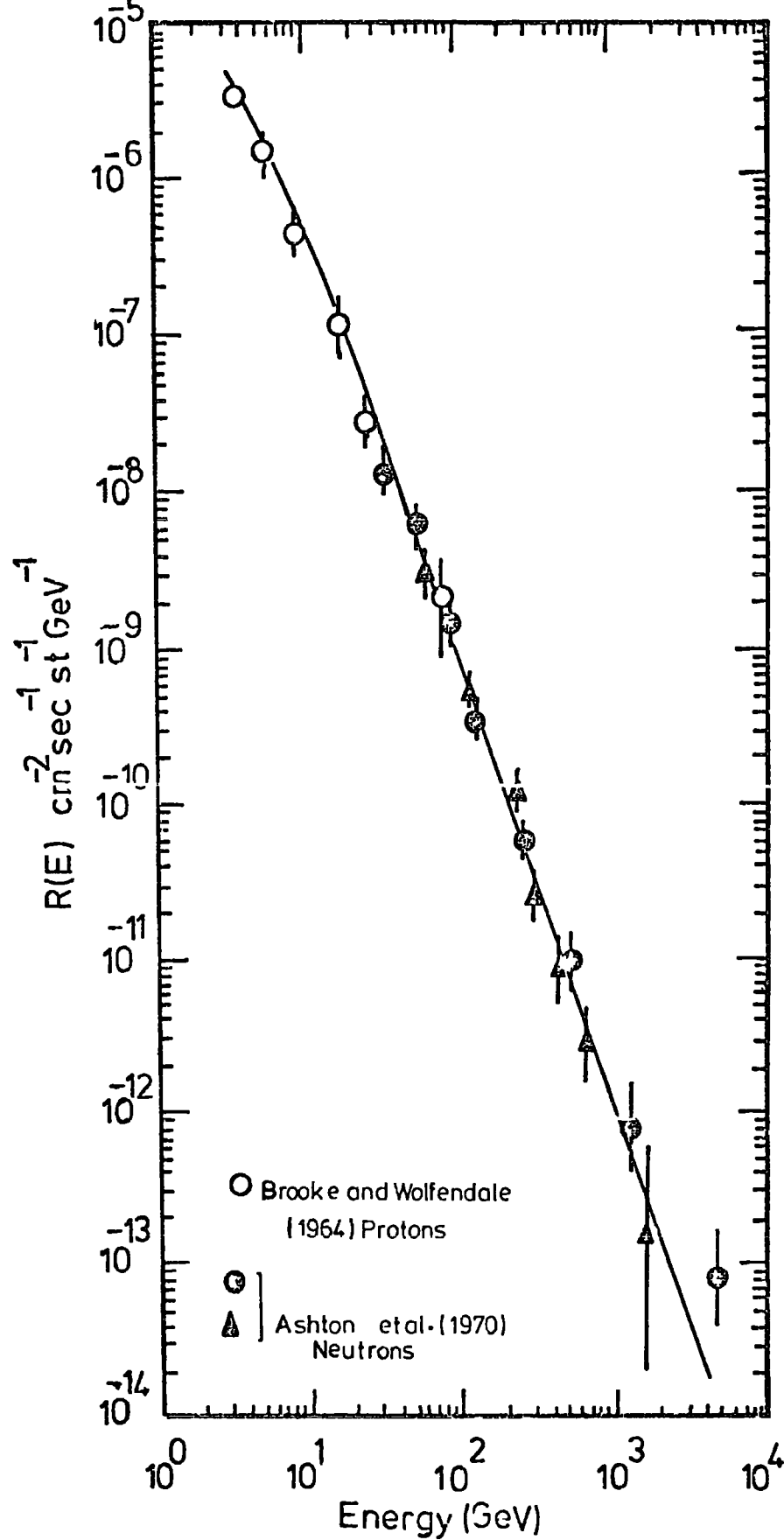


Figure 2.4

The vertical differential energy spectrum of neutrons at sea level. Over the range 50 - 1,000 GeV, the differential spectrum can be represented by $N(E)dE = K E^\gamma dE$ where $\gamma = 2.95 \pm 0.10$, Ashton et al. (1970). The proton measurements are from Brooke and Wolfendale (1964). (After Ashton, 1973).

The array of overall dimensions 5.8 m by 1.6 m by 0.9 m was operated at 250 m above sea level. A total of 1,167 single cosmic ray particles has been observed in 0.85 year and with a solid angle area $0.65 \text{ m}^2 \text{ sr}$. The neutral to charge ratio was measured for incident particles which interacted in one of the layers of carbon, the value found being 0.295 ± 0.035 at an average energy of 330 GeV. The energy spectra of pions and protons have been calculated from the measured charged spectrum using the neutral to charge ratio and Cowan and Matthews took this ratio to be 0.9. Hayakawa (1969) gave a value greater than 0.9 at sea level, although this would be a lower limit at large atmospheric depths. Assuming the neutron to proton ratio is 0.9 Cowan and Matthews found almost exactly twice as many pions as protons. The result for the energy spectrum of charged hadrons is shown in figure 2.5.

2.3.6 Siohan et al. (1973a).

They have measured the charged hadron flux at sea level using an ionization calorimeter. The calorimeter, of area 4 m^2 , consisted of 8 interaction lengths of iron in 8 layers of 15.2 cm each. The device estimates the energy of an incident hadron by measuring the development of its nuclear - electromagnetic cascade, sampled after each interaction length by liquid scintillation detectors. The threshold for triggering corresponded to > 900 equivalent muons (~ 300 GeV hadron). A Monte-Carlo simulation for the calorimeter was used to obtain the energy of primary incident hadrons from the equivalent muons ($E \sim N^{0.9}$). Muon bursts accounted for about 3% of all triggers. The measured vertical spectrum of hadrons in the energy range 350 - 1,000 GeV, gives the result:

$$R(E) = (2.6 \pm 0.75) \times 10^{-7} (E/350)^{-\gamma} \quad \text{m}^{-2} \text{ sec}^{-1} \text{ st}^{-1} \text{ GeV}^{-1}.$$

Where $\gamma = 5.3 \pm 0.9$ and E in GeV, for single hadrons unaccompanied over 4 m^2 .

$$R(E) = (1.23 \pm 0.24) \times 10^{-6} (E/350)^{-\gamma} \quad \text{m}^{-2} \text{ sec}^{-1} \text{ st}^{-1} \text{ GeV}^{-1}.$$

Where $\gamma = 3.35 \pm 0.25$ and E in GeV, for all single hadrons.

In figure 2.5 the spectrum of all single hadrons is shown.

2.3.7 Dmitriev et al. (1960)

Dmitriev et al. (1960) studied high energy nuclear active particles (NAP) using ionization chambers and the method of detecting those particles from the bursts they produce in thick absorber by high energy NAP (hadrons) was used. A single detector layer contained four ionization chambers with total effective area of 1 m^2 . A total of 720 Geiger Counters were used to register the charged particles accompanying the nuclear active particles. The absorber of this experiment consists of several layers, a layer of lead 5 cm thick (used also as shielding to the experiment), a layer of graphite 70 cm thick and a layer of lead 2 cm thick. The energy of NAP with energy ($E \geq 10^{12} \text{ eV}$) can be estimated by measuring the amount of ionization in the chambers. The layer of lead immediately above the ionization chambers was chosen such that cascades resulting from interactions in the graphite were near maximum development at the ionization chambers, cascades from interactions in the lead layer (top) would be well past maximum development. During the operating time 1,300 hours 948 bursts were registered each corresponding to the passage of $\geq 1,000$ relativistic particles. The mean frequency of bursts $N \geq 1,000$ was found $0.7 \pm 0.04 \text{ hr}^{-1} \text{ m}^{-2}$. The energy spectrum of the nuclear active particles (hadrons) in the energy range from 510^{12} eV to 510^{13} eV is shown in figure 2.5.

2.3.8 Babecki et al. (1961)

This work was performed using an array designed for the study of

interaction processes involving particles of energy $10^{12} - 10^{13}$ eV. The array consisted of four rows of ionization chambers between which were lead and graphite filters of different thickness. The arrangement of the chambers made it possible to determine the coordinates of the shower produced by recorded bursts. The pulses from each of the chambers were individually recorded, and events were recorded if the total ionization is greater than a given threshold value simultaneously in each of any two of the layers of ionization chambers. The data on the ionization bursts in the chambers, obtained during 2,640 hours are shown in figure 2.6 and the integral burst spectrum was given with exponent -1.9 ± 0.03 .

2.3.9 Baruch et al. (1973)

A study of the hadron energy spectrum still continues in the high energy region and a recent experiment reported by Baruch et al. will be discussed in this section. They have operated a single interaction calorimeter at site F of the Haverah Park array, 240 meter above sea level. The calorimeter has a sensitive area of 4 m^2 , is surrounded by air shower detectors, and is designed to measure the energy of hadrons interacting in a 60 g cm^{-2} thick graphite target. Under a further length of steel are two crossed layers of proportional counters separated by 3.5 radiation lengths of lead. There are 112 counters in each layer, and their diameter is 3.5 cm. The signals from each detector are recorded individually. The electron-photon cascades, or bursts, produced by hadrons reaching their maximum at depths in the lead near the layers of the proportional counters are recognized from the relative amounts of ionization in the two layers. The calorimeter does not measure the total ionization of the cascades subsequent to hadron interactions in the calorimeter, but the maximum N_{max} ,

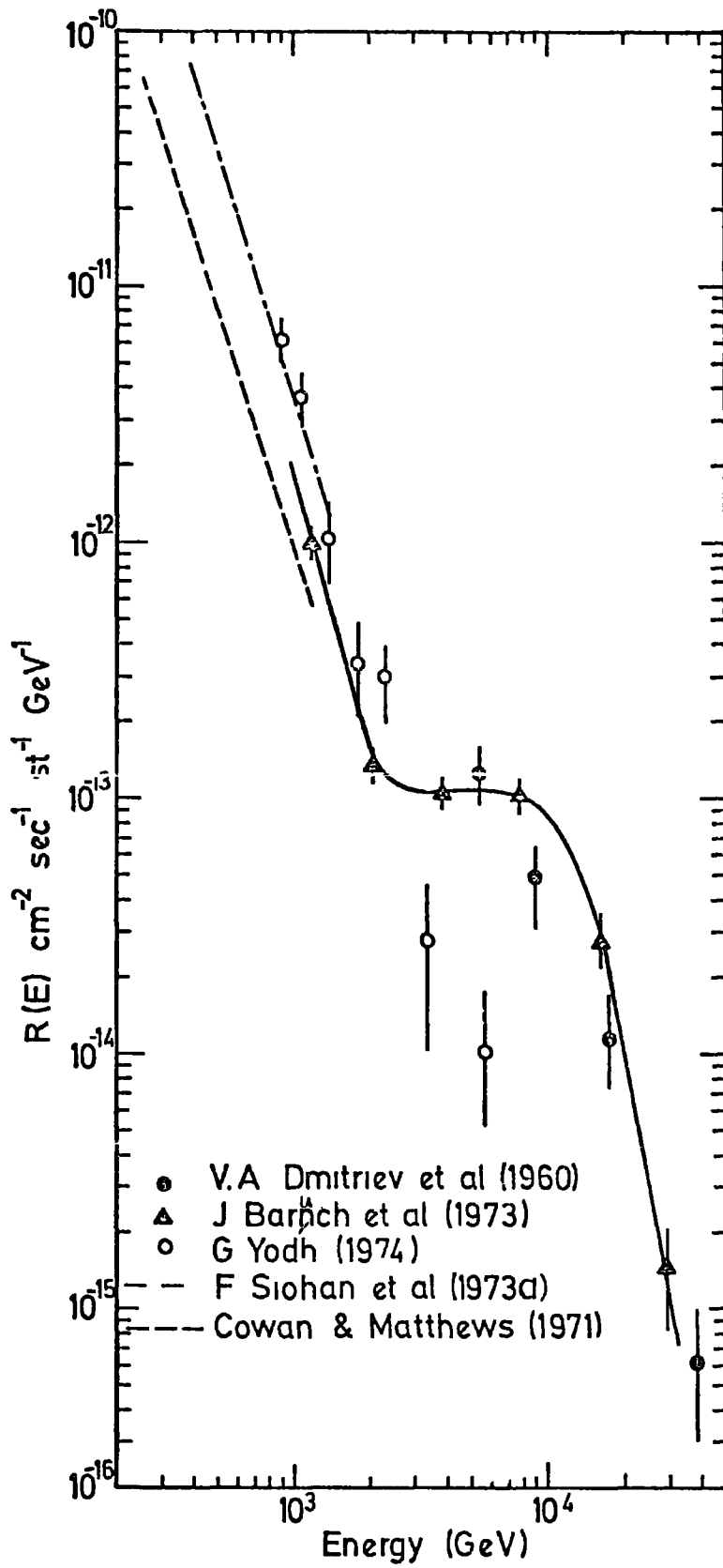


Figure 2.5

Summary of the sea level vertical high energy hadron spectrum.

of the cascade. They estimate cascades are at maximum development if the ratio of the number of electrons (burst size) in the top tray of the proportional counters is within a factor 2 of those recorded in the bottom tray.

The triggering threshold was taken as more than 1,500 electrons in each layer, or by a minimum shower size recorded by the shower detectors. The absolute energy calibration of the apparatus was made by studying its response to artificially accelerated electrons of known energies, the response at other energies being calculated from the cascade curves given by Buja (1963). However, the result given by Baruch et al. (1973) for the differential energy spectrum of all hadrons at sea level shows a step 'kink' between 2.0 - 8.0 TeV in the spectrum. It was suggested that this result in which the slope changes can be interpreted as evidence for a new particle called "Mandela" of mass $40 - 70 \text{ GeV}/c^2$, a mean life time $2 \cdot 10^{-7}$ second and an interaction length of $1,000 \pm \frac{1000}{700} \text{ g cm}^{-2}$. The fraction of the energy, K_γ , given to the electromagnetic cascade by this particle would be 40 - 95%.

The differential energy spectrum of all hadrons measured by Baruch et al. with the kink appearing at $\sim 2 \text{ TeV}$ is shown in figure 2.5.

2.3.10 G.B. Yodh (1974)

A result on high energy hadrons at sea level using the same ionization calorimeter discussed in section 2.3.6 has been given by Yodh (private communication). The new results were extended to a few TeV, and the differential energy spectrum measured in a running time of 447 hours and energies between 1 TeV to 6 TeV is also shown in figure 2.5.

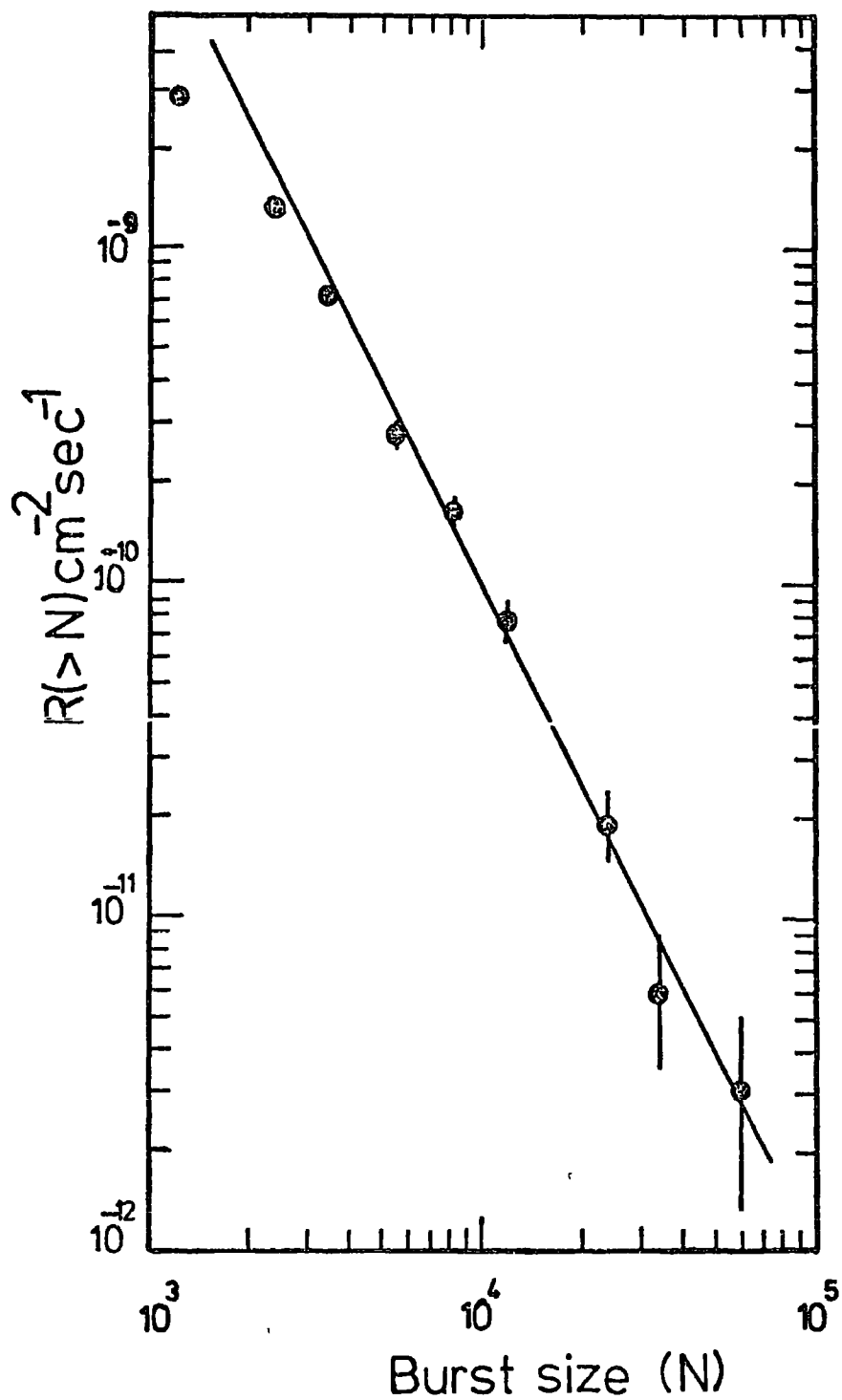


Figure 2.6

The integral spectrum of bursts from single NAP(hadrons) at sea level, given by Babecki et al. (1961).

The spectrum can be represented by $R (> N) = AN^{-1.97}$

2.4 Measurements at high altitude

2.4.1 Kaneko et al. (1971)

They have observed at Mt. Chacaltaya, 550 g cm^{-2} , a high energy nuclear burst produced by hadrons with energy greater than $3 \cdot 10^{12}$ eV and without accompanying shower particles. These are most likely to be produced by surviving primary protons arriving at Chacaltaya without interaction in the atmosphere. The basic experimental arrangement consists of 10 vertical telescopes each consisting of 2 and 3 unshielded counters placed above one shielded counter under 386 g cm^{-2} of absorber. The integral energy spectrum of surviving primary protons is shown in figure 2.7.

2.4.2 Grigorov et al. (1965)

The measurements were made at Mt. Aragats, $\sim 700 \text{ g cm}^{-2}$, using an ionization calorimeter of 10 m^2 operating area. The calorimeter contained 12 trays of ionization chambers placed under filters of lead, graphite and iron. The flux of nuclear active particles of energy up to $3 \cdot 10^{12}$ eV has been measured. The 633 events were recorded during 1,015 hours and from the measured angular distribution, $\cos^6 \theta$ was found. The integral energy spectrum of the particles without air accompanying showers is shown in figure 2.7.

2.4.3 Jones et al. (1970)

A cosmic ray experiment at Echo Lake, 700 g cm^{-2} , Colorado, has been used to study the interactions of cosmic ray hadrons with protons. This experiment, which used 2000 - liter liquid hydrogen target, spark chambers and an ionization calorimeter was carried out at Echo Lake, and produced approximately 1,000 interactions above 70 GeV. The calorimeter was constructed from iron and plastic scintillator with a total thickness $1,130 \text{ g cm}^{-2}$. The energy of an incident hadron was determined from the pulse heights of the calorimeter counters. The energy resolution of the calorimeter was estimated to be about $\pm 15\%$. From the data on hadrons, the integral flux was represented by $N(>E) = (3 \times 10^{-7})E^{-2} (\text{m}^{-2} \text{ st}^{-1} \text{ sec}^{-1})$, with E in GeV. The slope of the spectrum is greater than that usually found because the anticoincidence counters reject a larger fraction of high energy hadrons as they are more probably accompanied by secondaries from prior collisions in the atmosphere. The result is shown in figure 2.7.

2.4.4 Siohan et al. (1973b)

An ionization calorimeter has been operated at an altitude of 2,900 meters (730 g cm^{-2}) at SRCRL in New Mexico, to measure the charged hadron flux. The calorimeter is the same as the one operated at sea level and is described in section 2.3.6. The triggering threshold of the calorimeter varied between 55 and 100 GeV. A large plastic scintillator of total area 3.3 m^2 was placed in anticoincidence to record the shower accompanied hadrons.

The differential vertical flux of charge single hadrons unaccompanied over 5 m^2 is shown in figure 2.7 with:

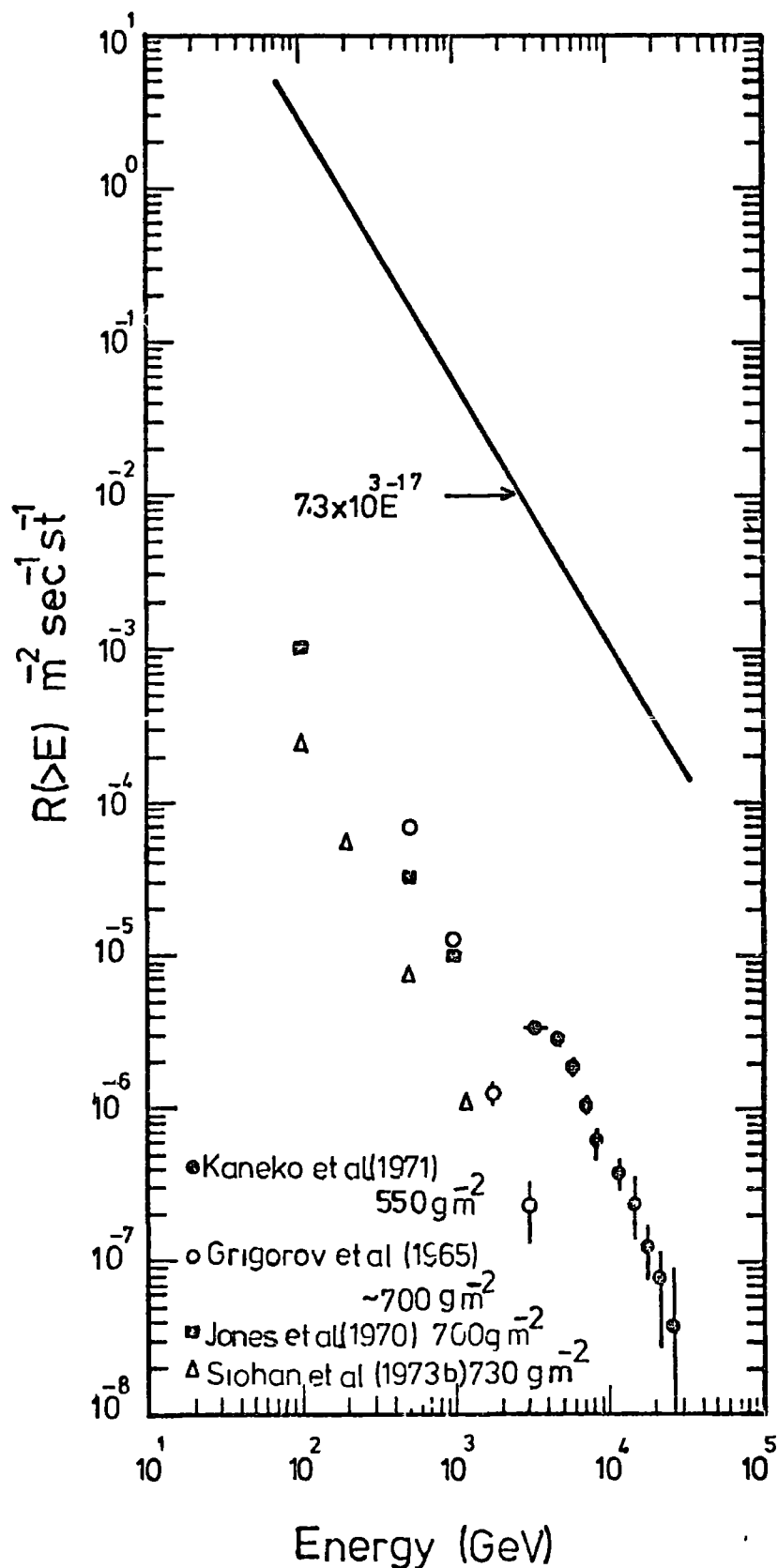


Figure 2.7

Integral hadron spectrum $R(>E, X)$. The upper line for $X = 0$ corresponds to the primary spectrum of protons given by Ryan et al. (1972). The lower points corresponds to unaccompanied hadron spectra as measured at different depths in the atmosphere. The difference between the upper and lower curves is a measure of the interaction length of protons in air, (after G. Yodh, 1972).

$$dN/dE = (7.95 \pm 0.9) \times 10^{-5} (E/100)^{-3.2 \pm 1} \text{ particles/ m}^2 \text{ sec st GeV}$$

for $100 < E < 1,200$ GeV.

2.5 Discussion

In this survey, the best estimate momentum spectrum for protons between 1 - 100 GeV/c has been given. The shape of the spectrum in this region is consistent with that expected for a primary spectrum with constant exponent when ionization loss in the atmosphere is taken into consideration; it is assumed that the protons observed at sea level have traversed half the atmosphere on average, as neutrons. The previous measurements by Brooke and Wolfendale are in good agreement with the later measurements of Diggory et al.

Also the best measurements on the neutron energy spectrum summarised by Ashton (1973) provided the best evidence for the behaviour of the nucleon spectrum at high energies, this measurement gives a slope

$$\gamma = -2.95 \pm 0.1 \text{ in the energy range } 50 - 1,000 \text{ GeV.}$$

The spectrum of negative pions has been measured by Brooke et al. and Diggory et al. The intensities obtained in Diggory et al. are systematically higher by a factor of two up than those of Brooke et al., part of this discrepancy may be due to the different normalization procedures used to obtain the flux but there still remains a discrepancy of more than 1.5 at all momenta. No direct measurements have been made on the high energy ($> 10^{11}$ eV) pion flux, the only method of separation pions from charged particles producing bursts is the statistical method which will be discussed in chapter 6. The most interesting thing in this survey is the result given by Baruch et al. showing a bump in the hadron spectrum between 210^{12} eV to 810^{12} eV which they suggested is due to a new particle (this

is discussed in detail in section 2.3.9). Unfortunately there is no other experimental result that covers this region. Dmitriev et al. measurements started after the kink, they found there is an increase in the intensity of their bursts and the slope of their differential spectrum is $\gamma = -2.5$. Babecki et al. in their measurements of bursts covered the region where the bump is, but they did not find it. G. Yodh shows in his later measurements that there is no change in the slope in his spectrum ($\gamma = -3.6$). However, if we start to look to the experimental results at high altitude, one can see that most of them covered the bump region, but also there is no sign of any step. Baruch et al. suggested that the experiments which study high energy hadrons at high altitude might miss it, because the new particle has a very long interaction length $1000 \pm \frac{1000}{700} \text{ g cm}^{-2}$. One can derive intensities at sea level by multiplying them by a factor $e^{-X/\lambda}$ where X is the depth in g cm^{-2} and λ is the interaction length. However, the work in this thesis covered a very wide energy range in the spectrum and the result obtained will be discussed in chapter 5.

CHAPTER 3

THEORY OF THE PRODUCTION OF BURSTS IN THICK IRON AND LEAD ABSORBERS

3.1 Introduction

It was noted in chapter 2 that most of the experiments used to measure hadron energy spectra and study the interaction of high energy hadrons at different depths in the atmosphere usually employ some type of ionization calorimeter. Such calorimeter consist of a sandwich arrangement of thin absorbers and detectors used to measure the development of the cascade produced in the nuclear interaction. The energy of the hadron can be estimated from the ionization produced by the particles in the cascade.

In this experiment two different absorbers were used (iron and lead) and a single detector under each absorber was used to measure the number of particles emerging from the absorber due to a hadron interacting strongly with the target nucleus. The energy of the incident hadrons can be determined if the physical processes occurring are understood and can be predicted. In this chapter the problem of a hadron (nucleon, pion) initiating a nuclear-electromagnetic cascade has been studied and a method of obtaining the energy of the hadron will be discussed. Initially pure electron-photon cascades will be discussed, consideration then being extended to nuclear-electromagnetic cascades.

3.2 Outline of the cascade process

Assume a hadron incident on a dense absorber of depth, X , then the

probability that the hadron undergoes a strong interaction follows the exponential form $e^{-x/\lambda}$ where λ is the interaction length. When the hadron interacts, secondaries will be produced (mainly pions). If the incident particle is a nucleon then a fraction of 1.8 energy goes to the secondary pions and the nucleon continues through the absorber, possibly to interact again. If the incident particle is a charged pion then it loses all of its energy to the secondary pions.

It was assumed that the number of charged pions produced in each interaction is twice the number of neutrals. The charge pions interact deeper in the absorber producing more pions to contribute in the cascade again. The neutral pions decay to two gamma rays which can then initiate an electron-photon cascade either by materialising into an electron-positron pair or by undergoing Compton scattering. If the electron (positron) energy is above the critical energy of the medium, then the electron can produce more photons by radiation loss (bremsstrahlung), and the photon in turn producing more electrons. Because of this, an electron-photon shower is built up in the medium. After a certain depth in the medium the cascade reaches a point where the mean energy of the electrons in the cascade falls below the critical energy of the medium and the cascade starts to die out because the collision losses become more important than the radiation loss and all the energy is lost in excitation and ionization in the medium.

It is important to point out that the secondary pions and the cascade development moves in the absorber almost in the same direction as the parent incident hadron this means the cascade has been considered as one-dimensional process in the medium.

Over a considerable time many workers have attempted to explain theoretically the behaviour of an electron-photon cascade in various media. The approach can be divided into two categories: 1. The analytical method,

in which a set of diffusion equations are used to represent the development of the shower at a given depth. 2. The Monte Carlo method, in which the primary particle and all subsequent particles are followed through the material.

3.3 One dimensional electron-photon shower development

3.3.1 Basic equations

To derive the number of electrons and photons at a given depth in an absorber produced by a primary electron or photon of energy E is mathematically very difficult.

The equations of the one-dimensional cascade theory, which include pair production and Compton scattering by photons and bremsstrahlung and ionization losses by electrons are derived in detail by Rossi (1952) by considering the various production and absorption phenomena taking place in an infinitesimal layer of thickness dt . The diffusion equations relating the number of electrons and photons at depth, t , to the number of electrons and photons at depth $(t + dt)$ are:

$$\begin{aligned} \frac{\delta \pi(E, t)}{\delta t} = & \int_E^{\infty} \gamma(E', t) \varphi_p(E, E') dE' + \int_E^{\infty} \pi(E', t) \varphi_e(E', E' - E) dE' \\ & - \int_0^E \pi(E, t) \varphi_e(E, E') dE' - \beta \frac{\delta \pi(E, t)}{\delta E} \end{aligned}$$

$$\frac{\delta \gamma(E, t)}{\delta t} = \int_E^{\infty} \pi(E', t) \varphi_e(E, E') dE' - \int_0^E \gamma(E, t) \varphi_p(E, E') dE'$$

Where, $\pi(E, t) dE$ represents the number of electrons of energy E to

$E + dE$ at depth t , $\gamma(E,t) dE$ is the number of photons of energy between E and $E + dE$ at depth t , β is the average ionization loss per radiation length, $\varphi_e(E,E')$ is the differential probability per radiation length for the production of a photon of energy E' by an electron of energy E and $\varphi_p(E,E')$ is the differential probability per radiation length for the production of an electron of energy E' by a photon of energy E .

To solve these equations analytically certain simplifying assumptions can be made. For example, the equations can be solved by numerical integration using exact probabilities for each process.

3.3.2 The analytic solution using Approximations A and B

Rossi (1952) has given in detail the assumption of Approximations A and B to solve the diffusion equations. If we consider energies large compared with the critical energy of the medium then the theory of the showers can be developed by considering only radiation processes and pair production (Approximation A). Furthermore, if the energies are also large compared with $137 M_e c^2 Z^{\frac{1}{3}}$, radiation processes and pair production can be described by the asymptotic formula for complete screening, in this Approximation A the collision processes and Compton effect were neglected. It is interesting to note that Approximation A shower theory gives identical results for all materials provided thicknesses are measured in radiation lengths. When the energies involved become comparable with the critical energy the Compton effect can be neglected but collision processes must be taken into account with the pair production and radiation process (Approximation B). Also, it should be noted that Approximation B yields identical results for all elements provided one measures thicknesses in radiation lengths and the energies in terms of the critical energy.

3.3.3 Method of moments

The method of Approximations A and B which utilise what are known as functional transformations to solve the diffusion equations gives a complete solution to the problem describing one-dimensional cascades in light media. The method, however, breaks down in light elements when the energy of the particle which initiates the cascade becomes comparable with the critical energy of the medium in which the shower develops. Since in heavy media (high Z) this becomes invalid because the total photon absorption coefficient depends strongly on energy and the back scattering of electrons plays an important role.

The approach, the method of moments, calculates the average behaviour of the cascade (i.e., the number of electrons or photons with energy greater than E which emerge from a layer of thickness t). These moments are simpler to compute than the probabilities given on the right hand side of the diffusion equations. The accuracy of this method depends on the order to which the moments are calculated. This approach has been used by Ivanenko and Samosudov (1959, 1967a, 1967b) who evaluate the first four moments, with an accuracy of 5 - 10% to obtain the transition (shower) curves. Ivanenko and Samosudov have produced a series of shower curves covering a wide range of energies for different absorbers (copper, lead, iron, aluminium and graphite) and for different cut off energies for the electrons and photons. The curves have been calculated taking into account the energy dependence of the total photon absorption coefficient and also include the effect of the increased track length due to multiple scattering of the electrons.

Figures 3.1 and 3.2 show the transition curves for photon - initiated cascades in iron and lead for an energy cut-off of ~ 1 MeV.

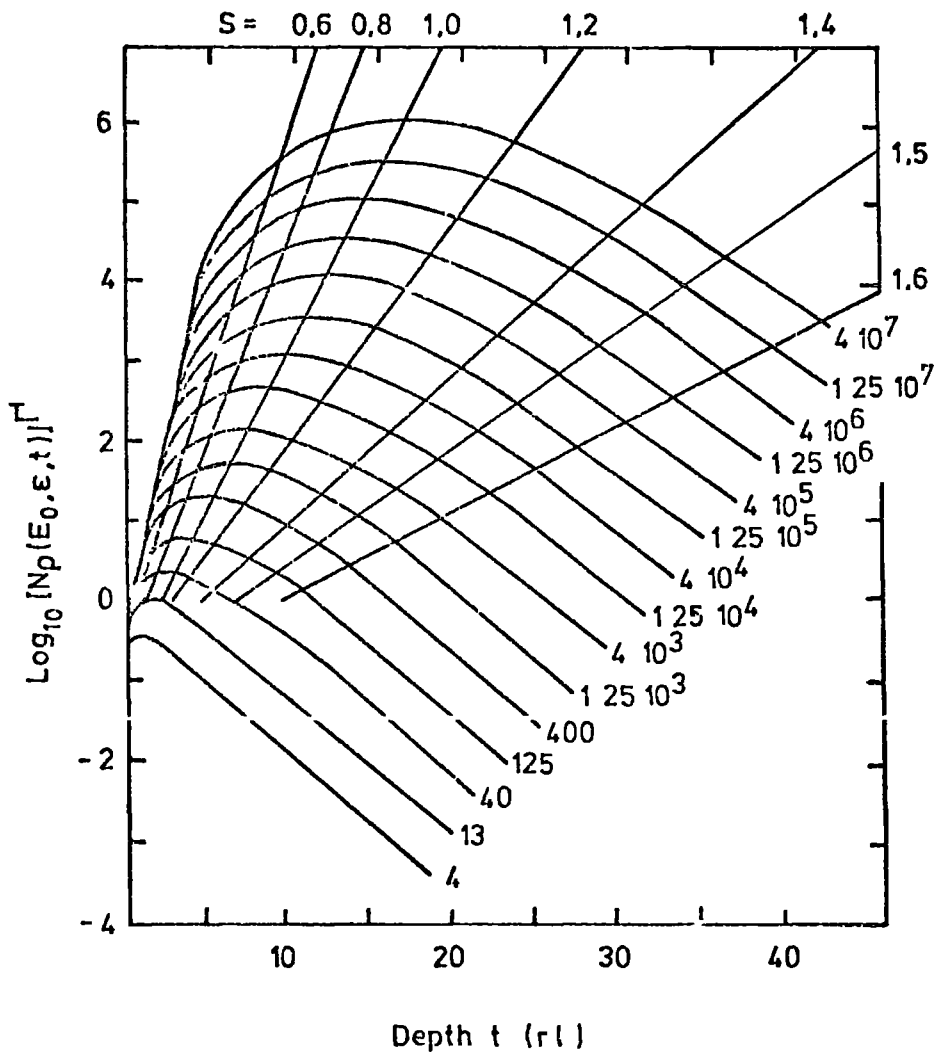


Figure 3.1

Transition curves for photon induced cascades in Iron predicted by Ivanenko and Samosudov. The number by each curve refers to the energy of the primary photon. All energies are in units of 0.437β , where β is the critical energy of the absorber. The cut-off energy ϵ is 0.1 or ~ 1 MeV. Lines of constant age parameter (s) have been calculated from Approximation A.

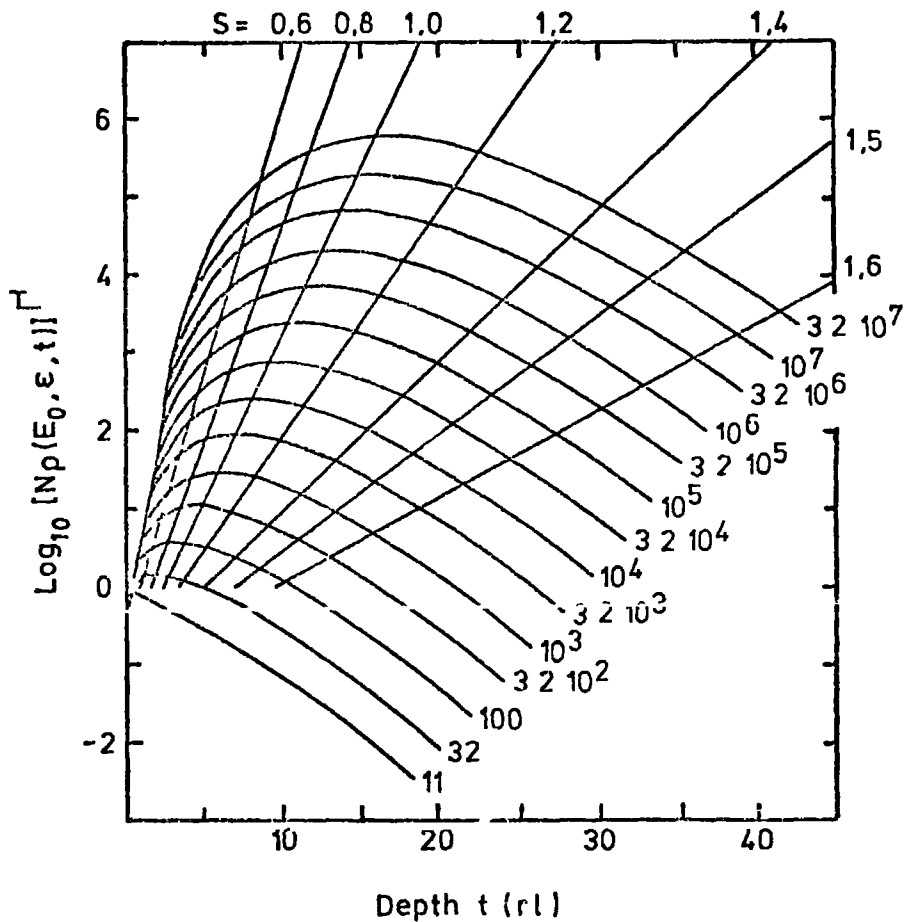


Figure 3.2

Transition curves for photon induced cascades in lead predicted by Ivanenko and Samosudov. The number by each curve refers to the energy of the primary photon. All energies are in units of 0.437β , where β is the critical energy of the absorber. The cut-off energy ϵ is 0.35 or ~ 1.62 MeV. Lines of constant age parameter (s) have been calculated from Approximation A.

3.3.4 Monte Carlo method

Several Monte Carlo calculations have been performed on the development of electron-photon showers in different materials. The method is based on following the primary electron or photon and its progeny continuously through the absorber. However, this gives accurate results if one can use the exact interaction probabilities. The results concerning the average shower behaviour are subject to fluctuations because the error depends on the number of simulations performed at each energy. One of those results is given by Messel and Crawford (1970). They studied the three dimensional cascade problem in copper for various primary and secondary energies. They produced extensive tables of electron and photon number distributions, together with radial and angular distributions.

3.3.5 A comparison between calculations and experiments

Coats (1967) has made a comparison between some experimental results on electron-photon cascade showers in iron with the results of Ivanenko and Samosudov and finds a reasonable agreement.

A comparison has also been made between experimental results and calculations for two different primary electron energy induced cascades in lead. Figures 3.3 and 3.4 shows this comparison. At low energy the calculation of Ivanenko and Samosudov and the Monte Carlo simulation of Crawford and Messel look in a good agreement (figure 3.3). Two of the experimental results show higher curves above the calculations and the experimental curve of Heutch and Prescott. This apparent disagreement between the experimental results is likely to be due to experimental difficulties in defining the cut off energy. The results at high energy show there is no direct experimental results or Monte Carlo results, but

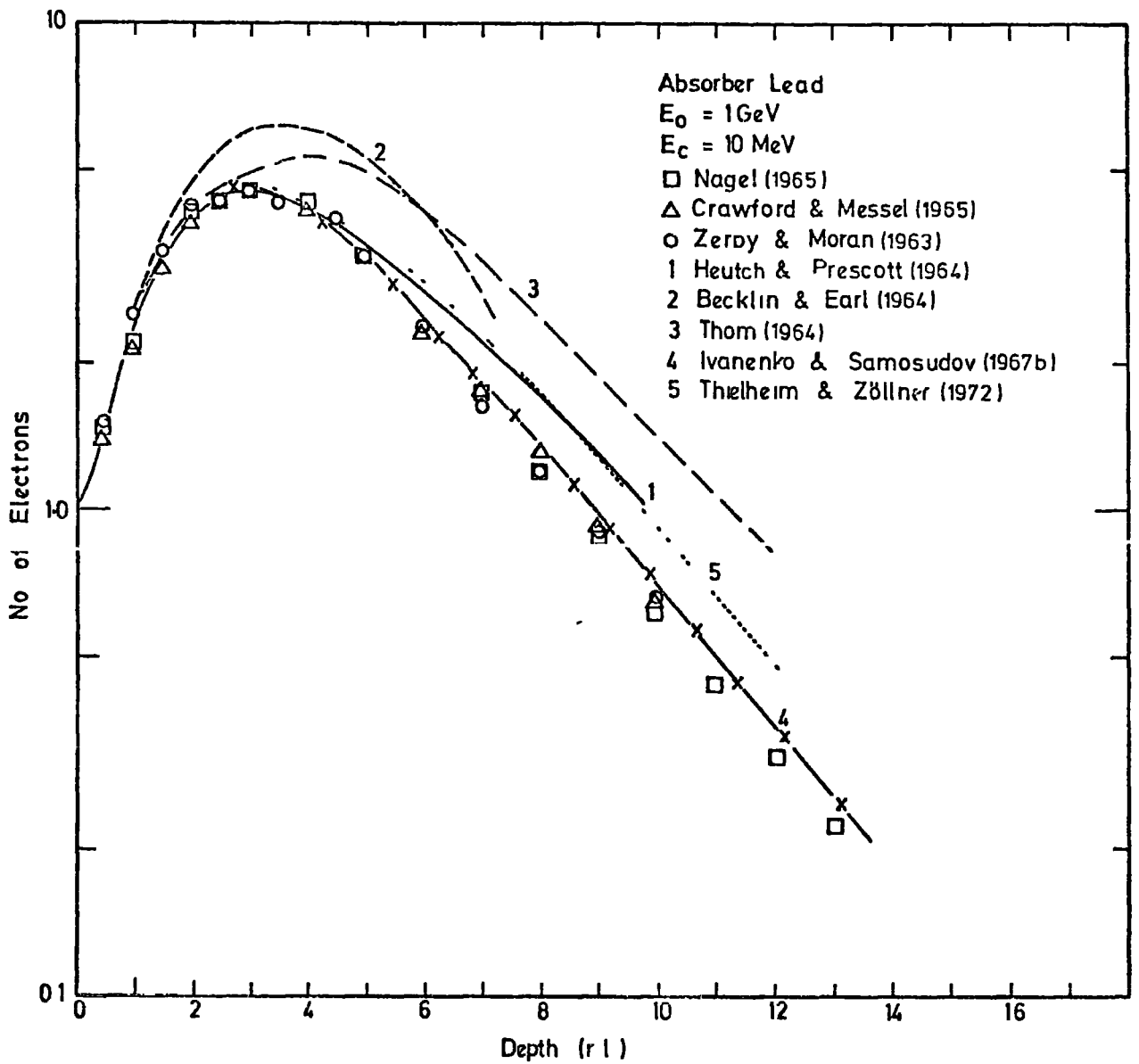


Figure 3.3

Transition curves in lead absorber for primary electron of 1 GeV energy. The cut-off energy E_c is 10 MeV. The points are results of Monte Carlo calculations, curves, 1, 2 and 3 refer to experiments and curves 4 and 5 are the results of calculation

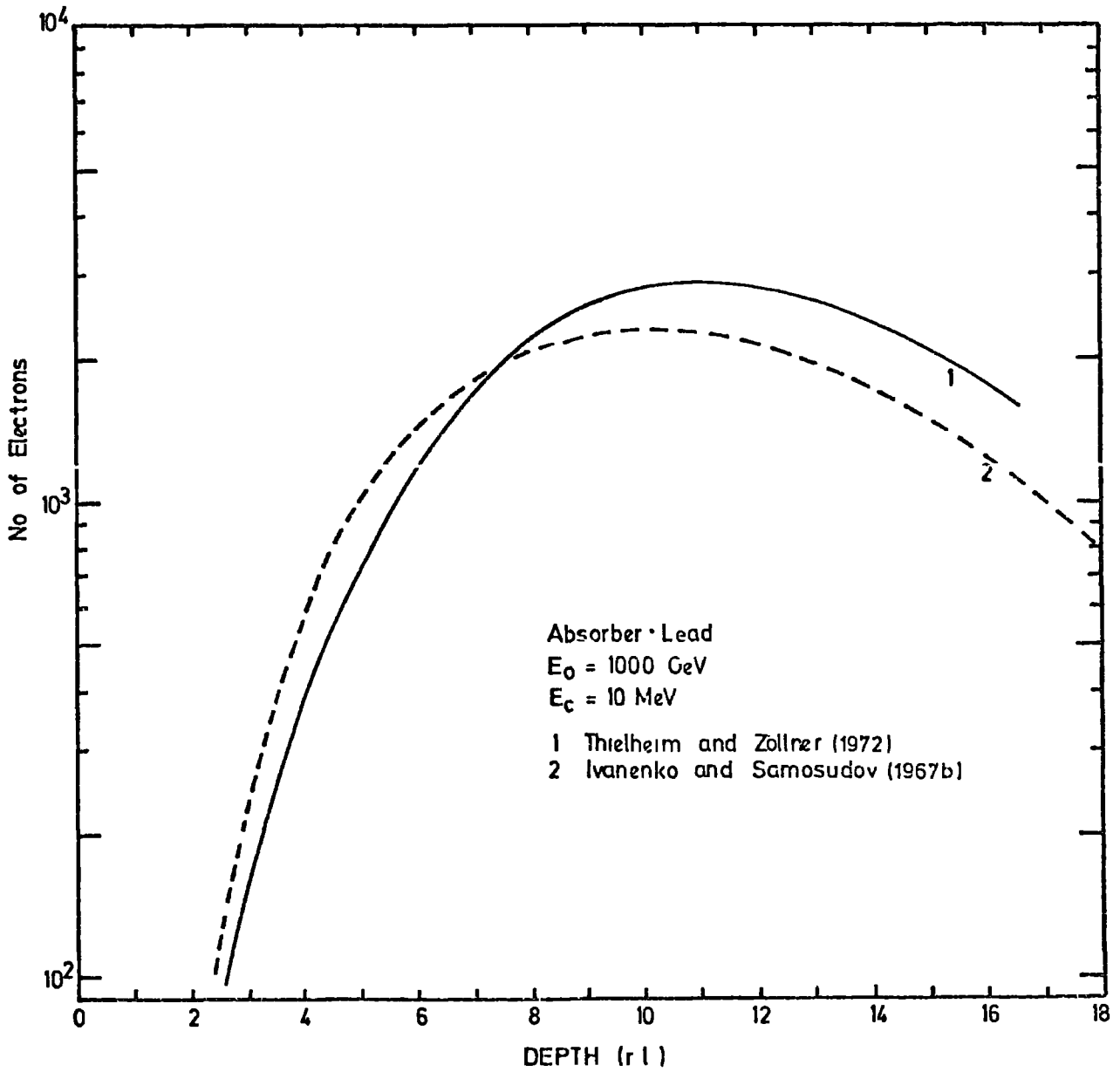


Figure 3.4

Transition curves in a lead absorber for primary electron of energy 1000 GeV. The cut-off energy E_c is 10 MeV. Curves 1 and 2 are results of calculations.

the numerical calculation of Thielheim and Zollner are shown (figure 3.4) with the calculation of Ivanenko and Samosudov.

3.4 Simulation of nuclear interactions in a thick absorber

3.4.1 General remarks

Any experiment performed to measure the energy spectrum of hadrons depends on a knowledge of their interaction characteristics. The energy of the interacting hadron has to be estimated from the burst size, that is measured by a scintillation counter and in order to do this a model for their interaction with the target nuclei has to be adopted.

Several people have done calculations using the Monte Carlo technique to study the nuclear-electromagnetic cascade in their experiment. Jones (1969a, 1969b) has simulated the longitudinal nuclear-electromagnetic cascade development in an ionization spectrometer using a Monte Carlo calculation. Calculations have been performed to correspond to an actual spectrometer which was exposed to 10, 20.5 and 28 GeV/c incident protons at Brookhaven. The comparisons of the calculated and measured particle distributions indicate that the Monte Carlo method used does indeed provide a reasonable simulation of the nuclear electromagnetic cascade development in the longitudinal direction. Vatcha et al. (1972) have performed Monte Carlo calculations for hadrons interacting in iron. The simulations were carried out for the same geometry as was used in a multiple cloud chamber. From the calculation of the hadron electromagnetic cascade the relation between the primary hadron energy and the track lengths corresponding to different stages of development and absorption of the cascade were obtained. They found it is possible to determine the energy up to 10^{13} eV with an

accuracy better than 50% in the chamber.

Vatcha et al. conclude that the cascades in the energy range 1 - 10 TeV show much faster absorption after the cascade maximum than that predicted by any of the models used. They suggest that a higher inelasticity combined with a higher multiplicity could explain their observation. Alternatively, Vatcha et al. suggested that a possible interpretation for this feature is the gammanisation process suggested by Nikolsky (1967) in which high energy photons are produced directly in nuclear interactions above some threshold.

The total number of electrons has been calculated by Pinkau and Thompson (1966) for different air, glass and iron absorbers using the model of Cocconi, Koester and Perkins (CKP), the calculation helped in the design of the ionization spectrometers for the measurement of the total energy of the particles. In this experiment the total number of electrons observed in the bottom of the absorber due to nuclear interaction was calculated using a model basically similar to the CKP model. This will be discussed in the next section.

3.4.2 Model of nuclear interactions

An average treatment calculation was made to calculate the nuclear cascade in a thick absorber produced by incident protons and pions on iron and lead absorber. The properties of the model introduced for nuclear interaction can be summarized as follows:

- (a) The hadron is incident vertically on the absorber.
- (b) The hadron energy loss by ionization processes were neglected.
- (c) The incident hadron was allowed to interact at successive depth t (radiation length) according to the probability distribution:

$$P(t) dt = \frac{1}{\lambda} e^{-\left(\frac{t}{\lambda}\right)} dt \quad \text{where, } \lambda \text{ is the interaction}$$

length of the primary particle in radiation lengths.

- (d) The inelasticity, K , for the pions was assumed to be unity, i.e. all its energy goes to the secondary particles produced in each interaction. For protons, the mean inelasticity was assumed to be a function of the absorber material.
- (e) The mean multiplicity of the secondary particles is of the form:

$$\bar{n}_s = 3.0 A^{0.19} (KE)^{\frac{1}{4}}$$

where A is the atomic mass of the absorber and E is the energy of the incident particle. This equation is based on a combination of surveys (e.g. Greider 1970, Wdowczyk 1973) and on the hydrodynamical model Belenkij and Landau (1956). All the secondary particles are assumed to be pions and the number of charged pions (π^\pm) twice the neutral pions (π^0).

- (f) It was assumed that in the nuclear interaction all secondary pions created moved in the forward cone and the mean multiplicity was used to determine the mean energies of the forward pions. Each pion has on average equal energy and the probability energy distribution for these secondaries in the laboratory system is given by:

$$P(E) dE = e^{-E/E'} \frac{dE}{E'} \quad \text{where, } P(E)dE \text{ is the differential probability of the secondary pions having energy between } E \text{ and } E + dE, E' \text{ is the mean energy of the forward cone.}$$

Having all these assumptions known, the method adopted to determine the nuclear cascade in a lead and iron absorber was as follows:

The absorber (15 cm of iron, 15 cm of lead) was divided into four

layers (A,B,C and D) of equal thickness. The incident primary particle with a given energy E GeV was allowed to interact in each layer according to the probabilities calculated from the equation given item C. In the first interaction secondary pions are produced and it was assumed $2/3$ of the pions are charged and $1/3$ neutral. A cut-off was applied for the charged pions with energy ≤ 1 GeV and for neutral pions with energy ≤ 0.2 GeV. The total number of charged pions with energy > 1 GeV and the total number of neutral pions of energy ≥ 0.2 GeV was calculated using the CKP distribution (item C). The mean energy for the charge pions with energy cut-off > 1 GeV is $(1 + E')$ GeV and for neutral pions with energy cut-off ≥ 0.2 GeV is $(0.2 + E')$,

This was calculated from:

$$\bar{E} = \frac{\int_E^{\infty} E e^{-E/E'} \frac{dE}{E'}}{\int_E^{\infty} e^{-E/E'} \frac{dE}{E'}}$$

where, E' is the mean energy of produced pions in GeV.

The neutral pions were assumed to decay immediately into two photons with equal energy which can then initiate an electron-photon cascade. The charged pions either interacted deeper in the absorber or emerged from it without interaction. The average depth of the successive interactions was calculated from:

$$X = \lambda_{\pi} - \frac{X}{\exp(X/\lambda_{\pi}) - 1}$$

where X is the distance from the bottom of the absorber for the first interaction. (The first interaction is assumed to happen in the

middle of the layers A, B, C and D). λ_{π} is the interaction length of the pion. As mentioned before if the incident primary particle is a pion then all its energy goes to the secondary pions because the inelasticity was assumed to be unity. But if the incident primary was a proton, the mean inelasticity was assumed to be a function of the absorber material. Jones et al. (1969) have given a summary, figure 3.5, showing the relationship between the mean inelasticity and the atomic mass number A. The inelasticity of protons was taken to be 0.63 for iron and 0.8 for lead absorber. Different values of K was given by various workers. Bradt and Rappaport (1967) assumed λ value of the inelasticity of protons interacting with air nuclei to be a flat distribution between $K - 0.25$ and $K + 0.25$ where K is 0.5.

The nuclear cascade terminated when all of the hadrons (primary and produced in the interactions) had either passed out of the absorber or their energy had fallen below the cut-off.

The energy cut-off of 1 GeV for charged pions is based on the fact that the inelastic cross-section of pions drops very sharply at this value (Hayakawa 1969). This means that the pions would not contribute to the cascade. A cut-off was applied also for created neutral pions π^0 if their energies were less than 0.2 GeV since the photon produced by the decay of the π^0 almost at rest would not contribute significantly to the electromagnetic cascade. A full list of values of constants used in this calculation is given in table 3.1.

3.5 Result of the Calculation

3.5.1 Energy - burst size relation

Different primary energies: 10 GeV, 100 GeV, 1 TeV and 10 TeV were

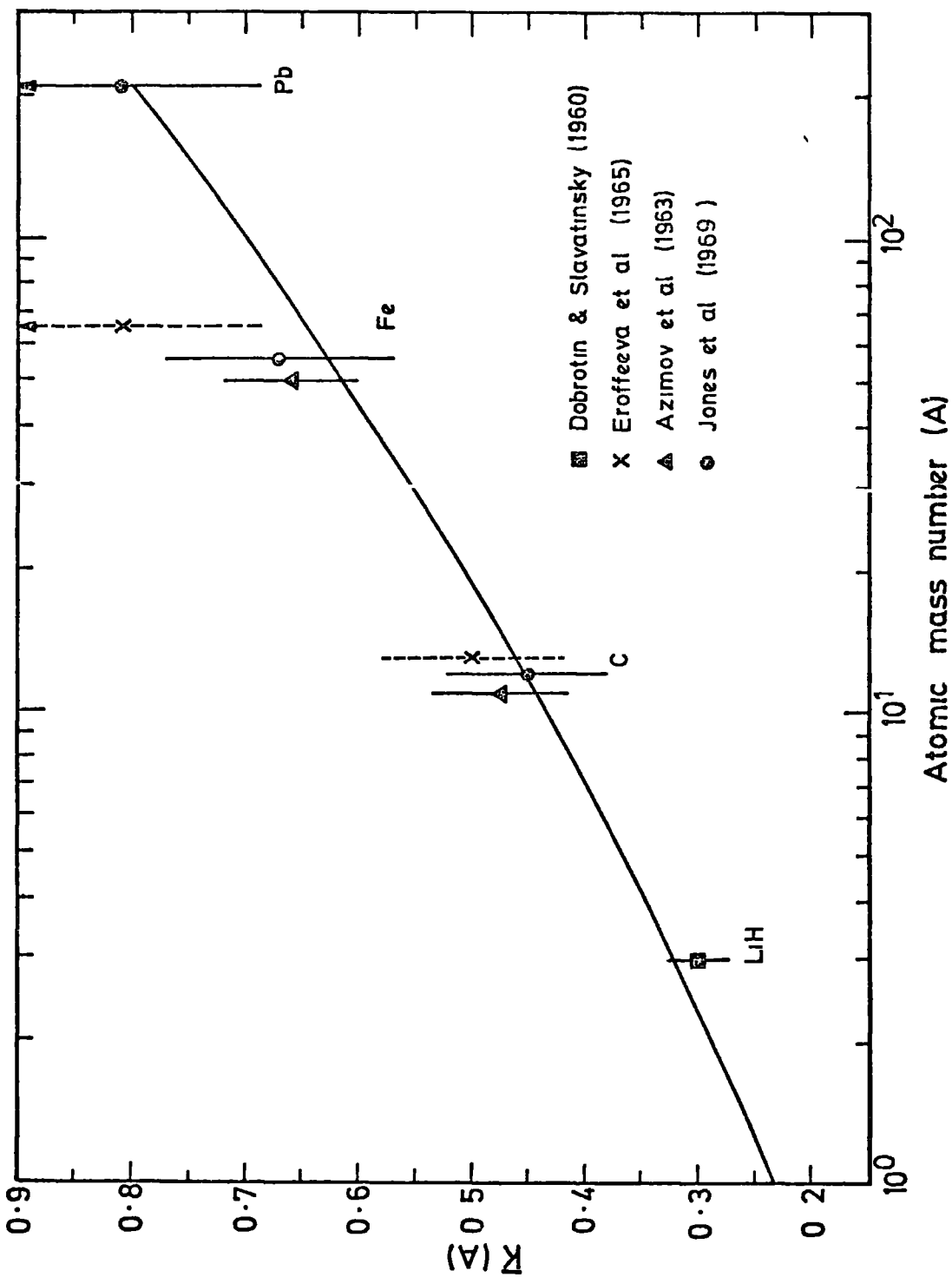


Figure 3.5

The variation of mean inelasticity with atomic number for proton interactions with three different nuclei (Carbon, Iron, lead). A comparison has been made between the experimental values given by different workers and the relation $\bar{K}(A) = 1 - (1 - \bar{K}_{n-n})^\alpha$, $\alpha = A^{-0.45}$, the curve is normalized to the value $\bar{K} = 0.45$. (After Jones et al. 1969).

Material	Density (g cm ⁻³)	E ₀ (MeV), with density effect.	Radiation length X ₀ (g cm ⁻²)	λ _π	λ _p
Fe	7.6	21	14.1	11.6 X ₀	9.94 X ₀
pb	11.34	7.6	6.5	34.54 X ₀	33.08 X ₀
A	2.7	-	24.5	5.37 X ₀	4.25 X ₀
glass	2.5	-	26.3	5.01 X ₀	3.95 X ₀

Table 3.1(a)

A list of constants used in the calculation.

Material	Mean multiplicity of protons \bar{K}_p	Mean multiplicity of pions \bar{K}_π
Fe	0.63	1.0
pb	0.80	1.0

Table 3.1(b)

The mean inelasticities used for proton-nucleus
and pion-nucleus collisions in the calculation.
See figure 3.6.

taken to calculate the burst size energy relation for protons and pions incident on a 15 cm lead and 15 cm iron absorber. The average number of electrons obtained as a function of incident particle energy are shown in figures 3.6 and 3.7. It can be seen that for a given material the pion and proton curves are almost parallel, the difference in the burst size (electron number) for a given energy being approximately proportional to the inelasticity. As it is noted from the two figures, there is almost a linear relationship between burst size and the energy ($E \sim N$) for protons and pions in lead over all the energy ranges. In the case of iron at high energies the curves show a flattening. One can interpret this as due to the fact that the cascade at high energy can not fully develop in the relatively thin iron absorber thickness 8.19 radiation length. Whereas in the lead saturation is not reached because of the relatively greater depth available for the cascade development, thickness 26.17 radiation length.

Also, 100 TeV proton induced cascades in lead were calculated and this is shown in figure 3.7.

3.5.2 Burst size distribution

The average treatment gives useful information about the average properties of the cascade through the absorber. The distributions of the produced burst size below the iron and lead as a function of the depth of the first interaction are shown in figures 3.8 and 3.9 for pions and protons with different energies incident on iron, figures 3.10 and 3.11 for pions and protons with different energies incident on lead. As shown in figures 3.8 and 3.9 there is no maximum for the burst size distribution at high energies, because as mentioned before the cascade is

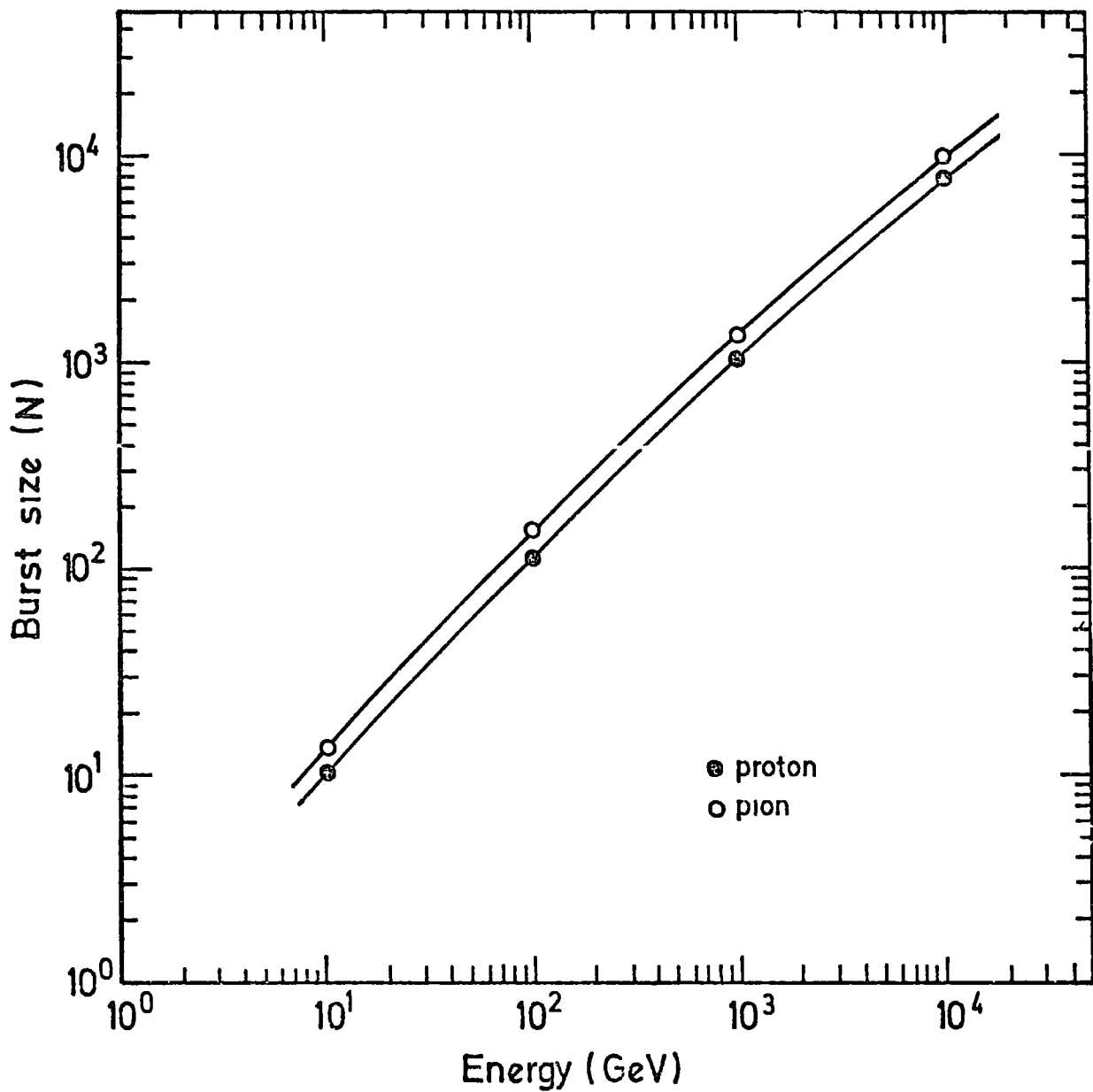


Figure 3.6

The average burst size (N) produced by primary protons or pions incident on 15 cms iron as a function of energy.

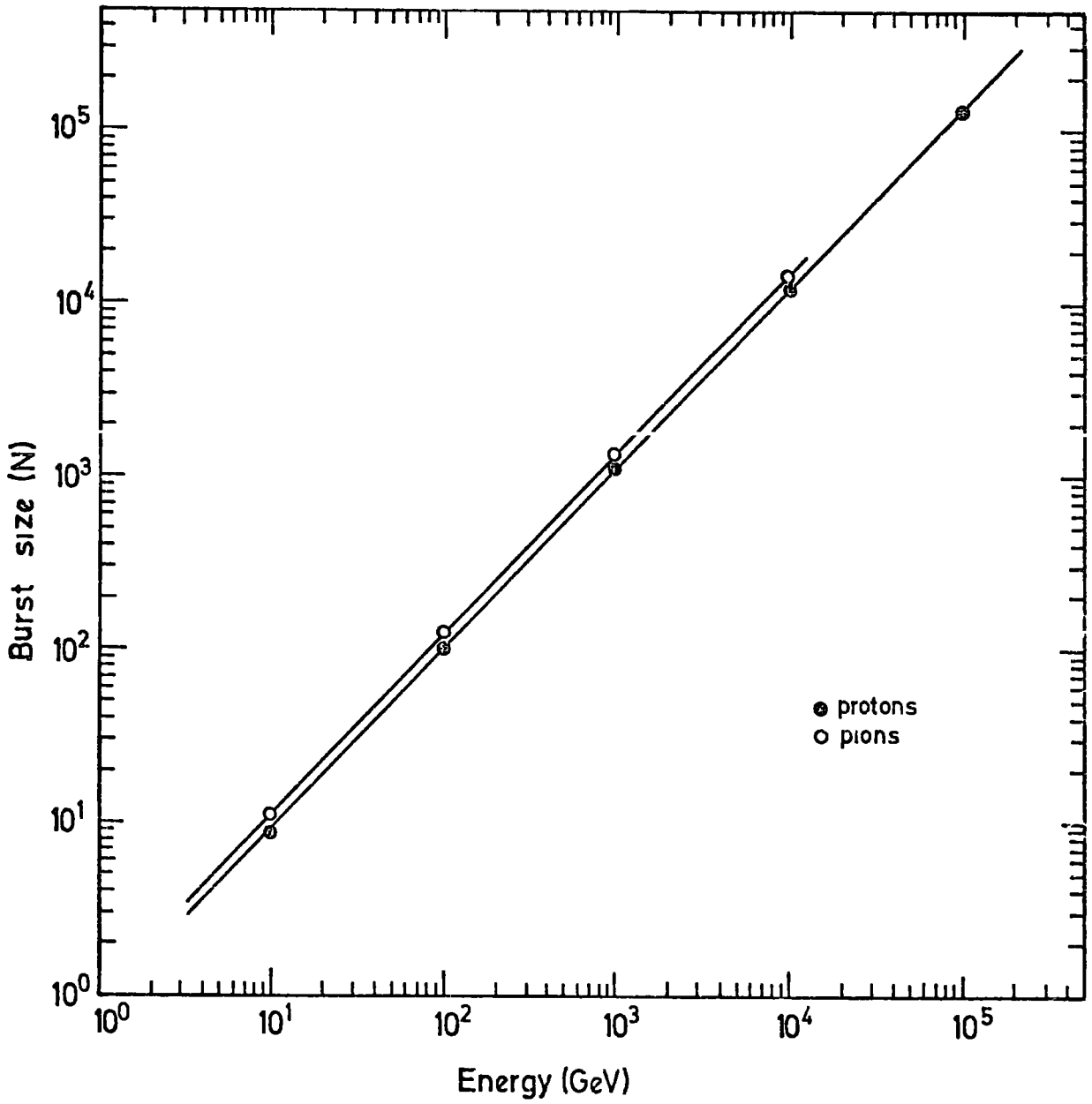


Figure 3.7

The average burst size (N) produced by primary protons or pions incident on 15 cms lead as a function of energy.

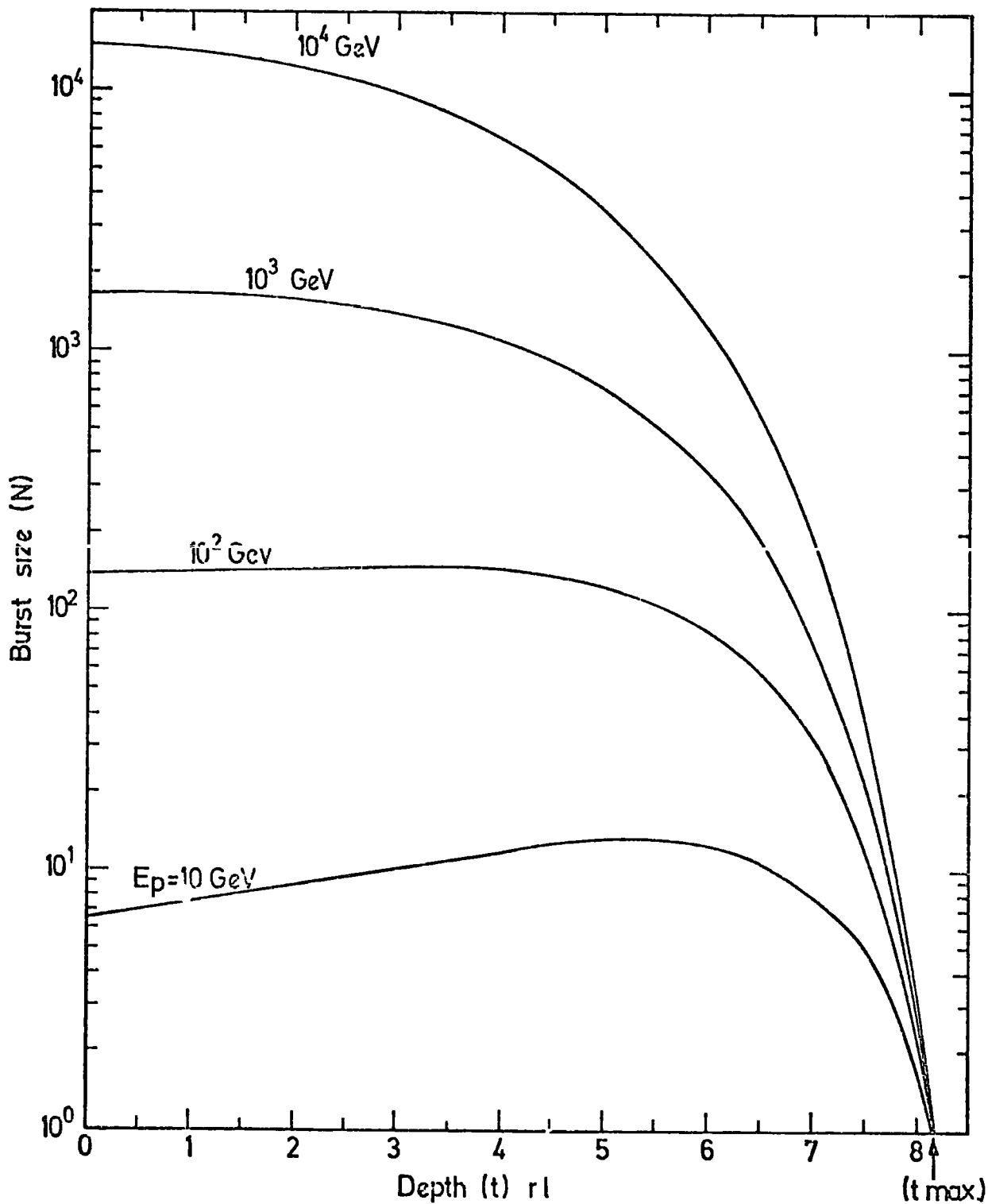


Figure 3.8

The relation between the depth of the first interaction for a proton with different primary energies (E_p) and the burst size (N) below 15 cms of iron.

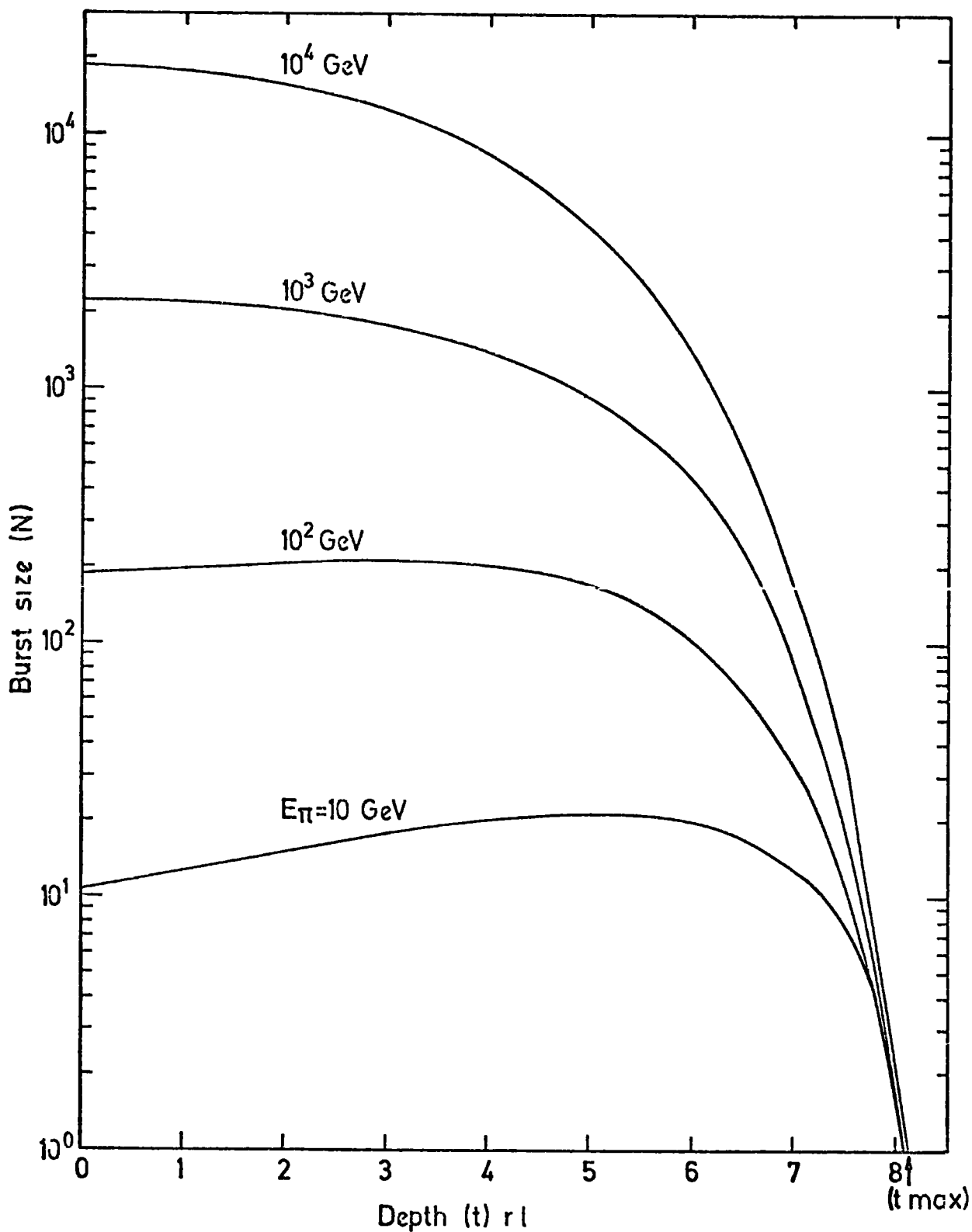


Figure 3.9

The relation between the depth of the first interaction for a pion with different primary energies (E_{π}) and the burst size (N) below 15 cms of iron.

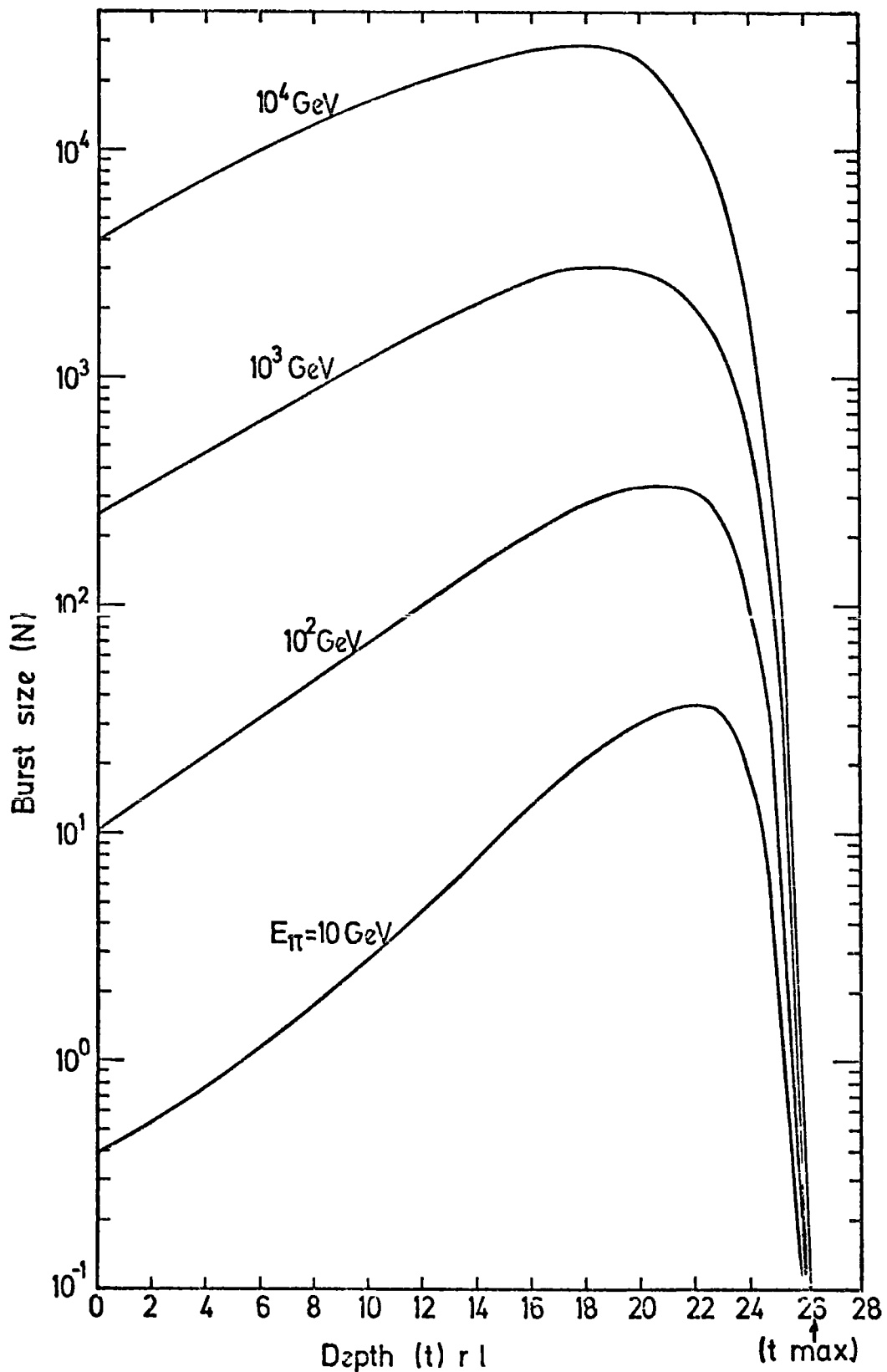


Figure 3.10

The relation between the depth of the first interaction for a pion with different primary energies (E_{π}) and the burst size (N) below 15 cms of lead.

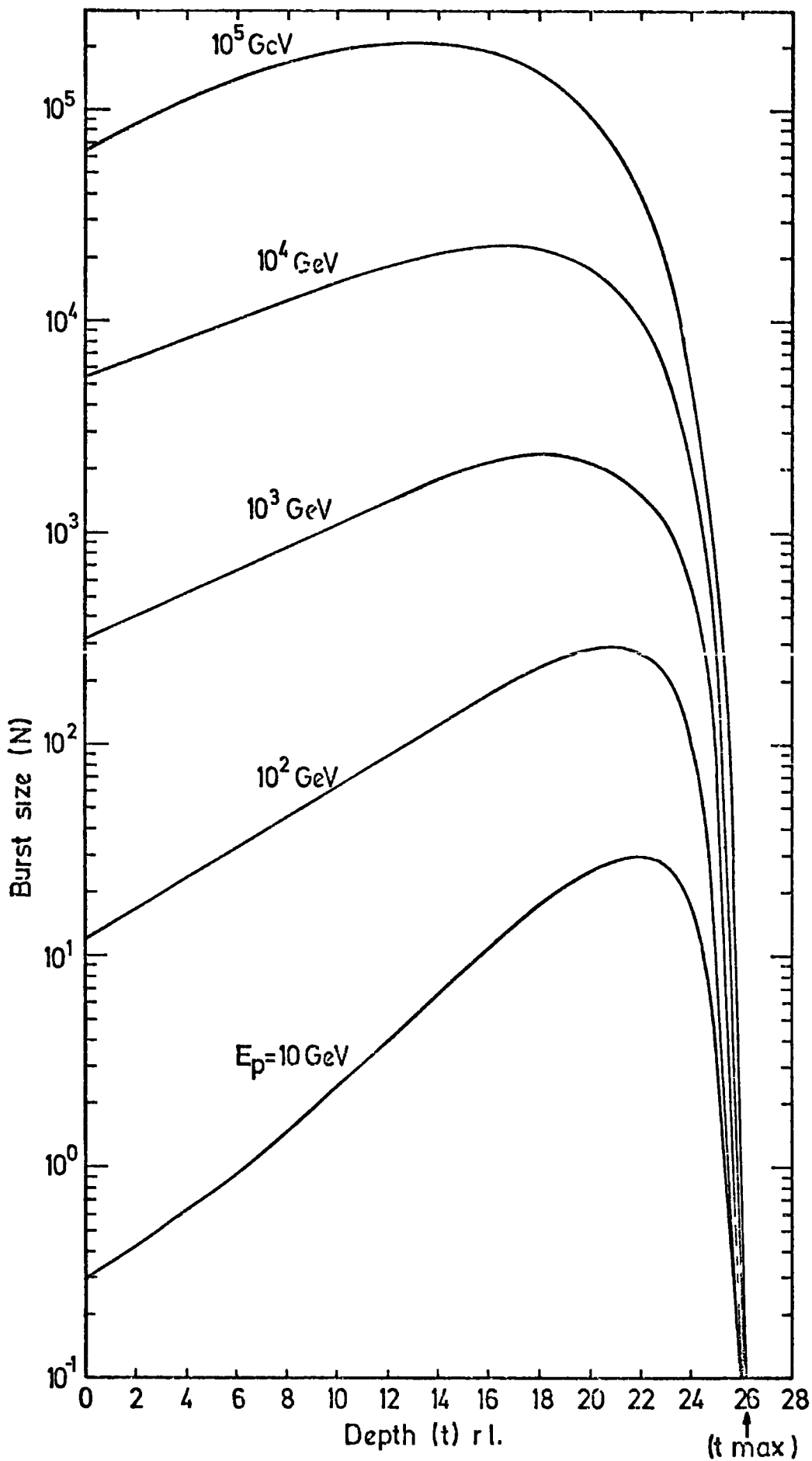


Figure 3.11

The relation between the depth of the first interaction for a proton with different primary energies (E_p) and the burst size (N) below 15 cms of lead.

not fully developed through the iron which has a thickness 8.19 radiation length. For a given energy the probability of observing a burst size $\geq N$ particles could be calculated from the above distribution. The integral probability of pions with energy E_π producing a burst size $\geq N$ below the iron and lead are shown in figures 3.12 and 3.13.

The Monte Carlo method has been used to calculate the burst size-energy relationship also for proton and pion incident on lead and iron absorber (Cooper, 1974, private communication). Similar nuclear - physical assumptions were made in both cases. Such that the two approaches should be directly comparable. Approximately 1,000 cascades were generated at each of four energies.

Figure 3.14 shows a comparison between the results from both calculations. There is good agreement between both methods in calculating the mean number of electrons as a function of incident primary energy. Cooper has also simulated cascades incident with a zenith angle of 30° in order to estimate the sensitivity of the results to the zenith angle. These results are consistent with the conclusions reached above. In the lead target the cascades incident at 30° produce less electron below the absorber because of the greater depth through which the cascade passes. In the iron, however, the increased path length allows the cascade to develop more fully at high energies producing larger burst size.

Figures 3.15 and 3.16 shows the comparison for pions interacting at different depth in 15 cm of iron and lead. A total of 200 cascades were simulated at each energy in the case of iron and 100 cascades in the case of lead. The simulation results are shown as a scatter plot and the full curves are the result of the numerical method. It can be seen that the results are quite close, although the small discrepancies at highest energies are to be expected.

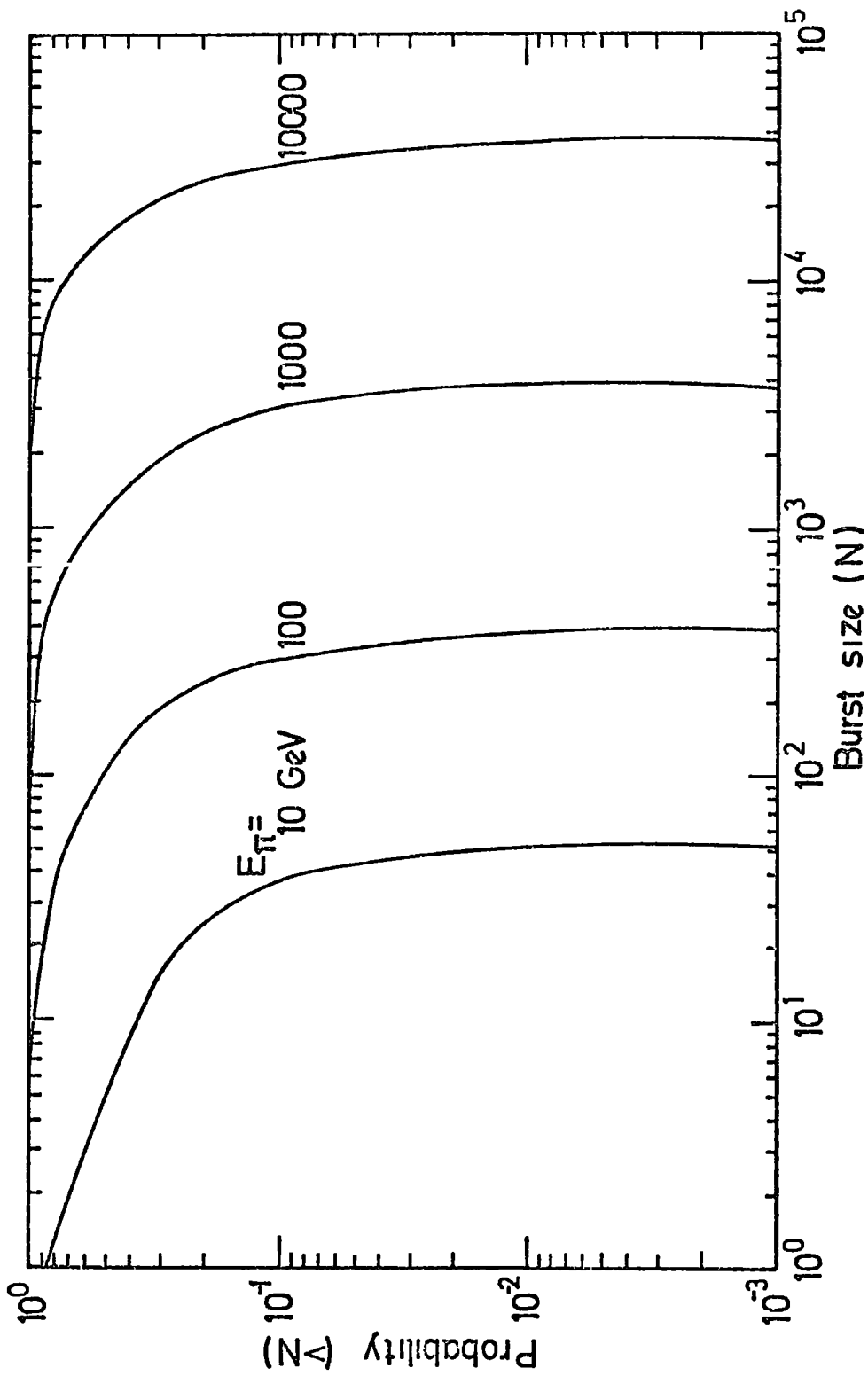


Figure 3.12

The integral probability that a pion of energy E_π will produce a burst of size $> N$ below 15 cm of lead.

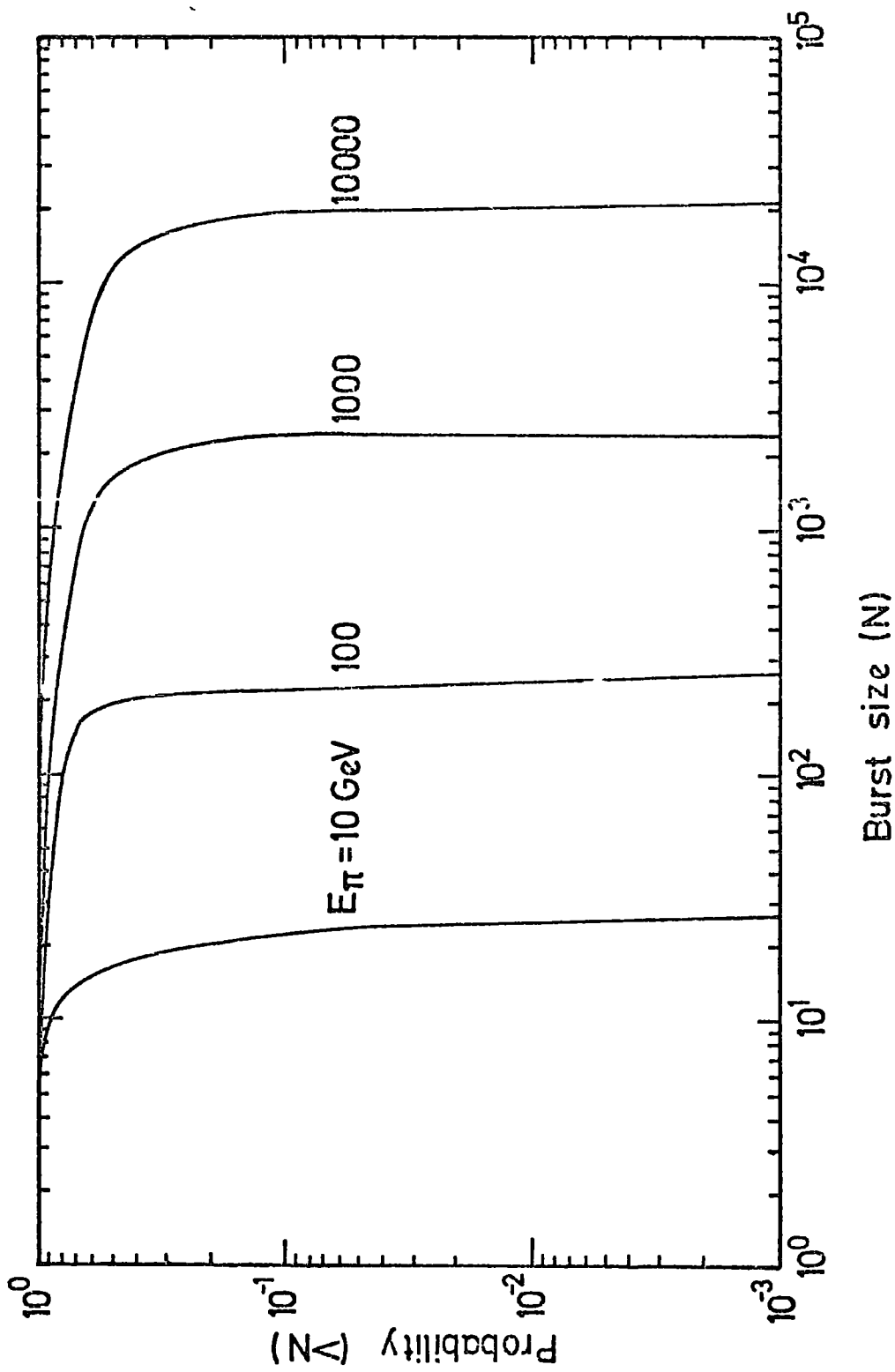


Figure 3.13 The integral probability that a pion of energy E_π will produce a burst of size $> N$ below 15 cm of iron.

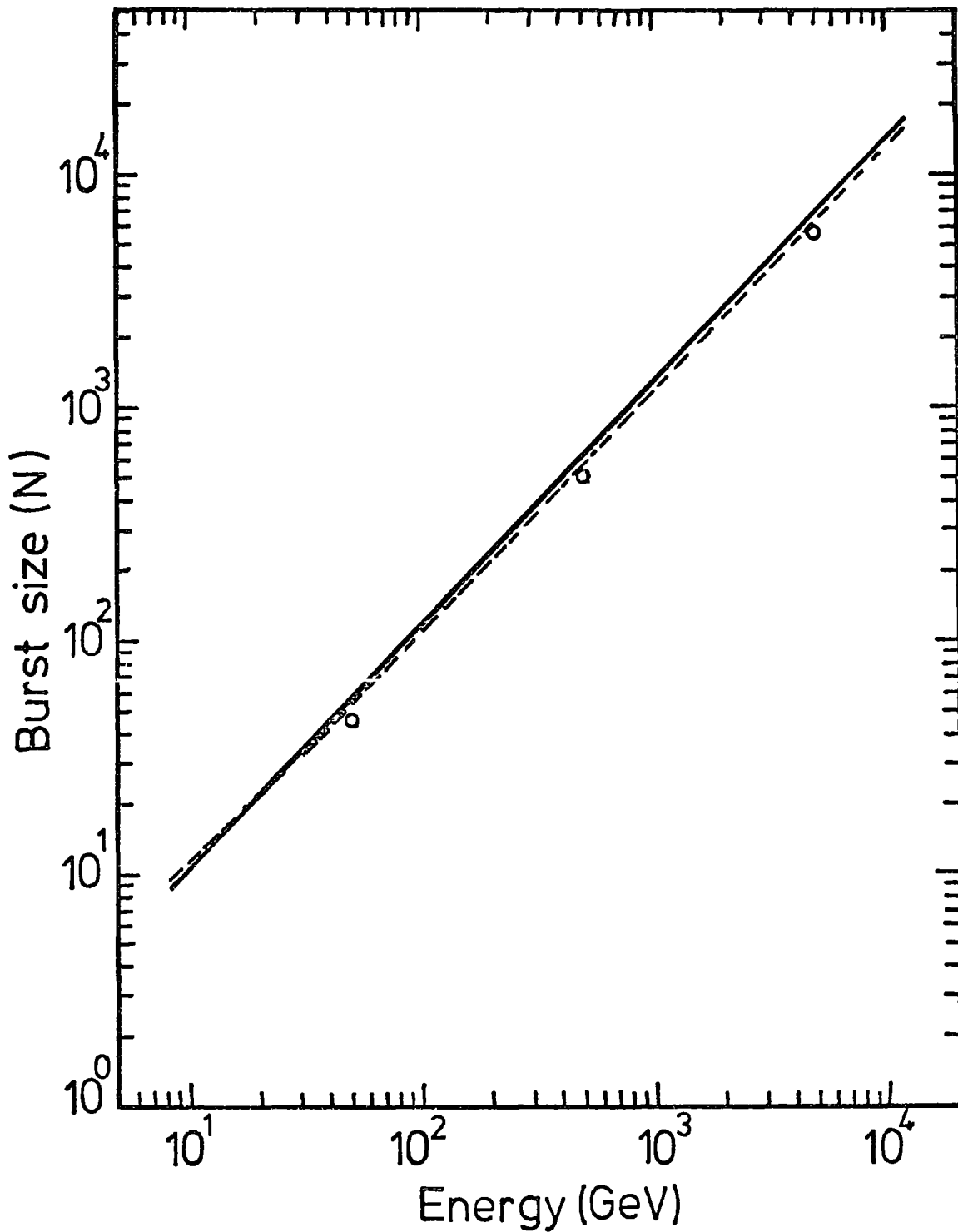


Figure 3.14

A comparison between the average treatment method (solid line) and Monte Carlo method (broken line) in calculating the average burst size (N) produced by primary pions incident on 15 cms of lead absorber as a function of energy. The open circles represent Monte Carlo calculations for pions incident at a zenith angle of 30° .

3.6 Discussion

The methods described in this chapter make it possible to predict the development of nuclear-electromagnetic cascades in the iron and lead absorber of the flash tube chamber. There was a good agreement between the numerical calculation and the Monte Carlo calculation to predict the size of the cascade as a function of energy in lead and iron. The results on burst size energy relation give a large error if one tries to measure the energy of individual particles interacting in the absorber, but the method gives reasonable results for the energy spectrum when a large number of events are dealt with.

The relation between the burst size emerging from the absorber and the width of the burst falling on the flash tubes will be discussed in detail in chapter 4.

Figure 3.15

A comparison between the average treatment calculation (solid curves) and Monte Carlo calculation (Scatter plots) for the relation between depth of initial (first) interaction and the burst size below 15 cms of iron for pions at four energies. The results of calculations by Vatcha et al. are shown for comparison for 1 TeV pions.

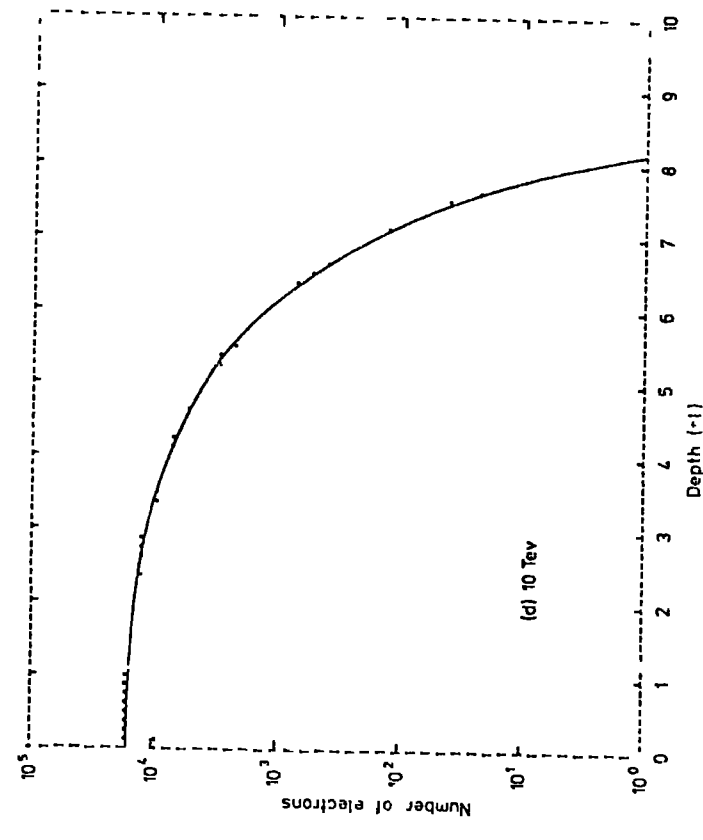
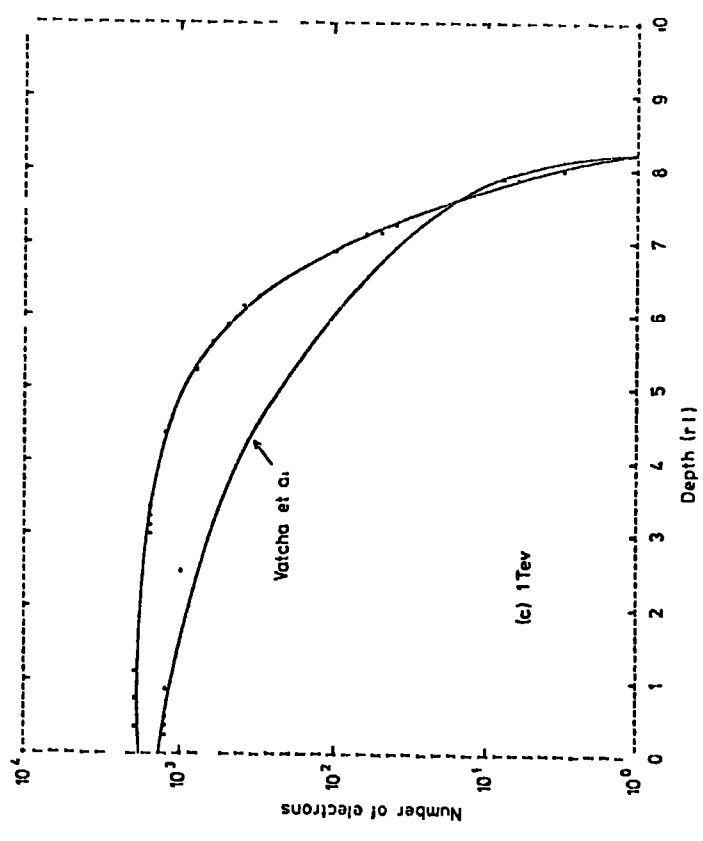
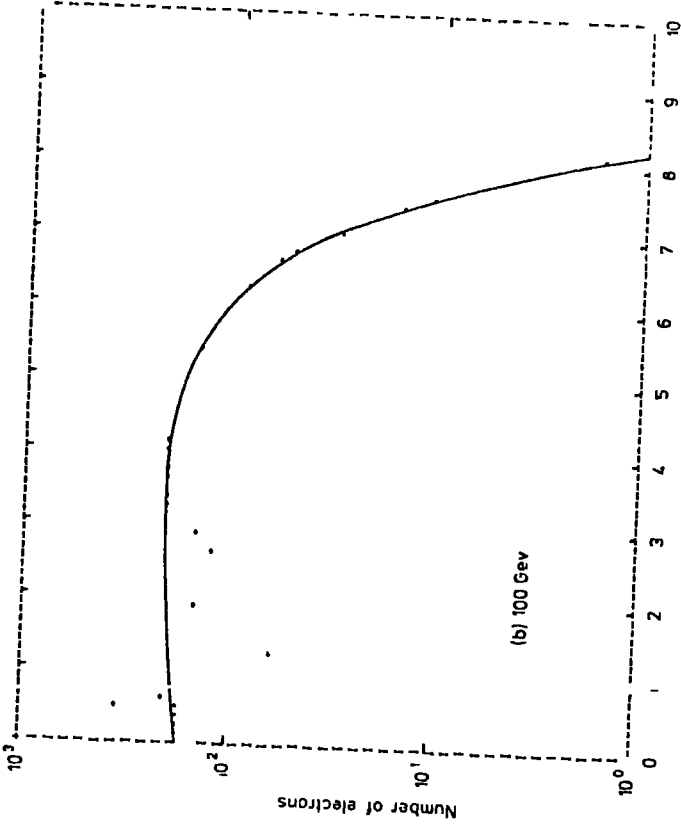
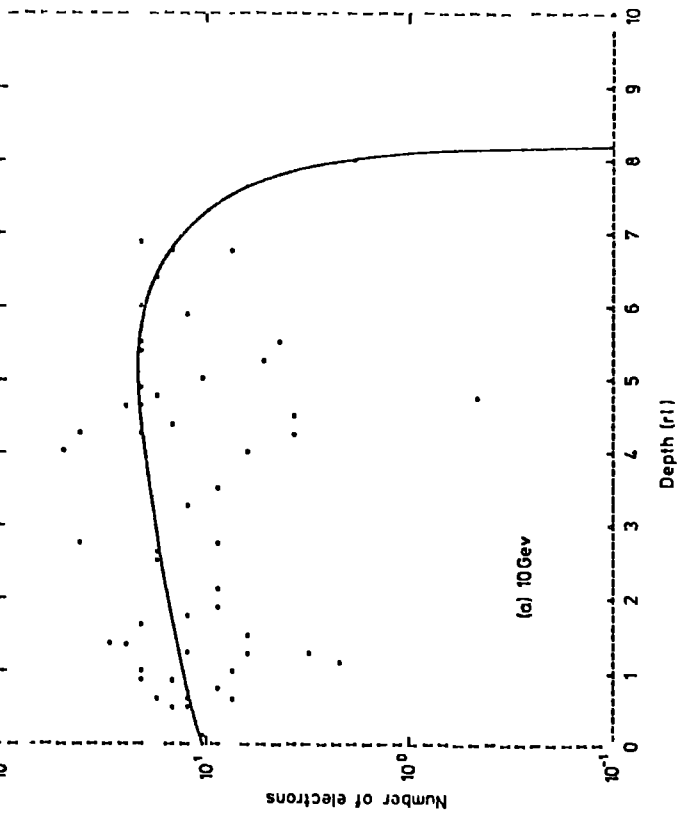
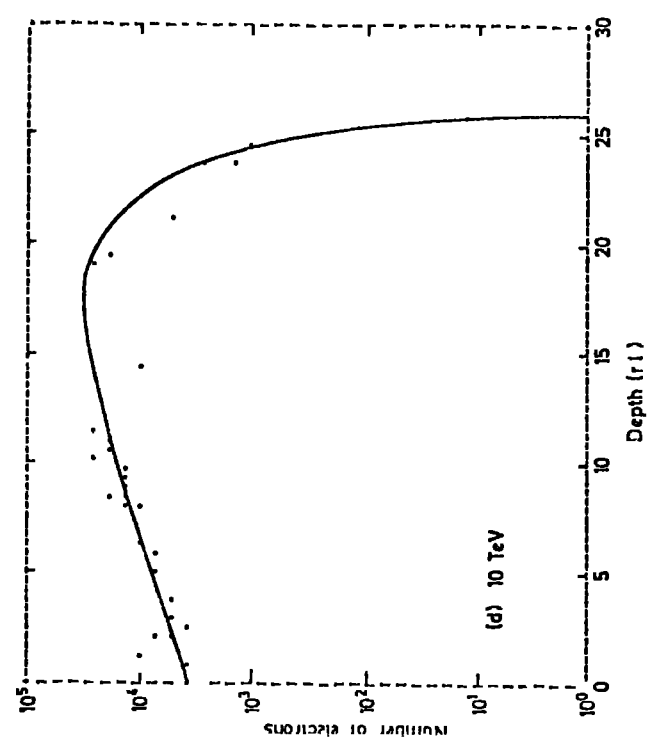
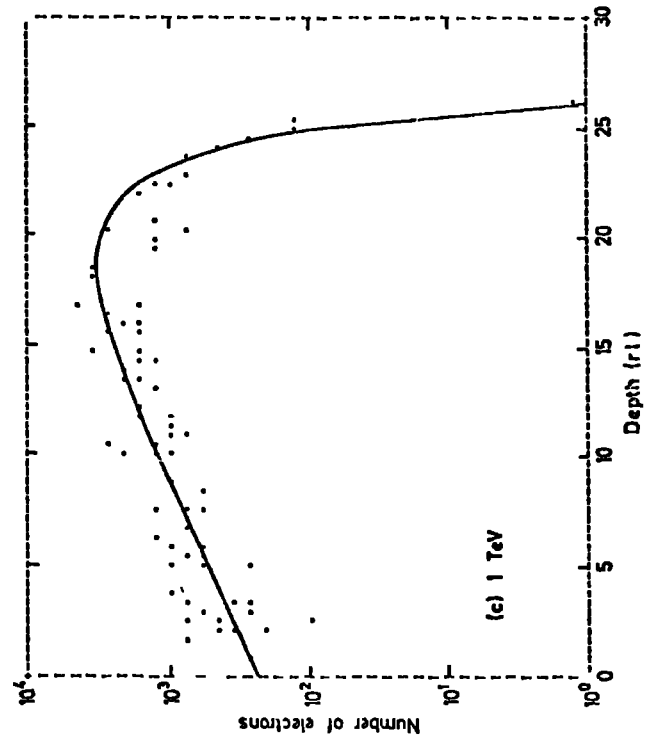
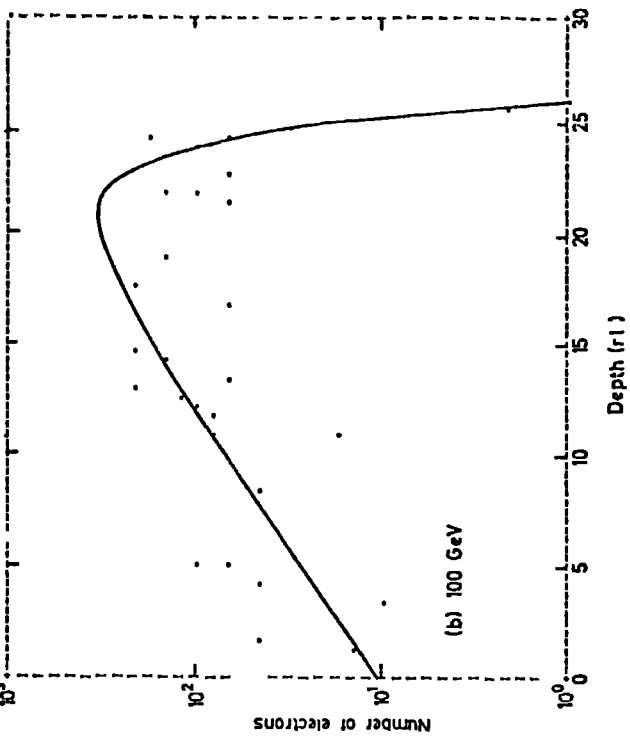
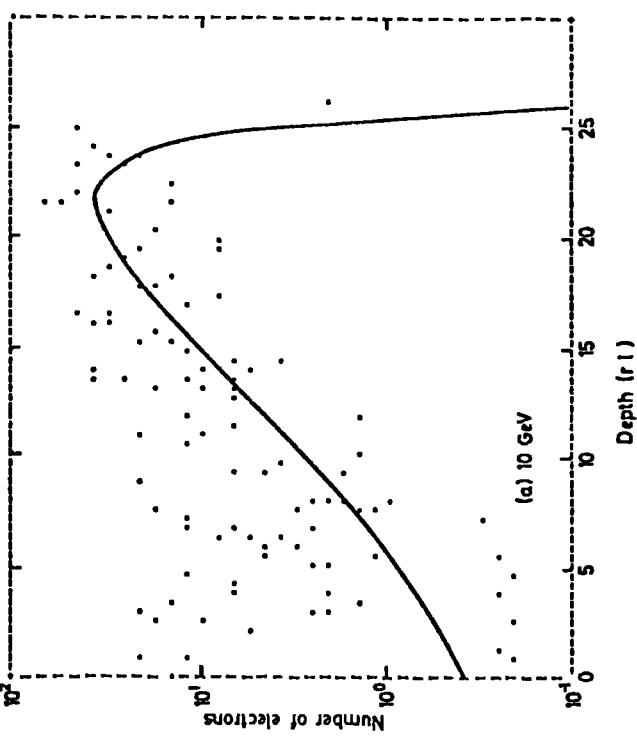


Figure 3.16

A comparison between the average treatment calculation (solid curves) and Monte Carlo calculation (Scatter plots) for the relation between depth of initial (first) interaction and the burst size below 15 cms of lead for pions at four energies.



CHAPTER 4

THE FLASH TUBE CHAMBER AND THE VERTICAL BURST EXPERIMENT

4.1 Introduction

The flash tube chamber as a big visible detector was used to study the characteristics of cosmic ray particles at sea level. The chamber was constructed originally to search for quarks in extensive air showers (EAS), using a local electron density to trigger the chamber. The results of this research will be discussed in Chapter 8.

Throughout the search for quarks it was noted that there are some events showing nuclear active particles interacting in the absorber inside the chamber and producing bursts which show on the flash tubes as a width defined by a solid number of flashed tubes. Therefore, the idea was to measure these events and to estimate their energies. To estimate the energies of these particles one has to know the relation between the burst size produced below an absorber of lead or iron and the width of the burst as measured in the flash tubes directly below the absorber.

The results of the energy spectrum of hadrons in EAS will be discussed in Chapter 9. A modification to the flash tube chamber has been made which allowed bursts in either the iron or lead absorber to be selected and their sizes measured under each absorber by a scintillation counter. The full experimental arrangement will be discussed in detail in this chapter.

4.2 The flash tube chamber

4.2.1 Construction of the chamber

A scale diagram of the flash tube chamber is shown in figure 4.1.

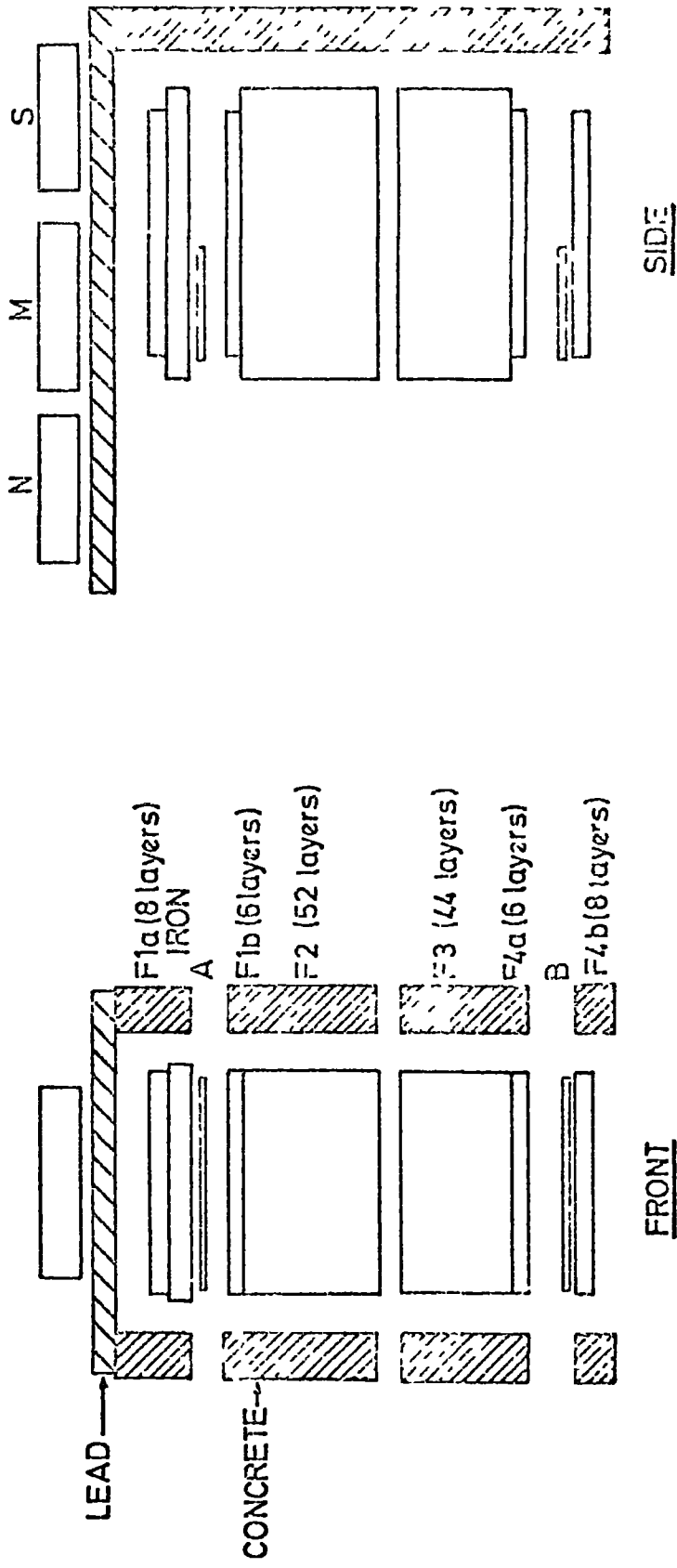


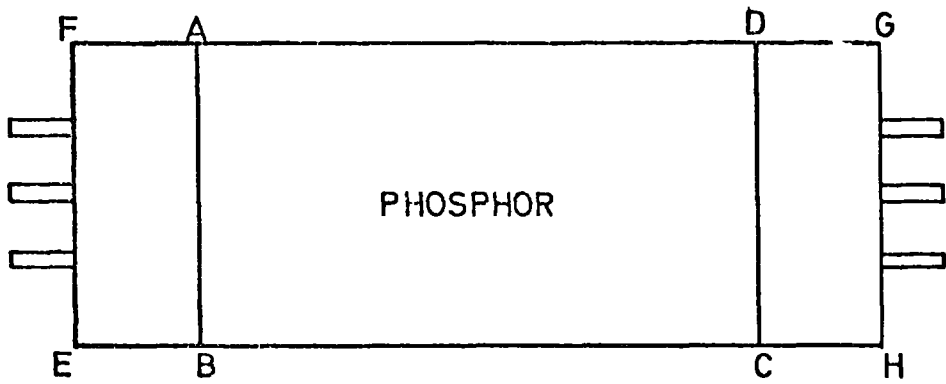
Figure 4.1 Scale diagram of the flash tube chamber.

The chamber uses 10,478 flash tubes of mean internal diameter 1.58 cms. and mean external diameter 1.78 cms. Each flash tube is 2 metres in length and made from soda glass filled with neon gas (98%) and helium gas (2%) to a pressure of 60 cms. Hg. The flash tubes are distributed in 124 layers. Alternately, the layers contain 84 and 85 tubes stacked side by side. Every tube is covered with polythene sleeving to stop light transferring to the neighbouring tubes.

Between every two layers there is a sheet of aluminium of 0.122 cm. in thickness. The front view of the chamber shows 6 blocks of tubes, F1a (8 layers), F1b (6 layers), F2 (52 layers), F3 (44 layers), F4a (6 layers) F4b (8 layers). In the sections F2 and F3 (figure 4.1) the area of the electrode is 2.94 m^2 , while in F1a, F1b, F4a and F4b the electrodes are shorter by 30 cms. and cover an area of 2.48 m^2 .

A 15 cms. of iron absorber was placed between F1a and F1b to study the interaction of nuclear active particles and to recognise penetrating particles in the chamber. The plastic scintillators A and B positioned inside the chamber, (see figure 4.1) each of area 1.05 m^2 , the phosphor of each counter was a large slab of 5 cms. thickness NE102A. The five 53 AVP photomultiplier tubes and one 56 AVP tube viewed the phosphor by light guides of solid perspex, see figure 4.2a. The construction of these counters has been described by Ashton et al. (1968a). Scintillator A placed directly below the iron and scintillator B placed between the two flash tube layers F4a and F4b. These two scintillators were used in coincidence to select single penetrating particles (muons) for calibrating the efficiency of the flash tubes.

The chamber was shielded above with 15 cms. of lead absorber. This absorber was designed to cut out the soft components (electrons and photons) in extensive air shower while allowing penetrating particles to pass through the chamber. The chamber is situated in a tunnel of rectangular cross-



0 20cms

ABCD = Plastic scintillator
 ABEF, CDGH = Perspex light guides

Figure 4.2.a

The basic design of a plastic scintillation counter.

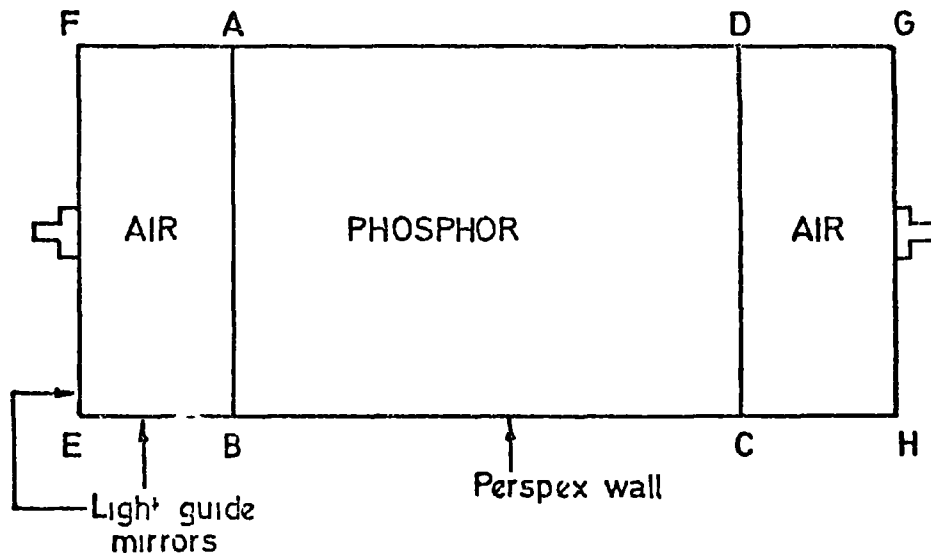


Figure 4.2.b

The basic design of a liquid scintillation counter.

section with 30 cms. thick barytes concrete walls. This also acted as a filter to absorb the soft components. Above the lead three liquid scintillators were used to select extensive air shower triggers. Each scintillator of area 1.24 m^2 and depth 15 cms employed two photomultipliers EMI 9583B viewing the phosphor through rectangular holes in the light guide mirrors, see figure 4.2b. The construction of these counters has been described by Ahston et al. (1965).

The whole chamber is in the dark when the experiment is running, allowing the use of a camera without shutter so it is always sensitive to an event. The camera wound on automatically by one frame after each event.

4.2.2 The high voltage pulsing system

The high voltage pulsing system consists of a H.T. pulsing unit and an air spark gap. A 5 volts trigger pulse is used to trigger a thyristor producing an output of +300 volts. This output is fed into a high voltage pulse transformer and the output produces the trigger pulse spark gap, figure 4.3. A voltage of 16 kV is applied across the main spark gap. The trigger spark cause the gap to break down largely by the production of photoelectrons. The high voltage pulse applied to the electrodes is approximately rectangular of height 8 kV. and length $10 \mu\text{s}$. Figure 4.4 shows the circuit diagram for the spark gap and the delay line which has four elements, each of capacitance $C = 0.1 \mu\text{f}$ and inductance $L = 22 \mu\text{H}$. The capacity of the flash tube chamber which this unit drives is $0.087 \mu\text{f}$.

4.2.3 Characteristics of the flash tubes

The operation of the flash tubes depends on the ionization left by a charged particle passing through a tube. However, when the trigger occurs

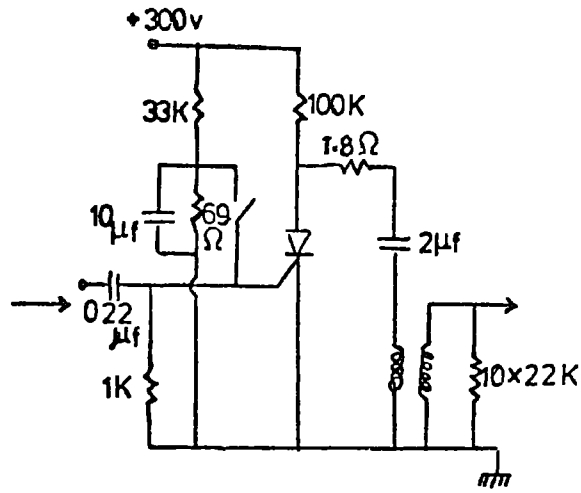


Figure 4.3 High voltage pulsing unit

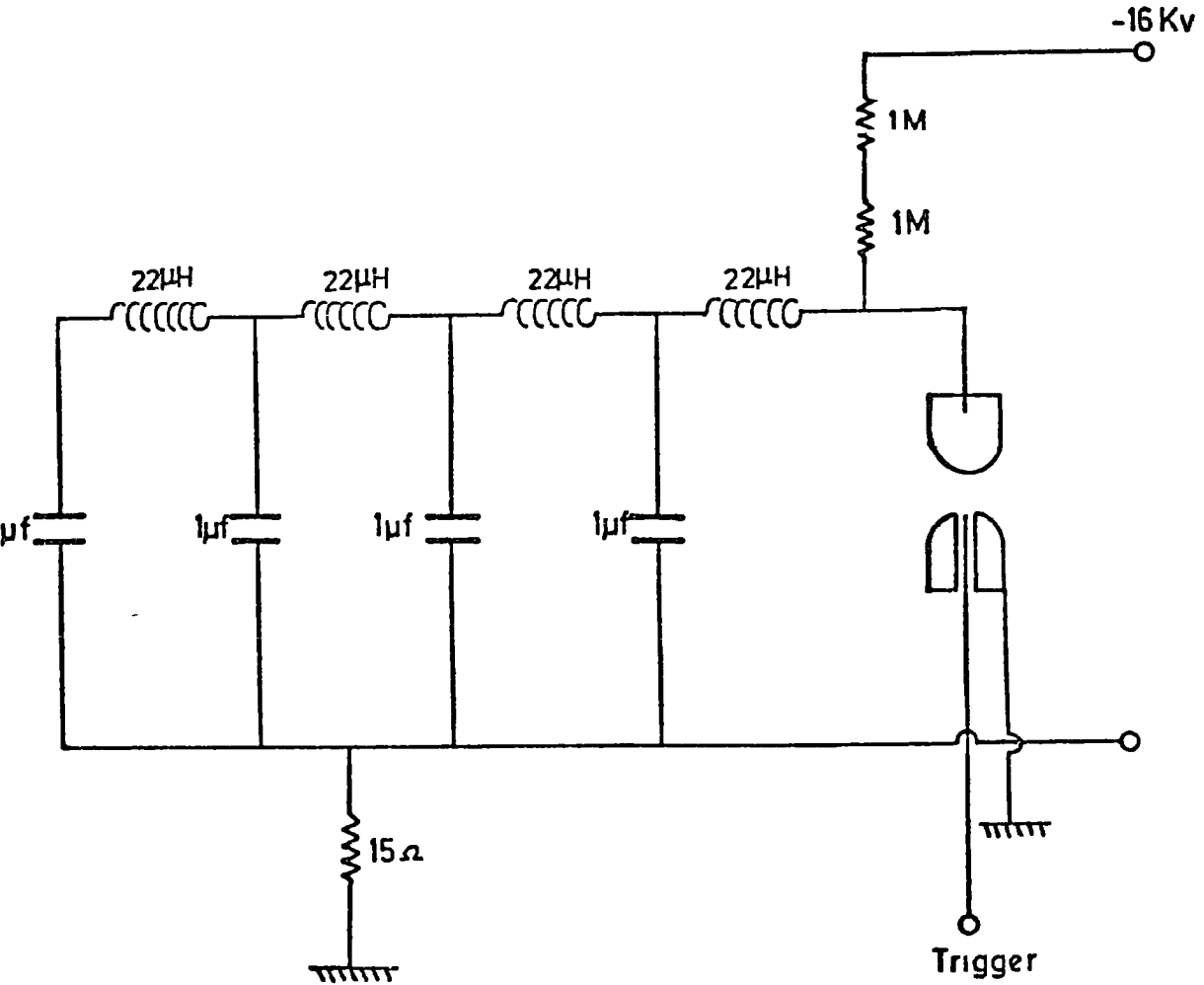


Figure 4.4 Air Spark Gap and Delay Line

a high voltage pulse must be applied to the electrodes creating an electric field across the flash tubes. Thus the ionization due to the passage of the charged particle will break down and a visible discharge will occur in the tube. The sensitivity of the tube to the ionization can be varied by varying the time delay between the passage of the charged particle and the application of the high voltage pulse across the tubes. The most important characteristic for the present application is the efficiency - time delay dependence. The problem of the ionization and what causes the discharge has been discussed in detail by Lloyd (1960). He has concluded that only free electrons which are produced initially can cause the discharge. The positive ions and the neon atoms do not contribute to the probability of a discharge and similarly the resonance or non-resonance photons which are radiated by excited atoms can have little or no effect.

A solution to the diffusion equations for the electrons produced in the ionization has been given by Lloyd using the probability of discharge occurring if a high voltage pulse is applied to the tube in a time T_D after traversal by a charged particle. A universal curve given by Lloyd for the expected variation of efficiency with time delay Dt/a^2 in terms of the parameter af_1Q_1 , where D is the diffusion coefficient of a thermal electron in neon at the relevant pressure, a is the tube radius, f_1 is the probability that a single electron is capable of producing a flash when a high voltage pulse is applied and Q_1 is the number of initial electrons produced per unit length in the neon gas.

The relation between the time delay T_D and the internal efficiency (η_1) has been calculated for different values of af_1Q_1 using the Lloyd method for the flash tubes used in this experiment, figure 4.5.

In order to determine the best value of the parameter af_1Q_1 to fit the experimental results, incoherent muons were selected by the two plastic scintillators A and B which were used in coincidence.

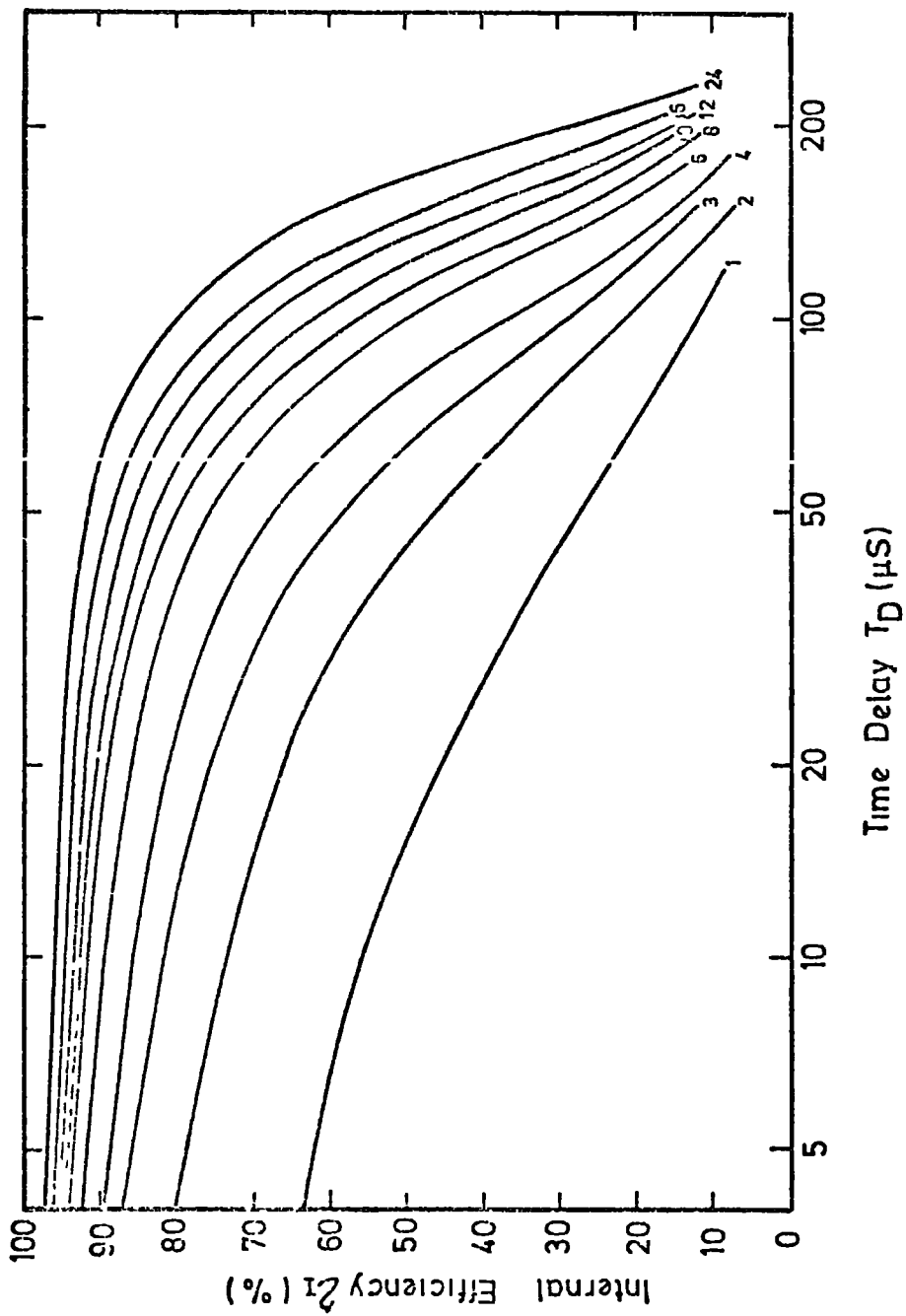


Figure 4.5

Predicted variations between the internal efficiency of the flash tubes and time delay. The numbers attached to each curve refer to the value of the parameter of $af_j^{1.0}$.

4.2.4 The efficiency-time delay measurement

As mentioned above single muons can be selected by a two-fold coincidence between the plastic scintillators A and B. The block diagram for this selection is shown in figure 4.6. The rate of single particles was calculated from 1.05 m^2 scintillators area and 250 cms. distance between the centre of A and B to be 12 sec^{-1} . Due to this high rate, a dead time of 30 seconds was imposed after each event. This dead time being applied by means of an RC - controlled delay circuit which switched a relay earthing the coincidence pulse line. The pulse from the coincidence between A and B was fed firstly to this 30 seconds delay generator and then allowed to trigger the spark gap applying the high voltage pulse to the flash tubes and to start the cycling system which triggers microswitches controlling fiducial lights on the chamber, illumination for the clock, and also for winding on the camera. This cycle takes approximately 7 seconds and during this time the paralysed electronics gave time for the high voltage capacitor to get charged again and make the experiment sensitive to the next event.

For each time delay T_D , a large number of events were photographed and studied in detail. The method of analysing those events was by projecting the films onto the scanning tables. The event was not only accepted when the track passed through F2 and F3 but must also appear in F1 and F4. The second condition proves that muons do not traverse the front or rear edges of the chamber, since it has been shown by Ashton et al. (1971b) that a tube may flash with a low efficiency if the charged particle passes through the tube a small distance beyond the electrode edge. The layer efficiency (η_L) was measured by counting the number of tubes flashed in successive layers along the length of the track in F2 and F3

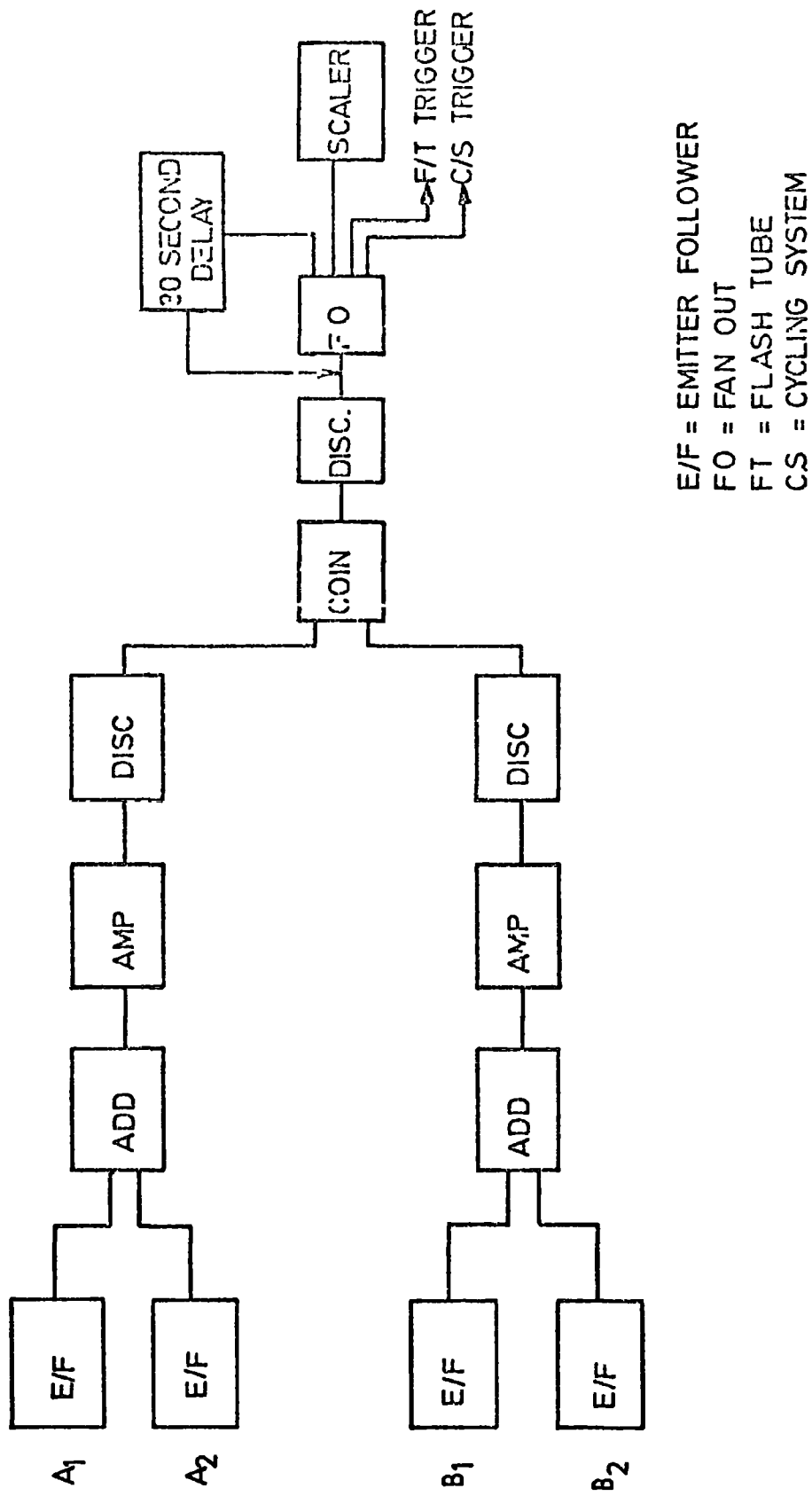


Figure 4.6 Block diagram of the electronics used in the selection of single particles by plastic scintillators A and B.

and divided by the total number of layers in F2 and F3 (96). To convert to internal efficiency (η_I), the layer efficiency was multiplied by the ratio between the mean external diameter to the mean internal diameter.

$$\eta_I = \left(\frac{1.81}{1.58} \right) \cdot \eta_L = 1.145 \eta_L$$

The results of the number of flashes along the track in F2 + F3 for various time delays are shown in figure 4.7. The dashed distribution corresponds to the binomial fit, since the variation of layer efficiency would be expected to be a binomial distribution for an array of randomly positioned tubes. Figure 4.8 shows the mean of these distributions plotted on the efficiency time delay curves with other experimental results. It was found that the best fit for Lloyd's parameter $af_1 Q_1$ to the experimental points is 9 ± 1 .

However, the flash tube technique makes it possible to search and study the idea of the existence of fractional charged particles (quarks) in cosmic rays because the only parameter depending on the charge of the particle is Q_1 and this is related to the ionization loss of the particle in the gas and is a function of the square of the electric charge. So for the quarks of charge $e/3$ the expected efficiency-time delay curve having the same value of $\gamma = E/mc^2$ (Lorentz factor), as the single muons is that given by Lloyd's curve with $af_1 Q_1 = \frac{1}{9} \times (9 \pm 1) = 1.0 \pm 0.1$, and this is also shown in figure 4.8. The quark research will be discussed in Chapter 8.

4.3 The arrangement for the vertical burst experiment

4.3.1 Introduction

The primary aim of the vertical burst experiment was to obtain a calibration for the data obtained on bursts produced by hadrons close to the core of extensive air showers. In order to obtain this calibration a

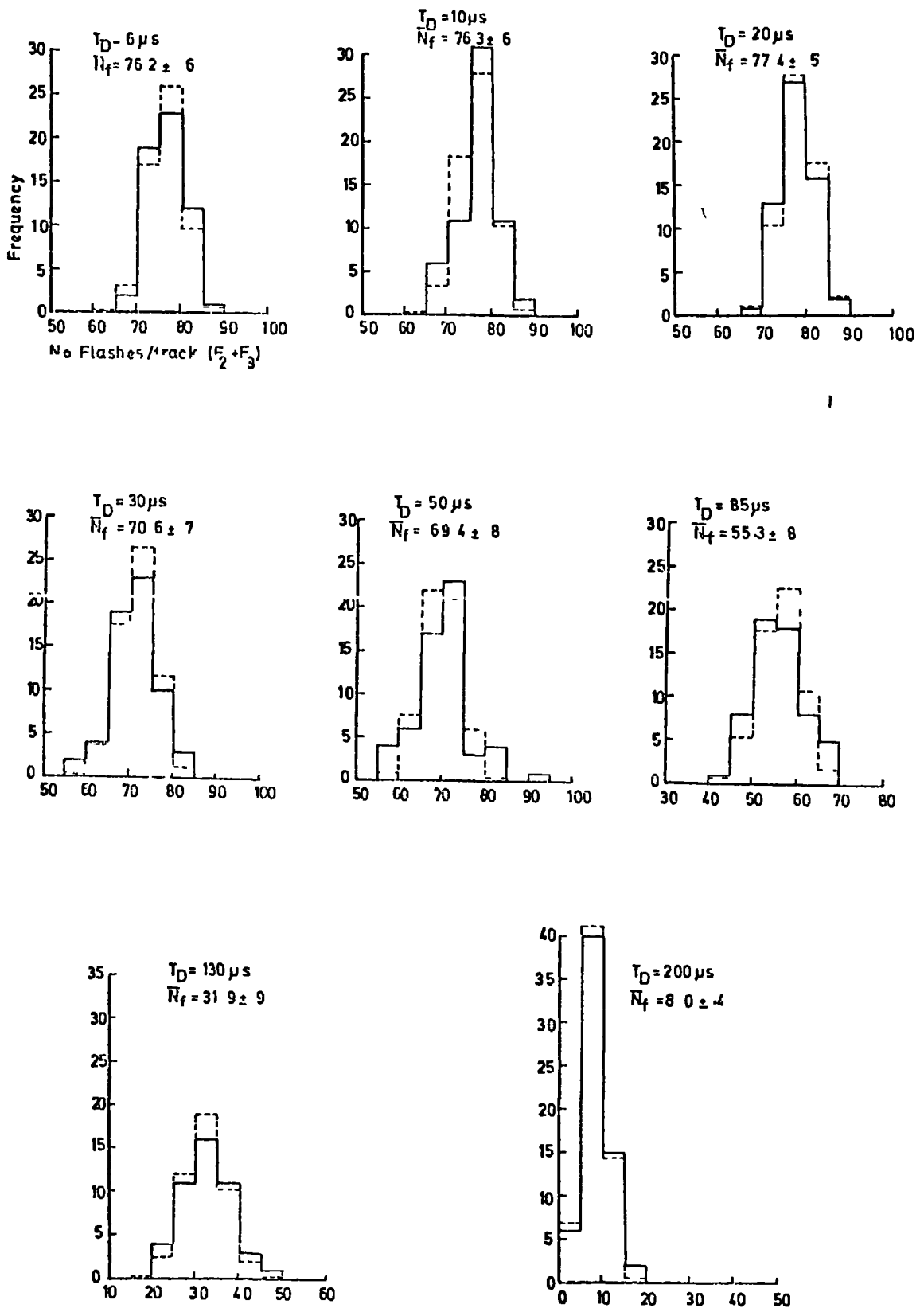


Figure 4.7

The distribution of the number of flashes along the track in F₂ + F₃ for various time delay, T_D. The dashed distributions represent the expected binomial distribution.

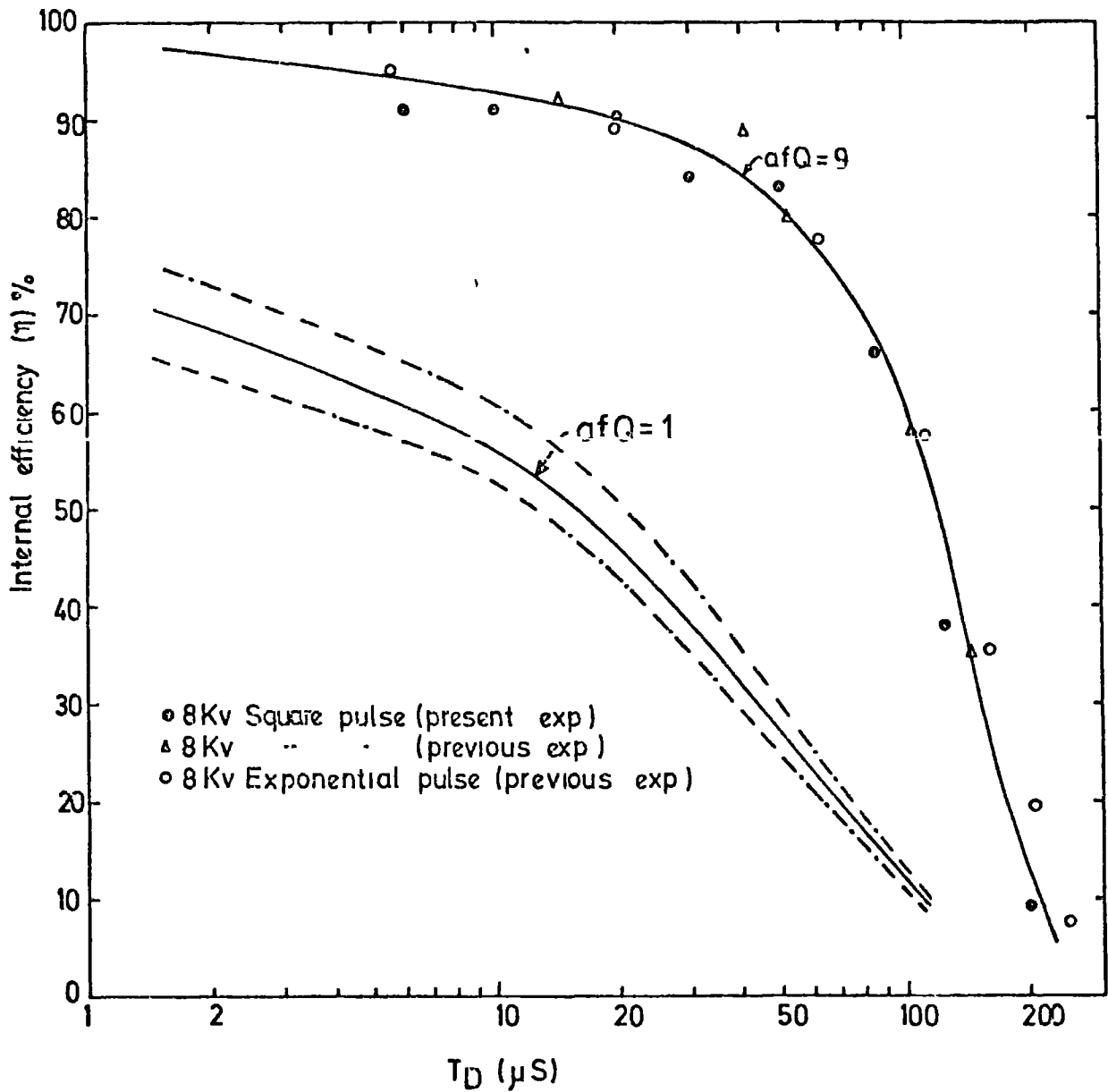


Figure 4.8

The variation of the internal efficiency of the flash tubes as a function of time delay, T_D . The full curve represents the theoretical prediction with $af_1Q_1 = 9$ as a best fit to the experimental points. The curve with $af_1Q_1 = 1.0$ corresponds to a particle of charge $e/3$. The curves — — — indicate the latitude of uncertainty.

slight modification to the chamber has been made and single hadrons were selected to trigger the experiment by either bursts produced in the iron or lead absorber.

In addition to the primary aim, it was hoped that this experiment could give a good resolution at high energy and provide information on features of the energy spectrum of single hadrons at sea level. The result will be discussed in Chapters 5 and 6.

4.3.2 Modification of the flash tube chamber

The flash tube chamber was modified such that bursts in the lead or iron absorber could be selected and measured.

The plastic scintillation detector was used to measure the size of the burst below the absorber. There was already a plastic scintillator in place below the iron absorber and this is called scintillator A (see figure 4.1). So the only addition was to position another similar scintillator (named scintillator C) below the lead absorber and in line with scintillator A. Fortunately there was enough space between the lead and the flash tubes Fla (see figure 4.1). Therefore, there was no need to raise the lead roof and change the dimensions which is an important factor. The flash tubes in the upper layer Fla (8 layers) were brought forward by 15 cms to make a sensitive area of 2.94 m^2 and covering completely the iron. This was done in order to recognise neutral particles producing bursts in the iron.

The middle liquid scintillator M was operated with the experiment in order to get some information about the hadrons accompanied by EAS. Figure 4.9 shows this new arrangement for the flash tube chamber.

4.3.3 Calibration of the scintillators

The calibration has been made for the three scintillation counters A,

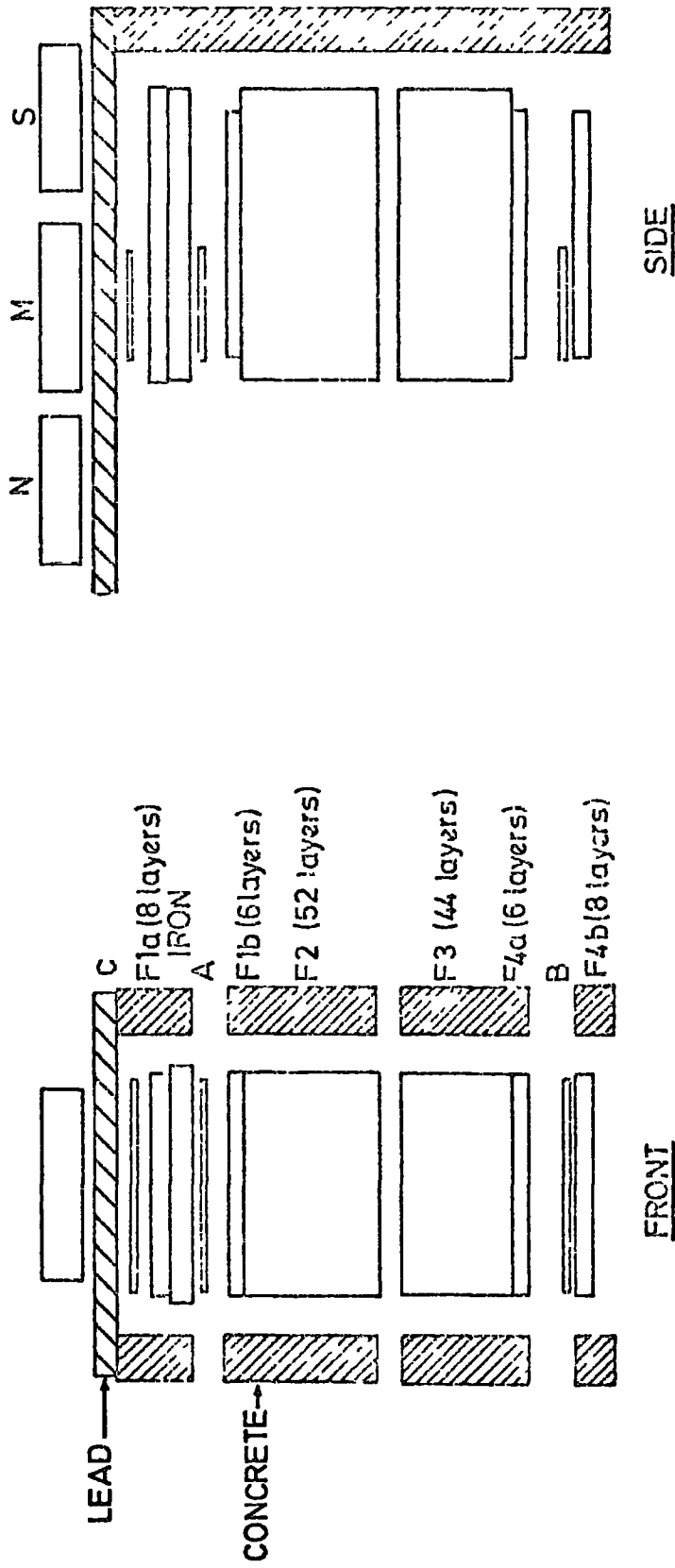


Figure 4.9 Scale diagram of the new Masl. tube chamber arrangement.

C and M. In case of the plastic scintillators A and C the two middle photomultipliers were not used, because one of them was for the fast timing measurements. To symmetrize the counter, the opposite photomultiplier tube was not used (see figure 4.2a). The construction and the response of the scintillator counters has been described by Ashton et al. (1968a).

Single particles were selected by a small geiger telescope and the pulse from the coincidence was used to trigger the scope. The scintillator pulses were delayed by means of delay line by approximately $1\mu\text{s}$.

Before the calibration, it was important to know the loss in pulse height for a pulse transmitted from the photomultipliers to the output of the delay line. For this reason a square pulse of 100ns width was chosen. The output/input characteristic for the scintillator A, C and M is shown in figures 4.10 and 4.11 and the circuit used is also shown in these diagrams. For single particles, reversing the centre of each scintillator in the vertical direction, the pulse height distribution was measured for different values of H.T. voltage applied to the tube. The means of each distribution are plotted against the voltage applied to the photomultiplier tubes and the result is shown in figure 4.12. It can be seen that all the photomultiplier tubes have approximately the same slope. A single power supply unit was used to supply the voltage and potentiometers were used to distribute the voltage across each photomultiplier tube. The potentiometers were adjusted for each tube separately to give identical output pulse heights for a charged particle traversing the centre of the scintillator. Thus it was possible to calibrate the complete scintillator by adding the outputs from the photomultiplier tubes. The pulse height distributions obtained for scintillators A and C are shown in figures 4.13 and 4.14. The means of these distributions were then corrected for the

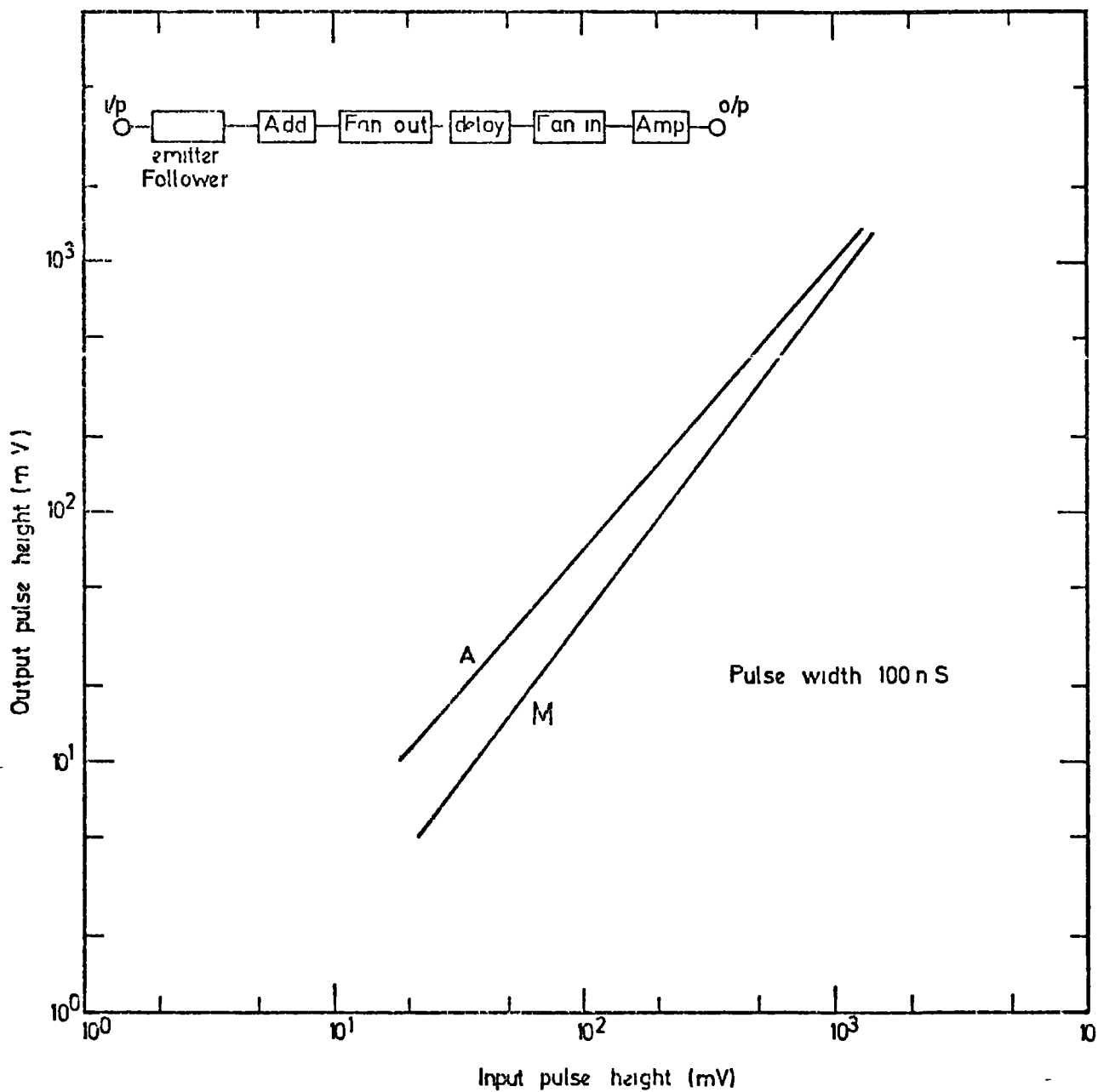


Figure 4.10

The input-output characteristics for the pulses transmitted through the circuit shown above associated with scintillators A and M, measured for square pulses of width 100 ns.

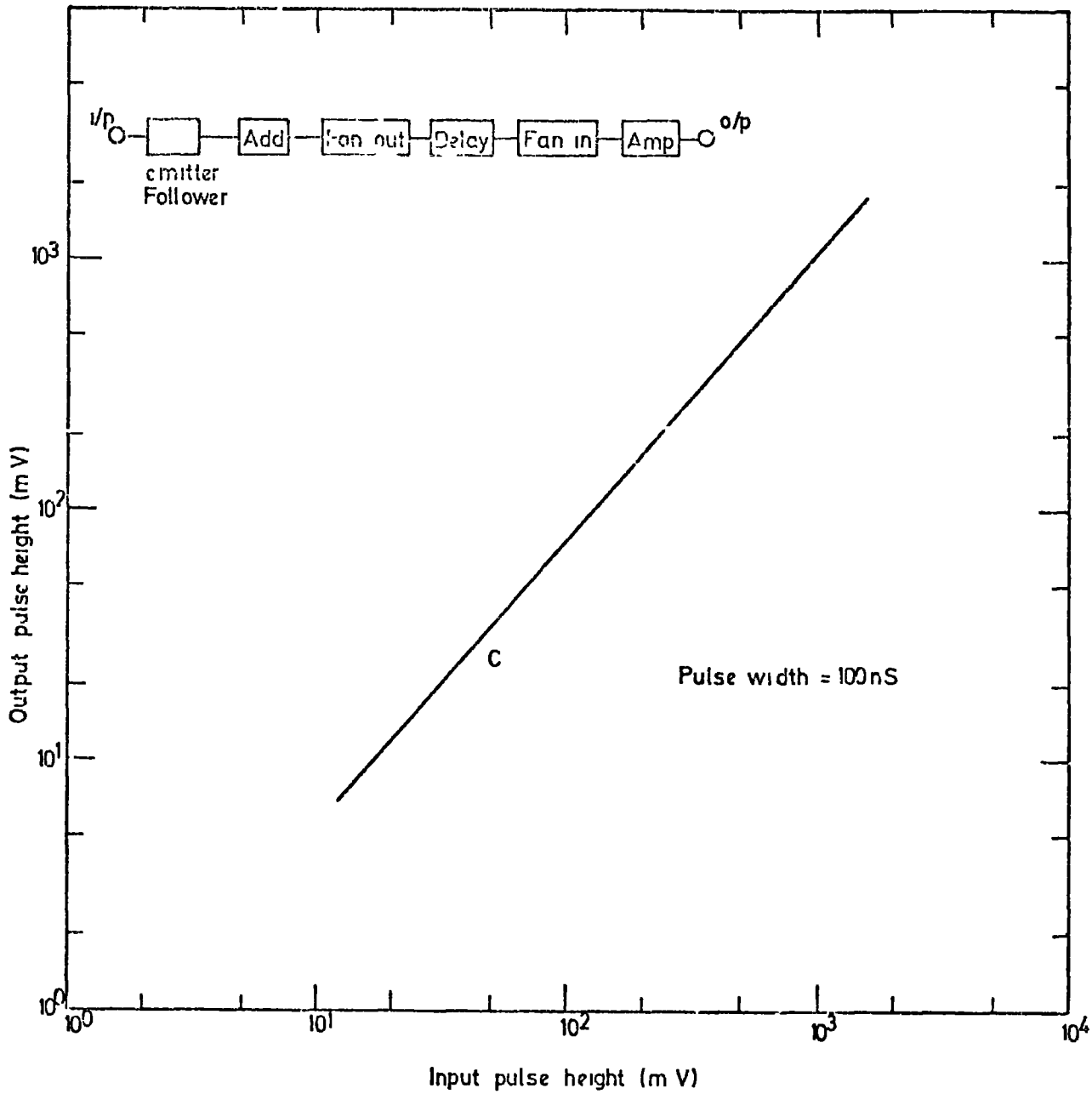


Figure L.11

The input-output characteristics for the pulses transmitted through the circuit shown above associated with scintillator C, measured for square pulses of width 100 ns.

Figure 4.12

The variation of single particle pulse height as a function of H.T. applied to each photomultiplier tube in the three scintillators. (a) scintillator A, (b) scintillator C and (c) scintillator B. The pulse height measured at the output of the amplifier (see figures 4.10 and 4.11).

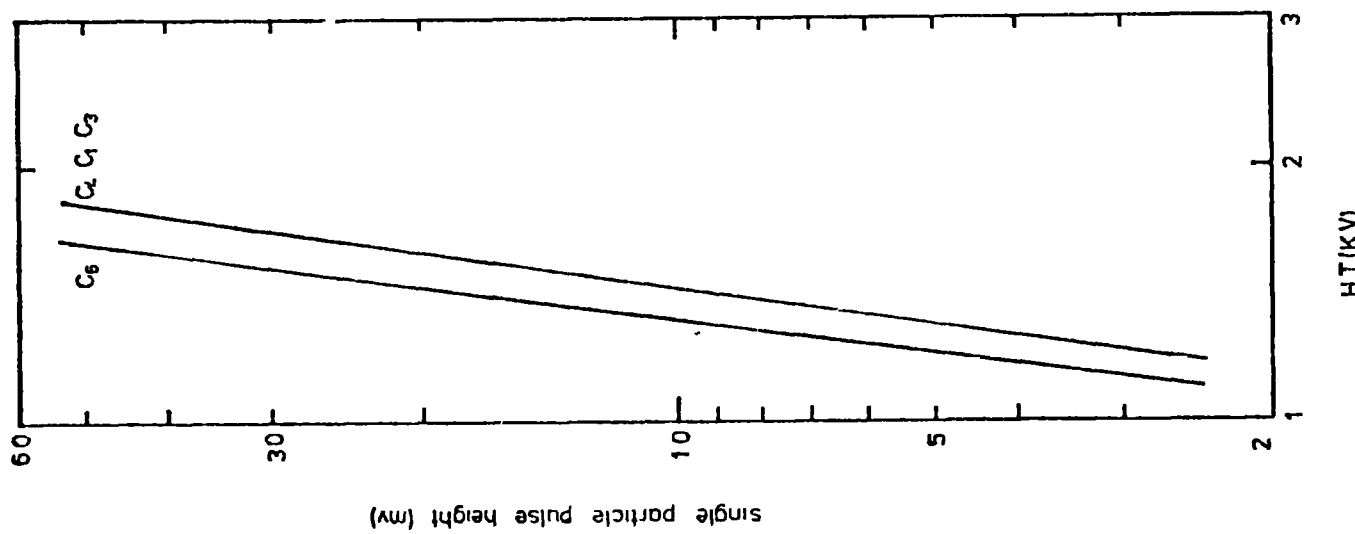
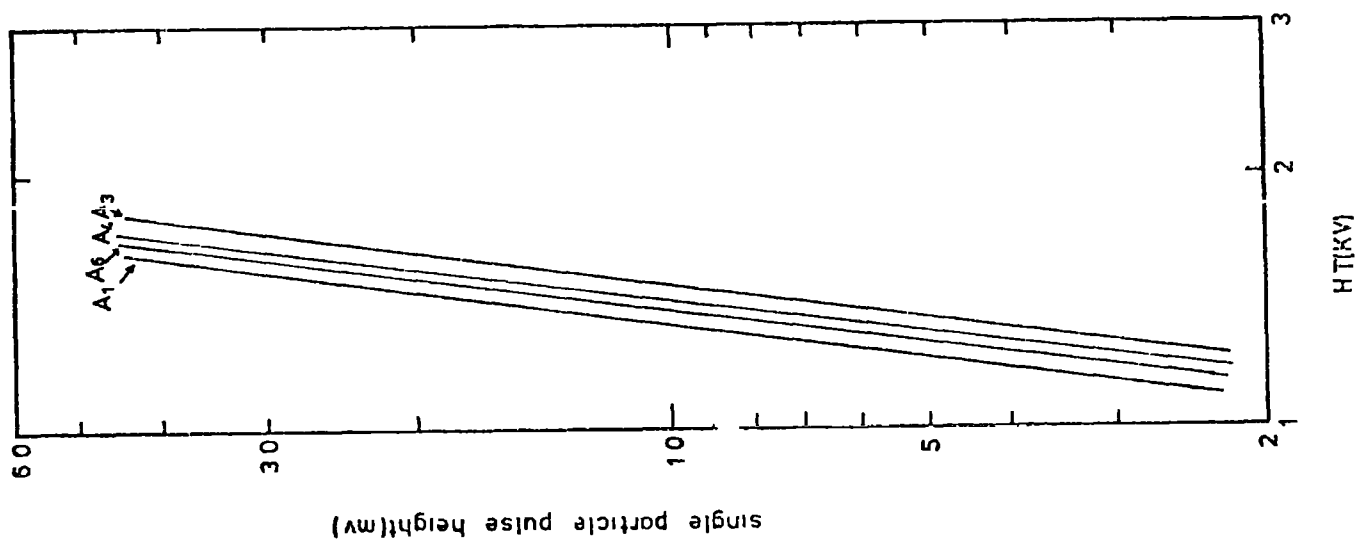
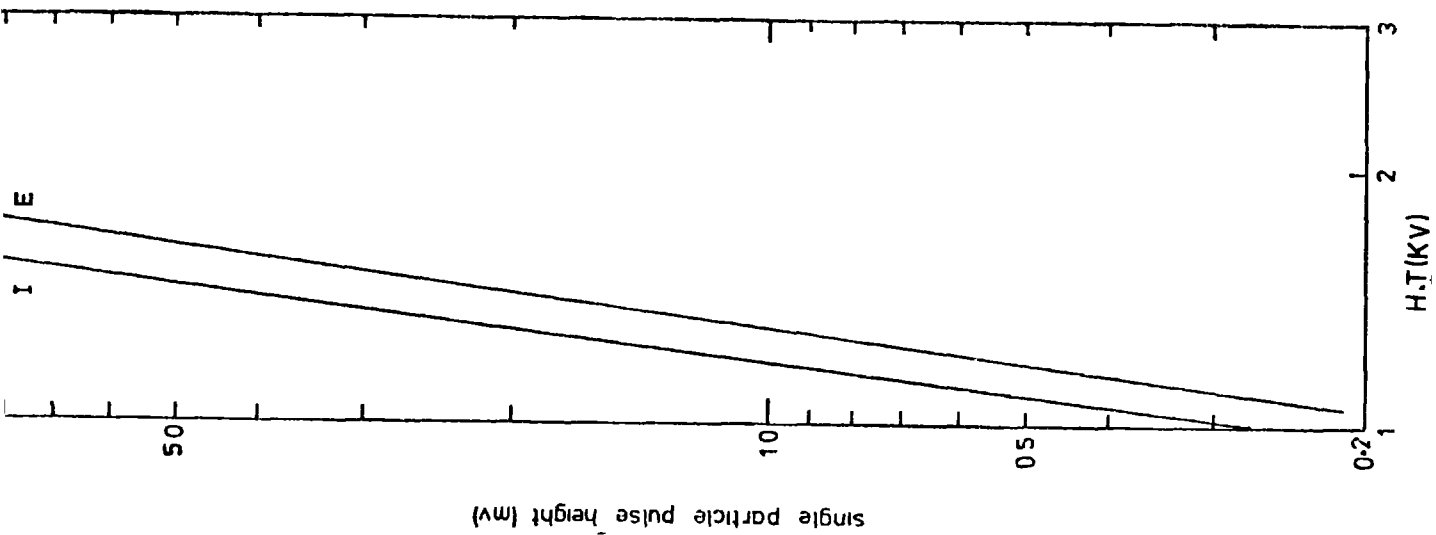


Figure 4.13

The single particle pulse height distribution for scintillator A.
The pulse height measured at the output of the amplifier (see figure 4.10).

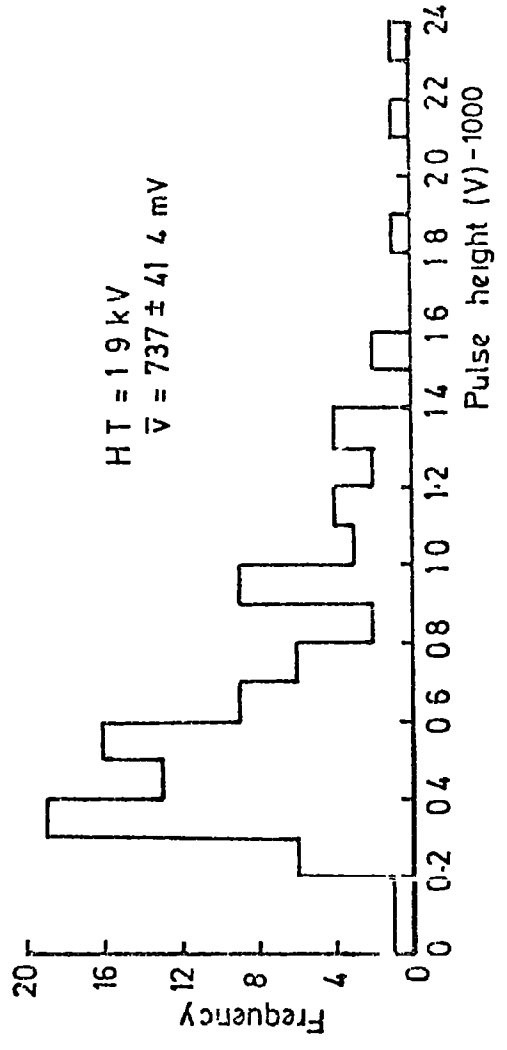
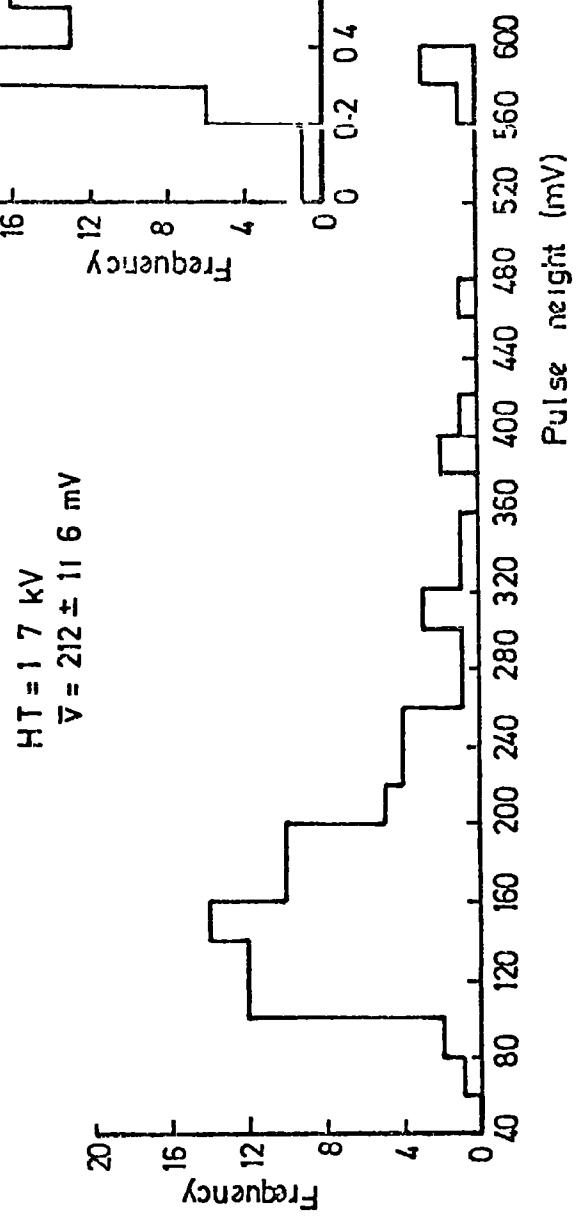
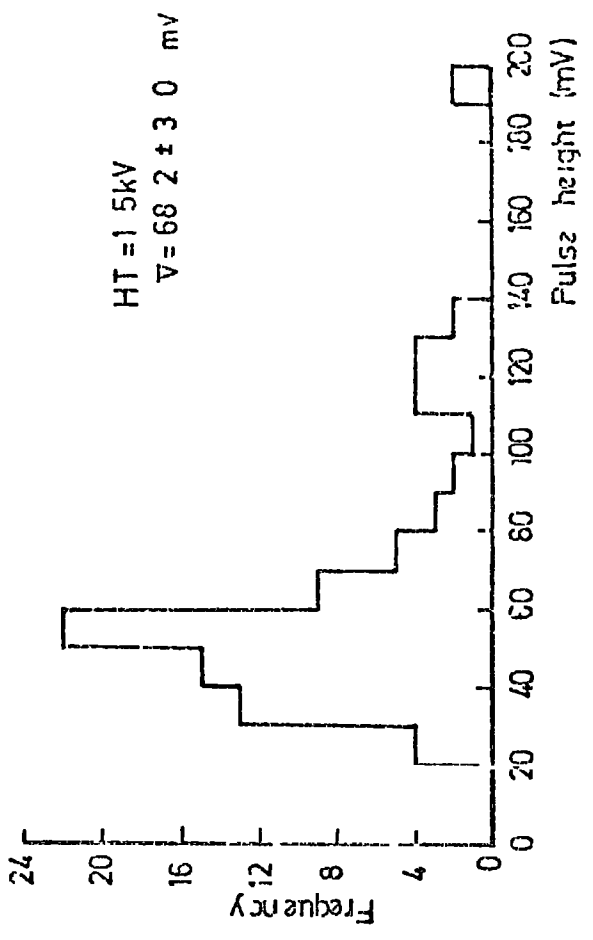
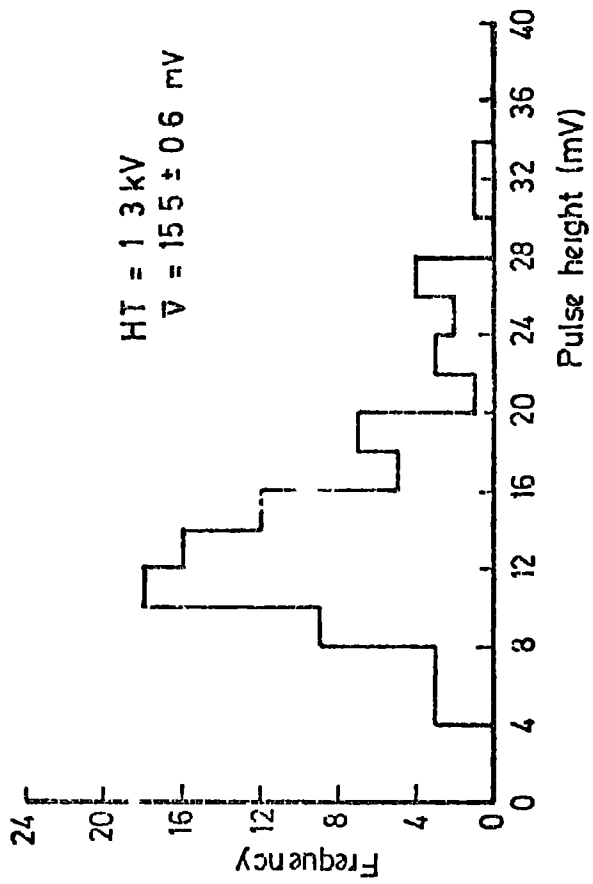
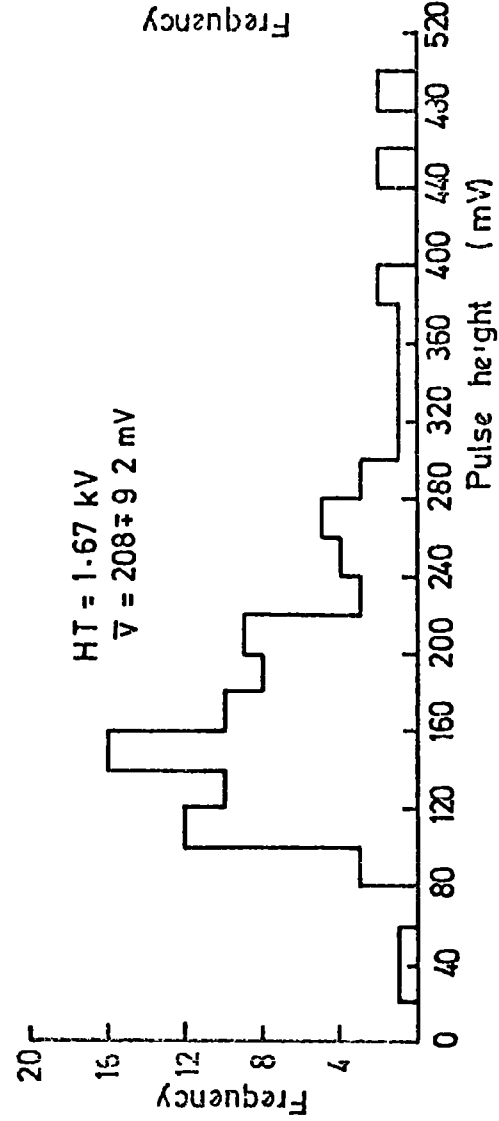
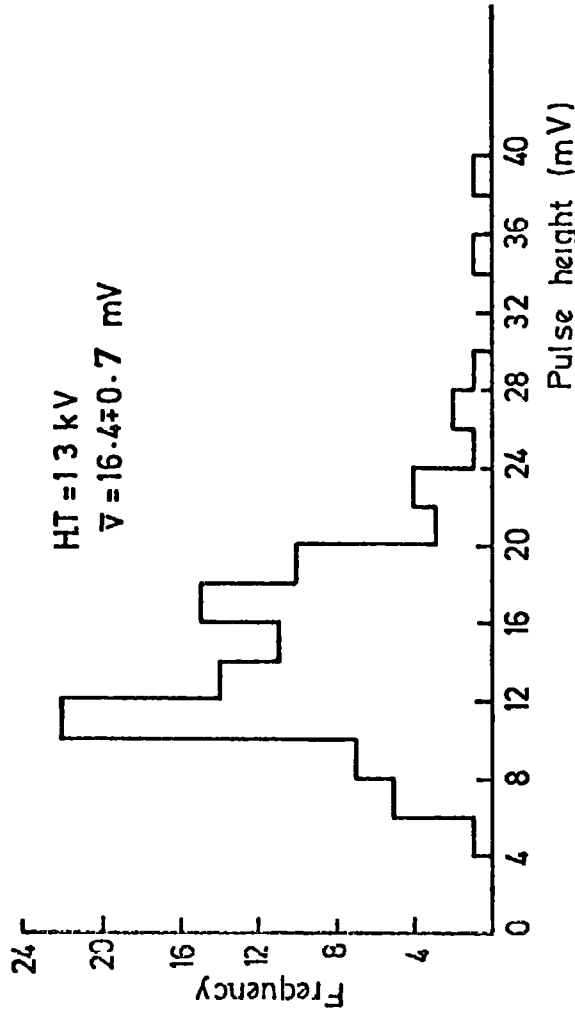
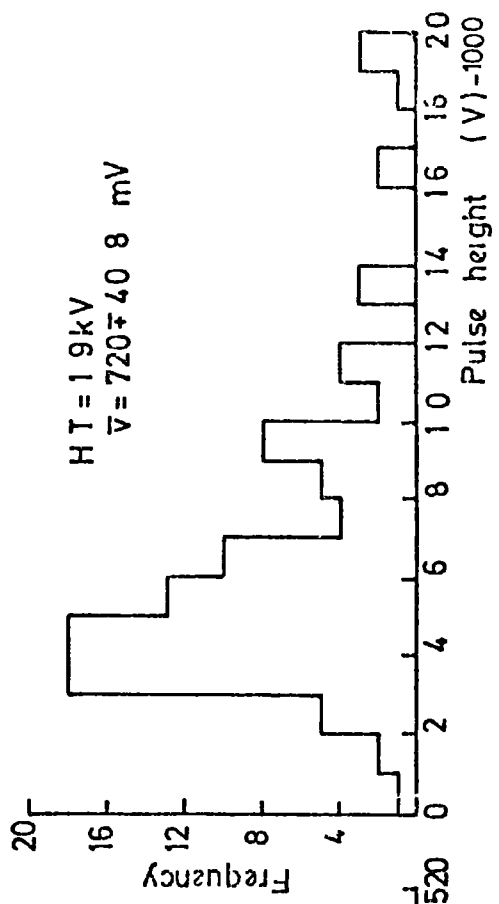
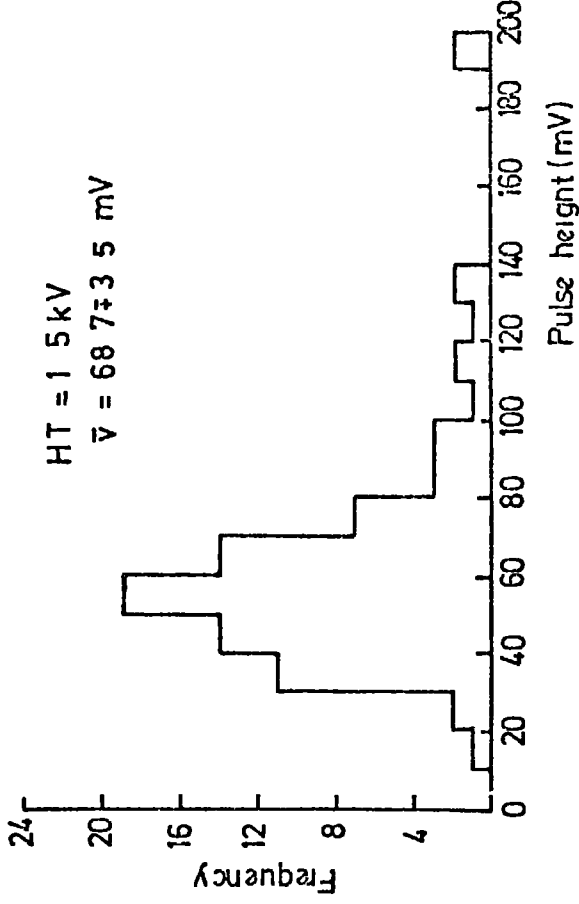


Figure 4.14

The single particle pulse height distribution for scintillator C.
The pulse height measured at the output of the amplifier (see figure 4.11).



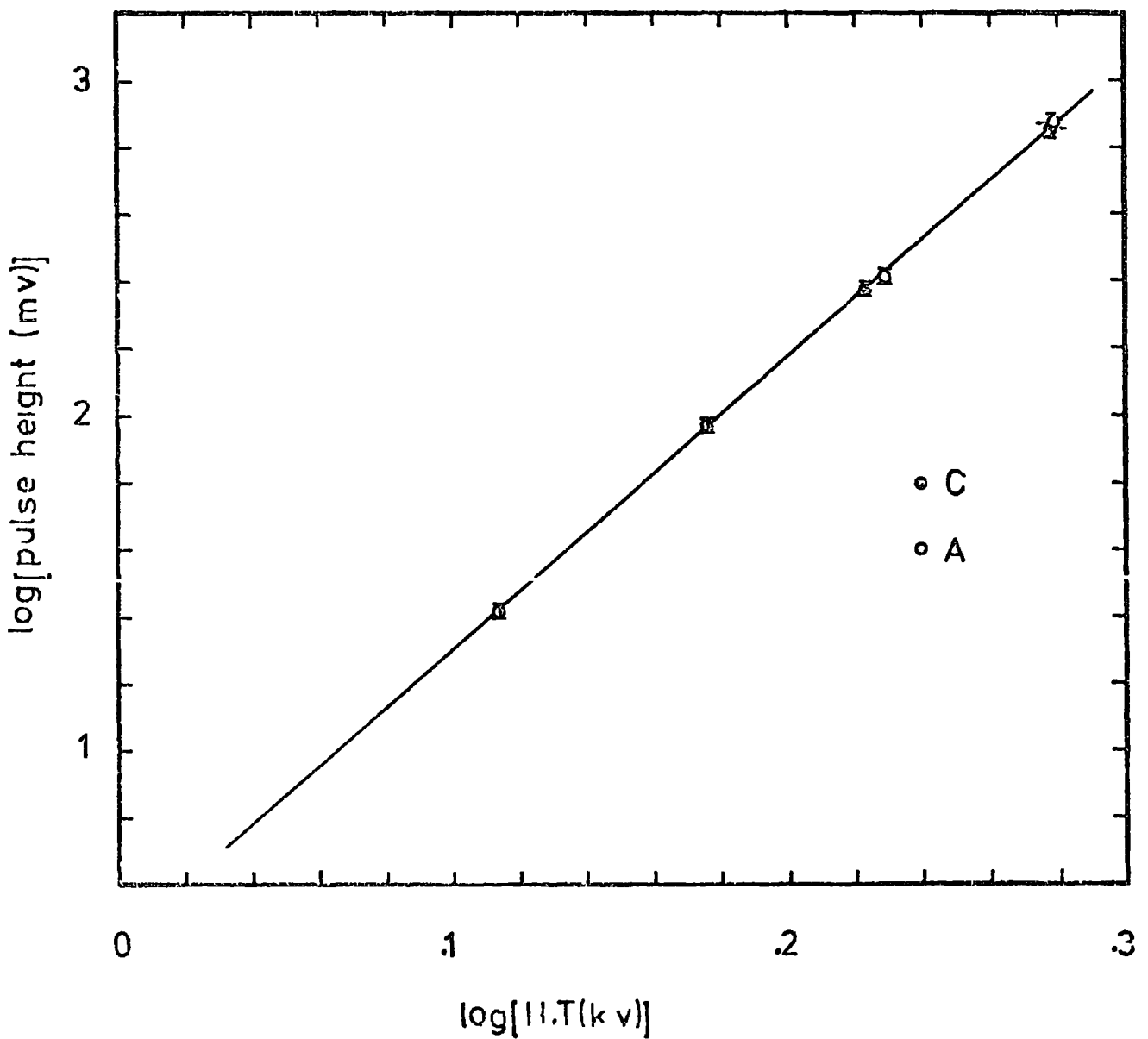


Figure 4.15

Variation of output pulse height with the H.T. voltage applied to the scintillators A and C. The pulse height is given at the output of the photomultipliers for a single penetrating particle traversing the centre of the counter at vertical incidence.

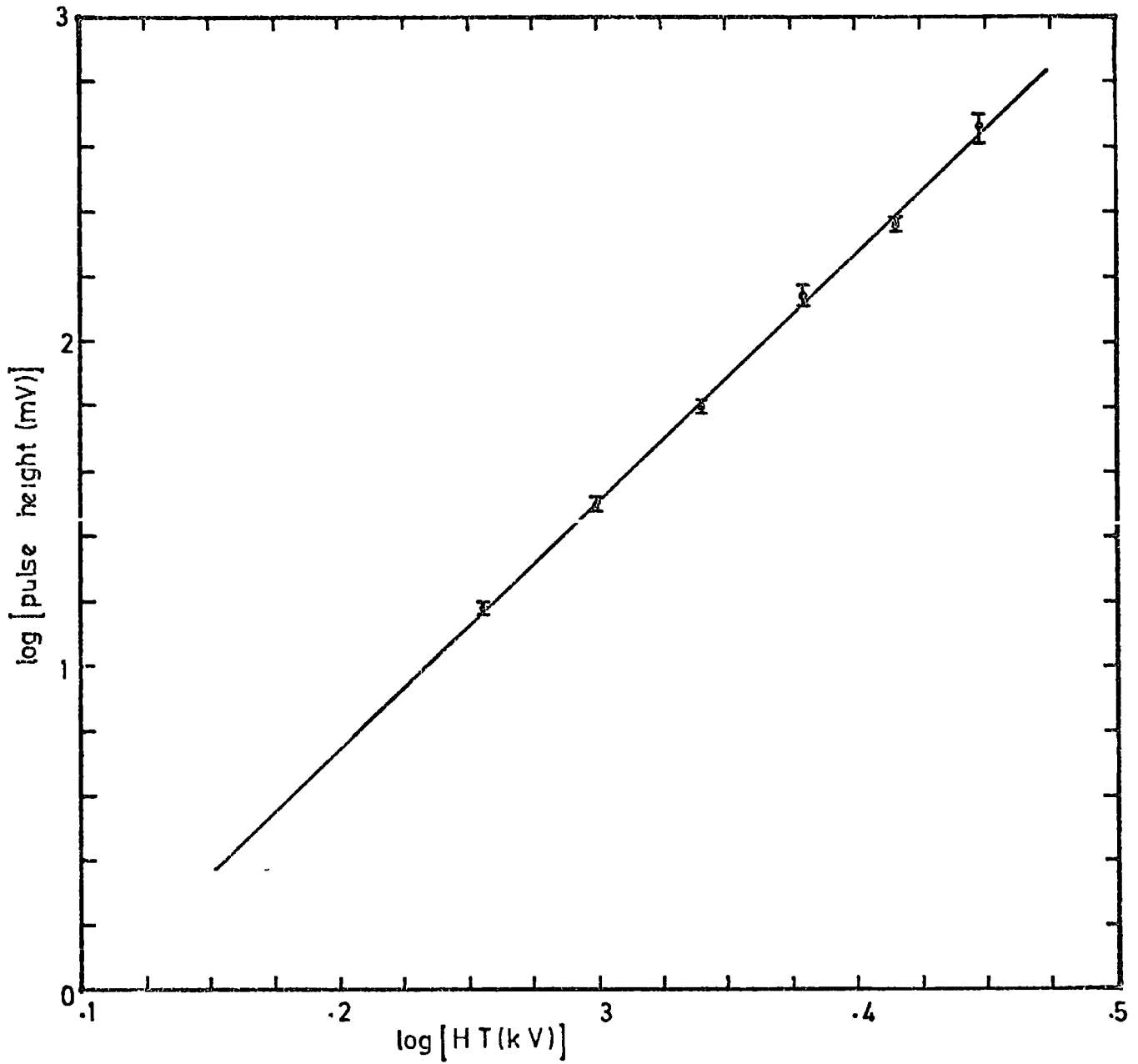


Figure 4.16

Variation of output pulse height with the H.T. voltage applied to the scintillator M. The pulse height is given at the output of the photomultipliers for a single penetrating particle traversing the centre of the counter at vertical incidence.

loss of the pulse height (see figures 4.10 and 4.11) through the electronics. However, the characteristics of the three scintillation counters obtained in this way are shown in figures 4.15 and 4.16.

4.3.4 Setting up the experiment

The experiment was set up to trigger off bursts greater than a certain size in either scintillator A or C. The burst size N was defined as a burst which produced a pulse height of N times the single particle pulse height. The block diagram for the electronics used in the experiment is shown in figure 4.17. When the trigger occurred the pulses from both scintillators A or C were displayed on an oscilloscope trace after being delayed by $0.3\ \mu\text{s}$ and $0.9\ \mu\text{s}$ respectively. Subsequently a high voltage pulse was applied to the flash tubes and a photograph showing the geometry of burst was obtained.

The triggering threshold was determined by discriminators which were set to a fixed level using a pulse generator, then it was possible to select a different triggering threshold by altering only the H.T. applied to the photomultiplier tubes. The liquid scintillator M was set at an H.T. value in which it could record more than two particles, the pulses from this scintillator being delayed by $1.6\ \mu\text{s}$.

The chamber was run with two different time delays ($20\ \mu\text{s}$ and $330\ \mu\text{s}$) between the occurrence of the burst and the application of the high voltage pulse to the flash tubes. Hence, the $20\ \mu\text{s}$ time delay used for this experiment was the same as that required for extensive air shower experiment to look for the quarks. A list has been given below showing the series of films with the trigger thresholds used during running this experiment.

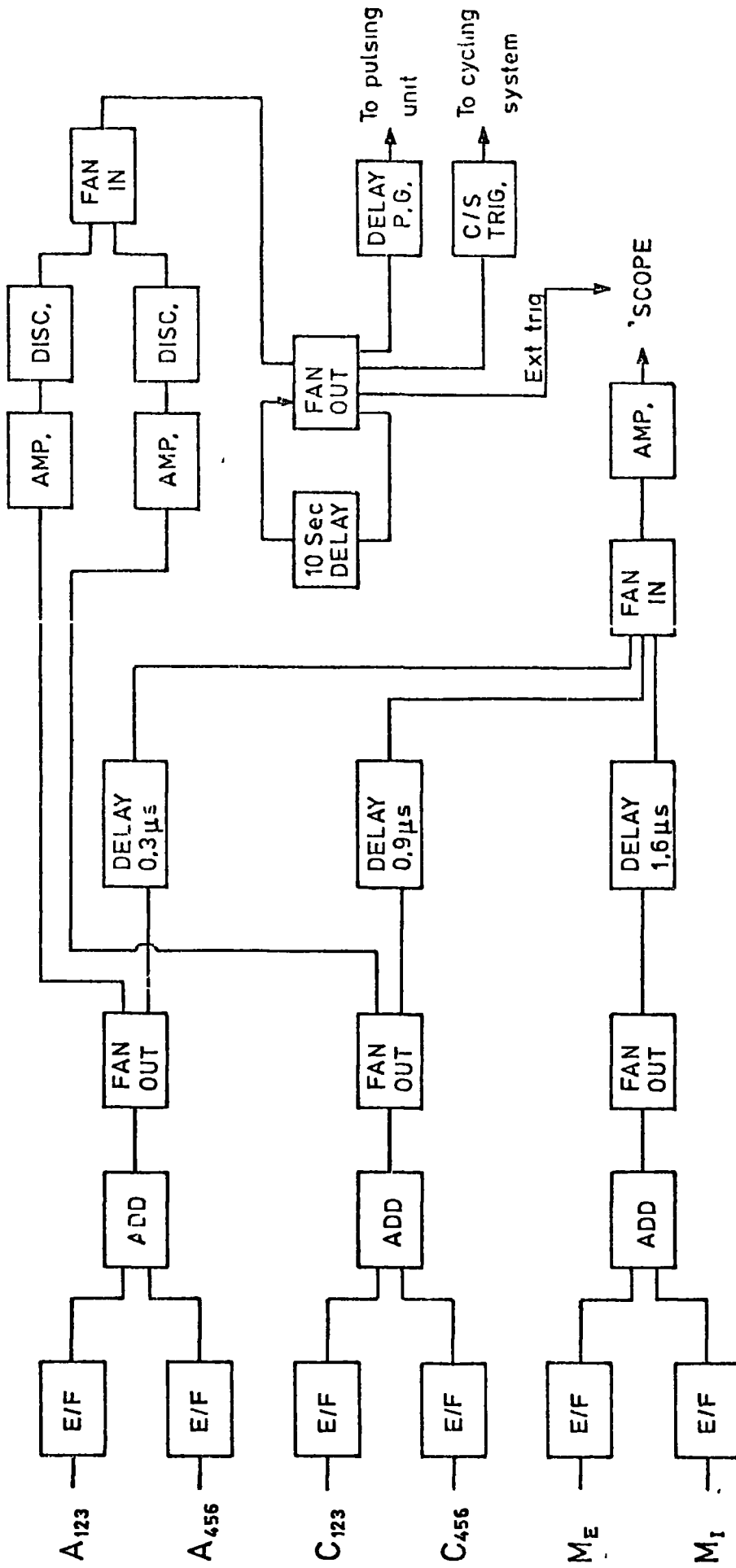


Figure 4.17

Block diagram of the electronics used in the vertical burst experiment

<u>Film number</u>	<u>triggering threshold</u>	
H1 - H2	≥ 20 particles] $T_D = 20 \mu s$
H3 - H9	≥ 100 particles	
H10 - H14	≥ 200 particles	
H15 - H24	≥ 400 particles	
H25 - H28	≥ 200 particles	
H29 - H35	≥ 400 particles	
H36 - H39	≥ 400 particles] $T_D = 330 \mu s$
H40 - H77	≥ 500 particles	

4.4 The experimental data

4.4.1 The procedure of analysing the data

The information from both films were taken after projecting the films onto scanning tables. From the oscilloscope film one can get information about the pulse heights from the scintillators, the origin of the burst and the shower accompaniment (if any) with the incident hadrons. From the flash tube chamber film the width of the burst could be measured and the projected angle of the cascade through the chamber could also be measured.

The burst width was measured in cms on the scanning sheets, figure 4.18, hence to transform to real space the width must be multiplied by a factor of 20. Each event was studied, classified and measured carefully. Plates 4.1 to 4.4 show examples of events obtained from running the experiment on $20 \mu s$ time delay.

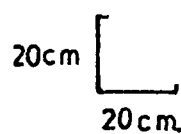
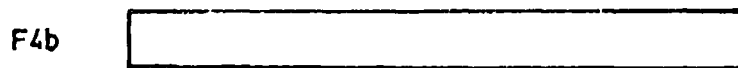
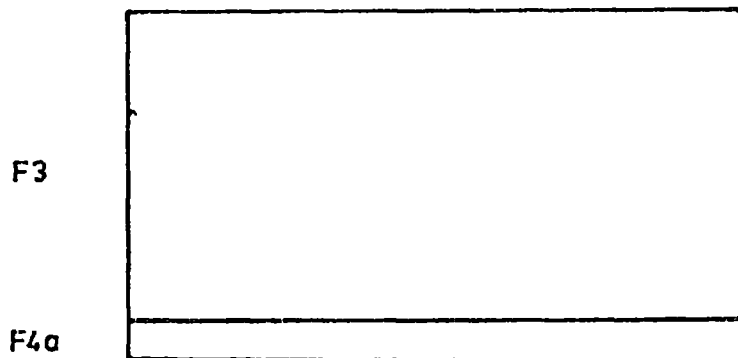
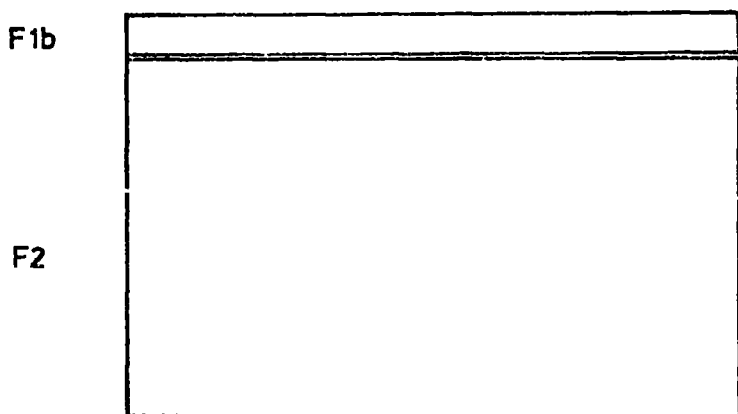
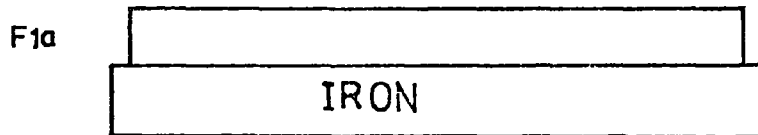
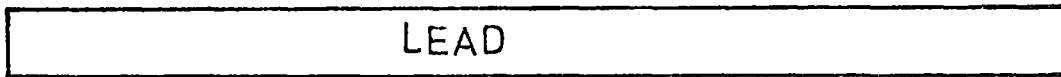


Figure 4.18

The front view of the flash tube chamber as drawn on the scanning sheet.

Plate 4.1

Event H23 - 30

A burst produced in the lead which penetrated the iron, producing output pulses from scintillators C and A.

There is also EAS accompaniment, seen in the liquid scintillator M.

From left to right of the oscilloscope trace, the scintillator outputs are A, C and M.

This was taken from a run using a time delay T_D of 20 μ s.

C = 620 particles.

A = 1,600 particles.

M = 31 particles.

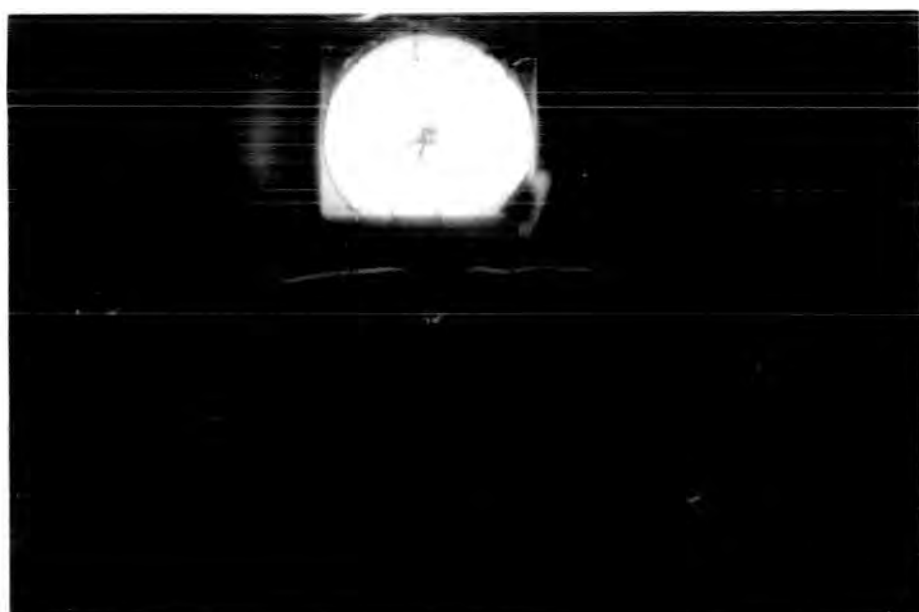
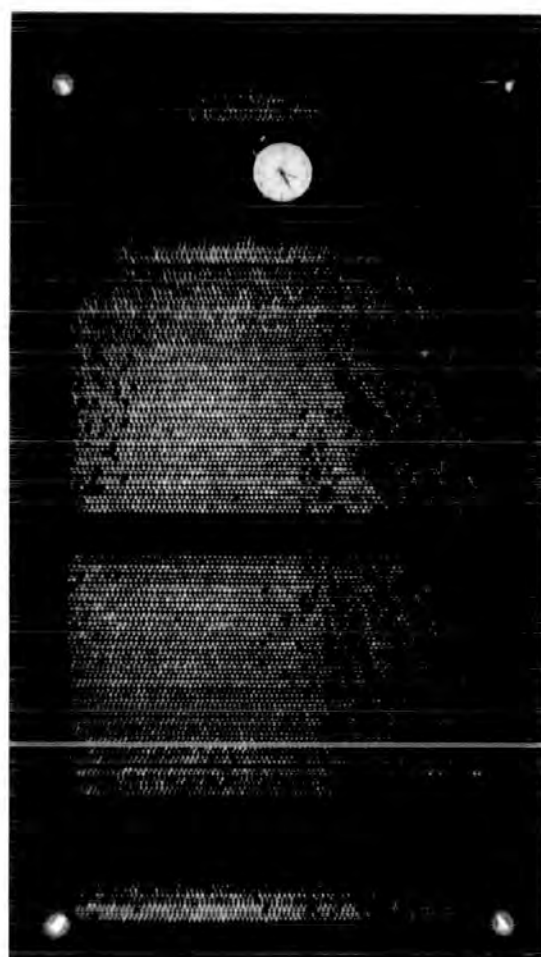


Plate 4.2

Event H35 - 14

A burst produced in lead which penetrates the iron, giving pulses from scintillators C and A.

This was taken from a run using a time delay T_D of $20\mu s$.

C = 880 particles.

A = 1,300 particles.

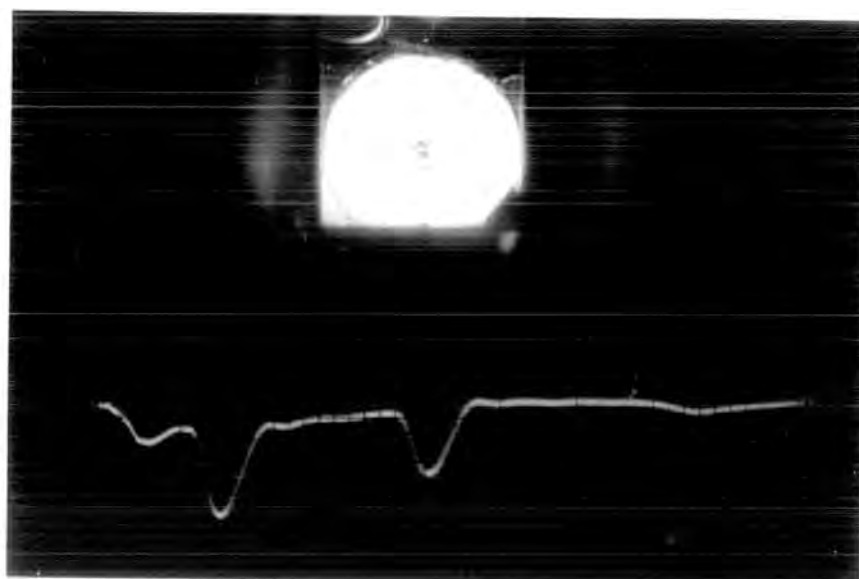
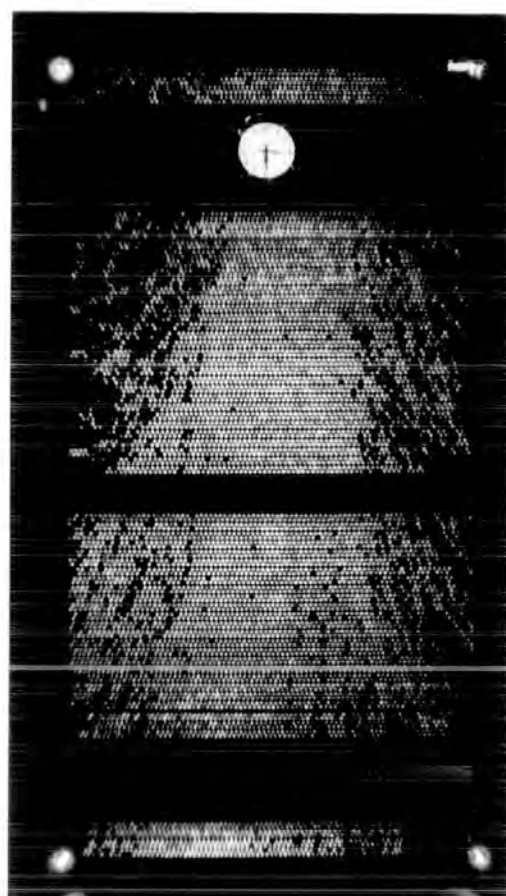


Plate 4.3

Event H29 - 14

A burst produced in the iron by a charged particle.

The oscilloscope trace shows a pulse from scintillator A.

This was taken from a run using a time delay T_D of $20 \mu s$.

A = 900 particles.

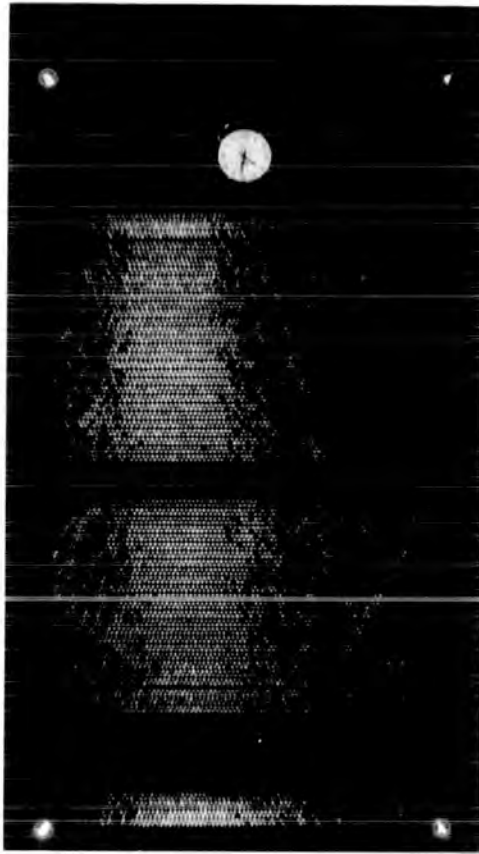


Plate 4.4

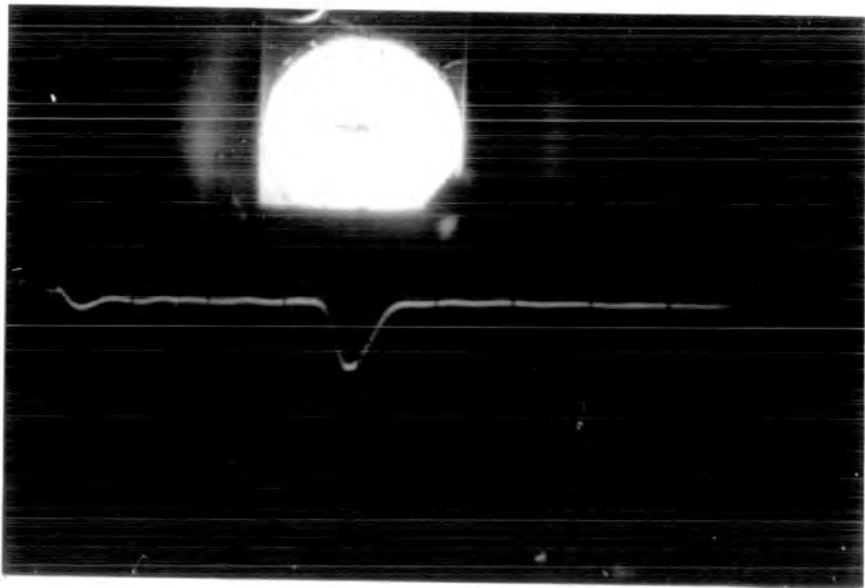
Event H31 - 2

A burst produced in the lead which is absorbed
in the iron.

The oscilloscope trace shows a pulse from
scintillator C.

This was taken from a run using a time
delay T_D of 20 μ s.

C = 840 particles.



4.4.2 Lateral spread of bursts

Before producing the exact form of the relation between the burst size measured in the scintillator and the burst width measured in the flash tubes directly below the absorber, it is important to predict this relation and see if there is any correlation between the width and the size of the burst.

(a) A theoretical expression for the lateral structure function of pure electromagnetic cascade has been given by Nishimura and Kamata (1952). This function can be approximated by the following simple expression given by Greisen (1956):

$$f\left(\frac{r}{r_1}\right) = C(S) \left(\frac{r}{r_1}\right)^{S-2} \left(1 + \frac{r}{r_1}\right)^{S-4.5}$$

where S is the age parameter, $C(S)$ is a normalization coefficient and r_1 is the radius in Moliere units.

A solution to the above expression has been made by Cooper (private communication). Cooper found that the distance at which the density falls to $\Delta\left(\frac{r}{r_1}\right)$ is related approximately to the burst size by the power law dependence:

$$r \approx N^{0.22} \quad (\text{under a reasonable assumption } S = 1)$$

However, a calculation has been made more accurately by Cooper to evaluate the above expression by integrating Nishimura - Kamata - Greisen (NKG) formula for three different age parameters. The density of electrons per tube calculated not by integrating radially, but along strips corresponding to the flash tube cross-sections. The results of the integration are shown in figure 4.19. The predicted relation between the burst size and the burst width on the flash tube will be shown with the experimental measurements later in this section.

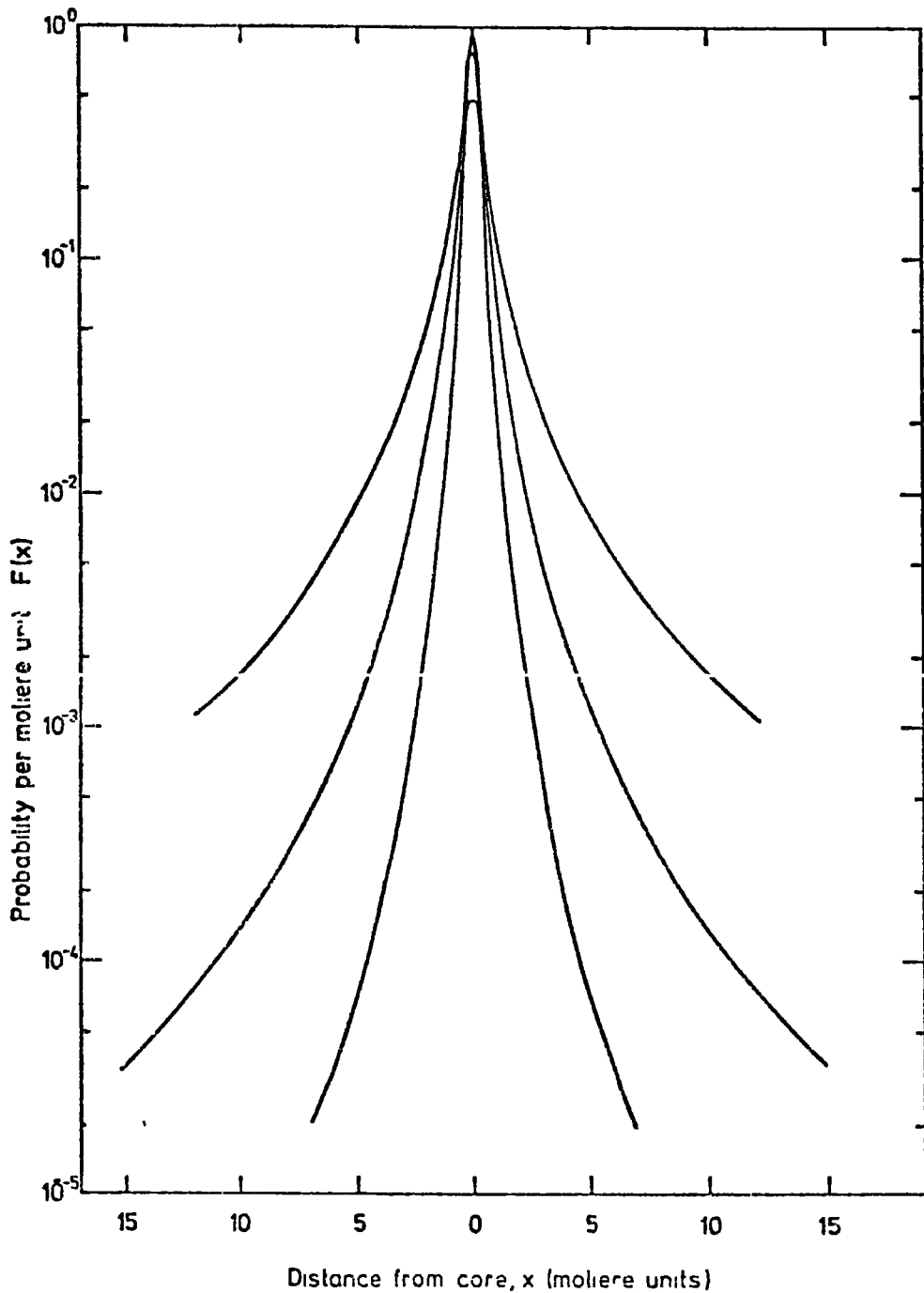


Figure 4.19

The probability of a particle traversing a flash tube as a function of distance from the core, expressed with width in Molieric units. The number of particles falling on a strip of width 1 Molieric Unit at a distance X from the core is $NF(X)$, where N is the burst size.

(b) Different triggering thresholds were used starting with ≥ 20 particles, the widths of the burst produced in the lead or iron were measured in the top of Fla and Flb respectively (see figure 4.9). The width was defined as the width in which all the flash tubes had flashed. So a few tubes which flashed far away from the core of the burst were not considered when the width of the burst was measured, because these might be produced by large angle single electron scattering. After scanning the films in the same procedure discussed in the previous section, the relation between the burst size and the burst width on the flash tube was measured and scatter plots were produced from the data on the $20\mu\text{s}$ run for the iron and lead absorbers as shown in figures 4.20 and 4.21. The points in the scatter plot were binned and their means found. An event was accepted if the whole width of the burst could be seen in the flash tubes, while as the burst width increases the probability of observing the whole burst decreases. The loss factor was $\frac{D-d}{D}$, where D is the width of the flash tube chamber and d is the measured width of the burst on the flash tubes. The burst width distribution was corrected by dividing each burst width cell by the loss factor. The results of the burst size - burst width relation are shown in figure 4.22 for the iron and figure 4.23 for lead. In figure 4.22 a comparison has been made between the present results and the results given by Coats (1967) for bursts produced in 25 cms of iron and the result of prediction using the NKG lateral distribution function which is discussed in item (a).

From the present results it was found that both results from lead and iron followed a power law dependence. These relations were used to derive the energy spectra of hadrons in extensive air showers as described in Chapter 9.

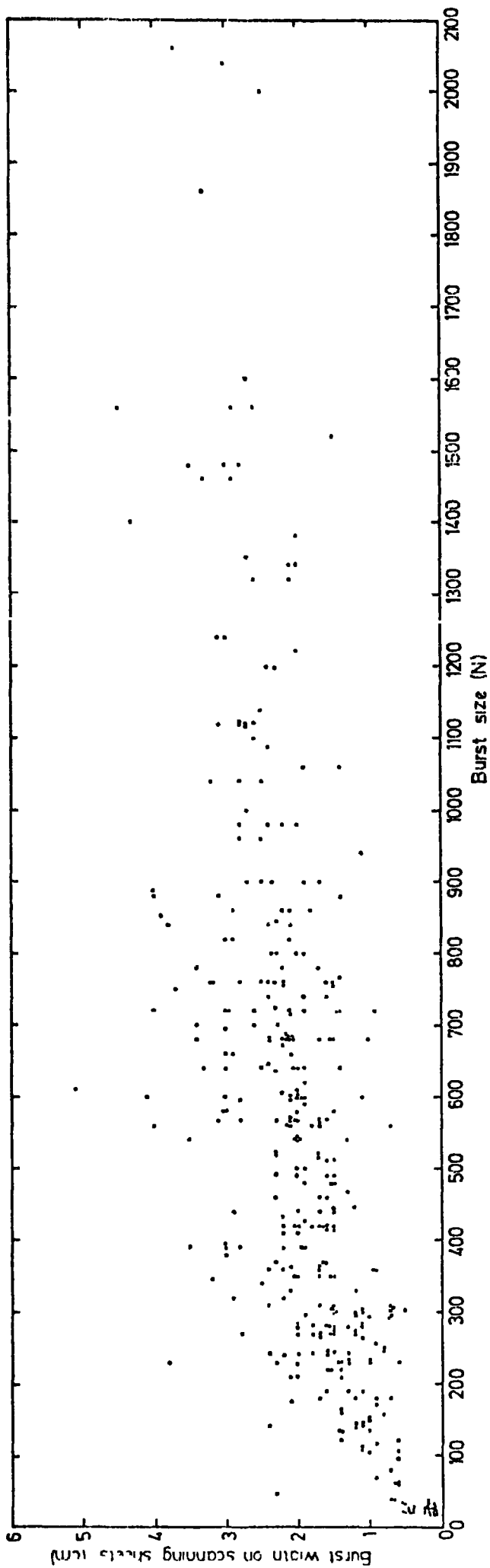


Figure 4.20

Scatter plot showing the relation between the burst size measured in scintillator A (burst in iron) and the burst width measured in the flash tubes on the scanning sheets (scale 1:20).

Data from run on $20\mu s$ time delay. (H1 - H35).

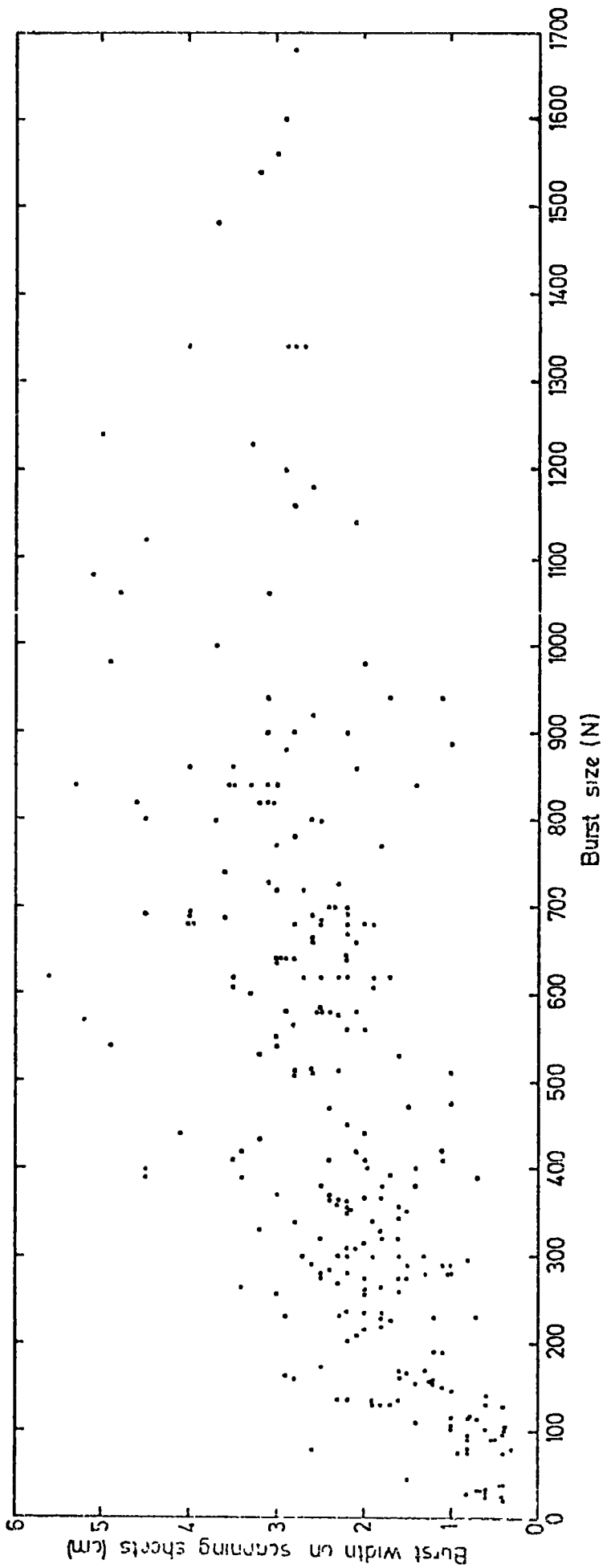


Figure 4.21

Scatter plot showing the relation between the burst size measured in scintillator C (burst in lead) and the burst width measured in the flash tubes on the scanning sheets (scale 1:20).

Data from run on 20 μ s time delay. (H1 - H35).

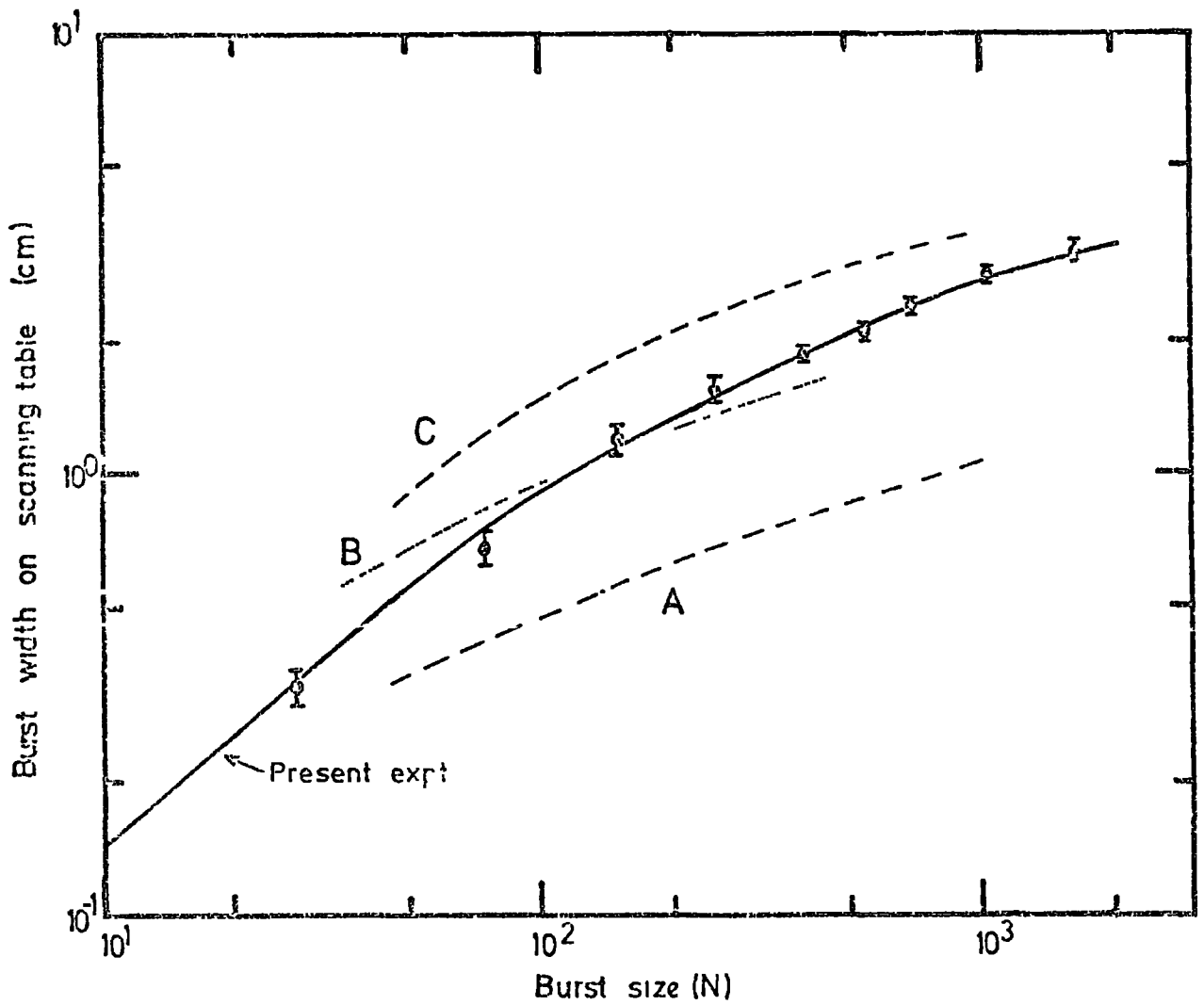


Figure 4.22

The variation of burst width (measured on the scanning sheets, scale 1:20) with burst size (N) for iron absorber. Data from run on $20 \mu s$ time delay, T_D . (H1 - H35). A comparison between the present measurements (points) and other results.
 Curve A - prediction for pure electron - photon cascade,
 Curve B - measured relationship for electromagnetic cascade (Coats, 1967).
 Curve C - measured relationship for nuclear - electromagnetic cascade (Coats, 1967).

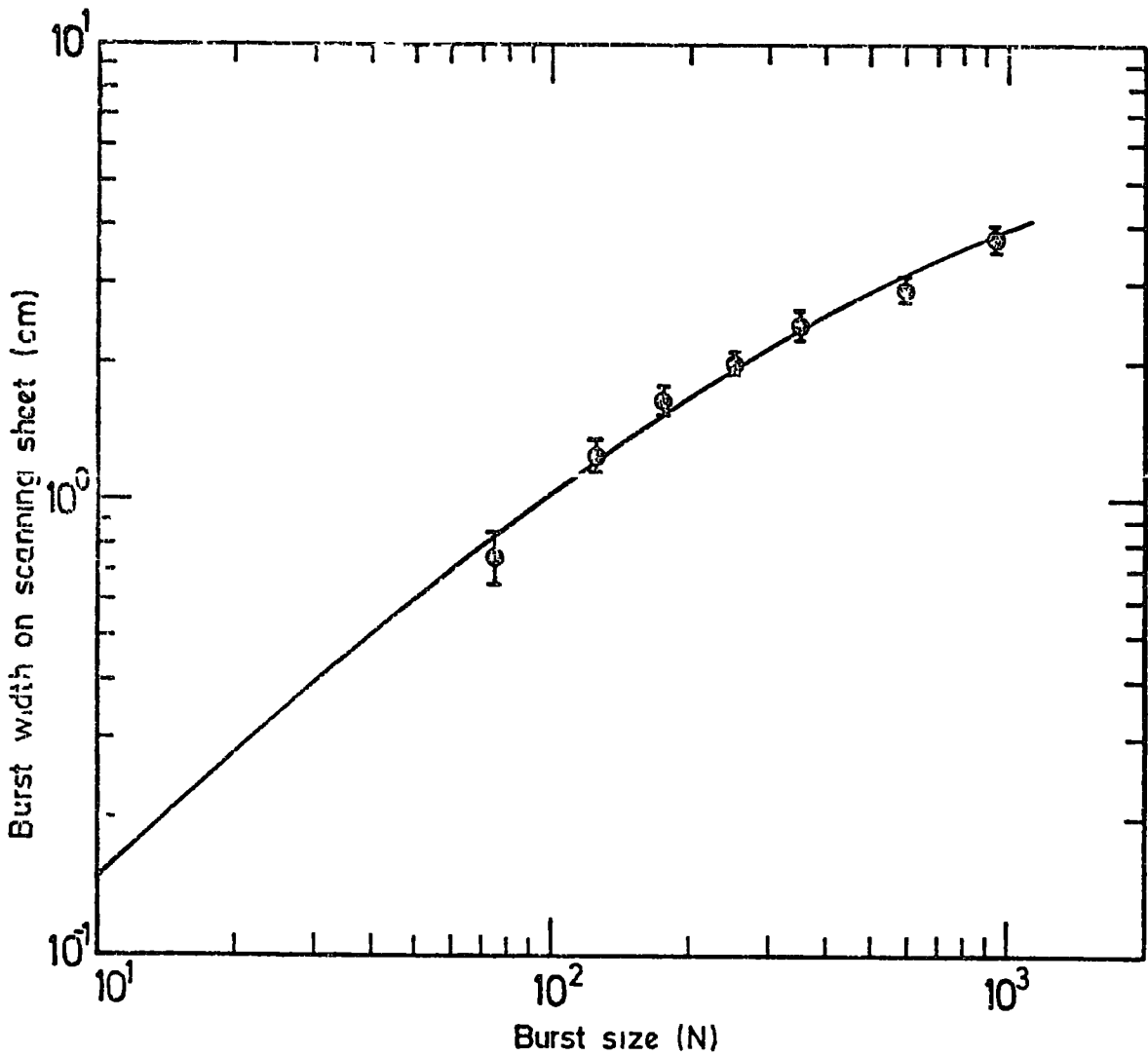


Figure 4.23

The variation of burst width (measured on scanning sheets, scale 1:20) with burst size (N) for lead absorber. Data from run on $20\mu\text{s}$ time delay, T_D . (H1-H35).

4.4.3 Extension to higher energies

An attempt has been made to measure the high energy events, i.e. large burst size ≥ 400 particles, but with the arrangement described above the rate of high energy events recorded in the flash tubes is reduced over the width observed with a $20\mu\text{s}$ time delay. This is due to the small aperture for a wide burst width observed. Plate 4.5 shows an example of this type of unmeasurable event. The operation of the flash tube chamber was modified so that the efficiency of defining the axis of large bursts is increased. For this the variation of flash tube efficiency with the delay T_D was used. From the internal efficiency - time delay curve shown in figure 4.8, it was noted that the efficiency fall off as the time delay increases. This arises from the loss of the initial electrons by diffusion to the walls of the glass tube in the time interval between the passage of the charge particle and the application of the high voltage pulse to the chamber. Lloyd's parameter for a single charge e particle was found to be $af_1Q_1 = 9$, and since the parameter is a linear function of the amount of ionisation produced, the value for traversal, for example, 20 charge e particles would be $af_1Q_1 = 180$. However, the relation between the internal efficiency η_1 and the time delay T_D for large values of af_1Q_1 was calculated and is shown in figure 4.24. From this figure one can say that for a given time delay the change in the efficiency is not big for different af_1Q_1 , figure 4.25. From figure 4.19 it can be seen that the density of electrons per tube decreases rapidly with distance from the core of the cascade, then instead of allowing a single electron to define the edge of the burst a long time delay of $330\mu\text{s}$ was used to diffuse all these single electrons and observed a solid core for the cascade in the chamber. Plates 4.6 - 4.9 shows examples of the events obtained from running this experiment on $330\mu\text{s}$

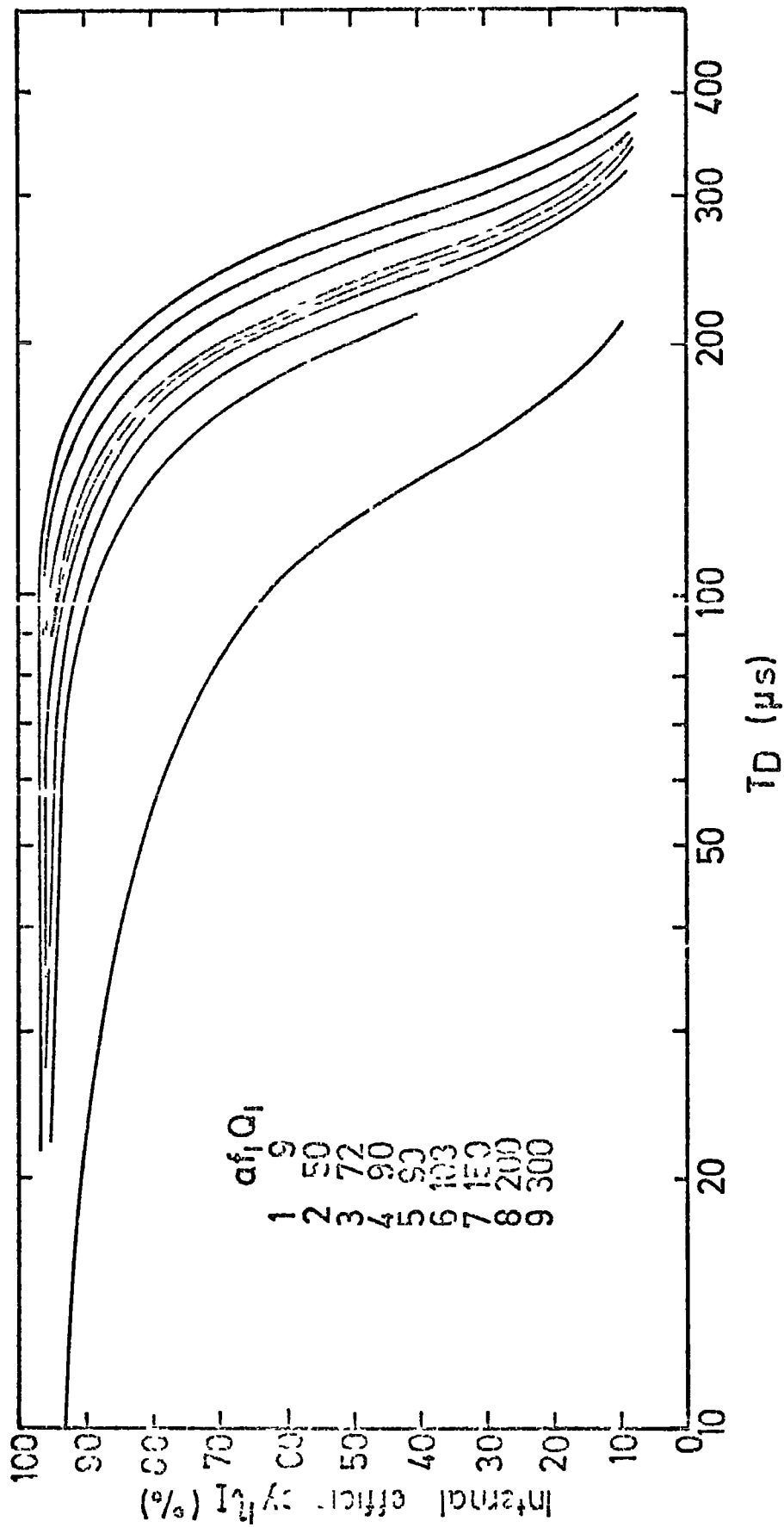


Figure 4.24 Predicted variation of the internal efficiency of flash tubes and the time delay for large values of parameter af_1Q_1 .

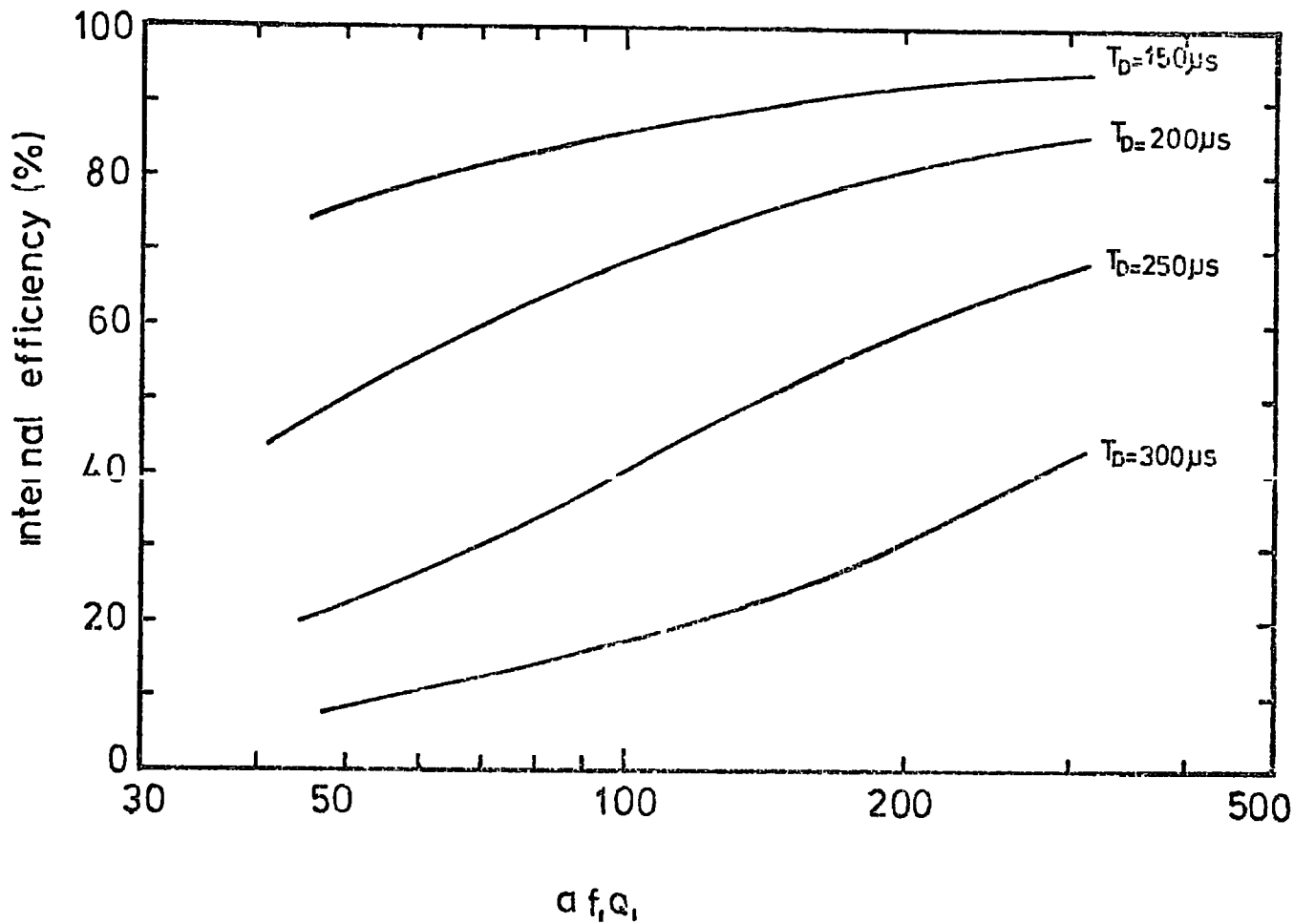


Figure 4.25

The predicted variation of the internal efficiency of flash tubes with af_1Q_1 for large values of af_1Q_1 , at different time delay (derived from figure 4.23).

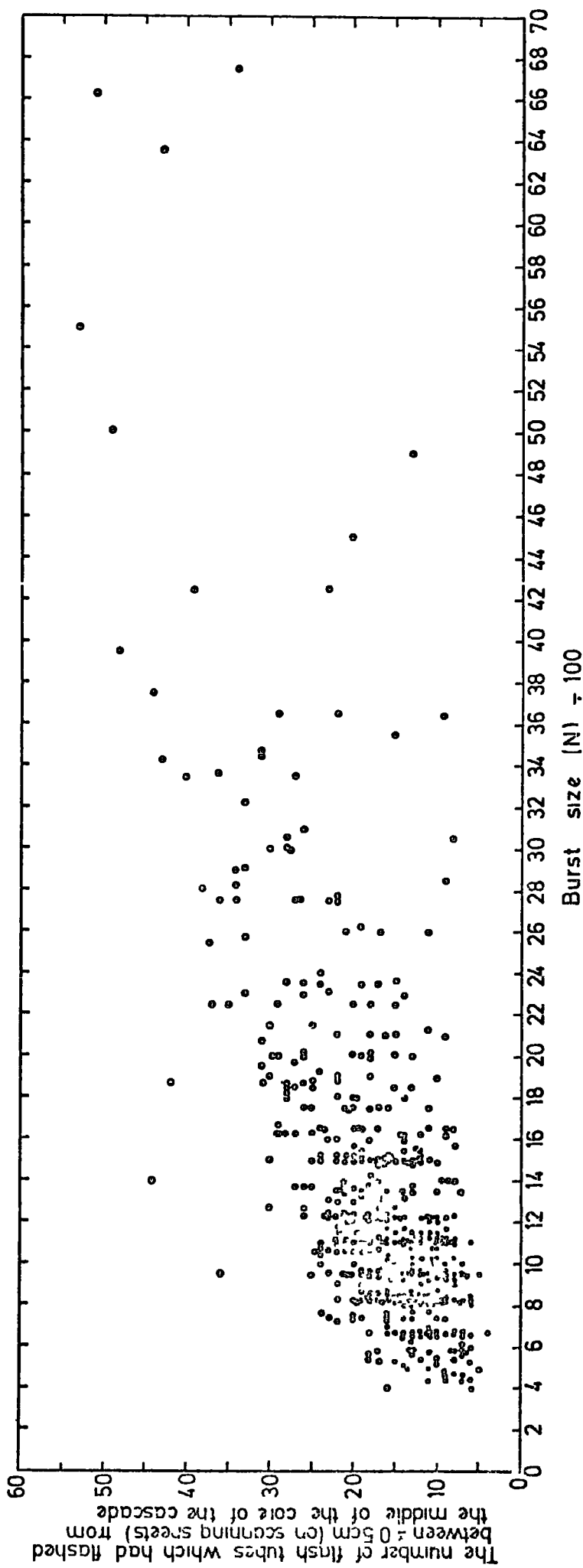


Figure L.26

Scatter plot showing the relation between the burst size (N) measured in scintillator A (burst in iron) and the number of flash tubes which had flashed between ± 0.5 cm from the core (1 cm full width) on scanning sheet (scale 1:20).
 Data from run on 330μ s time delay. (H36 - H77).

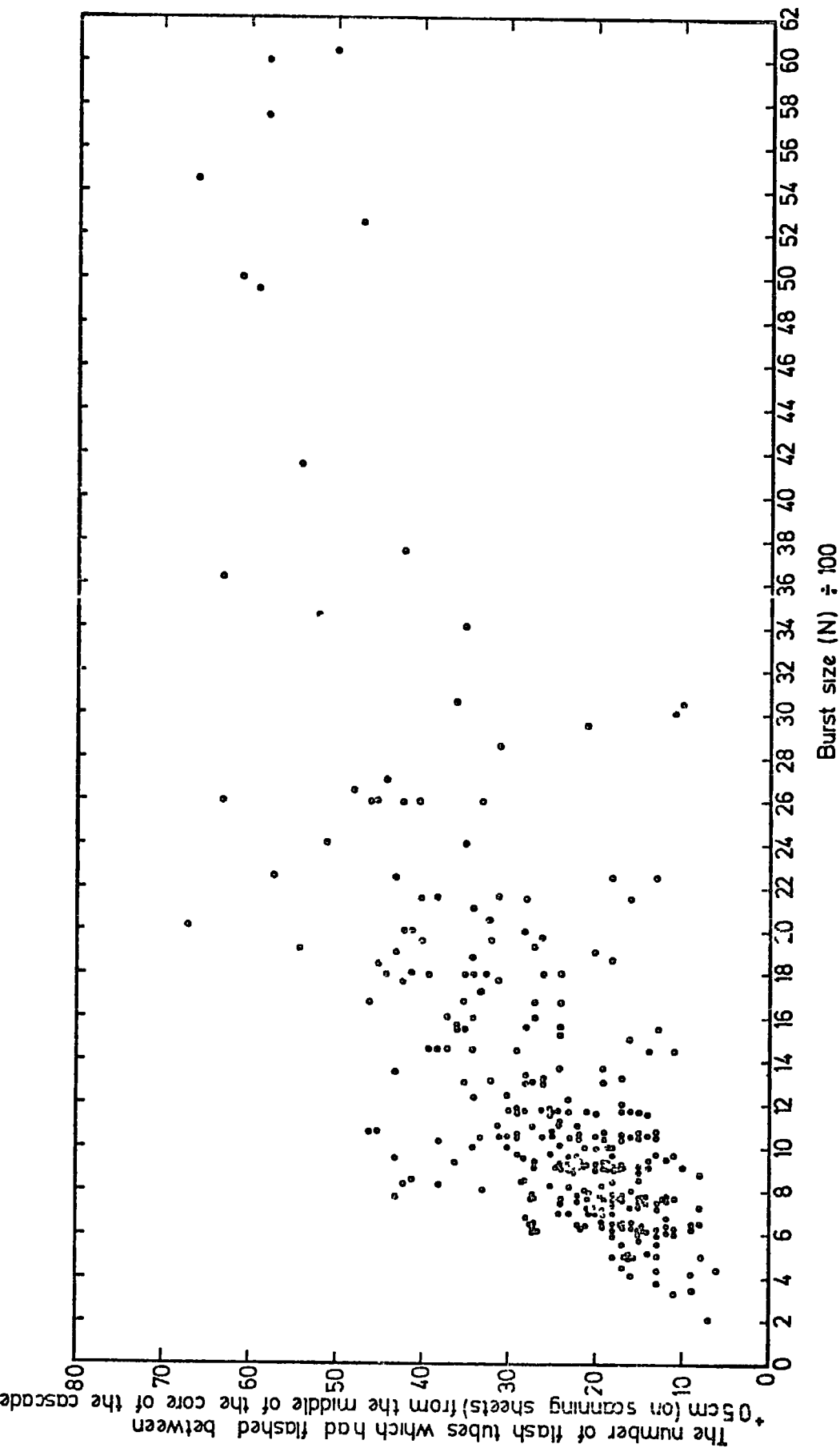


Figure 4.27

Scatter plot showing the relation between burst size (N) measured in scintillator C (burst in lead) and the number of flash tubes which had flashed between ± 0.5 cm from the middle of the core (1 cm full width) on scanning sheet (scale 1:20). Data from run on 330μ s time delay. (H36 - H77).

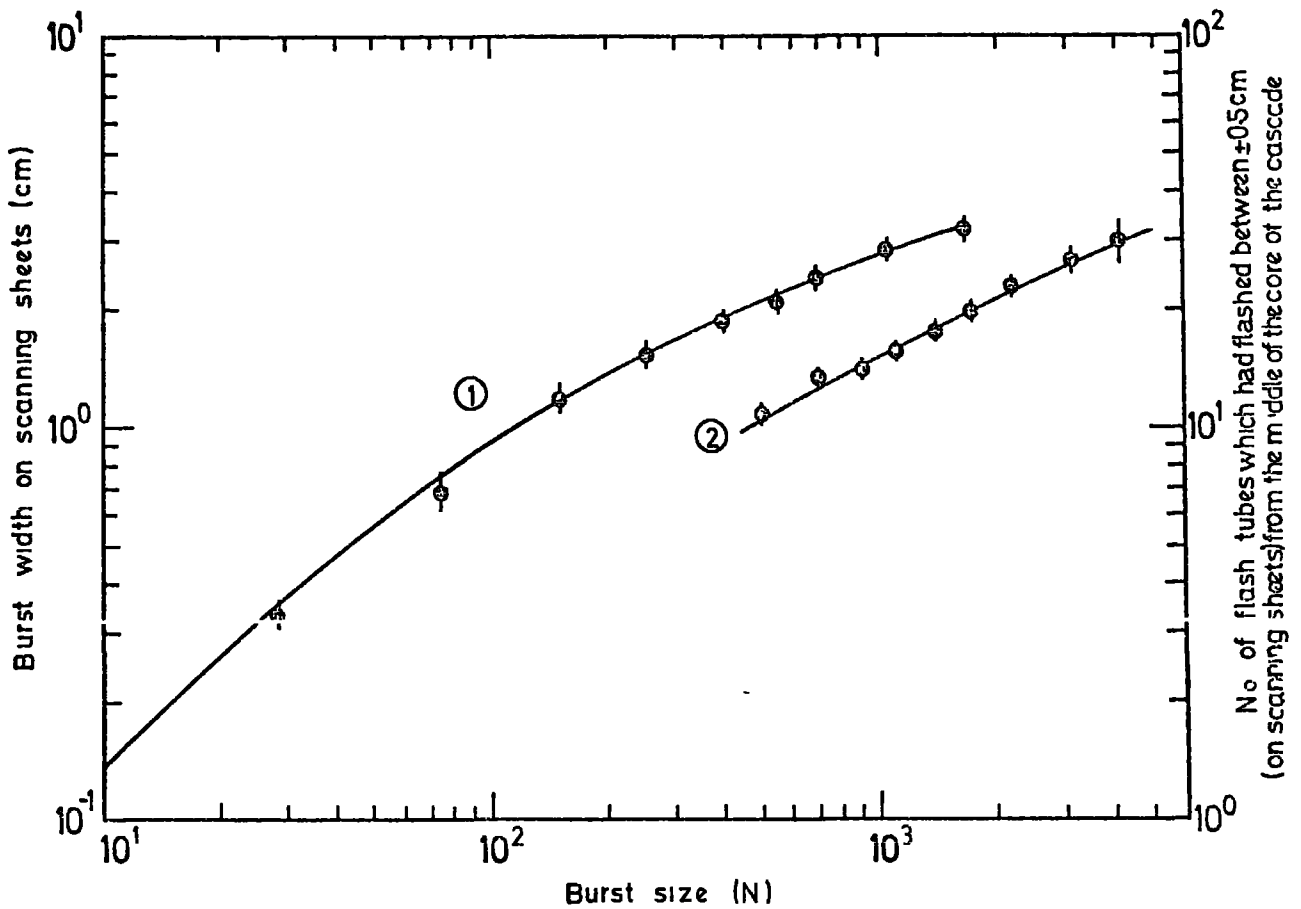


Figure 4.28

A comparison between the results on burst size (N) - burst width (measured on scanning sheets, scale 1:20) from run on $20 \mu\text{s}$ time delay. Curve (1) and the results on burst size (N) - number of flash tubes which had flashed in ± 0.5 cm from the middle of the core (1 cm full width measured on scanning sheets) from run on $330 \mu\text{s}$ time delay. Curve (2). The burst size measured under 15 cms of iron.

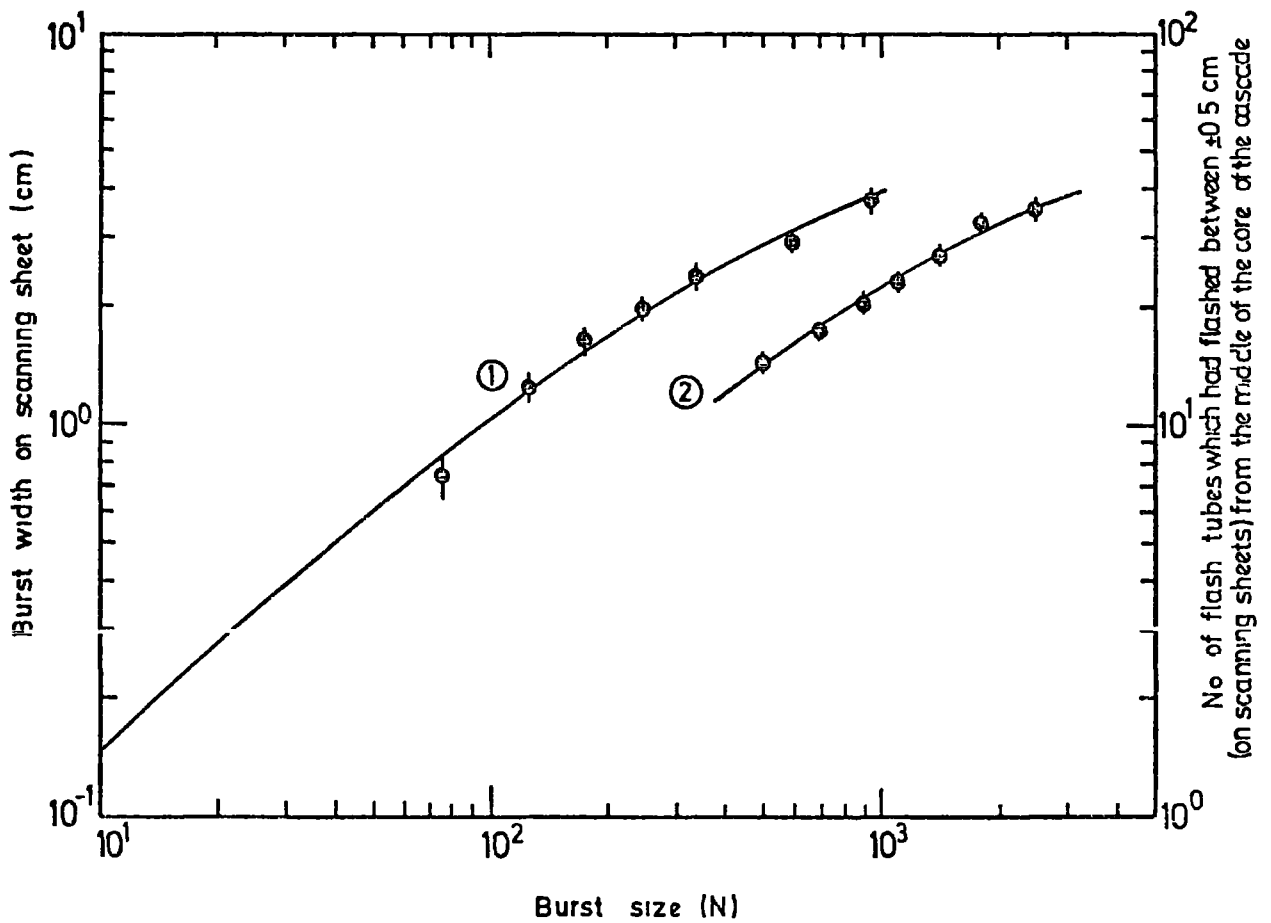


Figure 4.29

A comparison between the results on burst size (N) - burst width (measured on scanning sheets, scale 1.20) from run on $20 \mu s$ time delay, curve (1) and the results on burst size (N) - number of flash tubes which had flashed in ± 0.5 cm from the middle of the core (1 cm full width measured on scanning sheets) from run on $330 \mu s$ time delay, curve (2).
The burst size measured under 15 cms of lead.

time delay. The procedure for analysing the data from the flash tube film was changed. A fixed width was taken in this case corresponding to 1 cm on the scanning sheets (scale 1:20). Having the core of the cascade defined, the number of flash tubes which had flashed in that fixed width over 8 layers in Fla (burst in lead) and 6 layers in Flb (burst in iron) was measured. The scatter plot of the number of flash tubes which had flashed between ± 0.5 cms from the middle of the core (1 cm full width) as a function of burst size was plotted in figures 4.26 and 4.27 for bursts in iron and lead respectively. The points in each plot were binned and their means found. A comparison between this result and the result obtained on 20 μ s time delay run was shown in figures 4.28 and 4.29. It can be seen from both figures that the result from the long time delay run has almost the same slope as the result from the short time delay.

With the flash tube burst widths reduced the information on burst position can be used for defining the geometry while the energy is measured by the pulse height taken from the scintillators. With this arrangement the chamber gave satisfactory results and very high energy events were recorded.

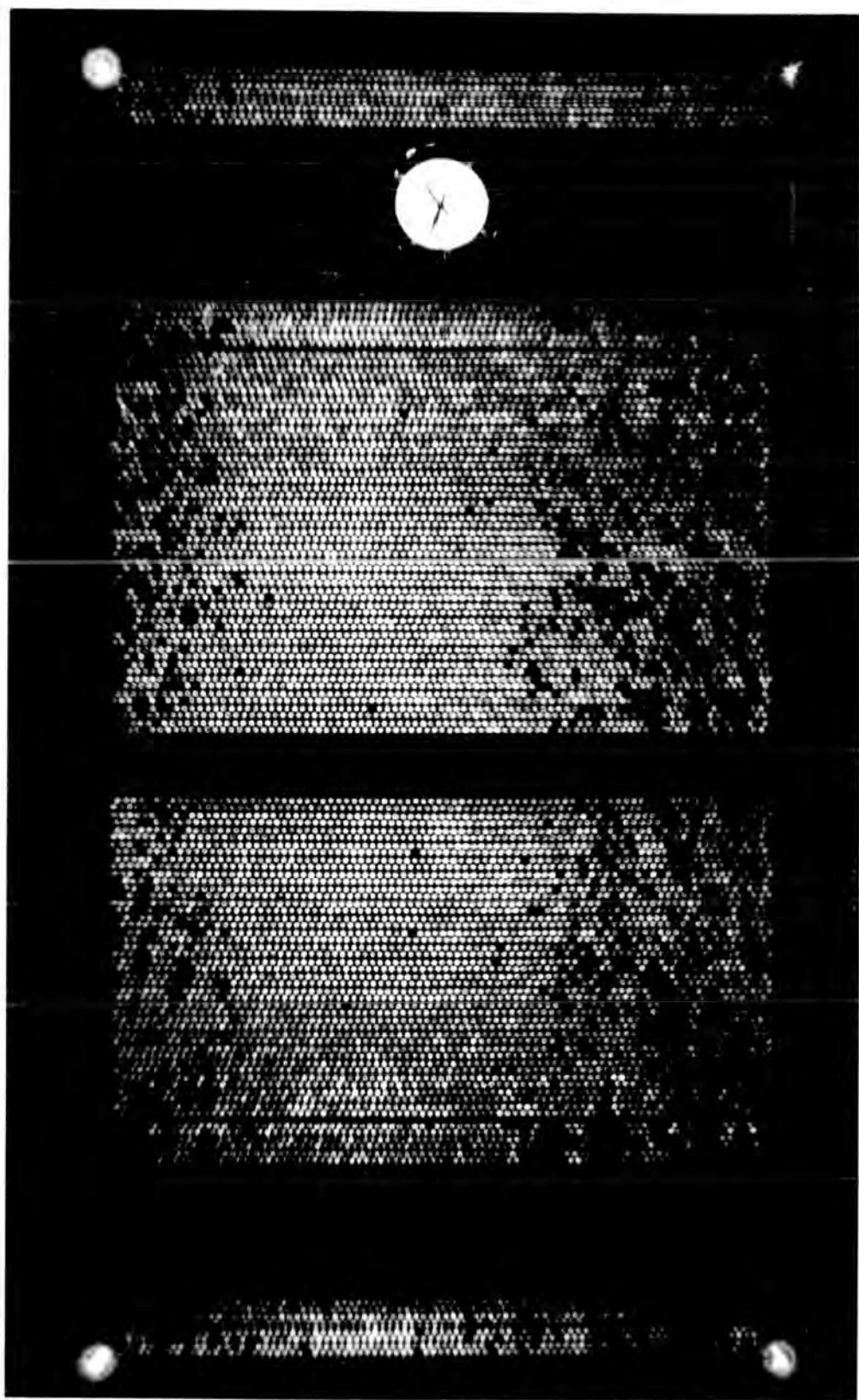
Plate 4.5

Event H30 - 47

An example of an unmeasurable burst produced in the lead in which the burst width, falling on the Fla layer, is out of the geometry.

This was taken from a run using a time delay

T_D of $20 \mu s$.



A burst produced in lead which penetrated the iron producing output from scintillators C and A.

There is also EAS accompaniment, seen in the liquid scintillator M.

From left to right of the oscilloscope trace, the scintillator outputs are A, C and M.

This was taken from a run using a time delay T_D of $330 \mu s$.

C = 1,000 particles.

A = 1,625 particles.

M = 35 particles.

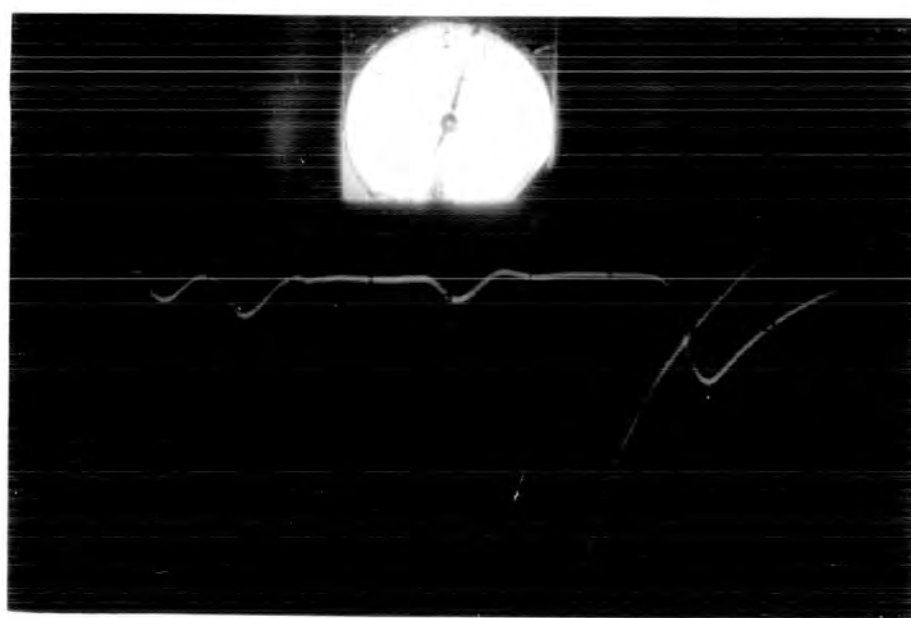
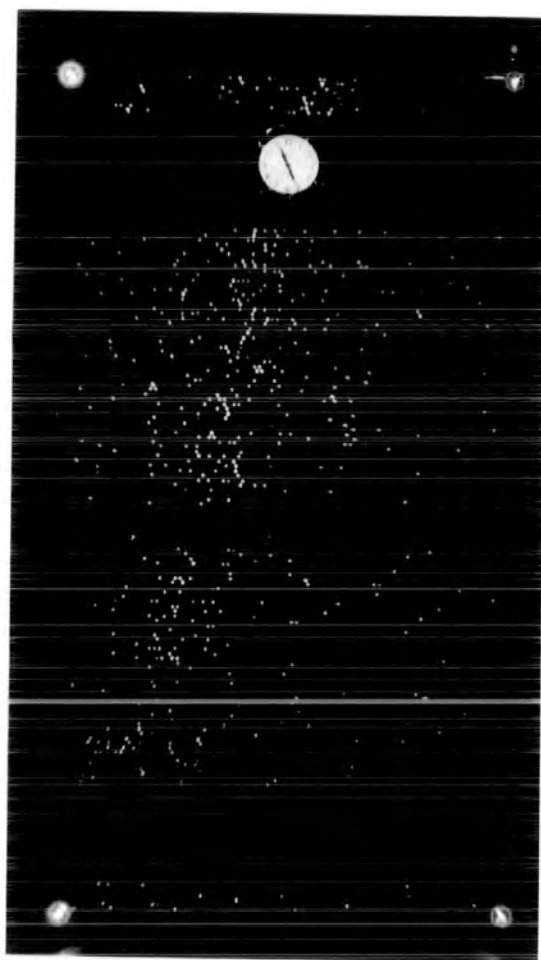


Plate 4.7

Event H50 - 24

A burst produced in lead which penetrates the iron, giving pulses from scintillators C and A.

This was taken from a run using a time delay T_D of $330 \mu s$.

C = 3,400 particles.

A = 1,500 particles.



Plate 4.8

Event H66 - 2

A burst produced in the iron. The
oscilloscope trace shows a pulse from
scintillator A.

This was taken from a run using a time
delay T_D of $330\mu s$.-----

A = 2,750 particles.

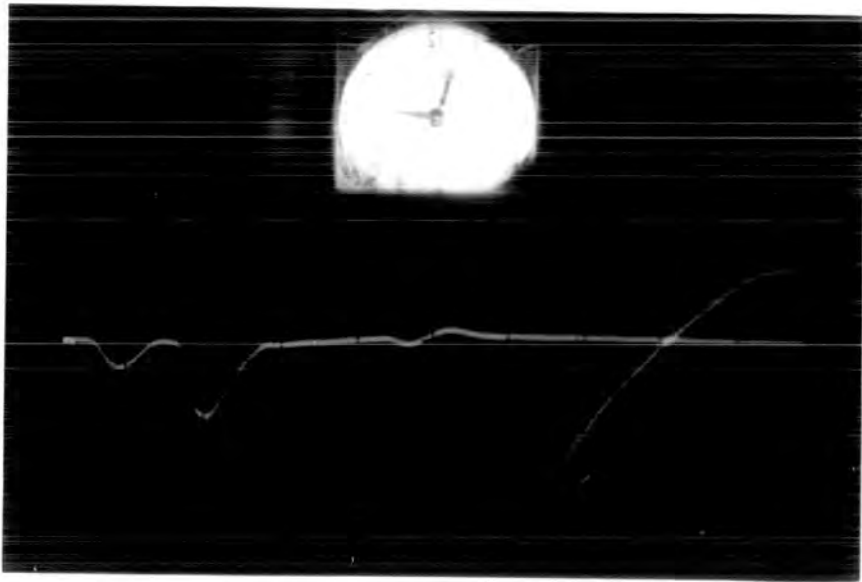
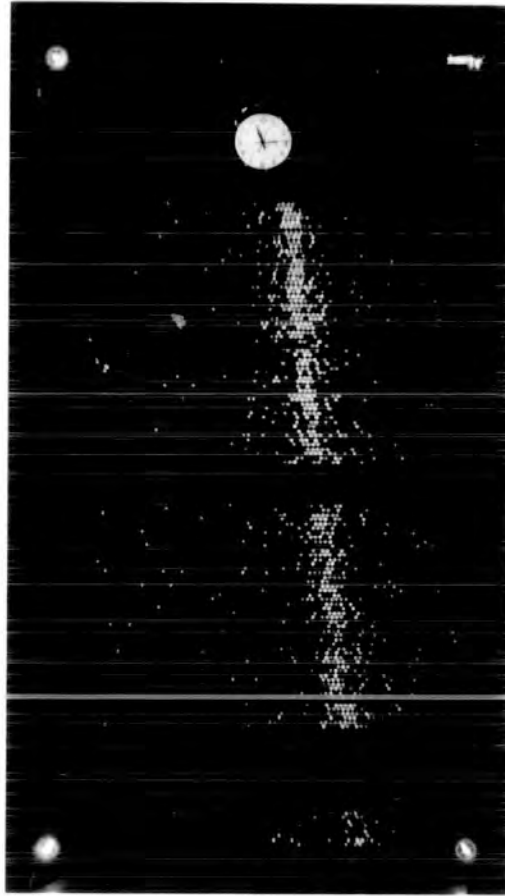


Plate 4.9

Event H53 - 22

A burst produced in lead, which is absorbed
in iron.

The oscilloscope trace shows a pulse from
scintillator C.

This was taken from a run using a time
delay T_D of $330 \mu\text{s}$.

C = 5,450 particles.



CHAPTER 5

THE ENERGY SPECTRUM OF HADRONS AT SEA LEVEL

5.1 Introduction

It was shown in chapter 4 that using the flash tube chamber the energy spectrum of hadrons (nucleons and pions) could be measured by observing their interaction in iron and lead absorbers. Briefly, charged and neutral particles were recorded and their burst size was measured, the mean energy of each particle interacting in lead or iron could be estimated using the burst size - energy relationship which has been discussed in chapter 3. The measurements on the energy spectrum was made in the energy range ~ 25 GeV up to 10^4 GeV.

The object of measuring the high energy range was to cover the same energy range in the spectrum published by Baruch, Brooke and Kollermark (1975). These workers measured the spectrum of hadrons at sea level and presented evidence for an anomalous behaviour in the energy range 2 - 8 TeV. For $E < 2$ TeV they found the differential vertical intensity to decrease with increasing energy as $E^{-2.6 \pm 0.1}$, for $2 < E < 8$ TeV the intensity is almost constant and for $E > 8$ TeV the intensity again decreases with increasing energy (see figure 2.5). The step (bump) in the spectrum for $2 < E < 8$ TeV is unexpected and Baruch et al. propose that it is produced by the interaction of a new particle (see section 2.3.9).

In the present work the result on the hadron energy spectrum shows a constant slope with $E^{-2.7 \pm 0.1}$ over the whole energy range from 10 GeV to 10 TeV.

5.2 The basic results

As mentioned in section 4.4, when an event is selected the scintillator

pulse is recorded on film from an oscilloscope, and the flash tubes are photographed by a camera. The pulses from the scintillators were converted so that they corresponded to the values at the output of the photomultiplier and then divided by the mean of the single particle pulse height to give the size of the burst in equivalent particles.

When the film is scanned, events are classified into two categories, (a) bursts produced in lead, (b) bursts produced in iron.

The chamber was run for a total of 4817.389 hours, in which time the trigger level was changed to different values, (see section 4.3.4). Table 5.1 shows the basic experimental results. From the table it is seen that the charge of the primary particles initiating bursts could only be determined for those occurring in the iron target when a time delay of $20\mu\text{s}$ was used between the occurrence of the burst and the application of high voltage pulse to the flash tubes, because in $330\mu\text{s}$ time delay all the electrons produced in the tube due to passage of charged particles are diffused resulting in a low ($\sim 5\%$) flashing efficiency and it becomes difficult to distinguish between the charged and the neutral particles.

In the present work bursts produced by charged primary particles were related to contributions from different particles (protons, pions and muons) and the bursts produced by neutral primary particles was related to neutrons. In table 5.1, the number of bursts produced in iron and lead within a projected zenith angle $\pm 30^\circ$ and in the acceptance geometry is given. The limit on the projected zenith angle was imposed in order to exclude side bursts produced in the walls of the chamber by high energy muons.

Figures 5.1 and 5.2 show the basic results on the burst size distributions in iron and lead absorbers for a trigger level ≥ 500 particles. All bursts represented in the distributions were in the angular range ± 30 to the vertical.

Trigger level ($\geq N$) particles	Time delay of high voltage pulse	Running Time	Number of Triggers	Number of bursts within $\pm 30^\circ$ to the vertical and in the acceptance geometry			
				nb	Fe		Total
					Charged	Neutral	
≥ 20	20 μ s	0.63 hrs	149	21	29	3	32
≥ 100	20 μ s	26.35 hrs	173	26	25	7	32
≥ 200	20 μ s	223.76 hrs	560	101	93	8	101
≥ 400	20 μ s	978.83 hrs	724	100	98	10	108
					Charged and Neutral		
≥ 400	330 μ s	176.47 hrs	122	23		39	
≥ 500	330 μ s	3411.25 hrs	1420	256		356	

Table 5.1 The basic experimental results.

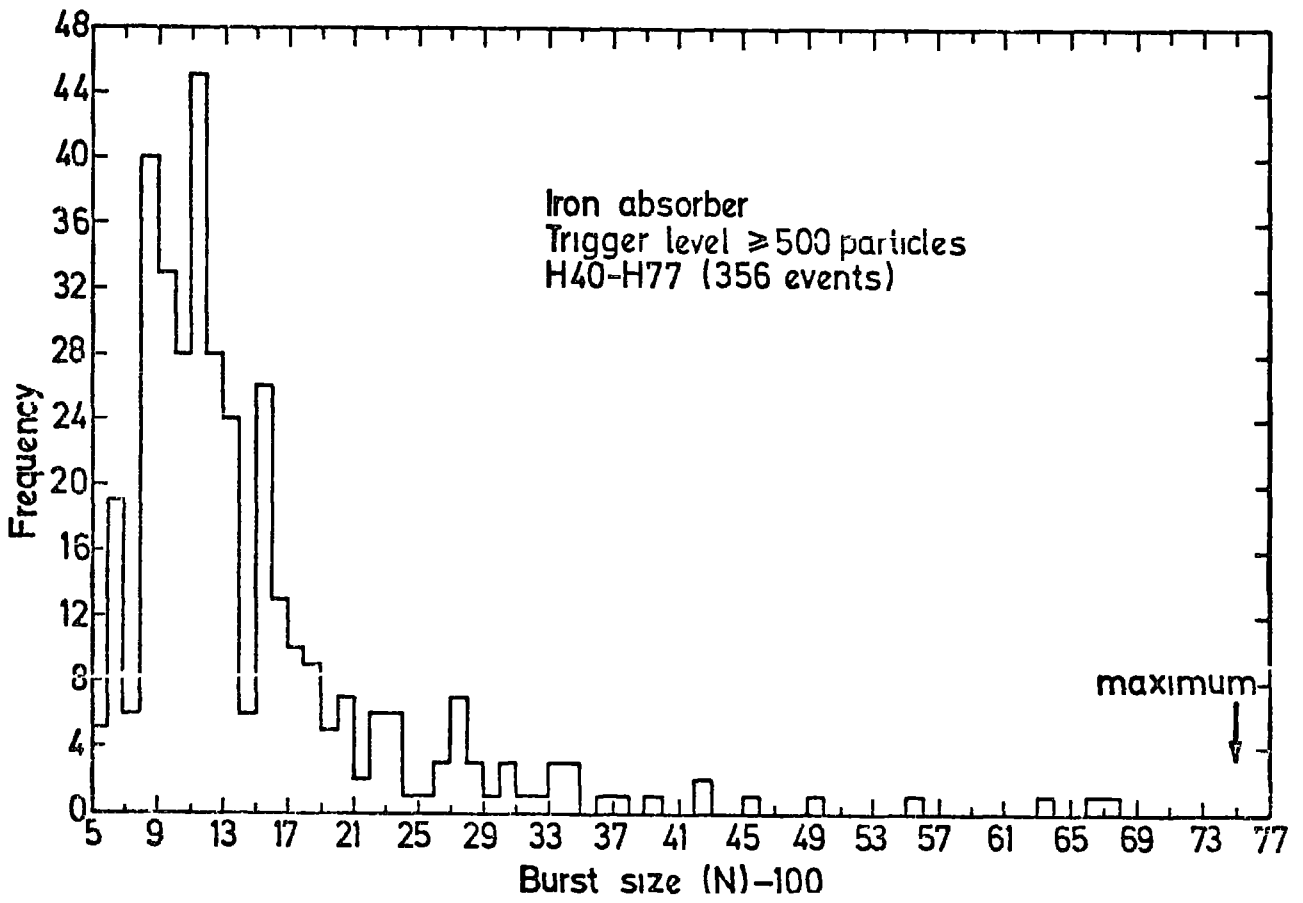


Figure 5.1

The burst size distribution for hadrons interacting in 15 cms of iron absorber. All the measured bursts in the distribution were between $\pm 30^\circ$ to the vertical.

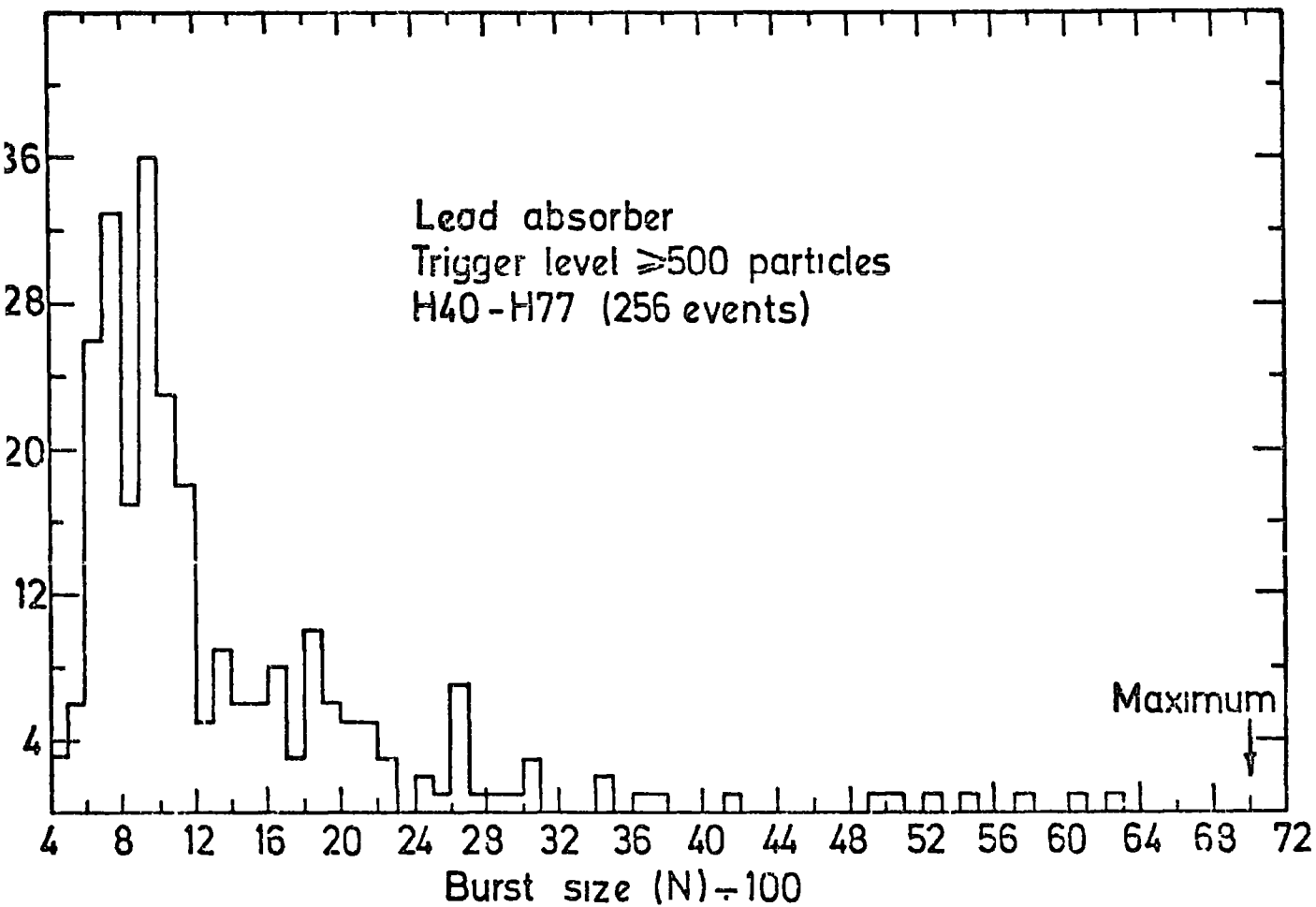


Figure 5.2

The burst size distribution for hadrons interacting in 15 cms of lead absorber. All the measured bursts in the distribution were between $\pm 30^\circ$ to the vertical.

Table 5.2 shows also some information about the experiment using a large trigger level. From this table the maximum number of particles one could measure from the trigger level of ≥ 400 particles was 2,600 and 2,700 particles for bursts in lead and iron respectively, and for the trigger level ≥ 500 particles it was 7,000 and 7,500 particles for bursts in lead and iron respectively. The energy corresponding to these values of the minimum burst size also is shown assuming the primary particles are either protons or pions.

5.3 Photography rate

The various counting rates are shown as integral plots in figure 5.3. It can be seen that the integral photography rate is greater than the rate of recording acceptable events.

A fraction of the events are rejected because they are passing outside the accepted geometry of the chamber. As mentioned before the events were accepted when the whole width fell in the flash tubes and a pulse height could be measured. Thus, if the threshold is set at 20 particles, $1/2.4$ frames would be useful but the ratio decreases to $1/1.8$ frames at 400 particles.

The non useful events for the > 400 particles trigger was not only because of the acceptance geometry, but some of the bursts around 400 - 500 particles were not seen in the flash tubes when the chamber was run on $330 \mu s$. The reason was that these bursts have only a small number of tubes flashed at this long time delay.

5.4 The chamber acceptance functions

In order to calculate the acceptance aperture of the chamber it is first necessary to define some acceptance limit for which the events

Scintillator	Scope sensitivity mV/cm	Trigger level ($\geq N$) particles	Minimum number of particles that can be measured	Maximum number of particles that can be measured	Energy of the primary particle to give the maximum number of particles	Equivalent pulse height at input to emitter follower for single particle	Voltage of photo tube power supply
C		≥ 400	400	2,600	2.0 TeV $\rightarrow \pi^{\pm}$ 2.25 TeV $\rightarrow p$ proton	0.25 mV	0.76 kV
A	200	≥ 400	400	2,700	2.2 TeV $\rightarrow \pi^{\pm}$ 2.9 TeV $\rightarrow p$ proton	0.25 mV	0.76 kV
C		≥ 500	500	7,000	5.4 TeV $\rightarrow \pi^{\pm}$ 6.0 TeV $\rightarrow p$ proton	0.2 mV	0.742 kV
A	500	≥ 500	500	7,500	7.5 TeV $\rightarrow \pi^{\pm}$ 10.0 TeV $\rightarrow p$ proton	0.2 mV	0.742 kV

Table 5.2 General information about the experiment at large trigger levels.

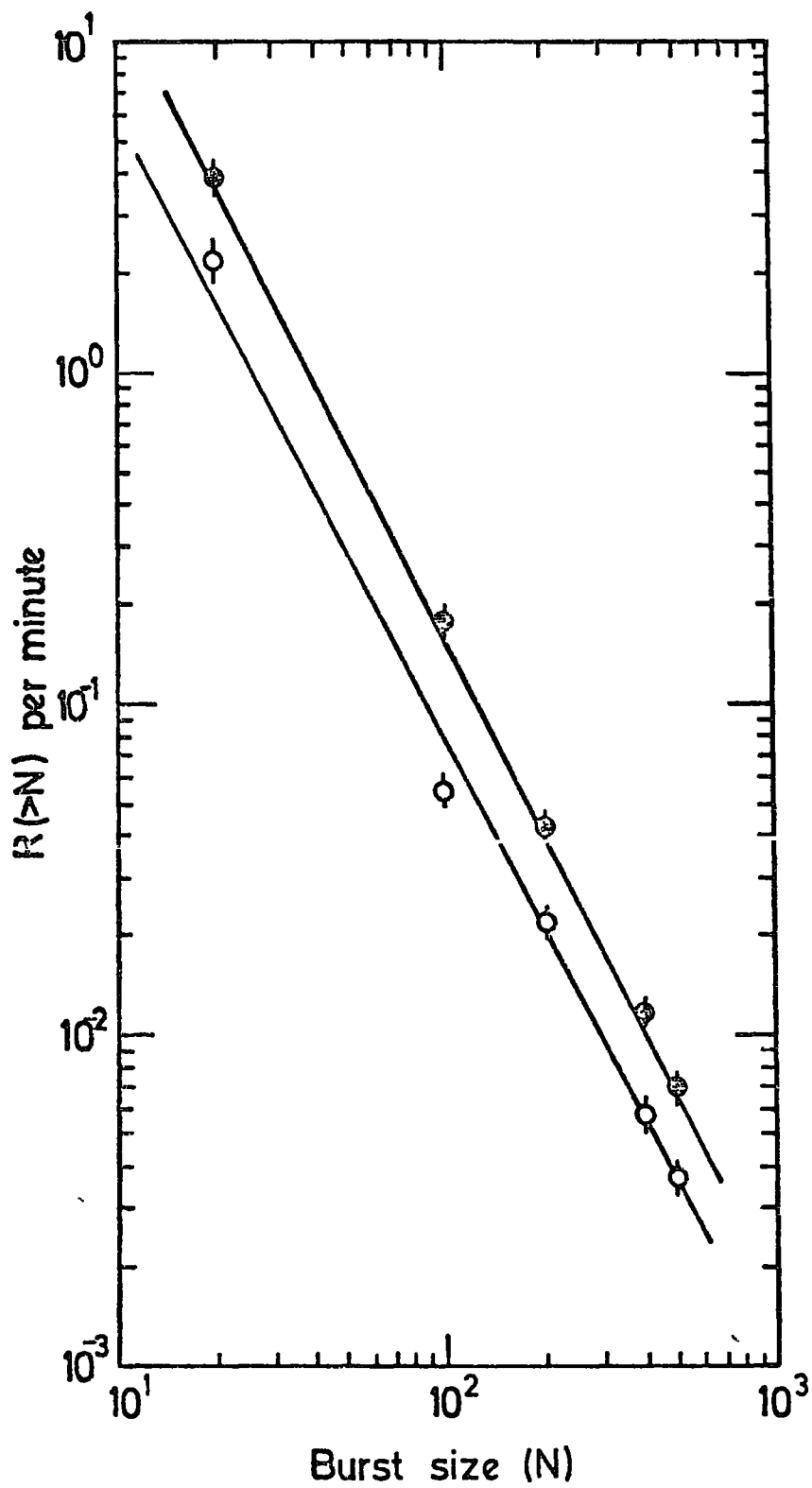


Figure 5.3

Integral counting rate of burst events recorded on the films in lead and iron absorbers.

- Total photography rate.
- Rate of measured burst in iron and lead.

will be selected. The limits have been chosen so that as large an acceptance volume as possible is defined without introducing too large a bias for events that may be lost. With this experimental arrangement two different geometrical acceptances were taken, one for bursts produced in iron and the other for bursts produced in lead.

The method adopted to determine the differential apertures of the chamber was similar to that used by Lovati et al. (1954).

Lovati et al. have introduced a method to convert the projected angular distribution of particles measured in perpendicular planes, into the distribution function of particles given by $\cos^n \varphi$ in real space. The procedure of calculation used by Lovati et al. was as follows: Consider two horizontal rectangular detectors A and B having dimensions $2Y$ cm by $2x$ cm, and $2Y'$ cm by $2V$ cm and placed one above the other at a distance Z cm, figure 5.4. The direction of motion of a particle crossing the detectors is indicated by the angles ϑ and ψ which are related to the zenith angle φ by

$$\cos \varphi = \cos \vartheta \cos \psi$$

Assume that the intensity of the incident particles is represented by the law: $I(\varphi) = I(0) \cos^n \varphi$, where $I(0)$ is the vertical intensity in units of $\text{cm}^{-2} \text{sec}^{-1} \text{st}^{-1}$ and $I(\varphi)$ is the intensity at zenith angle φ . Then the total flux of particles through the two rectangular detectors will be:

$$F_n = \iiint dx dy \cos \varphi I(\varphi) d\omega$$

$$= I(0) \iiint dx dy \cos \varphi \cos^n \varphi d\omega$$

where $d\omega$ is the elementary solid angle and it is represented by:

$$d\omega = \cos \psi d\psi d\vartheta$$

Thus

$$F_n = I(0) \iiint \cos^{n+1} \vartheta \, d\vartheta \cos^{n+2} \psi \, d\psi$$

$$= 2I(0) \int_{\vartheta_1}^{\vartheta_2} \int_{y_1}^{y_2} \int_{x_1}^{x_2} \int_{\psi_1}^{\psi_2} \cos^{n+1} \vartheta \, d\vartheta \, dy \, dx \cos^{n+2} \psi \, d\psi$$

On inverting the order of integration with the limits

$$\vartheta_1 = 0, \quad \vartheta_2 = \tan^{-1} \left(\frac{y+v}{z} \right)$$

$$y_1 = -y, \quad y_2 = y - z \tan \vartheta$$

$$x_1 = -x, \quad x_2 = x$$

and $\psi_1 = \arctan \left(\frac{w+x}{z} \cdot \cos \vartheta \right), \quad \psi_2 = \arctan \left(\frac{w-x}{z} \cos \vartheta \right)$

Define $N_n(\vartheta)$ as the orthogonal projection on the vertical plane yz of the angular distribution function, then

$$F_n = \int N_n(\vartheta) \, d\vartheta$$

Hence $N_n(\vartheta) = 2I(0) \cos^{n+1} \vartheta (y + v - z \tan \vartheta) \int_{-x}^x dx \int_{\psi_1}^{\psi_2} \cos^{n+2} \psi \, d\psi$

With the limitation that:

$$y + v - z \tan \vartheta \geq 0, \quad \text{i.e., } \tan \vartheta \leq (y+v)/z.$$

This equation can be integrated for integer values of the exponent n , and the results of the integration for the different values of n can be represented as follows:

$$N_0(\vartheta) = \frac{1}{2} K \cos \vartheta \left[(x-w) \arctan \left\{ \frac{(w-x) \cos \vartheta}{z} \right\} + (w+x) \arctan \left\{ \frac{(w+x) \cos \vartheta}{z} \right\} \right]$$

$$N_1(\vartheta) = \frac{1}{3} K \cos \vartheta \left[\frac{z^2 - 2(z^2 + (w-x)^2 \cos^2 \vartheta)}{A_-^{1/2}} - \frac{z^2 - 2(z^2 + (w+x)^2 \cos^2 \vartheta)}{A_+^{1/2}} \right]$$

$$N_2(\vartheta) = \frac{1}{8} K z^3 \cos^2 \vartheta (A_-^{-1} - A_+^{-1}) + \frac{3}{4} \cos^2 \vartheta N_0(\vartheta)$$

$$N_3(\vartheta) = \frac{1}{15} K z^4 \cos^3 \vartheta (A_-^{-3/2} - A_+^{-3/2}) + \frac{4}{5} \cos^2 \vartheta N_1(\vartheta)$$

Where $K = 4 I(C) (y+v-z \tan \vartheta)$ and $A_{\pm} = z^2 + (w \pm x)^2 \cos^2 \vartheta$

A general expression for $n > 1$ has been given by Pattison (1965) as follows:

$$N_n(\vartheta) = \frac{K z^{n+1} \cos^n \vartheta}{n \cdot (n+2)} \left(A_-^{-n/2} - A_+^{-n/2} \right) + \frac{n+1}{n+2} \cos^2 \vartheta N_{n-2}(\vartheta)$$

So, by defining the acceptance limits of the experiment, one can calculate the predicted angular distribution in the chamber and by comparison with the observed angular distribution one can find the value of n which gives the minimum Chi-square fit.

(a) Bursts in iron: in running the experiment on 20μ stimedelay, an acceptable burst in the iron was one in which the incoming particle track was observed in the flash tube tray Fla and the burst width seen on the flash tube tray Flb, this layer of flash tube (Flb) was located directly

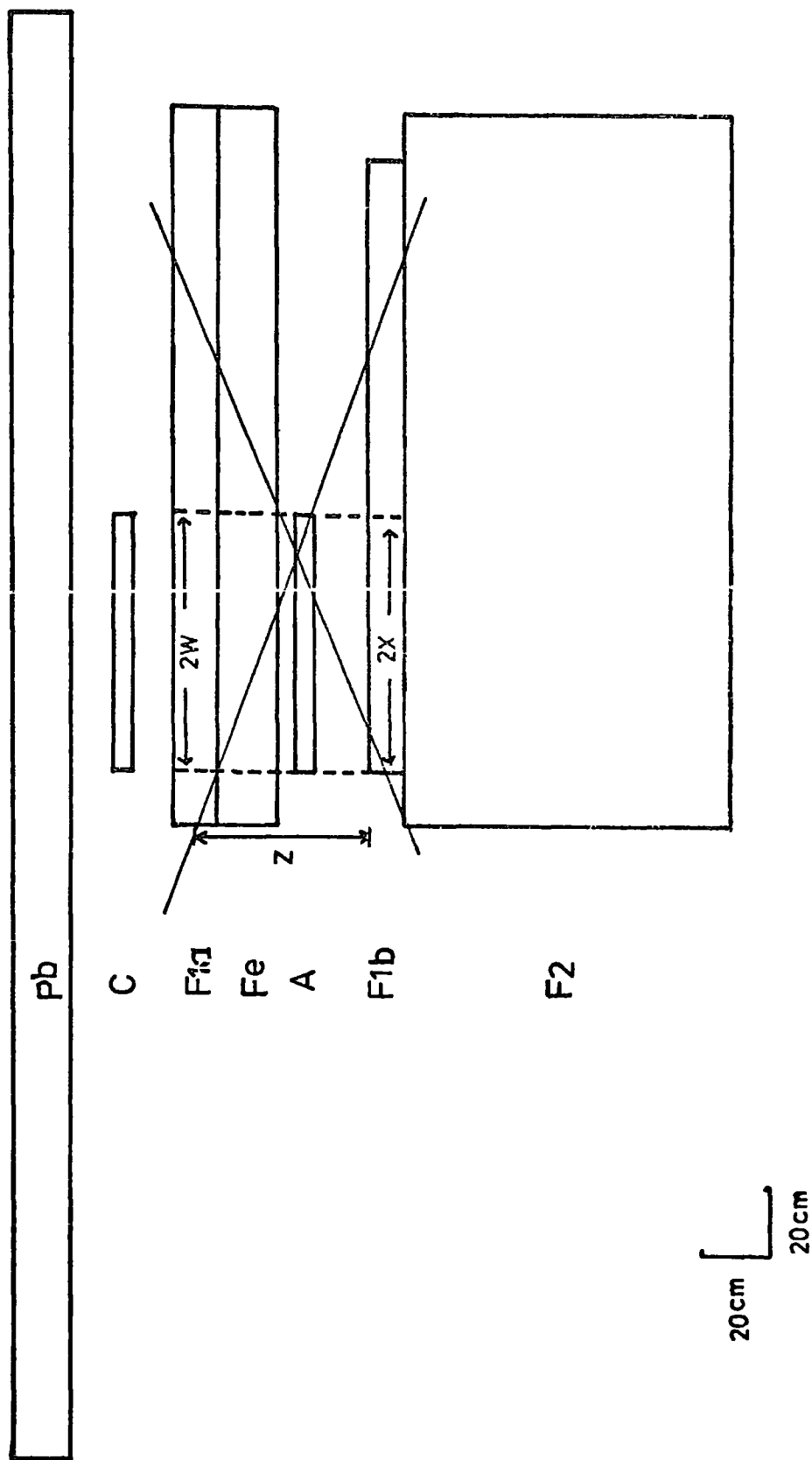


Figure 5.5 Scale diagram of the side of the chamber showing the restricted acceptance geometry for bursts produced in iron and passing through the scintillator A.

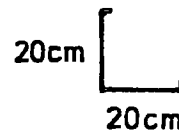
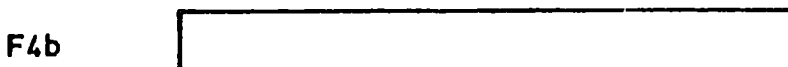
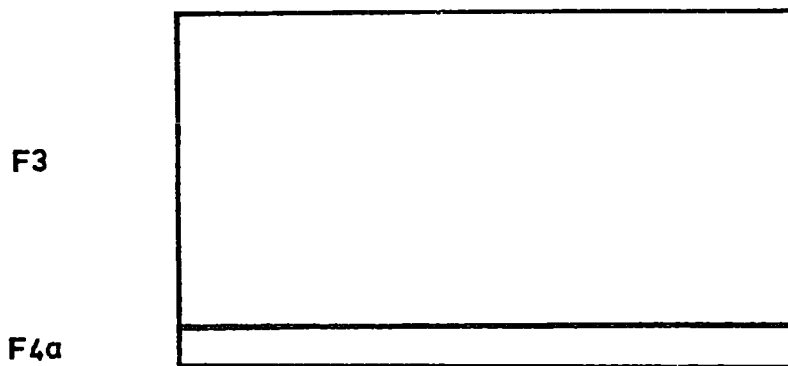
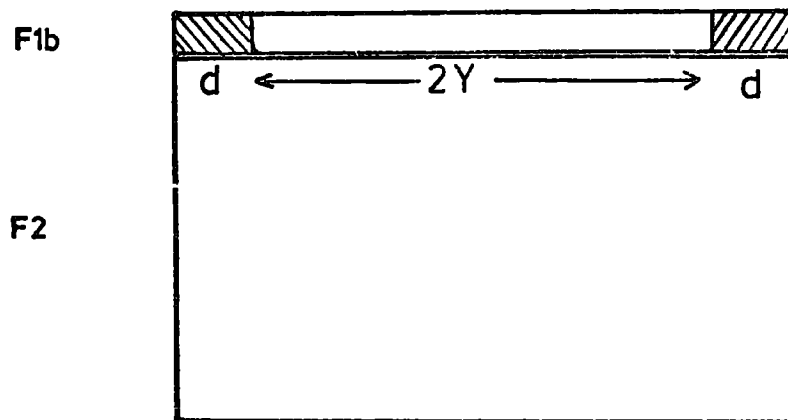
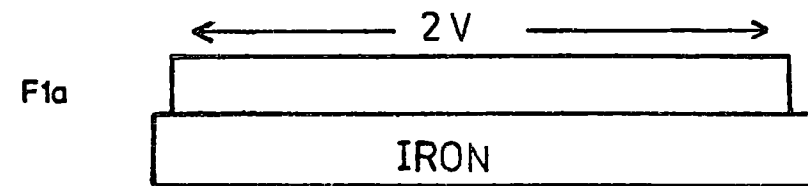


Table 5.6

Scale diagram of the front of the chamber showing the restricted acceptance geometry for bursts produced in iron. To be accepted, the core of the burst must lie between, but not in, the shaded areas.

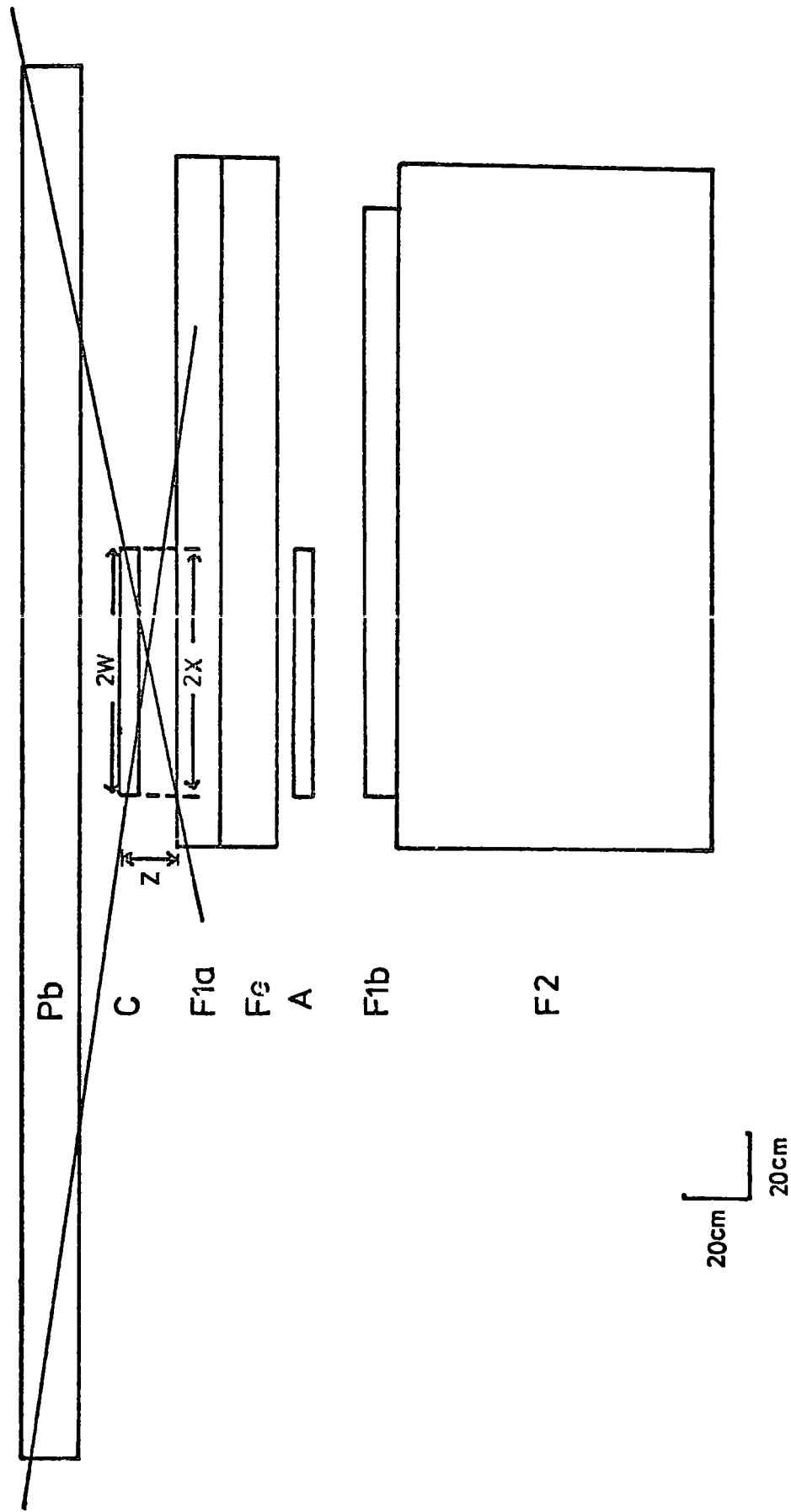


Figure 5.7 Scale diagram of the side of the chamber showing the restricted acceptance geometry for bursts produced in lead and passing through the scintillator C.

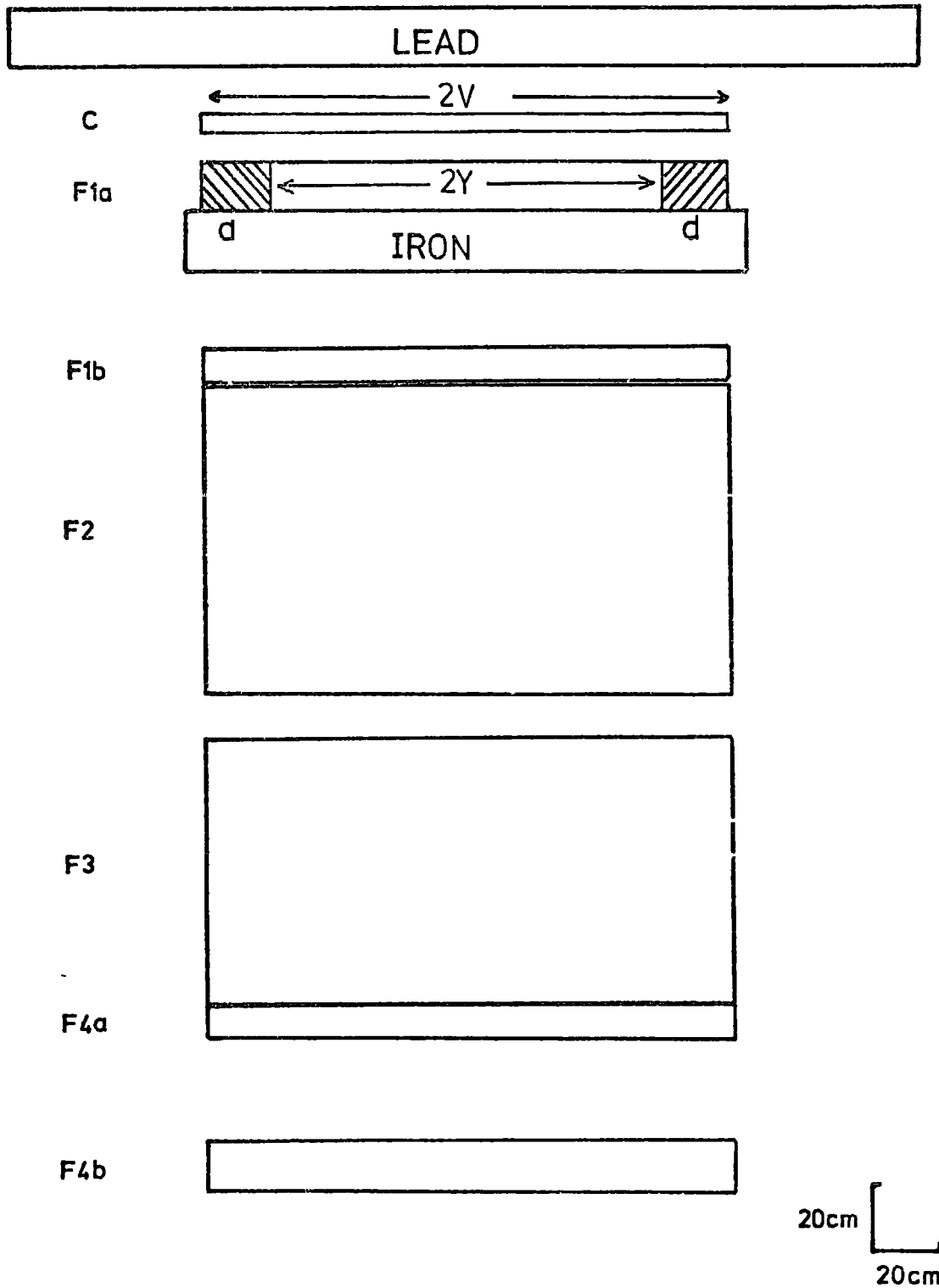


Figure 5.8

Scale diagram of the front of the chamber showing the restricted acceptance geometry for bursts in lead. To be accepted, the core of the burst must lie between, but not in, the shaded areas.

below the iron and this meant that all the bursts had passed through the scintillator A. However, the acceptance geometry which has defined for bursts produced in iron is shown in figures 5.5 and 5.6. In figure 5.5 it was shown that the maximum angle a measured burst could make with the vertical in the back plane was 70° .

During the run on $330\mu\text{s}$ time delay, it was impossible to recognize the track of the incoming particle in Fla, because of the diffusion of the low flash tube efficiency at this long time delay. So, the direction of the core of the cascade through the chamber was taken to define the direction of the incoming particle.

(b) Bursts in lead: figures 5.7 and 5.8 show the acceptance geometry which defined bursts produced in the lead absorber. In both time delays used, the burst width was measured in the flash tube tray Fla below the lead and this meant that the burst had passed also through the scintillator C. In figure 5.7 it was shown that the maximum angle a measured burst could make with the vertical in the back plane was 81° .

Using the above geometrical dimensions given in figures 5.5, 5.6, 5.7 and 5.8 one can calculate the differential aperture ($\text{m}^2 \text{ st rad}^{-1}$) for bursts observed in the flash tube chamber using the method discussed above. The results of the calculation are shown in figures 5.9, 5.10, 5.11 and 5.12 for the bursts produced in iron and lead respectively.

5.5 Angular distribution

The angular distribution for bursts of width ≤ 2.0 cms on the scanning sheets (scale 1:20) and requiring that the core of each burst fell within the limits defined over the flash tube layers Fla and Flb have been measured. This limit was taken to be 1 cm (on the scanning sheet) from each side of the flash tubes layer (see figures 5.6 and 5.8), this was for

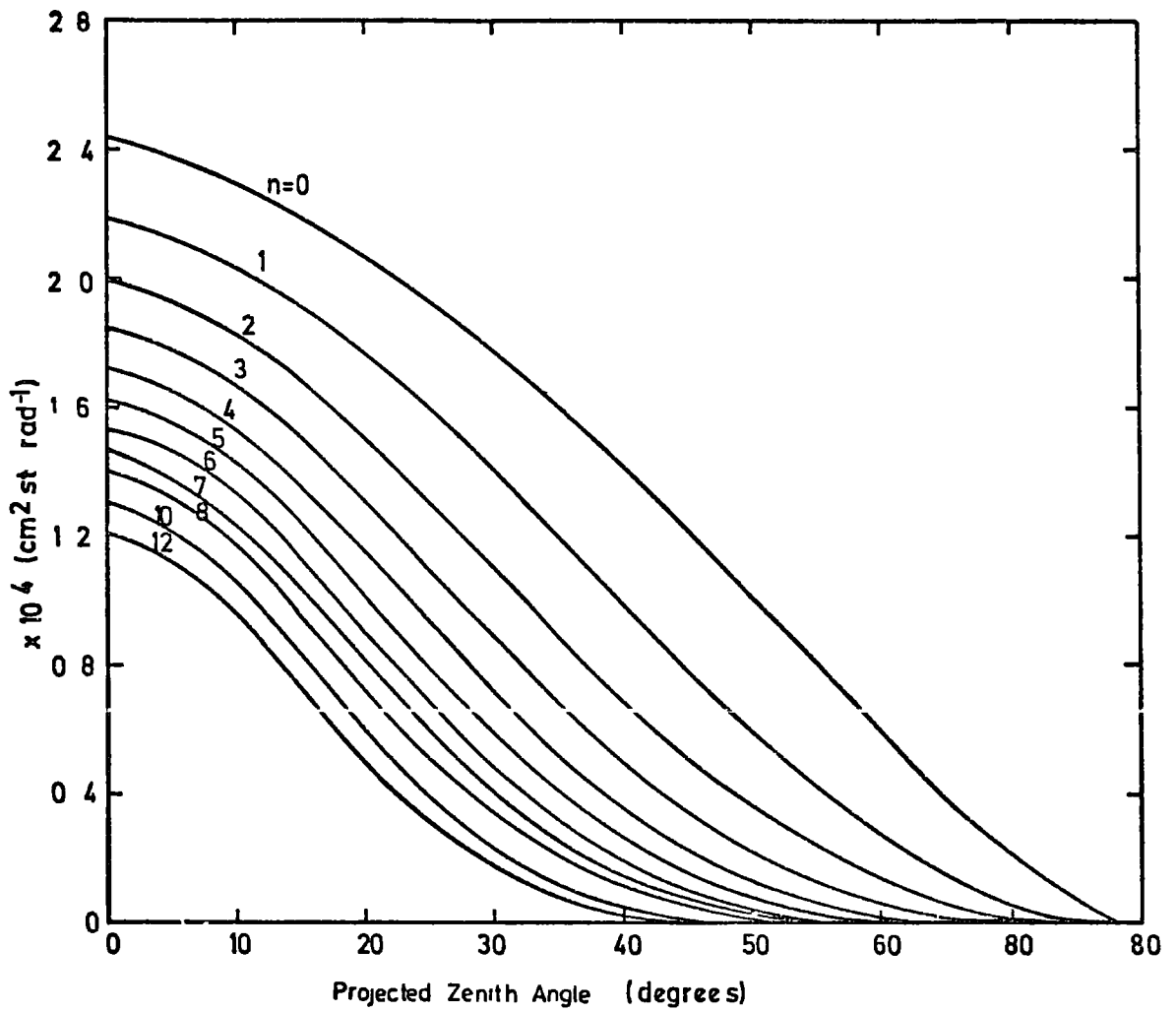


Figure 5.9

The chamber acceptance functions with n as parameter. For bursts produced in iron and observed on $20 \mu\text{s}$ time delay run.

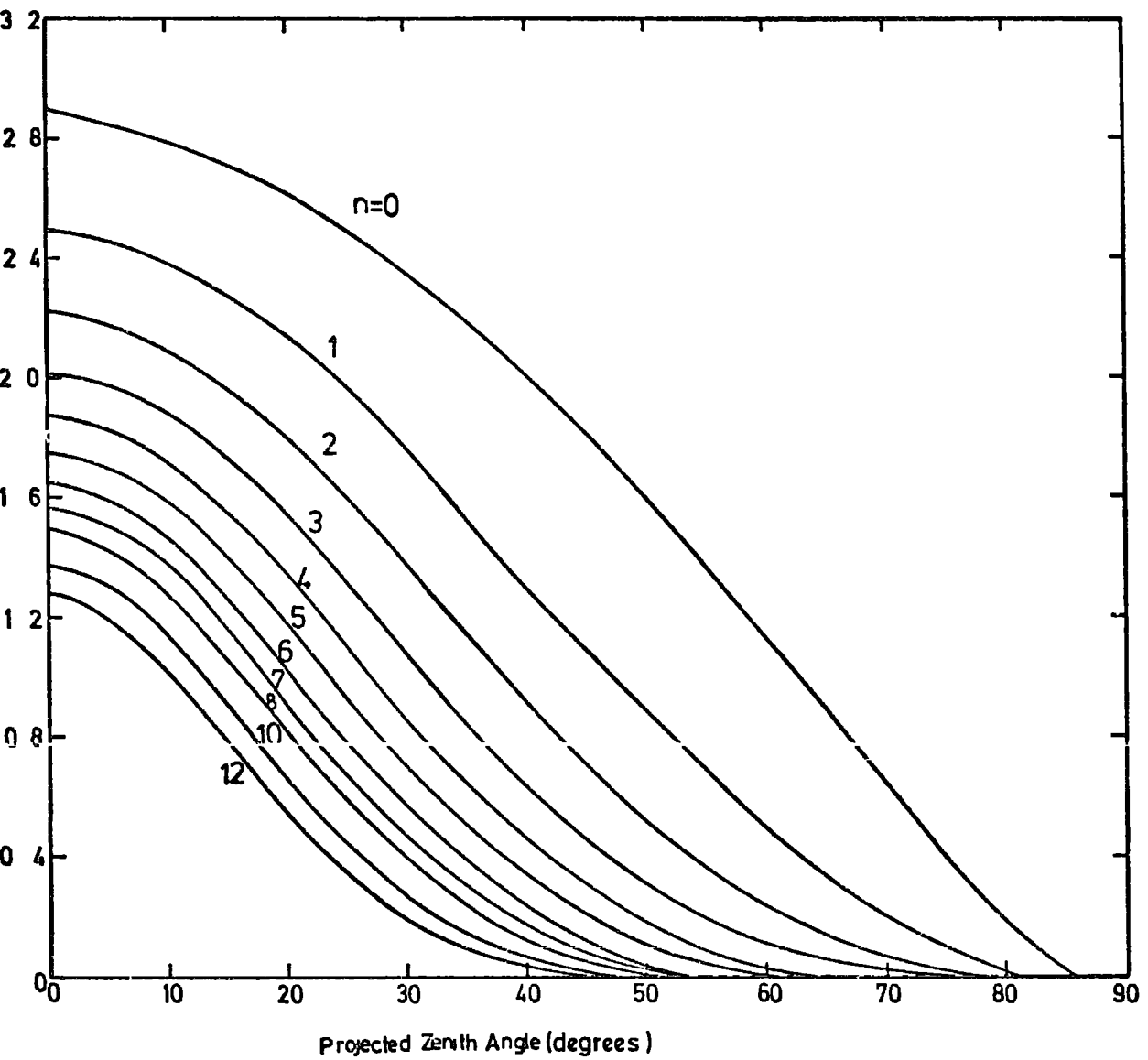


Figure 5.10

The chamber acceptance functions with n as parameter. For bursts produced in lead and observed on $20\mu\text{s}$ time delay run.

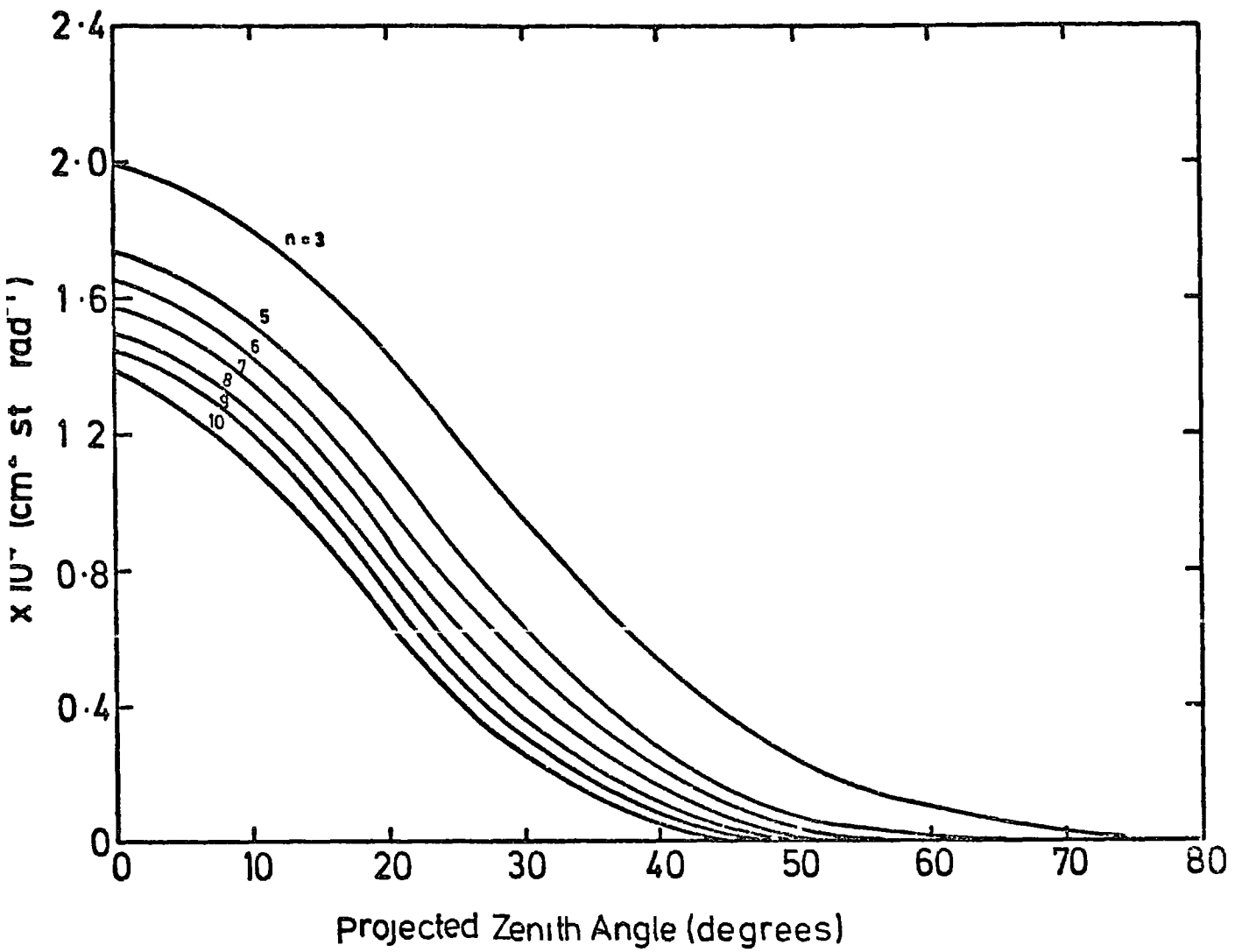


Figure 5.11

The chamber acceptance functions with n as parameter. For bursts produced in iron and observed on $330 \mu\text{s}$ time delay run.

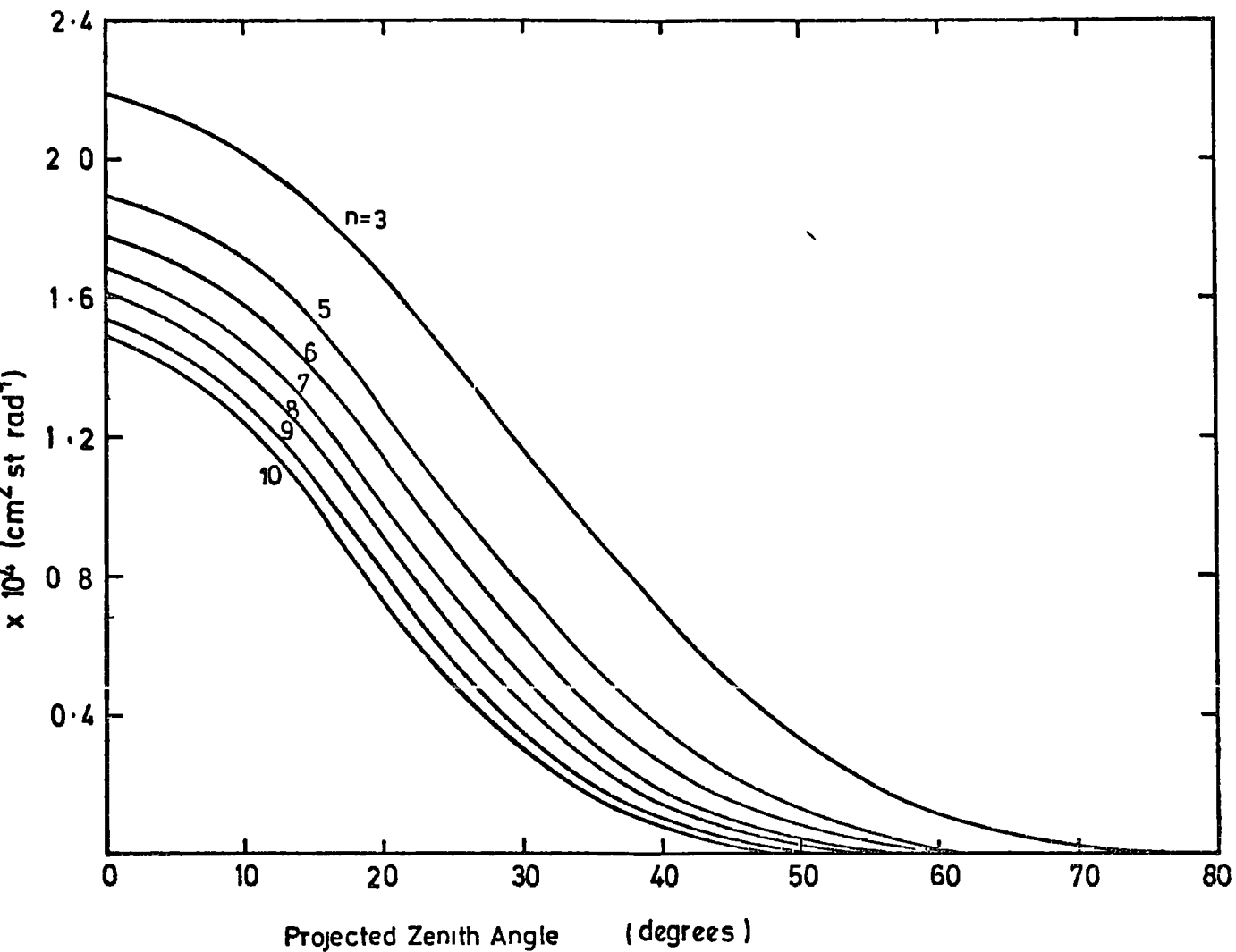


Figure 5.12

The chamber acceptance functions with n as parameter. For bursts produced in lead and observed on $330 \mu\text{s}$ time delay run.

the case of observing bursts when the chamber was running on $20\mu\text{s}$ time delay between the passage of the burst and the application of the high voltage pulse. In the case of the long time delay ($330\mu\text{s}$) the angular distribution was measured according to the direction of the core of the cascade through the chamber. For an event to be accepted the core was required to pass at least a distance of $1/2$ cm (measured on the scanning sheets) from the acceptance limits taken in Fla and Flb respectively. Figure 5.13 shows the measured projected angular distribution for particles which produced bursts in iron and lead. A comparison between the measured projected angular distributions and the predicted angular distributions have been made and the best fit determined by minimum Chi-square (χ^2) giving the value of the exponent, n . The corresponding values of the exponent are shown below:

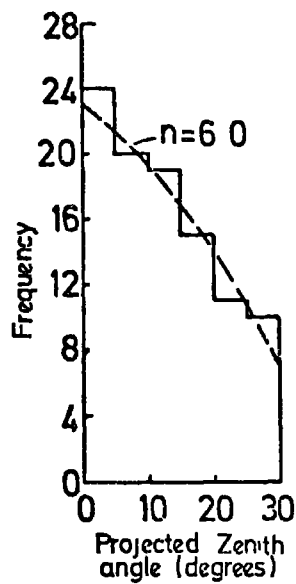
Angular distribution measured from data taken on:	Iron (Fe)	Lead (pb)
	Value of n in $I(\vartheta) = I(0) \cos^n \vartheta$	
20 μs time delay and small trigger threshold (between ≥ 20 to ≥ 400 particle)	4.0 ± 2.0	6.0 ± 2.5
330 μs time delay and large trigger threshold (≥ 400 particles)	7.5 ± 1.5	8.5 ± 1.5

Having the values of the exponent n estimated the aperture value m^2 st could be easily found.

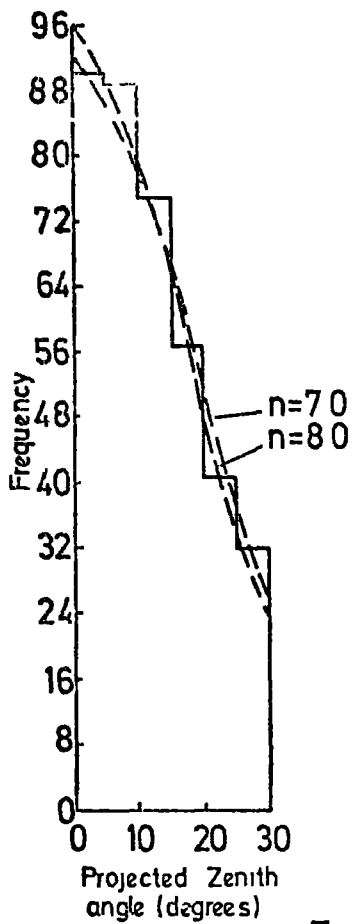
General curves were calculated to show how the aperture value could vary with the width of the flash tube chamber (over Fla or Flb) for differ-



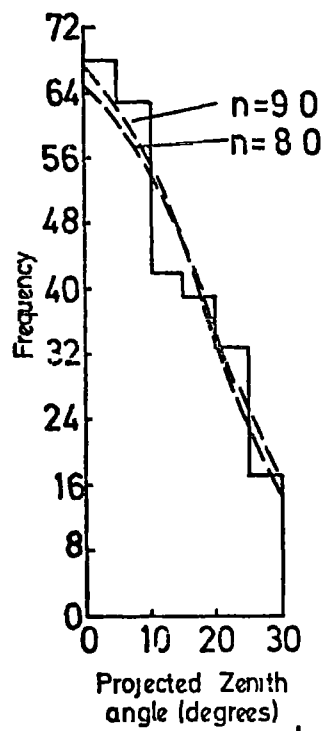
a Fe



b Pb



c Fe



d. Pb

Figure 5.13

The projected zenith angle distributions of bursts observed in iron and lead. The solid distributions are the measured and the dotted are the predicted. The values of the exponent n , given by the predicted curves show the best values of n obtained using the minimum - χ^2 method. (a and b) distributions measured from $20\mu\text{s}$ time delay run. (c and d) distributions measured from $330\mu\text{s}$ time delay run.

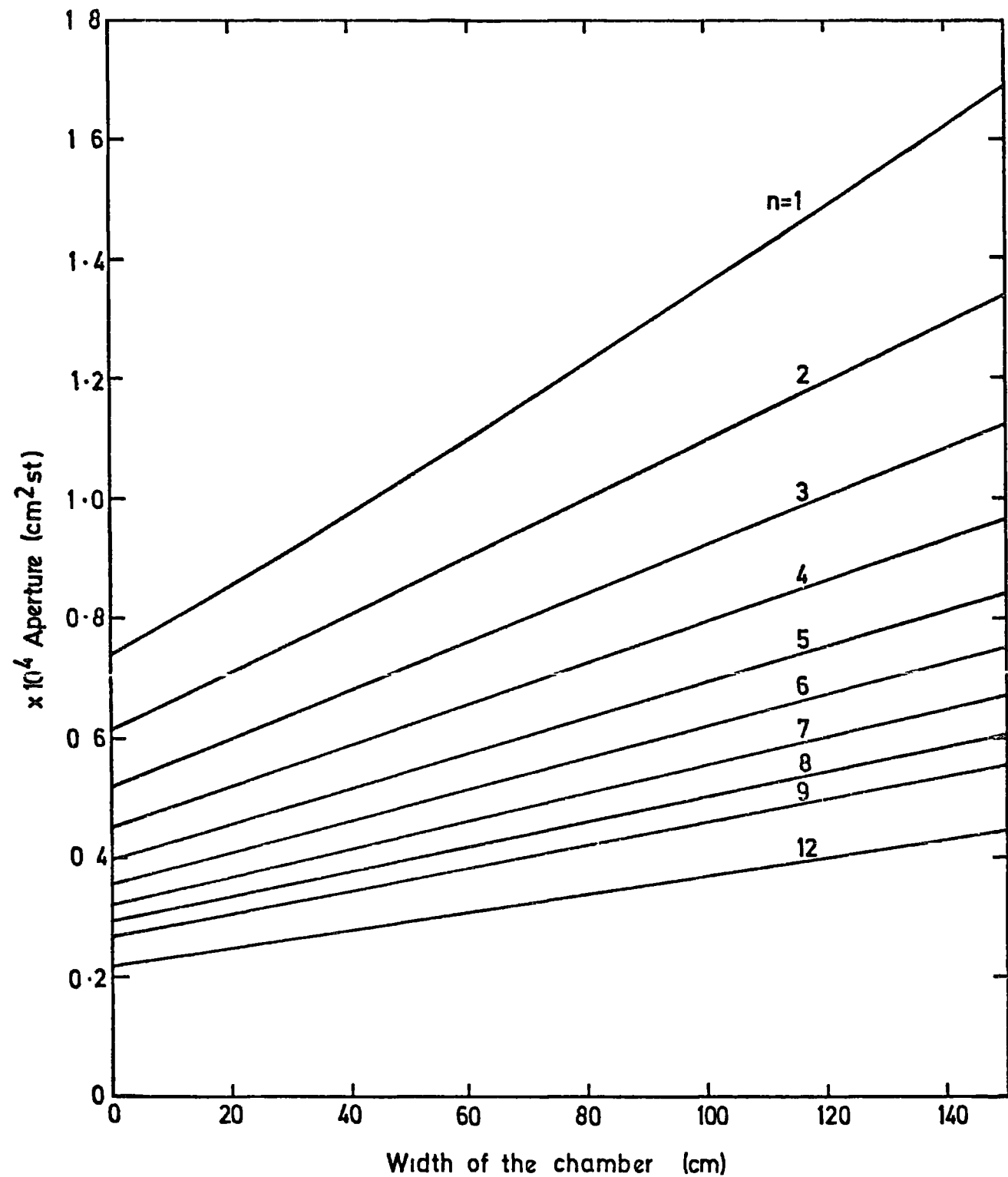


Figure 5.14

The aperture of the chamber for bursts produced in iron, as a function of the width of the chamber over the flash tube layer Flb. Numbers by the curves represent different values of n , the exponent in the assumed expression for the angular variation of intensity.

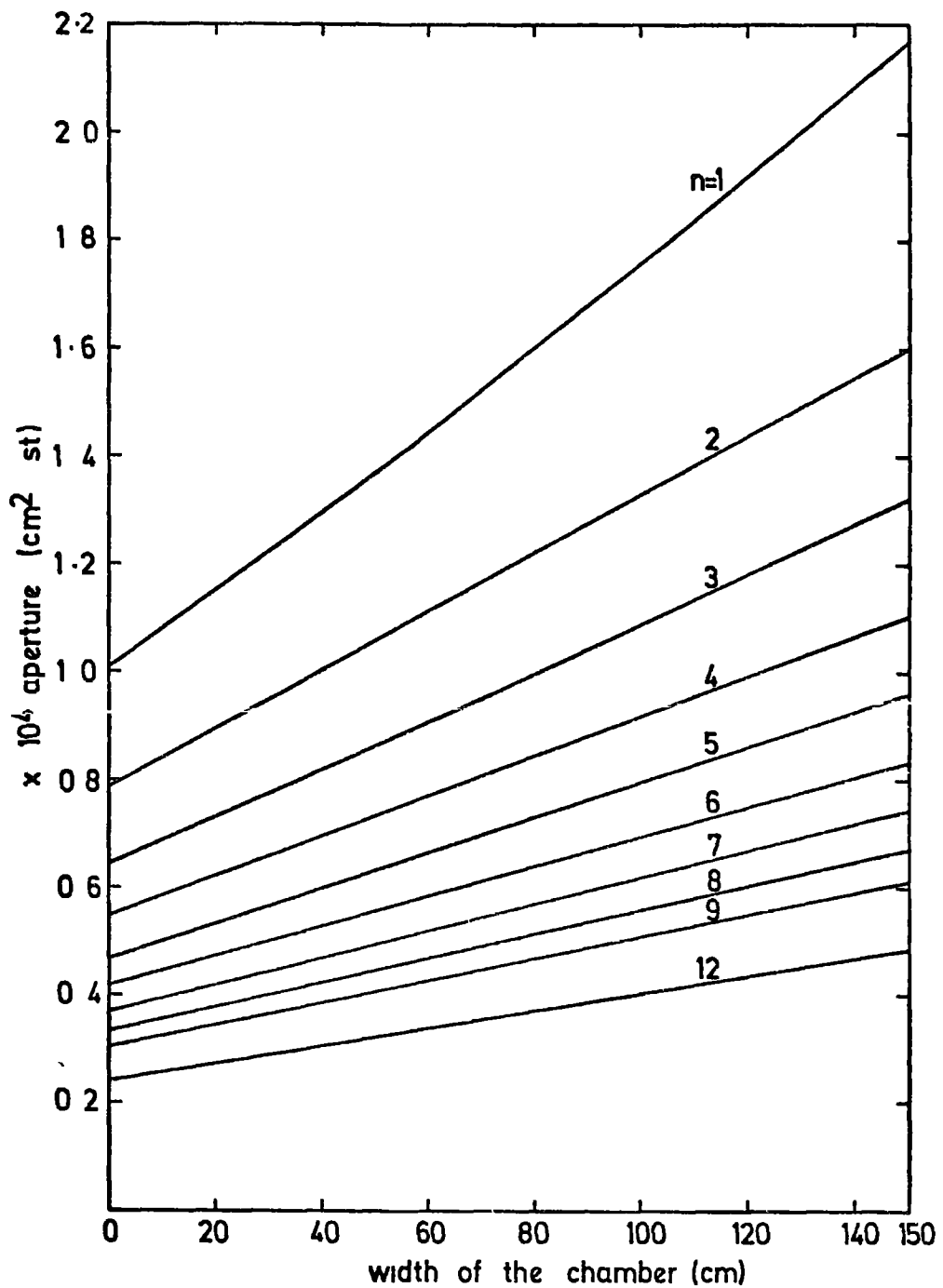


Figure 5.15

The aperture of the chamber for bursts produced in the lead, as a function of the width of the chamber over the flash tube layer Fla. Numbers by the curves represent different values of n , the exponent in the assumed expression for the angular variation of intensity.

ent values of n , figures 5.14 and 5.15. So, for any value of n given above, and for the fixed chamber width used over the flash tube layers Fla or Flb, one can get the exact value of the aperture in cm^2 st.

5.6 The attenuation length

The value of the exponent n could be related to the attenuation length λ of particles initiating the bursts. The attenuation length could be represented by $\lambda = 1,030/n$.

For bursts ≥ 400 particles the average value of n for the lead and iron targets was 8.0 ± 1.5 . So, for this value of n the attenuation length λ is $129 \pm 16 \text{ gm cm}^{-2}$. This value of λ indicates that the observed bursts of size ≥ 400 particles are produced predominantly by hadrons.

For bursts between ≥ 20 to ≥ 400 particles the average value of n for the lead and iron targets was found to be 5.0 ± 2.0 . The corresponding value of n shows that both distributions contain some contamination from muon induced bursts, and as the muon spectrum decreases relatively slowly with increasing θ , a small contribution from muons will effect the exponent considerably.

5.7 Estimate of the hadron energy spectrum

5.7.1 The measured spectrum

In the total running time of 4817.4 hours hadron induced bursts in the flash tube chamber absorbers were observed and measured. All these hadrons have been classed as protons, pions or neutrons. The integral spectrum of all hadrons in $\pm 30^\circ$ to the vertical inducing bursts in the iron and lead target are shown in figures 5.16 and 5.17 respectively. The conversion of burst size to energy has been discussed in chapter 3, and the curves calculated for proton initiated bursts in the iron and lead target (see figures 3.6 and 3.7) were used to evaluate the differential

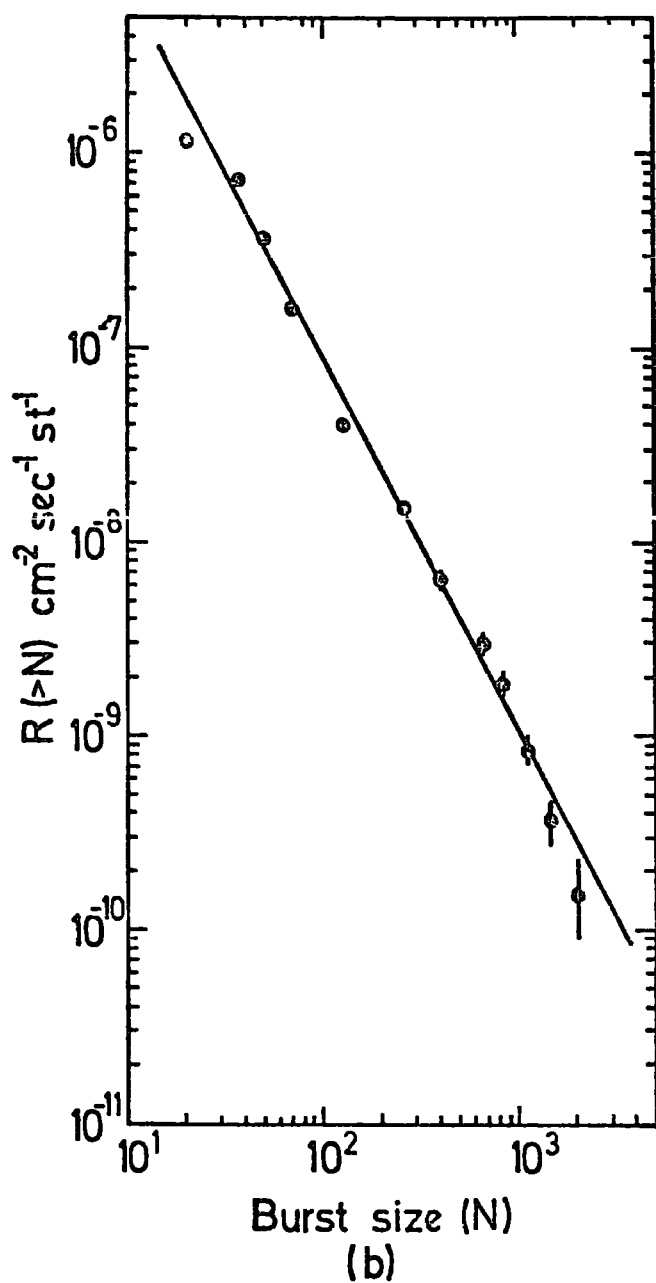
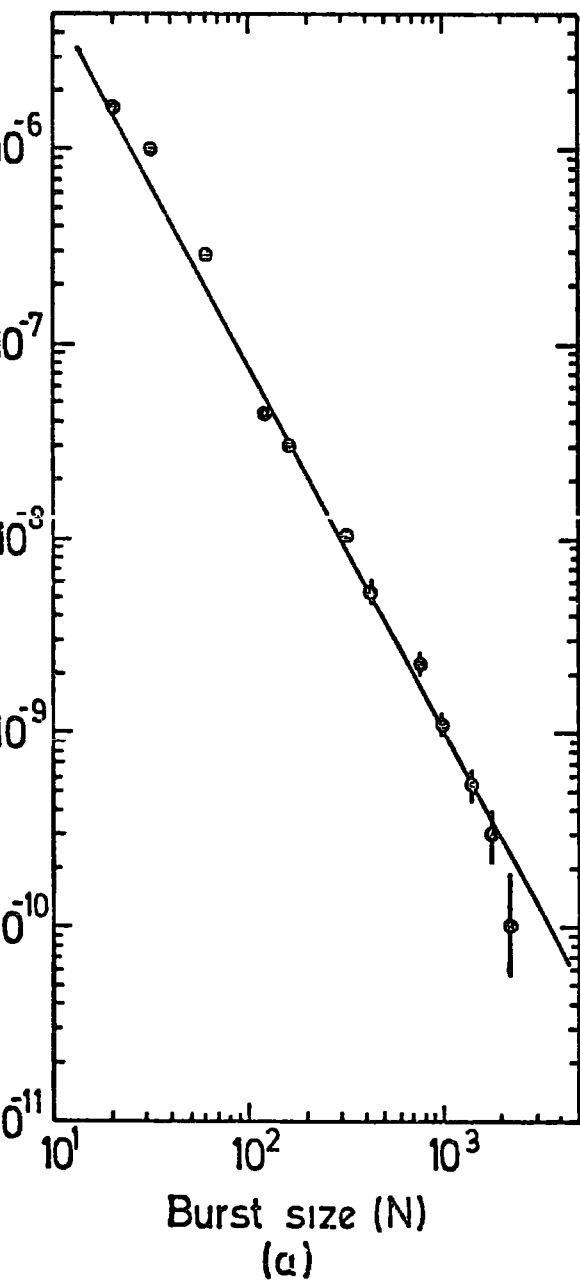


Figure 5.16

The integral burst spectrum for all hadrons measured in the iron (a) and the lead (b). Data taken from the experiment on $20\ \mu\text{s}$ time delay.

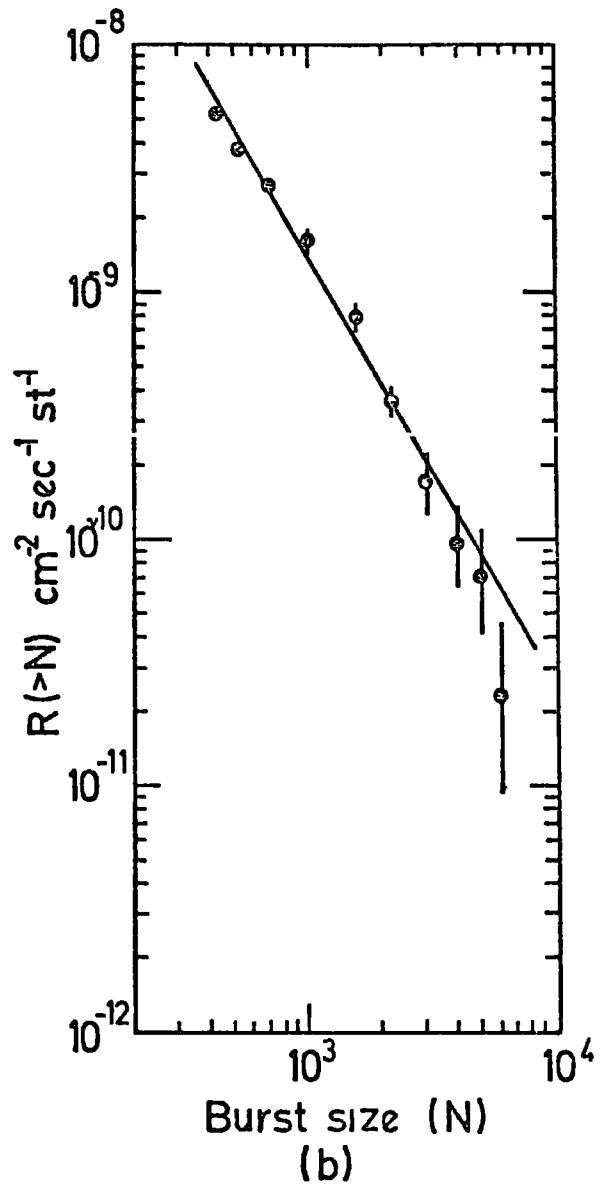
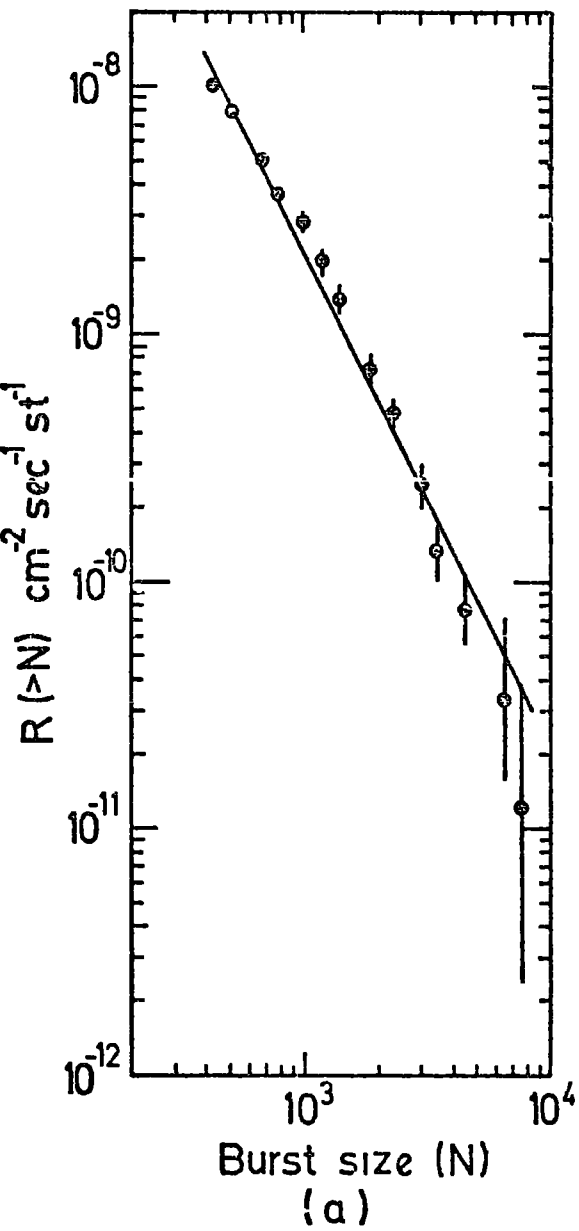


Figure 5.17

The integral burst spectrum for all hadrons measured in the iron (a) and the lead (b). Data taken from the experiment on $330\mu\text{s}$ time delay.

energy spectrum of hadrons at sea level. Table 5.3 shows the probability of incident protons and pions interacting in different parts of the chamber used in the calculation.

A calculation of the muon burst spectrum in the chamber has shown that the contribution of muons to the measured burst spectrum is small (this will be discussed in the next chapter). At a burst size of 1,000 particles in iron or lead the contribution of muons to the measured all hadron spectrum is 1% and 9% respectively, and at 500 particles the contribution of muons to the measured all hadron spectrum is 2% and 16% respectively. So, it was possible to neglect this contribution. Figures 5.18 and 5.19 show the vertical differential energy spectrum of hadrons at sea level measured from bursts observed in iron and lead respectively. Only one event was observed in which the width of the burst was falling within the geometry and the pulse height from the scintillator was showing a burst size in iron target $> 7,500$ particles, i.e. $> 10^4$ GeV energy (see table 5.2). So, the mean energy above 10^4 GeV was calculated and it was found $\bar{E} = 29.2$ TeV and the absolute rate also was calculated.

However, the final vertical hadron spectrum at sea level has been found by averaging the two spectra from the iron and lead target (the individual spectra were compatible) and the resulting energy spectrum is shown in figure 5.20.

5.7.2 Comparison with other results and discussion

A comparison could be made between the results of the present experiment and results obtained from other experiments, in particular the result of Baruch et al. (1973), who have suggested that there may be a step in the spectrum at an energy of a few TeV. Figure 5.21 shows the results of these experiments as well as the result of this experiment.

<u>Particle</u>	<u>Lead</u>	<u>Iron</u>	<u>Glass and aluminium electrodes in (F2+F3)(figure 4.9)</u>
Proton	0.55	0.25	0.12
Pion	0.53	0.23	0.12

Table 5.3

The probability of incident protons and pions interacting in different parts of the chamber.

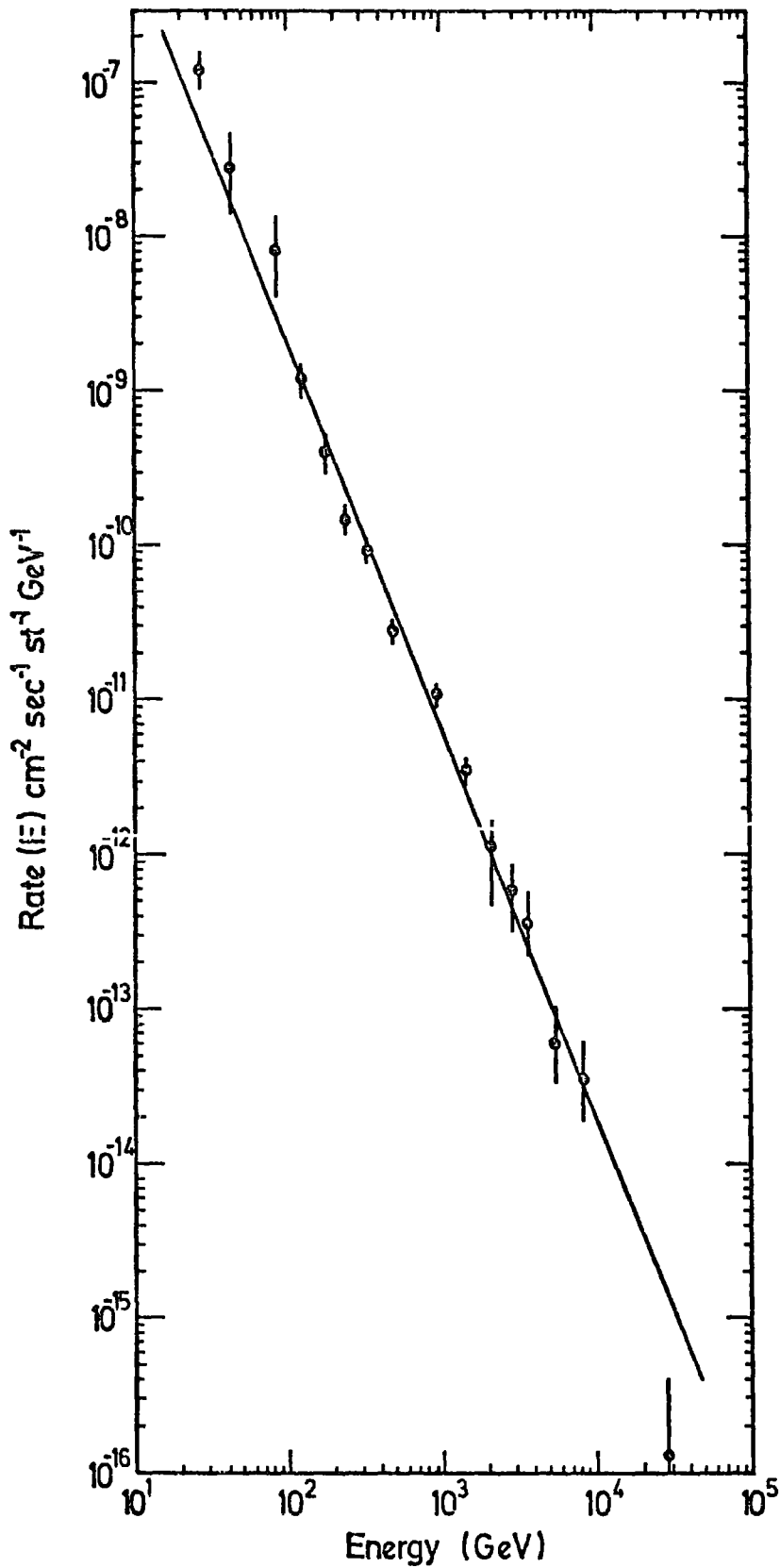


Figure 5.18

The vertical differential energy spectrum of hadrons at sea level (calculated from bursts measured in iron and assuming 100% nucleon contribution). $\gamma = 2.52 \pm 0.1$.

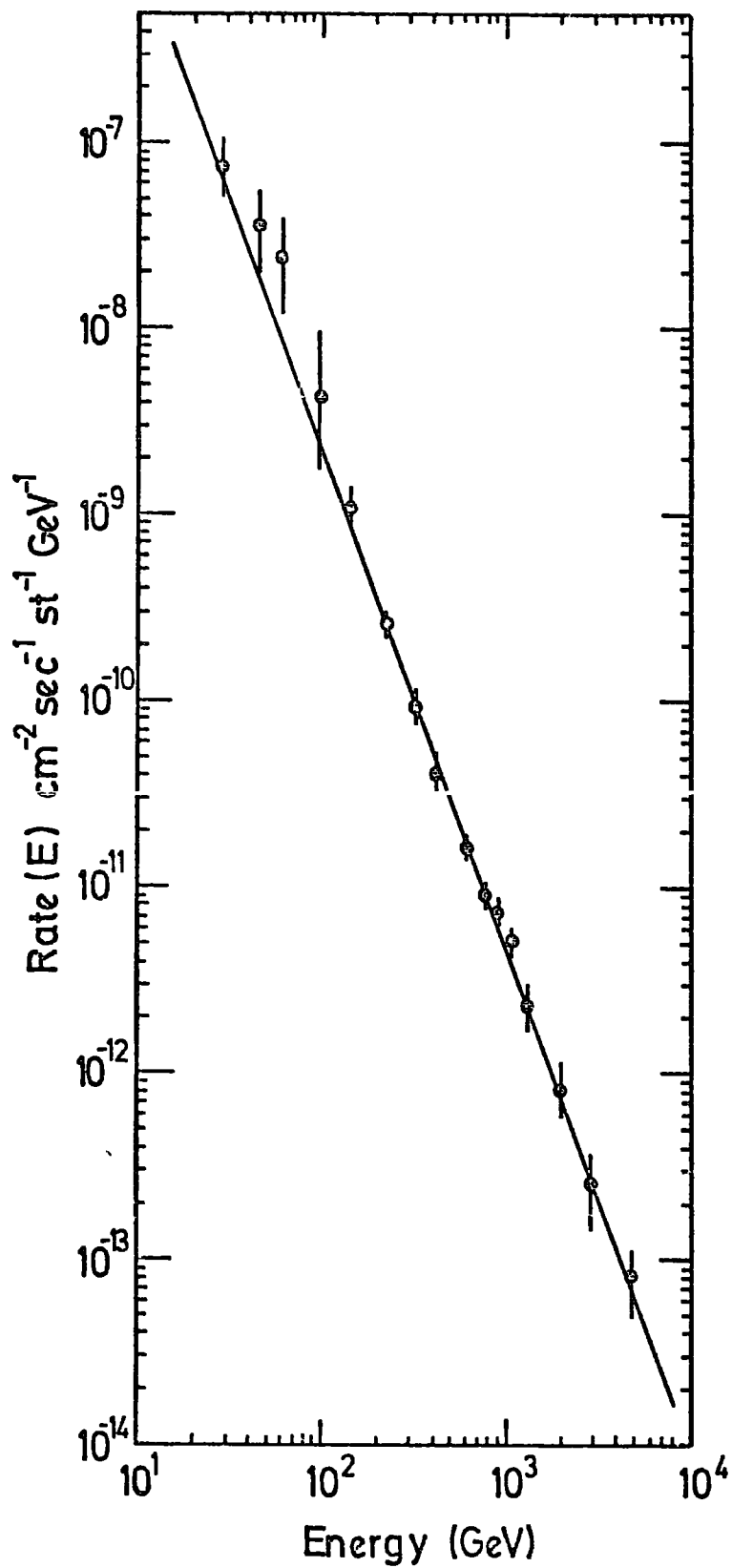


Figure 5.19

The vertical differential energy spectrum of hadrons at sea level (calculated from bursts measured in lead and assuming 100% nucleon contribution). $\gamma = 2.7 \pm 0.1$.

It is seen that the present result shows no evidence for a step in the energy range 2 - 8 TeV and they are in fact consistent with a spectrum of the form $E^{-2.7 \pm 0.1}$ over the whole energy range from 10 GeV to 10 TeV.

Recently the result given by Siohan et al. (1975) shows the upper limit of the hadron flux at sea level. The spectrum is of the form:

$$N(> E) = 3 \times 10^{-4} \left(\frac{E \text{ GeV}}{300} \right)^{-2.0} \text{ particle/m}^2 \text{ sec st.}$$

with E in the range $400 < E < 7,000$ GeV. The same result also was reported earlier by G. Yodh in August 1974. (See section 2.3.10) as private communication.

The Siohan et al. result also does not support the observation by Baruch et al. of the step. Their result is consistent with the present result.

The spread in the absolute fluxes of hadrons measured at sea level by the various groups can be attributed to the various techniques used. In the figure 5.21 it was shown that the present results are consistent with low energy data (≤ 100 GeV) which represented the total nucleon spectrum found by multiplying the measured proton intensities of Brooke and Wolfendale (1964) and Diggory et al. (1974) by factor of 2, (i.e. assuming equal numbers of protons and neutrons at sea level). Also in the same figure is shown the total nucleon spectrum found by increasing the measured neutron intensities summarised by Ashton et al. (1970) (see figure 2.4) by a factor of 2.

Finally, apart from the result of Baruch et al. all the experiments show that the hadron spectrum is smoothly decreasing in intensity with differential slope γ between 2.7 to 3.0 in the range $10 \text{ GeV} < E < 10 \text{ TeV}$.

5.8 Fluctuations

It has been suggested that there could be a small irregularity in the

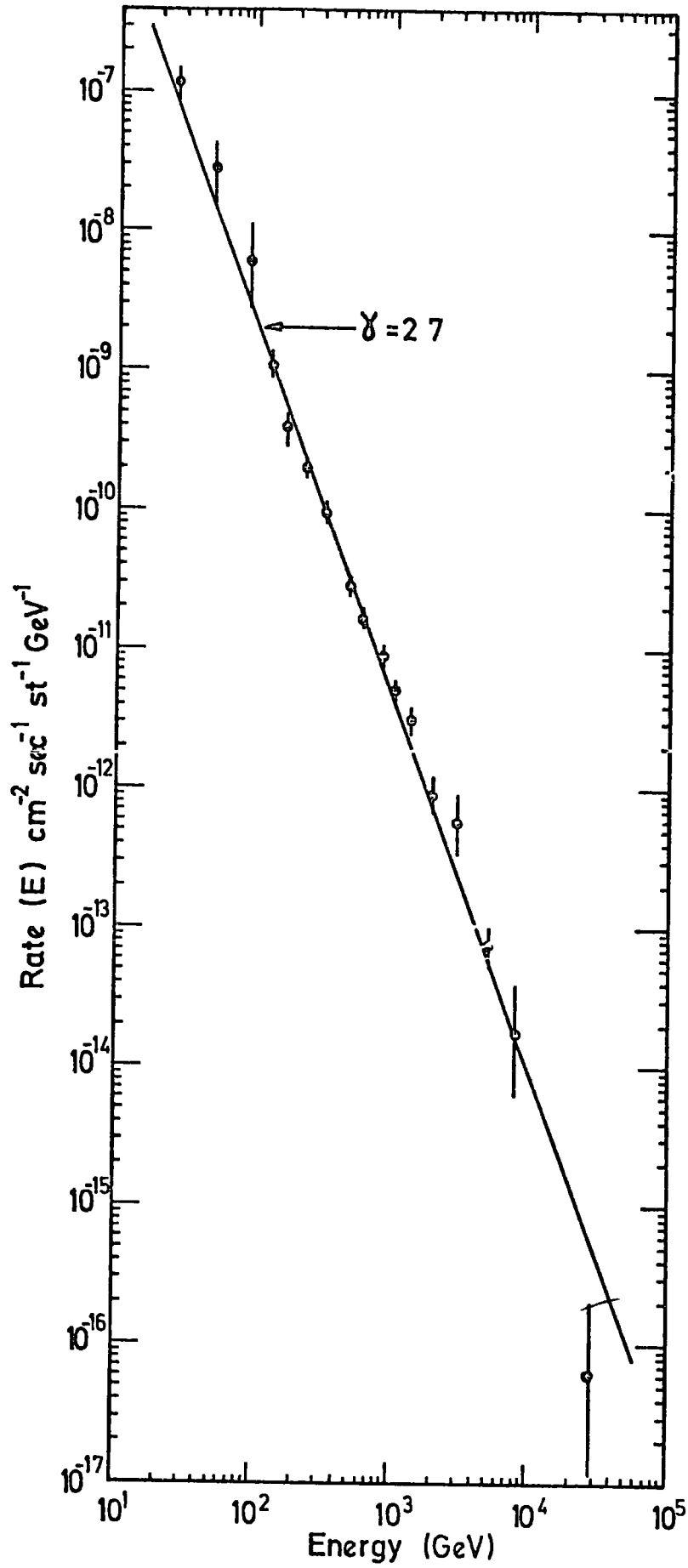


Figure 5.20

The final vertical differential energy spectrum of hadrons in cosmic rays at sea level measured by this experiment.

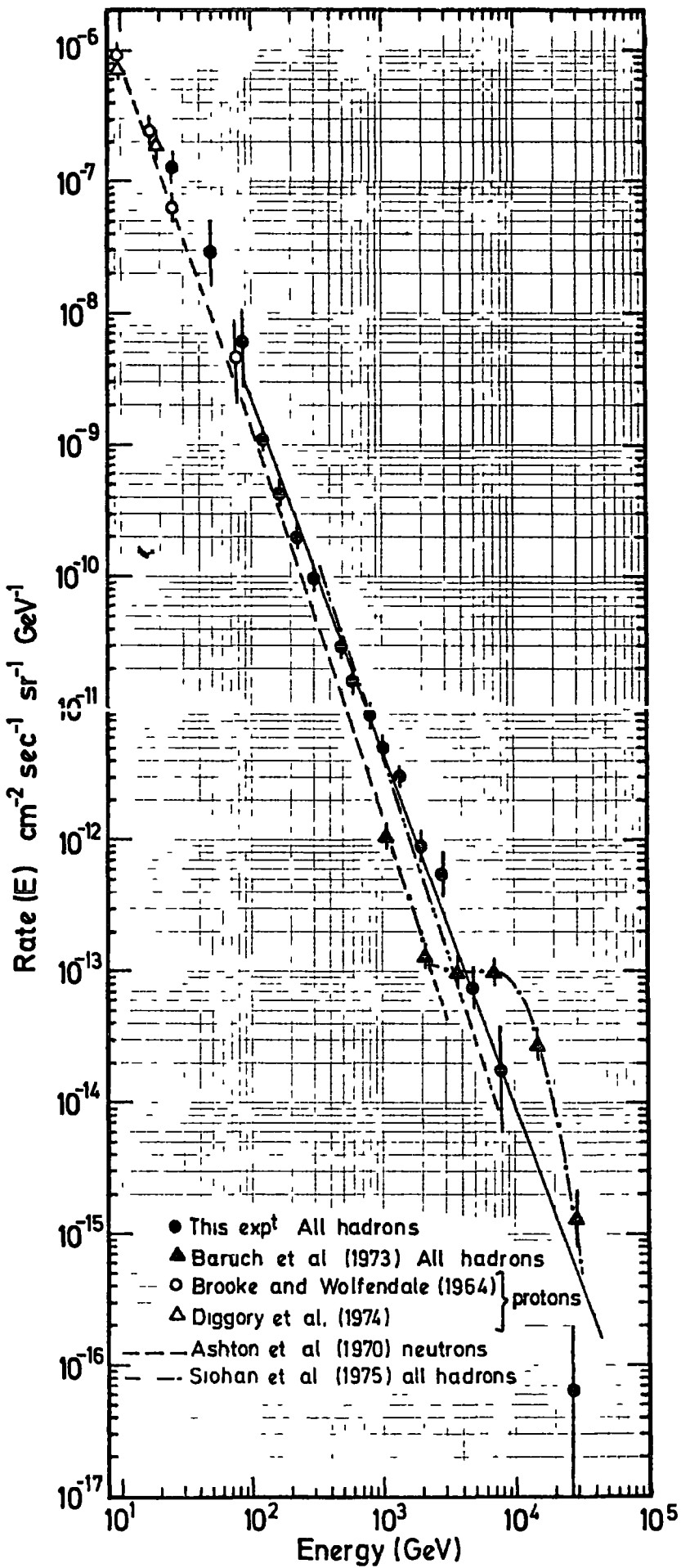
Figure 5.21

The vertical differential energy spectra of hadrons (and of nucleons alone) in cosmic rays at sea level measured by different groups. The low energy data (≤ 100 GeV) are estimates of the total nucleon spectrum found by multiplying the measured proton intensities of Brooke and Wolfendale (1964) and Diggory et al. (1974) by a factor of 2. (i.e. assuming equal number of protons and neutrons). The dashed line is an estimate of the total nucleon spectrum found by increasing the measured neutron intensities summarised by Ashton et al. (1979) by a factor of 2.

A solid line is the best fit to the present measurement of the energy spectrum of all hadrons (nucleons and pions).

The dotted line is the best line given by Baruch et al. (1973) through their measurements for all hadrons.

The double dotted line shows the recent result given by Sicaen et al. (1975) for all hadrons.



spectrum which can not be seen in this experiment, because of the smoothing introduced by the fluctuations in the burst size.

However, if the irregularity were big enough to produce the result seen by Baruch et al. with what is a very similar detection technique then it is believed that a large irregularity would have been seen in this result too.

A calculation has been made to overcome this problem and to prove that if there is any irregularity in the spectrum it would have been seen clearly. For this purpose the Baruch et al. (1973) hadron energy spectrum was assumed and their best line through their points and other experiment. points were taken, the slope of the spectrum for energy < 2 TeV was given by $\gamma = 3.37$.

The procedure of the calculation was as follows: the differential spectrum in the energy range 30 GeV up to 10^5 GeV was divided into many small cells and for each cell the frequency of events in units $\text{cm}^{-2} \text{sec}^{-1} \text{st}^{-1}$ was found. The distribution of the number of burst particles N as a function of the depth in the lead absorber was calculated for different proton energies (the energies of the incident proton was taken as the same as the energies defined in the middle of the cells).

Using the above distributions the probability that a primary proton produced N burst particles/unit N was found. These probabilities were folded into the frequency of each cell and the expected shape of the burst spectrum produced in the lead absorber was calculated and is shown in figure 5.22. The result from the burst spectrum shows that the step (bump) was clearly present in the spectrum. Therefore, this result shows that if the bump was a real effect then it would be possible to detect it in this experiment.

The burst spectrum, figure 5.22, was converted to an energy spectrum at sea level using the energy - burst size relationship for proton induced

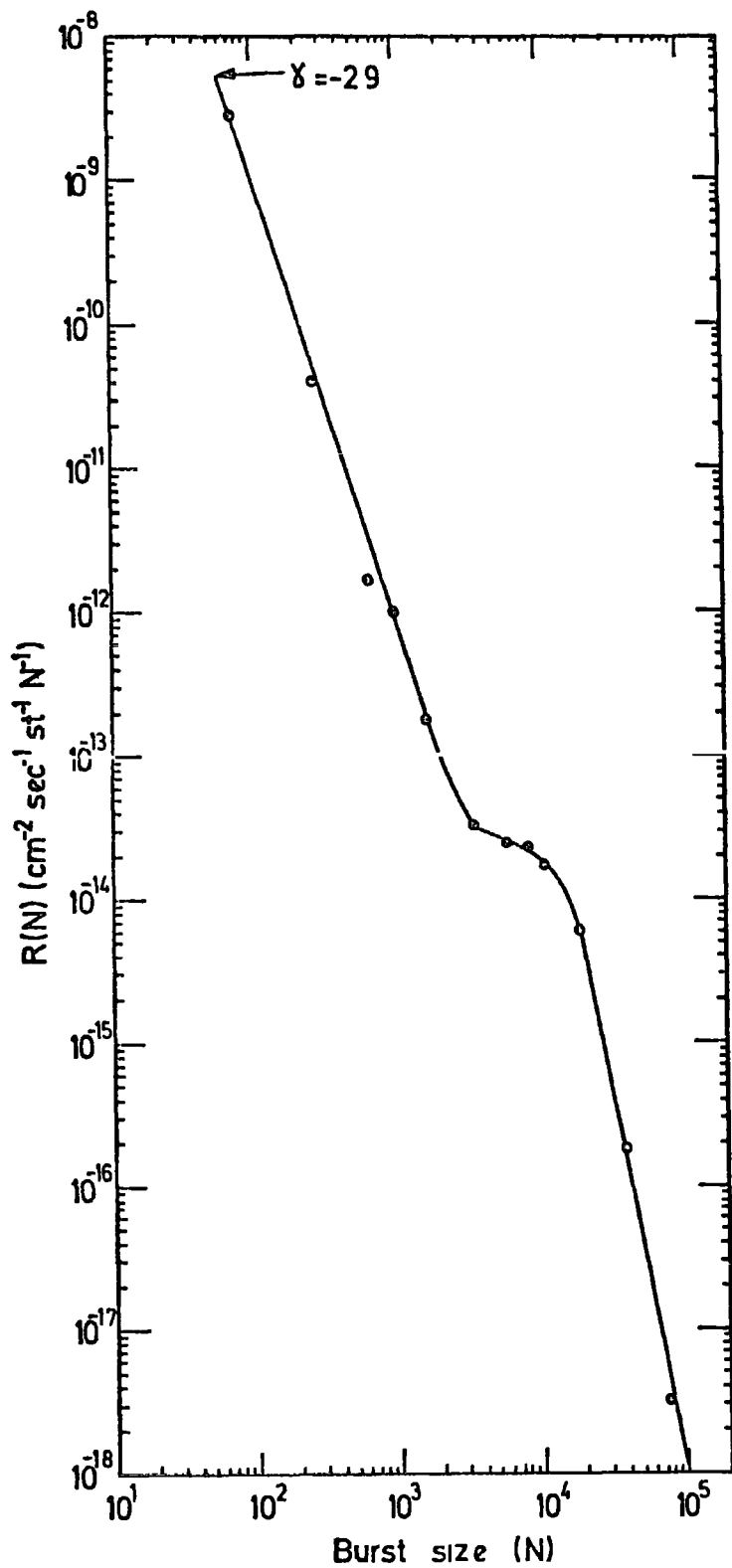


Figure 5.22

The differential bursts spectrum calculated under 15 cm of lead. This was calculated using the Baruch et al. energy spectrum and the burst size - energy relationship for proton induced bursts in lead.

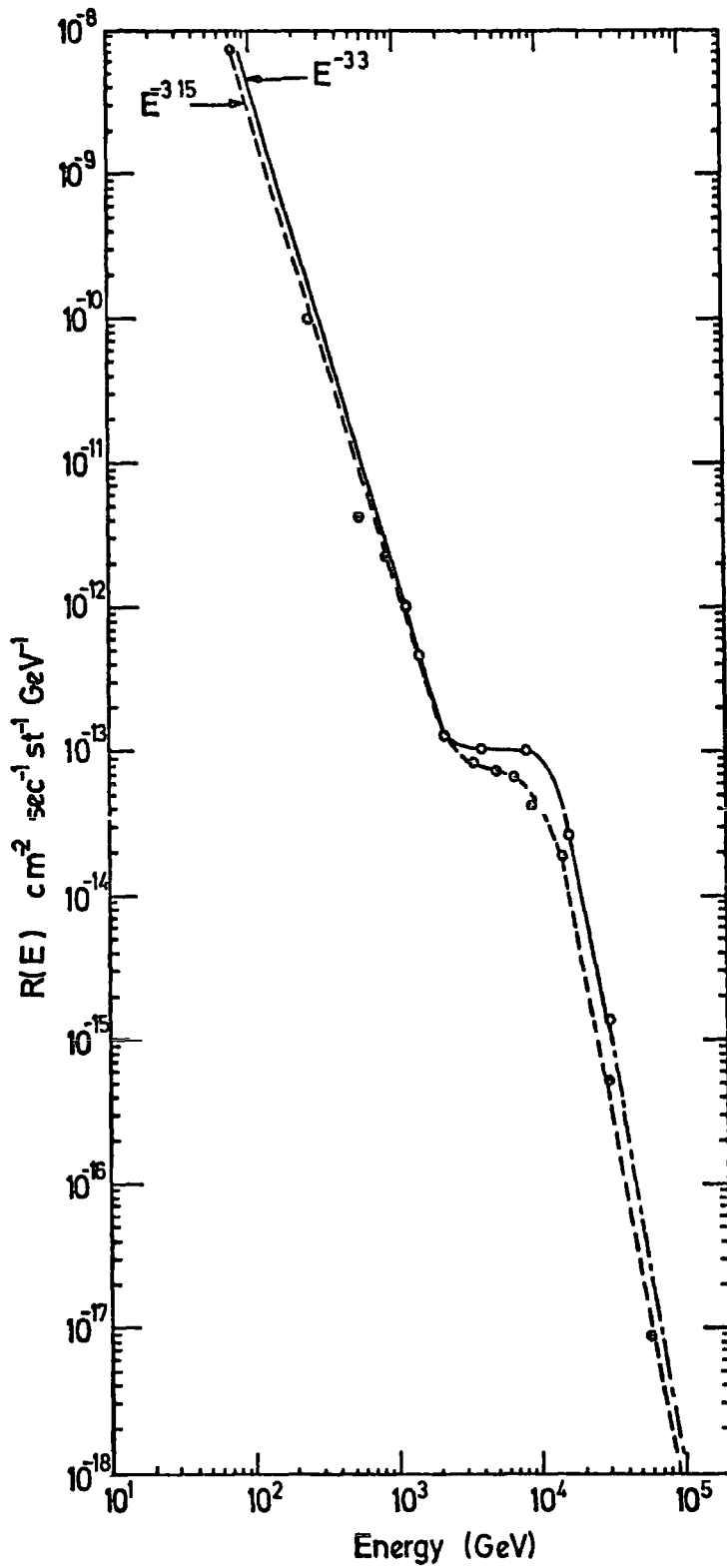


Figure 5.23

A comparison between the energy spectrum calculated from the burst spectrum given in figure 5.22 using the burst size - energy relationship for a proton induced burst in lead, and the original energy spectrum given by Baruch et al. measured in a calorimeter experiment.

bursts in lead.

The comparison between the calculated energy spectrum from the burst spectrum and the spectrum given originally by Baruch et al., has been made and figure 5.23 shows this comparison. From this comparison it is seen that both spectra are almost identical in shape.

5.9 Accompanied events

The middle liquid scintillator M was operated with the single hadron experiment to identify whether the hadrons interacting in the chamber are associated with extensive air shower particles or not. With this single detector placed on the top of the chamber (see figure 4.9) an accompanied event was identified when there was more than 2 particles passing through the scintillator. The number of particles passing through scintillator M could be measured from the pulse height recorded on the oscilloscope film, the pulses from this scintillator being delayed by $1.6 \mu\text{s}$. The characteristics of this scintillator have been discussed in section 4.3.3. A scatter plot given in figure 5.24 shows the relation between the number of particles recorded in scintillator M, (N_M), accompanied with the hadrons interacted in the chamber and the burst size measured in the plastic scintillators under the lead and iron targets. The points in the scatter plot were binned and the frequency distributions for the number of particles in scintillator M accompanied with the hadron produced burst in iron and lead are shown in figure 5.25. In this figure, the first column shows the number of the unaccompanied events ($N_M < 3$). So, by taking the mean of these distributions for $N_M > 3$ particles, one can plot the same relation between the number of particles in scintillator M as a function of burst size, this is shown in figure 5.26.

From this figure it is noted that, as the burst size produced by hadrons increases (i.e. the energy of the incident hadrons increase) the

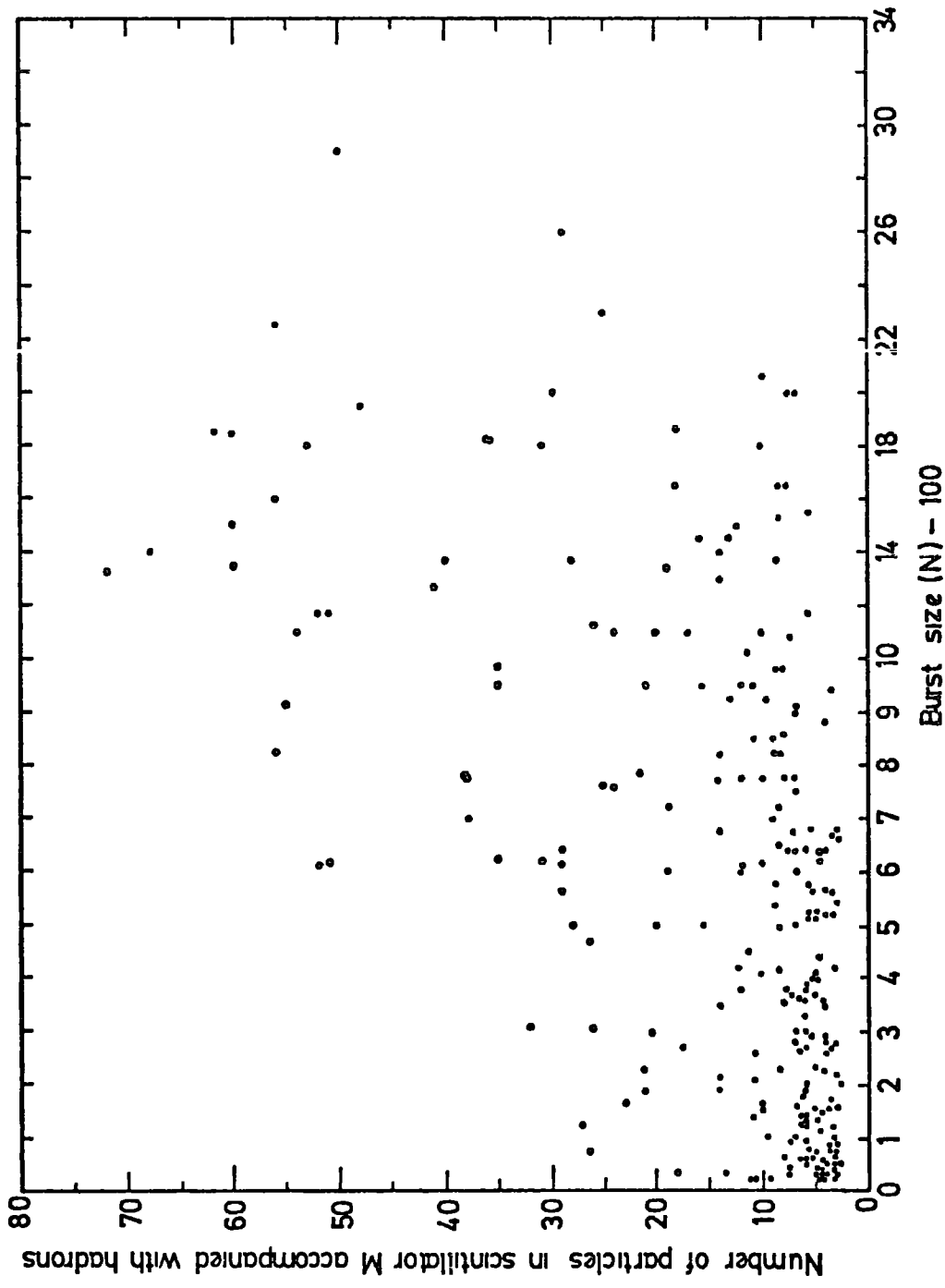


Figure 5.24 Scatter plot of the number of extensive air shower (EAS) particles recorded in scintillator M associated with burst observed in lead and iron.

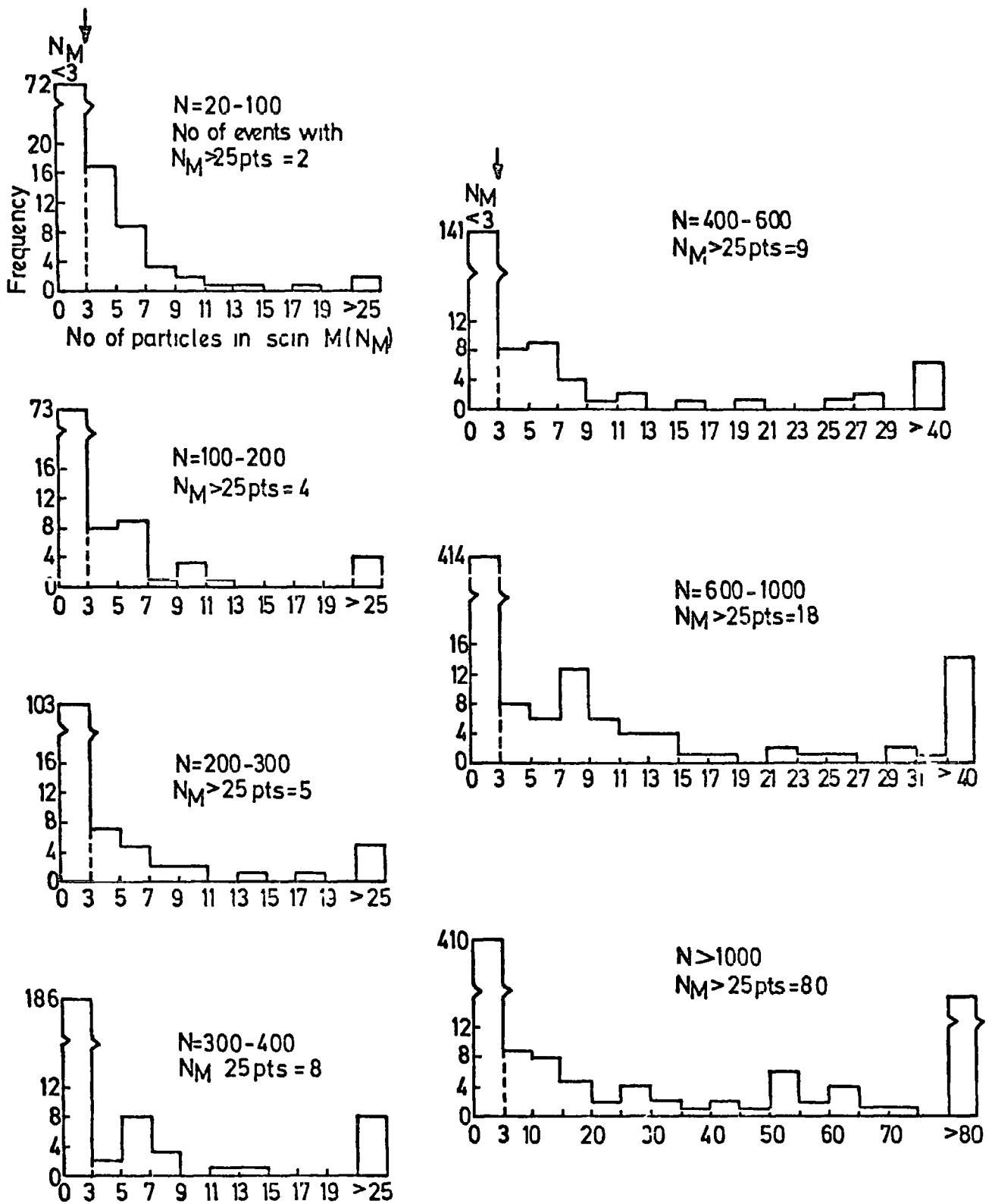


Figure 5.25.

The frequency distributions for the number of EAS particles in scintillator M , (N_M), associated with bursts in iron and lead. The first cell shows unaccompanied events.

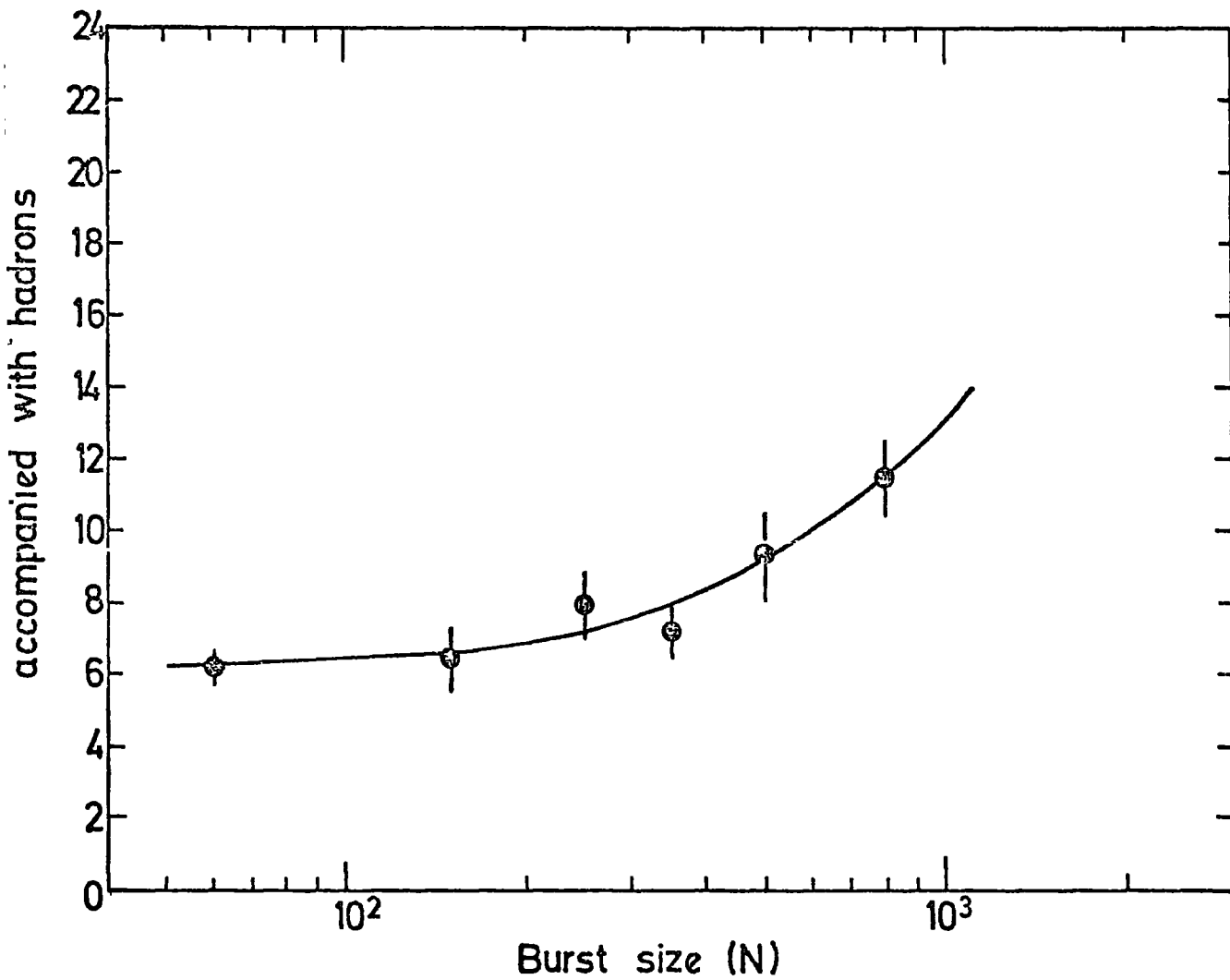


Figure 5.26

The relation between the number of EAS particles recorded in scintillator M associated with burst occurring in lead and iron.

number of accompanying particles increases (i.e. the shower size increases).

However, with this detector it is impossible to locate the position of the shower core and it is not possible to measure the size of the shower.

5.10 Conclusion

The sea level spectrum of all hadrons as measured in this experiment is shown in figure 5.21 and compared with other experimental measurements. The result from this experiment shows a constant slope with $E^{-2.7 \pm 0.1}$ over the energy range 10 GeV to 10 TeV. The present result gives no support to the suggestion of Baruch et al. (1973) that there is a step in the spectrum of hadrons in the region of 2 - 8 TeV and the existence of a new particle of rest mass in the range 40 - 70 GeV/c², mean life time $> 2 \cdot 10^{-7}$ second and an interaction length of $1,000 \pm \frac{1,000}{7,00}$ gm cm⁻².

The present spectrum was calculated assuming all the particles are nucleons and the conversion from burst size to mean energy was made using the proton burst size - energy relationship. But in fact not all the hadrons are nucleons. There is contribution of pions for which the conversion will be slightly different. The difference in burst size for incident protons and pions is not large, the size being about 30% larger for pions than protons in iron and 20% larger in lead (see figures 3.6 and 3.7). However one can expect that this difference does not affect the shape of the spectrum and it could not be distorted.

The difference between the energy spectrum of all hadrons (solid line) (see figure 5.21) and the energy spectrum of nucleons (dashed line) is due to the increase in the contribution of charged pions to the total hadron flux for energies > 100 GeV.

The muon contribution was assumed to be small and for large burst sizes corresponding to 4 or 5 TeV hadron energy, the effect is $< 1\%$ for the iron and $\sim 5\%$ for the lead.

From the measured angular distribution for the large bursts ≥ 400 particles the average value of n was found 8 ± 1.5 and this corresponds to particles with attenuation length $\lambda = 129 \pm 16 \text{ gm cm}^{-2}$. However, this supports the conclusion that the observed large bursts are produced predominantly by hadrons.

CHAPTER 6

THE HIGH ENERGY SPECTRUM OF NEUTRONS AND

PIGNS AT SEA LEVEL

6.1 The neutron spectrum

6.1.1 General remarks

While the chamber was run on the short time delay ($20\mu\text{s}$) neutral particle induced bursts in the iron target were recorded. The procedure to identify the neutral bursts from bursts produced by charged particles was from the incoming particle track in the flash tube tray Fla, (see figure 4.9). For neutral particles there should be no track seen the the tray Fla. A track was defined as ≥ 2 flashed tubes in one line and near the middle (core) of the burst.

All the neutral particles were classified as neutrons and the energy spectrum of the neutrons at sea level was determined from the burst spectrum produced in a 15 cms iron target.

Plate 6.1 shows an example of a neutral particle interacting in the iron target.

6.1.2 The measured spectrum

In the total running time 1229.7 hours, only 28 events showed neutral particles within $\pm 30^\circ$ to the vertical interacting in iron target, (see table 5.1). All these neutral particles have been classed as neutrons. With this insufficient number of events it was difficult to evaluate the value of the exponent n from the angular distribution of these 28 events. So, the value of n has been taken to be 7.5 and this was the same value

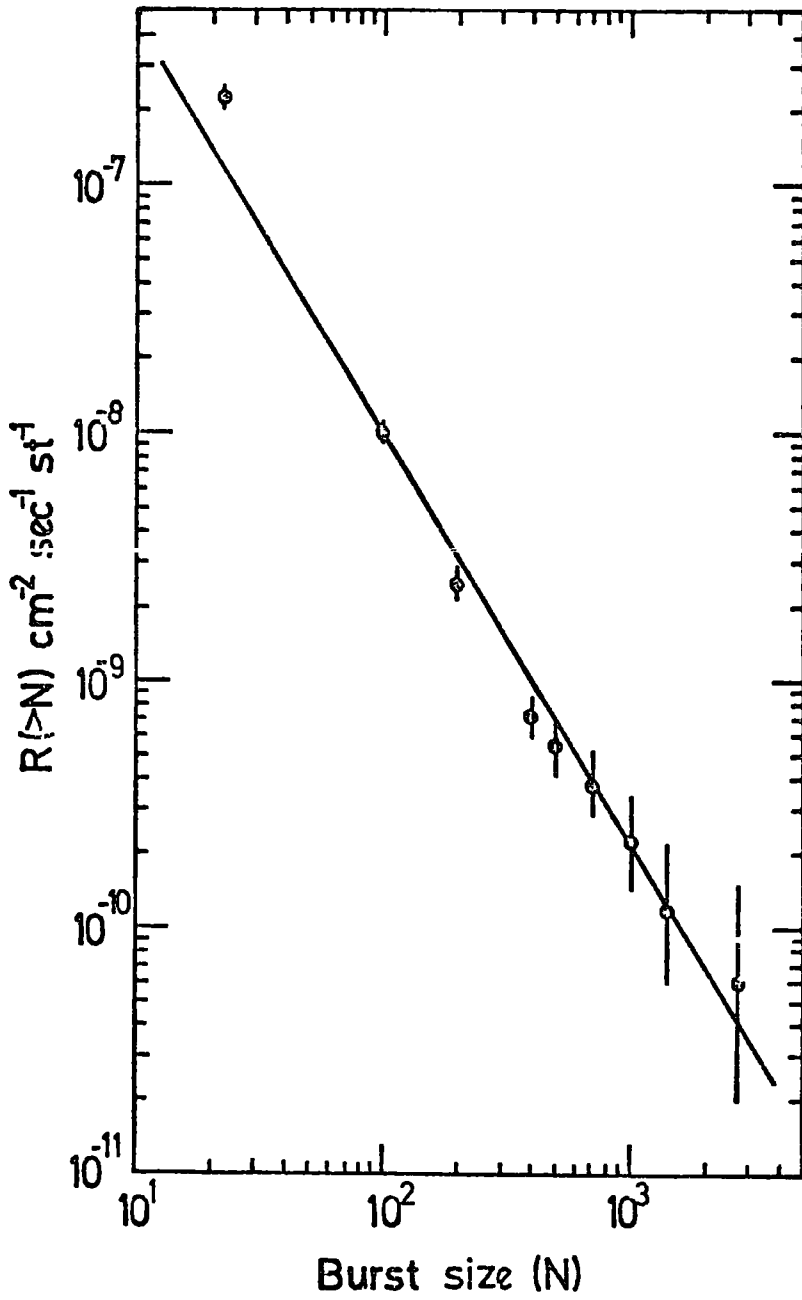


Figure 6.1

Integral burst spectrum of neutral particle induced bursts in 15 crs iron.

which was found for all hadrons interacting in iron in the long time dead time measurements. This value was used to evaluate the aperture in $\text{cm}^2 \text{sr}$, (see figure 5.14).

The integral spectrum of neutral bursts in the iron is shown in figure 6.1.

The conversion of burst size to energy has been made using a burst size - energy relationship for proton initiated bursts in iron.

Figure 6.2 shows the vertical differential energy spectrum of neutrons at sea level calculated from the burst spectrum. In this figure the proton measurements ($< 100 \text{ GeV}$) of Brooke and Wolfendale (1964) and Diggory et al. (1974) also were shown.

The spectrum can be represented in differential form by $N(E) = K E^{-\gamma}$ where $\gamma = 2.9 \pm 0.1$ in the energy range $50 - 1,000 \text{ GeV}$.

6.13 Comparison with previous measurements

The present measurement on the energy spectrum of neutrons was found useful to compare with other results, but the only results available in the same energy range were the measurements summarised by Ashton et al. (1970).

Figure 6.3 shows this comparison. Although of limited statistical weight the neutron spectrum estimated from this experiment is found to be consistent with the previous neutron spectrum summarised by Ashton et al. In the same figure, the best line through all the points was drawn and this shows a slope of $\gamma = 2.97 \pm 0.1$ in the energy range $50 - 1,000 \text{ GeV}$.

Hence, it is possible to compare the measured neutron spectrum with proton measurements of Brooke and Wolfendale (1964), assuming the neutron spectrum to be the same as that of the proton at sea level.

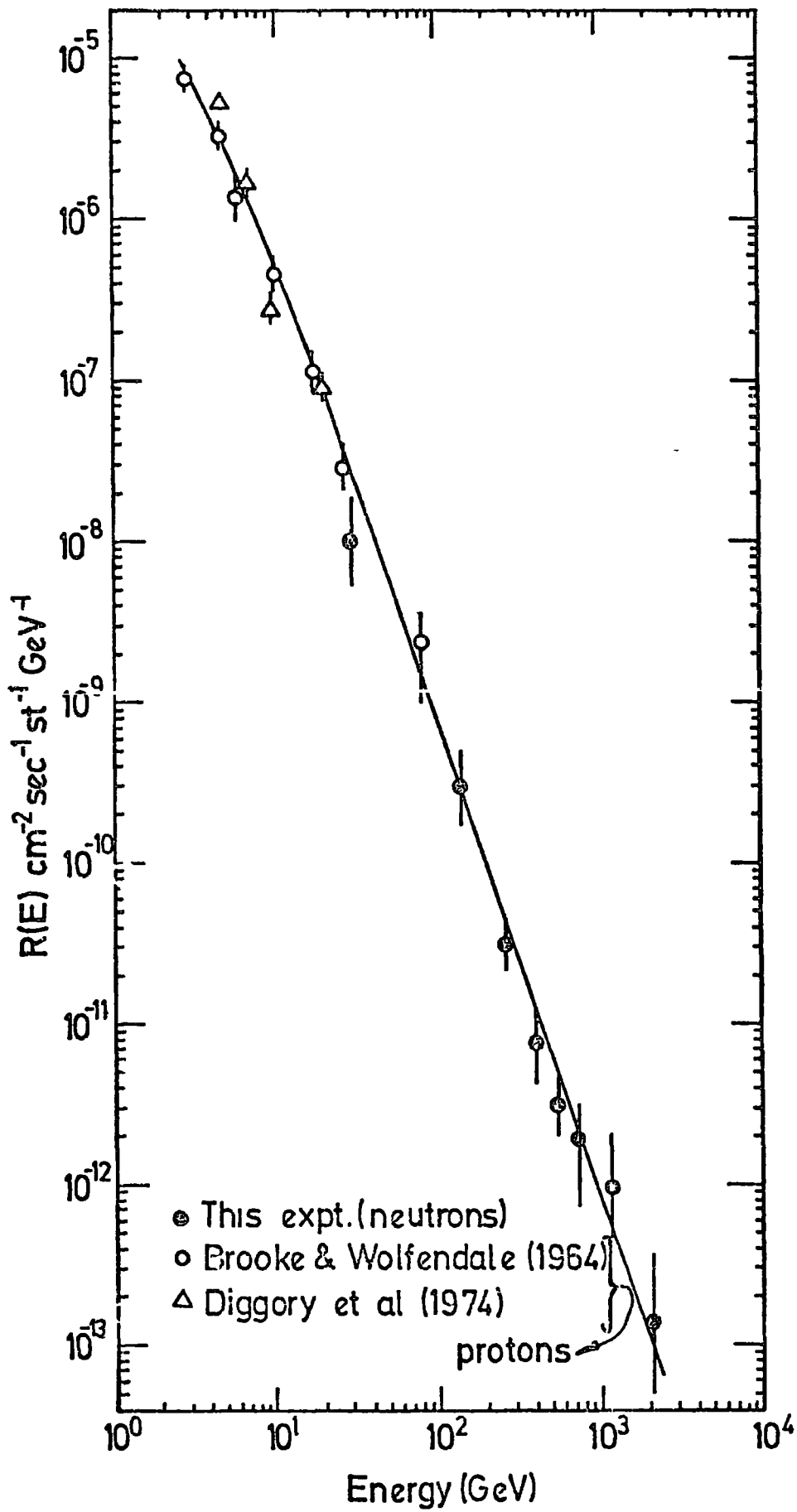


Figure 6.2

The vertical differential energy spectrum of neutrons at sea level measured in this experiment, compared with the low energy proton measurements.

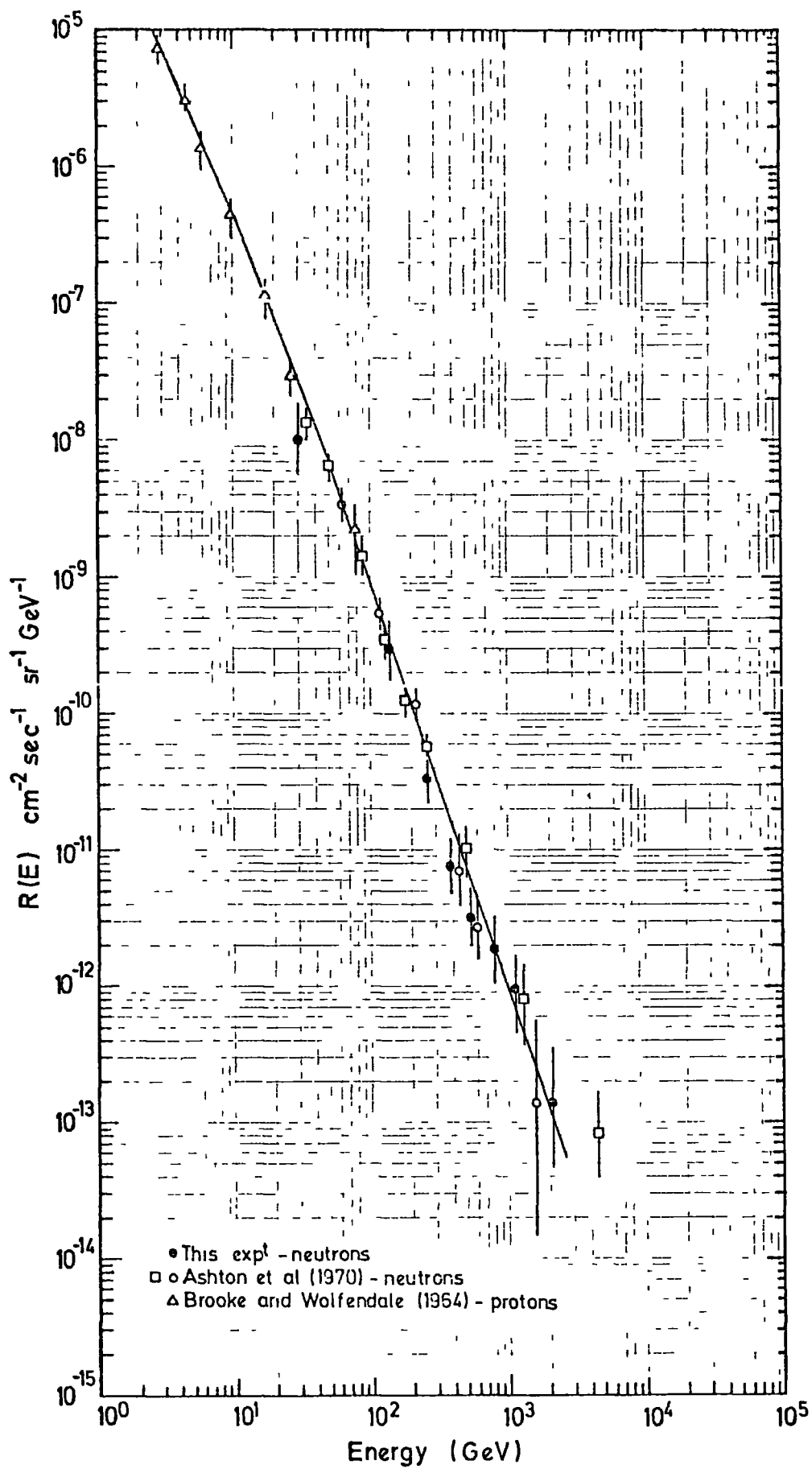


Figure 6.3

The summary of the vertical differential energy spectrum of neutrons at sea level compared with low energy proton measurements of Brooke and Wolfendale (1964).

Plate 6.1

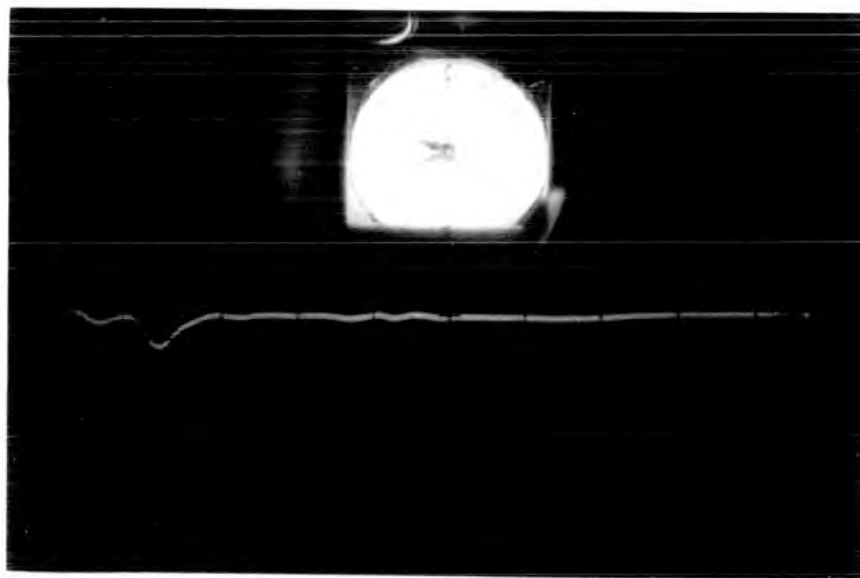
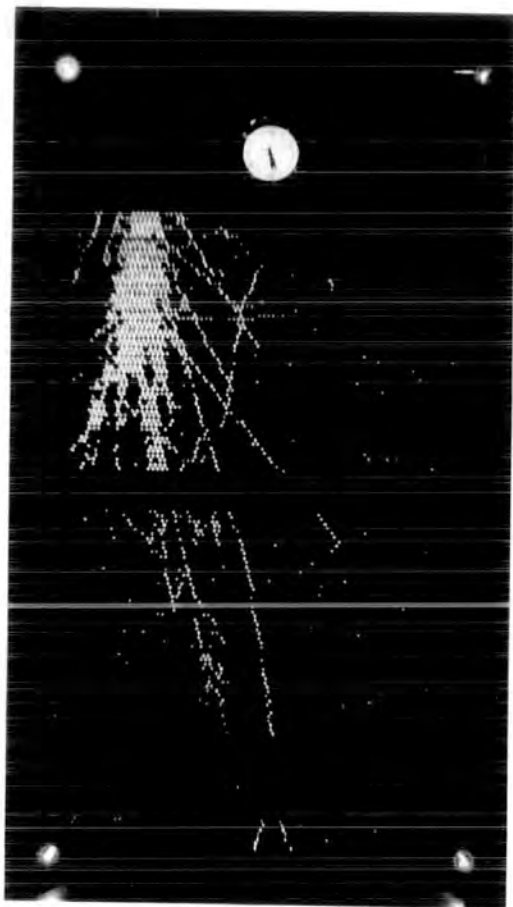
Event H8 - 38

A burst produced in the iron by a neutral particle.

The oscilloscope trace shows a pulse from scintillator A.

This was taken from a run using a time delay T_D of $20 \mu s$.

A = 107 particles.



6.2 Predicted muon burst spectrum in iron and lead

6.2.1 Introduction

Before going into details of the calculation of the muon burst spectrum, it is important to review the theoretical background first. The known interaction processes by which the muon can lose energy in traversing matter are: knock-on electron production, bremsstrahlung, direct pair production and nuclear interaction.

The first three processes produce comparatively frequent energy transfers and therefore are important in the present calculation. The contribution of the nuclear interaction to the probability of burst production in the present experiment is insignificant and therefore has not been included.

6.2.2 Theoretical considerations

The theories of the production of knock-on electrons and bremsstrahlung have been given by Bhabha (1938) and Christy and Kusaka (1941) respectively. The cross section for electron pair production by muons has been calculated firstly by Bhabha (1935) and independently by Nishina et al. (1935) and by Racah (1937) using classical quantum electrodynamics. The results of these calculations are given in convenient forms by Rossi (1952):

(a) Knock-on electrons:

The differential probability is given by:

$$\varphi_{\text{coll}}(E, E') dE' = \frac{2C_m e c^2}{\beta^2} \frac{dE'}{E'^2} \left[1 - \beta^2 \frac{E'}{E_m} + \frac{1}{2} \left(\frac{E}{E + mc^2} \right)^2 \right]$$

where $\varphi_{\text{coll}}(E, E') dE'$ is the probability per gm cm^{-2} of a charge particle (mass m and spin $1/2$) of energy E , transferring an energy between E' and $E' + dE'$ to an electron.

$C = \pi N \frac{Z}{A} r_e^2 = 0.15 \frac{Z}{A} \text{ gm}^{-1} \text{ cm}^2$ represents the total area covered by the electrons contained in one gram, each considered as a sphere of radius r_e , $r_e = \frac{e^2}{m_e c^2}$ the classical radius of the electron. Z and A are the atomic number and the atomic weight of the absorber respectively. N is Avogadro's number

βc is the velocity of the incident particle

E'_m is the maximum transferable energy and is given by:

$$E'_m = 2 m_e c^2 \frac{p^2 c^2}{m_e^2 c^4 + m^2 c^4 + 2 m_e c^2 (p^2 c^2 + m^2 c^4)^{1/2}}$$

where p is the momentum of the incident particle.

(b) Bremsstrahlung:

The differential radiation probability is given by:

$$\varphi_{\text{rad}}(E, E') dE' = \alpha N \frac{Z^2}{A} r_e^2 \left(\frac{m_e}{m}\right)^2 \frac{dE'}{E'} F(U, v)$$

where $\varphi_{\text{rad}}(E, E') dE'$ is the probability per gm cm^{-2} that a particle of rest mass $m c^2$ and kinetic energy E will emit a photon of energy between E' and $E' + dE'$.

U is the total energy of the incident particle.

α is the fine structure constant.

$v = E'/U$ is the fractional energy transfer.

$F(U, v)$ is a slowly varying function of U and v and it is given by:

$$F(U, v) = 4 \left[1 + (1 - v)^2 - \frac{2}{3} (1 - v) \right] x \left[\ln \left(\frac{2U}{m c^2} \frac{\hbar}{m c r_n} \frac{1 - v}{v} \right) - \frac{1}{2} \right]$$

where $r_n = 0.49 r_e A^{1/3}$ and $\hbar = \text{Planck's constant}/2\pi$.

The dependence of φ_{rad} on the energy transfer, E' , is mainly through $1/E'$.

(c) Direct electron pair production

The differential probability is given by:

$$\varphi_{\text{P.P.}}(E, E') dE' = \frac{8}{\pi} \alpha^2 \frac{N}{A} Z^2 r_e^2 H(U, v, \mu)$$

where $\varphi_{\text{P.P.}}(E, E') dE'$ is the probability per gm cm^{-2} that a particle of mass mc^2 and kinetic energy E will produce an electron pair with energy between E' and $E' + dE'$.

H is a dimensionless function of U , v and μ , and the other symbols have their usual meanings given in items a and b.

6.2.3 Muon burst spectrum

McDiarmid et al. (1962) have calculated the differential energy transfer production spectra per gm cm^{-2} of lead and iron for the three processes and for energy transfers in the ranges 1 - 100 GeV. This was obtained by taking the theoretical expressions given in section 6.2.2 and folding in the sea level muon spectrum. McDiarmid et al. have used the muon spectra given by Owen and Wilson (1955) up to 20 GeV and by Pine et al. (1959) between 20 and 100 GeV; above 100 GeV a differential form $E^{-2.8}$ was assumed.

For the present calculation only the muon bremsstrahlung cross section for energy transfers > 100 GeV was considered, because at high energy the radiation process is the process which dominates in electromagnetic interactions. So, the bremsstrahlung cross section was calculated for high transferable energies and for both iron and lead absorbers. The results of calculations carried out by Hansen (1975, private communication) for the bremsstrahlung cross section in the iron absorber have been used.

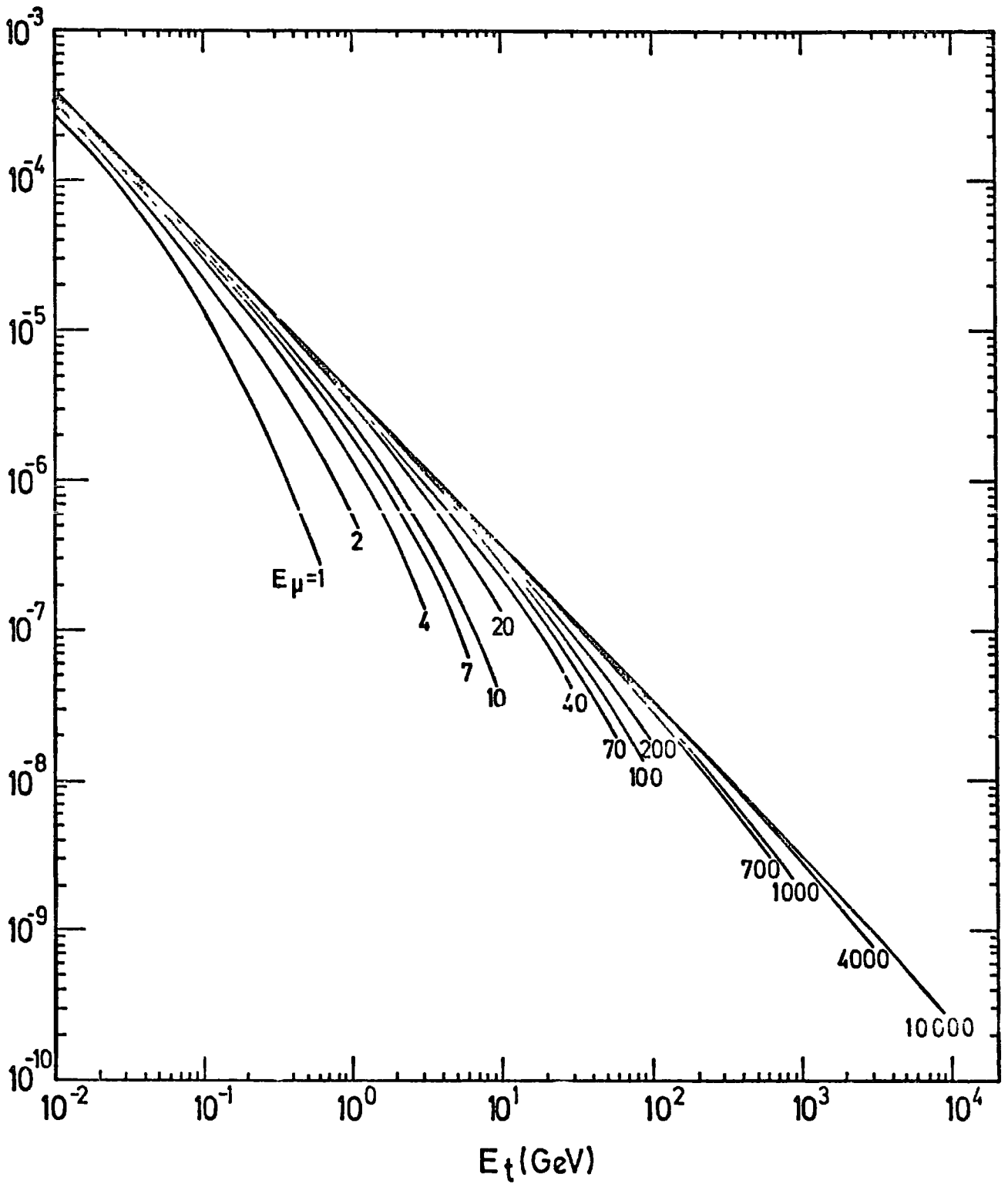


Figure 6.4

Differential probability of energy transfer, E_t GeV, for bremsstrahlung process in iron.

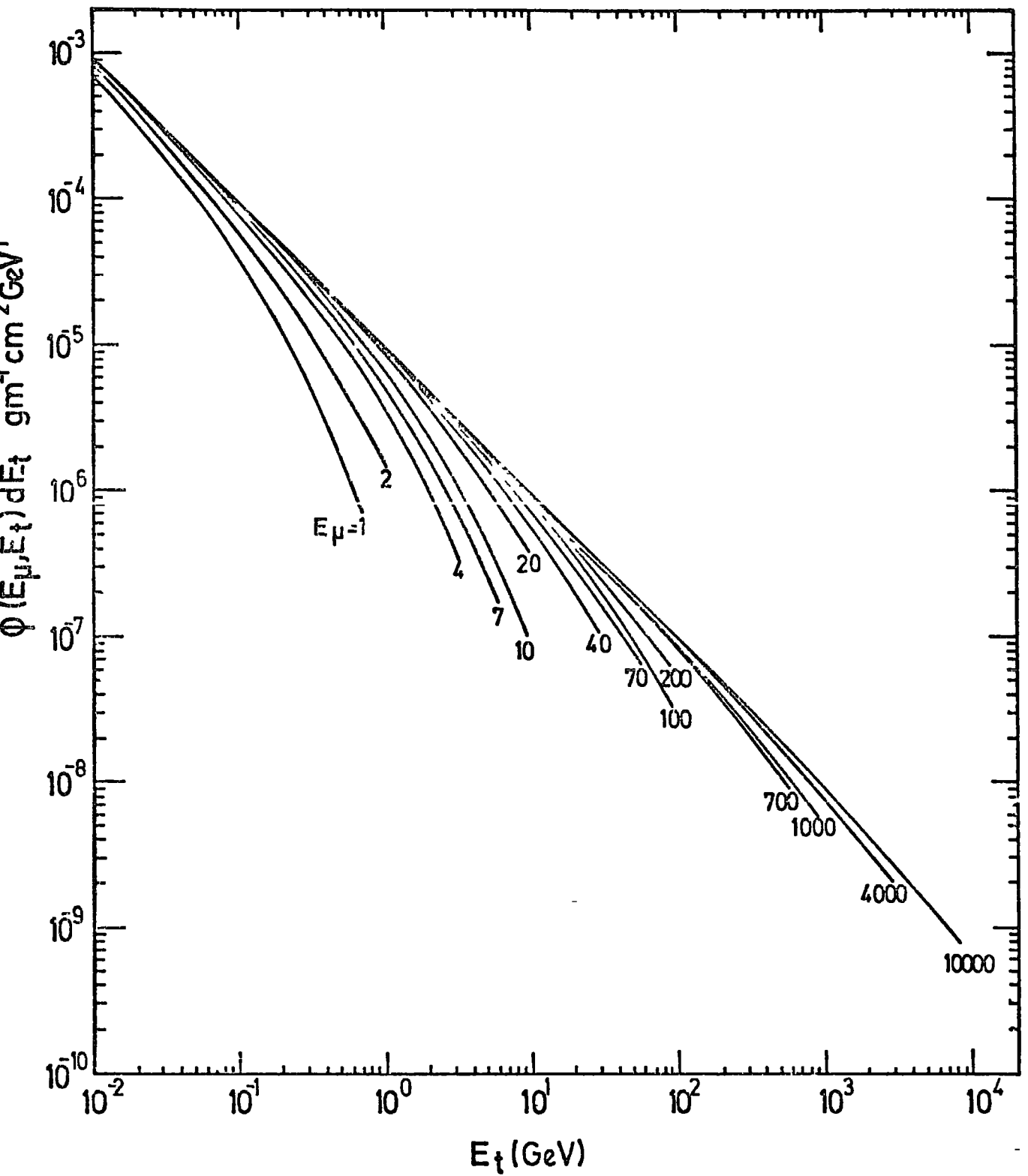


Figure 6.5

Differential probability of energy transfer, E_t GeV, for bremsstrahlung process in lead.

Figures 6.4 and 6.5 show the differential cross sections for the bremsstrahlung process in iron and lead respectively.

The muon spectrum given by Alkofer et al. (1971) up to 1,000 GeV was used with that given by Aurele et al. (1967) from 1,000 GeV - 7,000 GeV. The latter intensity was normalised at 1,000 GeV to that given by Alkofer et al. For higher energies the spectrum was assumed to be of the form $A E^{-2.67} \frac{1}{1 + E/91}$ with E in GeV. The differential muon spectrum which has been used is shown in figure 6.6.

By taking the calculated bremsstrahlung cross section and folding in the above muon sea level spectrum the differential energy transfer spectrum was obtained. The result of this calculation shows agreement with the calculated differential energy transfer production spectra per gm cm⁻² for bremsstrahlung in lead and iron given by McDiarmid et al. for energies < 100 GeV. The results of the differential energy transfer production spectra per gm cm⁻² given by McDiarmid et al. for the three processes and the present calculation for bremsstrahlung process is shown in figures 6.7 and 6.8 for lead and iron respectively. The rate of muons with energy > 1.3 GeV, $R(> E_t)$ in cm⁻² sec⁻¹ st⁻¹, as a function of E_t could be calculated after integrating over all the transferable energies and the absorber thickness in gm cm⁻².

Finally, the last step, to produce the muon burst spectrum was to calculate the relationship between the burst size Ne and the energy transfer in lead and iron. Since muons have a large attenuation length, the produced energy transfer size distribution will be independent of absorber thickness. The limiting energy which can produce bursts of a given size by the maximum energy cascade which can develop to shower maximum in the whole depth of the absorber. For the iron absorber, 8.19 radiation lengths, it can be seen from the cascade curves of Ivanenko and Samosudov, see figure 3.1, to be

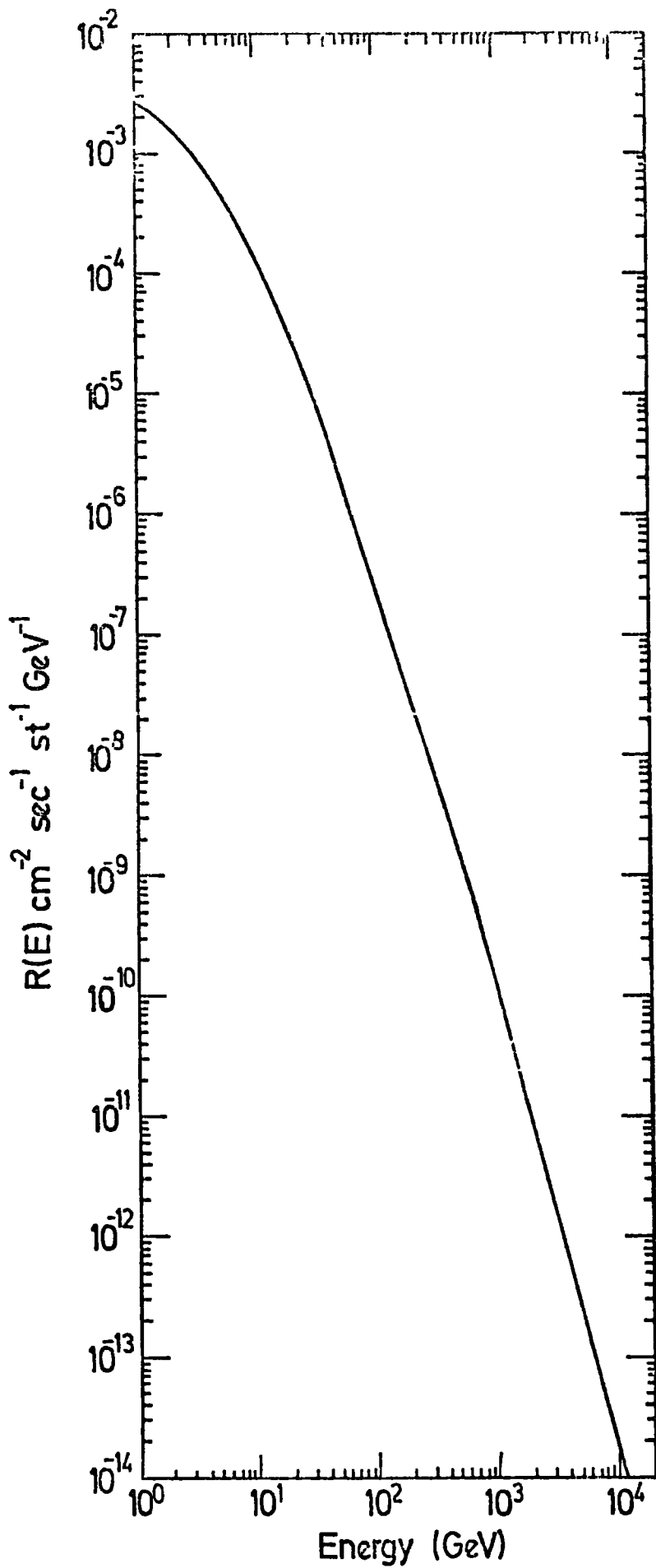


Figure 6.6

The differential energy spectrum of muons at sea level.

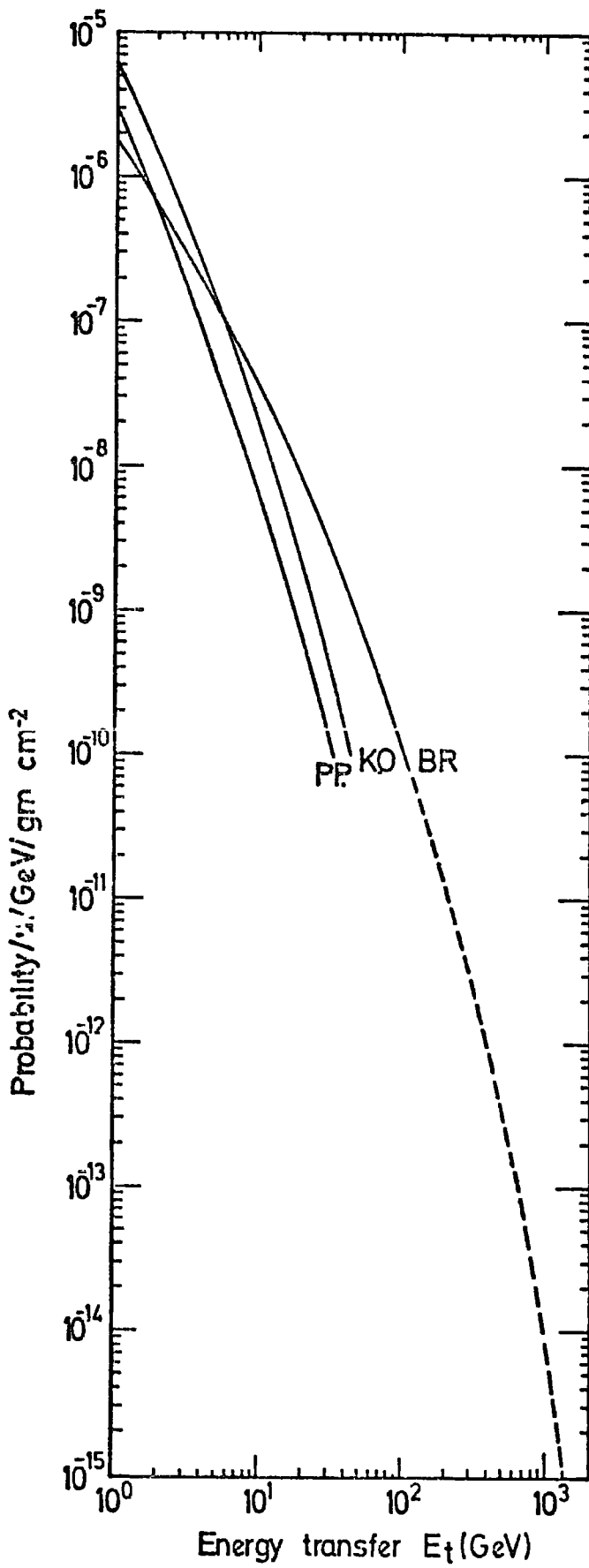


Figure 6.7

Differential probabilities for the electromagnetic interactions for muons in lead.

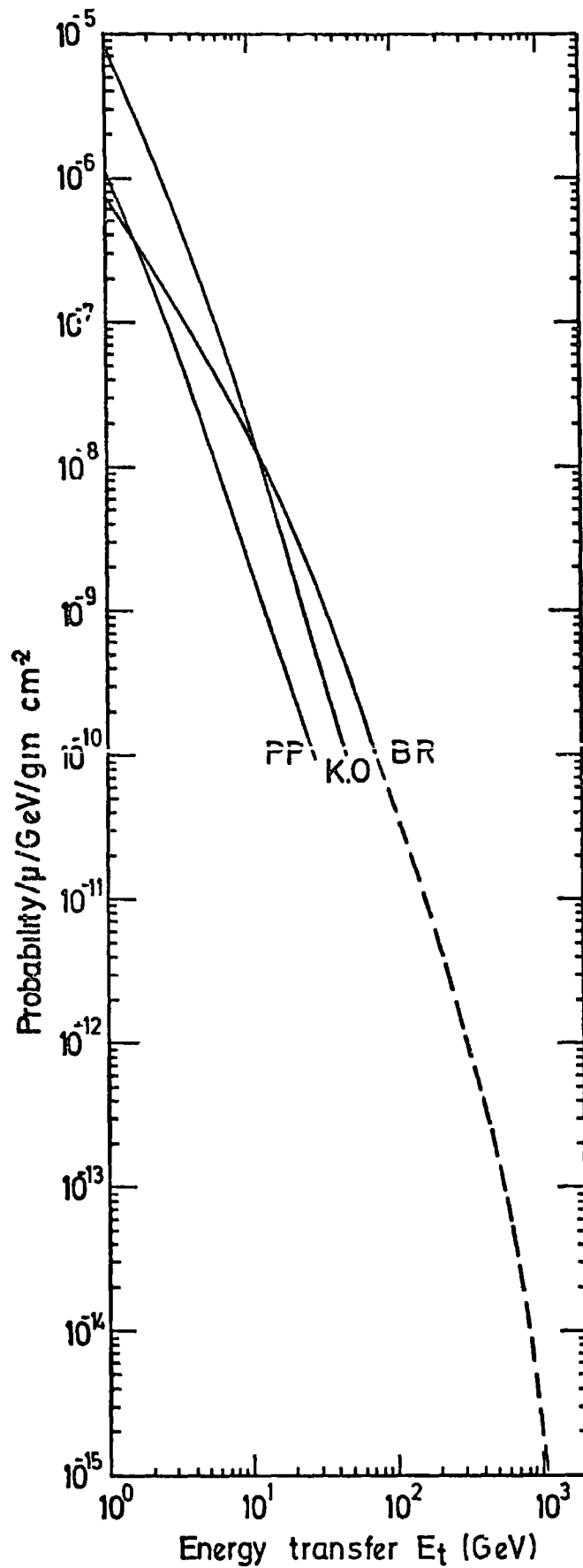


Figure 6.8

Differential probabilities for the electromagnetic interactions of muons in iron.

sufficient up to about 1,000 GeV.

However, by dividing each absorber into a large number of small layers and assuming equal probability for a muon to interact in the middle of each layer and by using Ivanenko and Samosudov transition curves for electron initiating cascades in iron and lead figures 6.9 and 6.10 for the knock-on and bremsstrahlung processes, and photon initiating cascade in iron and lead (see figure 3.1 and 3.2) for the direct pair production by muons, one can calculate the relationship between the burst size N_e and the energy transfer in iron and lead target, this relationship is shown in figure 6.11.

The final results on the muon burst spectrum will be presented in the next section compared with the total burst spectrum measured in this experiment and the nucleon burst spectrum.

6.3 The pion spectrum

6.3.1 Introduction

In this section the flux of high energy pions was determined by using a statistical method based on separating the pions from all measured hadrons. Briefly, bursts produced by charged (P , π^{\pm} , μ^{\pm}) and neutral (n) primary particles in lead and iron targets have been measured. If the neutron spectrum at sea level is known and then assuming equal numbers of neutrons and protons in cosmic rays at sea level, the contribution of pions and muons to the total burst spectrum can be found directly from the experimental data by subtracting the nucleon burst spectrum from the total burst spectrum. Also one can calculate accurately the contribution of muon (μ^{\pm}) produced bursts in the iron and lead targets (this was discussed in section 6.2). So, in this way the burst spectrum produced by pions (π^{\pm}) can be found and the pion (π^{\pm}) energy spectrum determined. In this section the differential energy spectrum of charged pions over the energy range $40 \text{ GeV} < E < 7 \text{ TeV}$

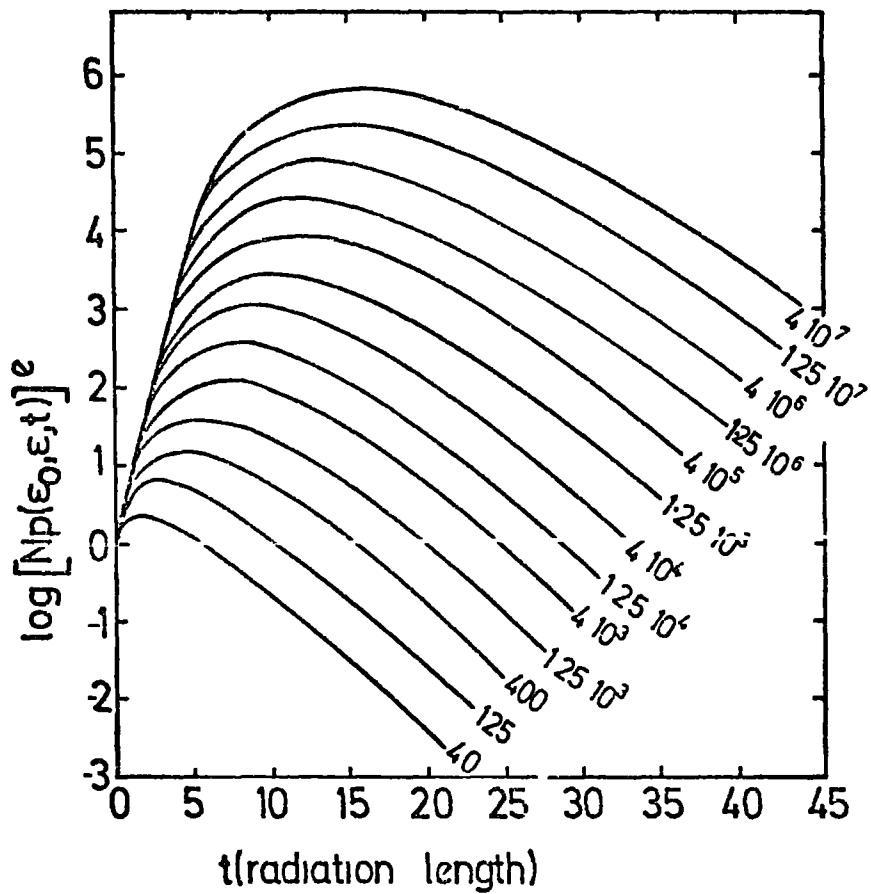


Figure 6.9

Transition curves for electron induced cascades in iron predicted by Ivanenko and Samosudov. The number by each curve refers to the energy of the primary electron. All energies are in units of 0.437β , where β is the critical energy of absorber. The cut-off energy ϵ is 0.1 or ~ 1 MeV.

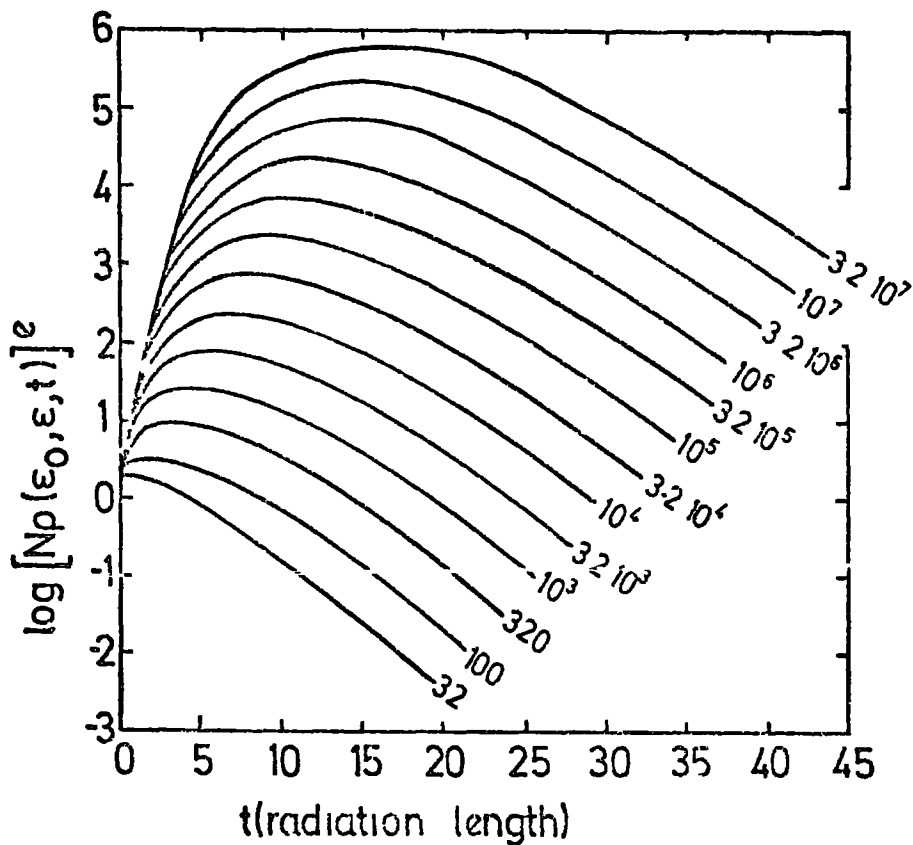


Figure 6.10

Transition curves for electron induced cascades in lead predicted by Ivanenko and Samosudov. The number by each curve refers to the energy of the primary electron. All energies are in units of 0.437β , where β is the critical energy of absorber. The cut-off energy ϵ is 0.35 or ~ 1 MeV.

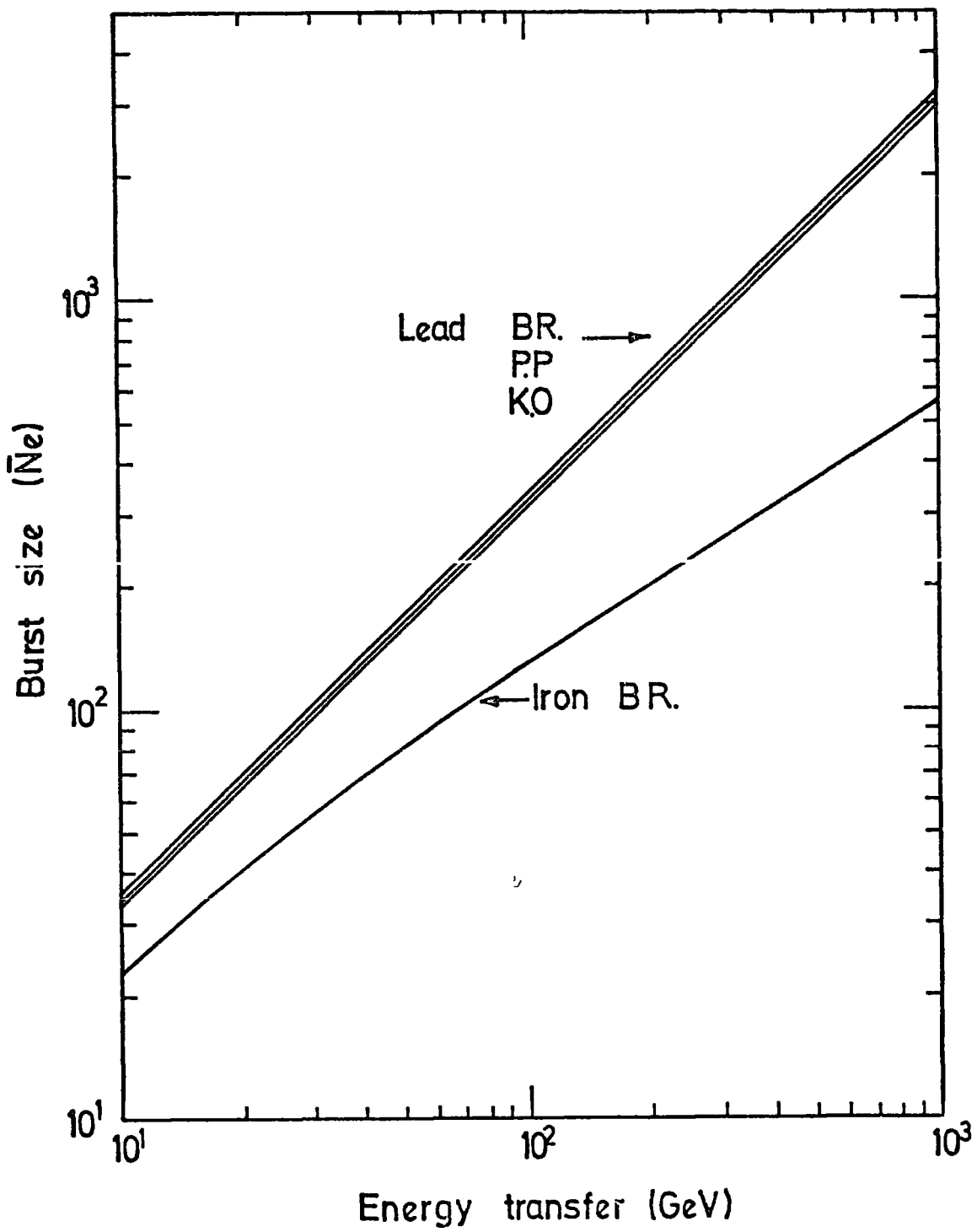


Figure 6.11

Burst size - energy transfer relationship for a muon produced burst in iron and lead by each process.

is given.

6.3.2 The measured pion spectrum

In chapter 5 the vertical burst spectra for all hadrons were given for the iron and lead targets (see figures 5.16 and 5.17). Having obtained this, the vertical burst spectrum produced by pions in iron and lead can be derived from the above spectra by subtracting the contribution of muon and nucleon interactions to the measured vertical burst spectrum. The muon burst spectrum was calculated theoretically.

The nucleon burst spectrum was calculated from the energy spectrum of neutrons at sea level, the best line through the experimental result on neutrons and the previous measurement by Ashton et al. (1970) was taken to calculate the neutron burst spectrum in iron and lead. However, figures 6.12 to 6.15 show the measured integral burst spectra for all incident particles (p, n, π^{\pm}) and a small contribution of μ^{\pm} . In these figures the calculated burst spectra for the neutrons and muons are shown.

The dotted line shows the calculated burst spectrum of pions under 15 cms of lead and iron.

A conversion from burst size to mean energy was made using the burst size - energy relationship for a pion interacting in the lead and iron target (see figures 3.6 and 3.7).

The sea level pion flux was determined from the measured rate of the pions interacting in iron as follows:

Rate of incident pions (π^{\pm}) at sea level ($\text{cm}^{-2} \text{sec}^{-1} \text{st}^{-1}$) = rate of pions observed in Fe divided by the probability of pions not interacting in lead \times probability that pions interact in iron.

$$R_{\pi}(\text{at S/L}) = R_{\pi}(\text{measured}) / (e^{-X_{\text{Pb}}/\lambda_{\pi}}) (1 - e^{-X_{\text{Fe}}/\lambda_{\pi}})$$

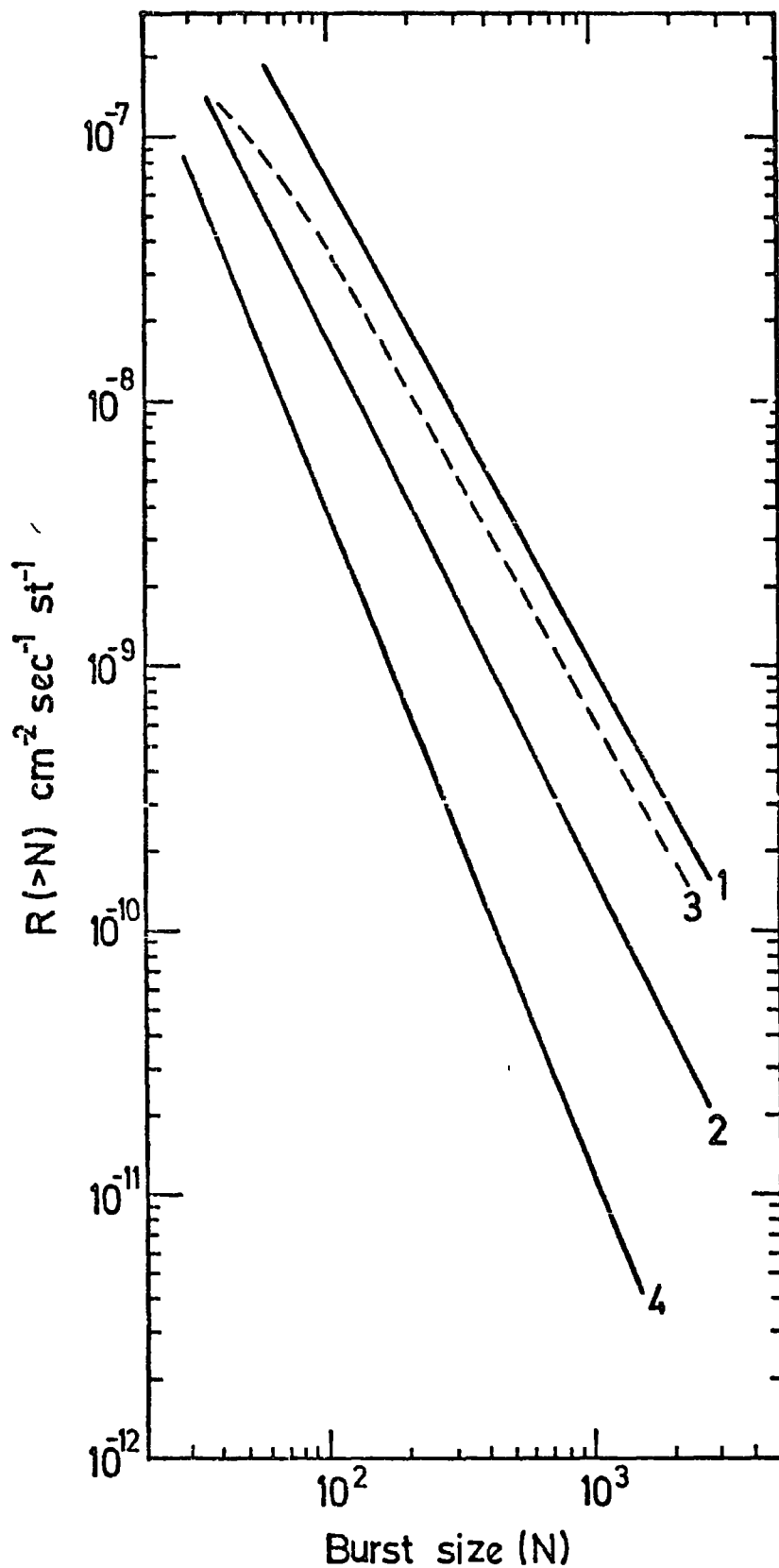


Figure 6.12

The integral burst spectrum of all particles interacted in iron target, data were taken from the $20 \mu\text{s}$ run. The relative contributions of the different particles to the total burst spectrum are shown.

- 1 - All particles (p, n, π^{\pm} and μ^{\pm})
- 2 - neutrons
- 3 - pions
- 4 - muons.

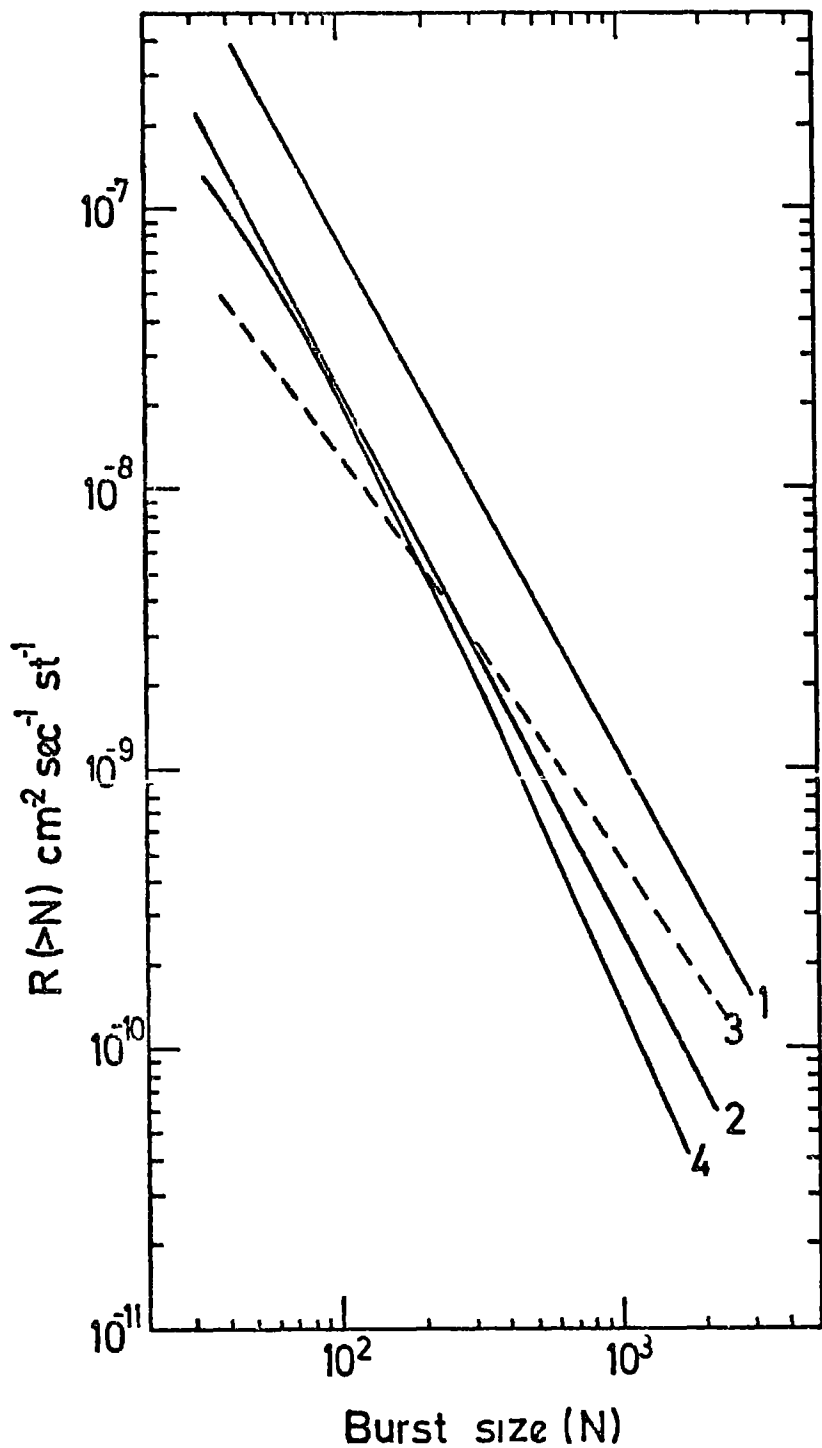


Figure 6.13

The integral burst spectrum of all particles interacted in lead target, data were taken from the 20 μ S run. The relative contribution of different particles to the total burst spectrum are shown.

- 1 - All particles (p, n, π^{\pm} and μ^{\pm})
- 2 - neutrons
- 3 - pions
- 4 - muons.

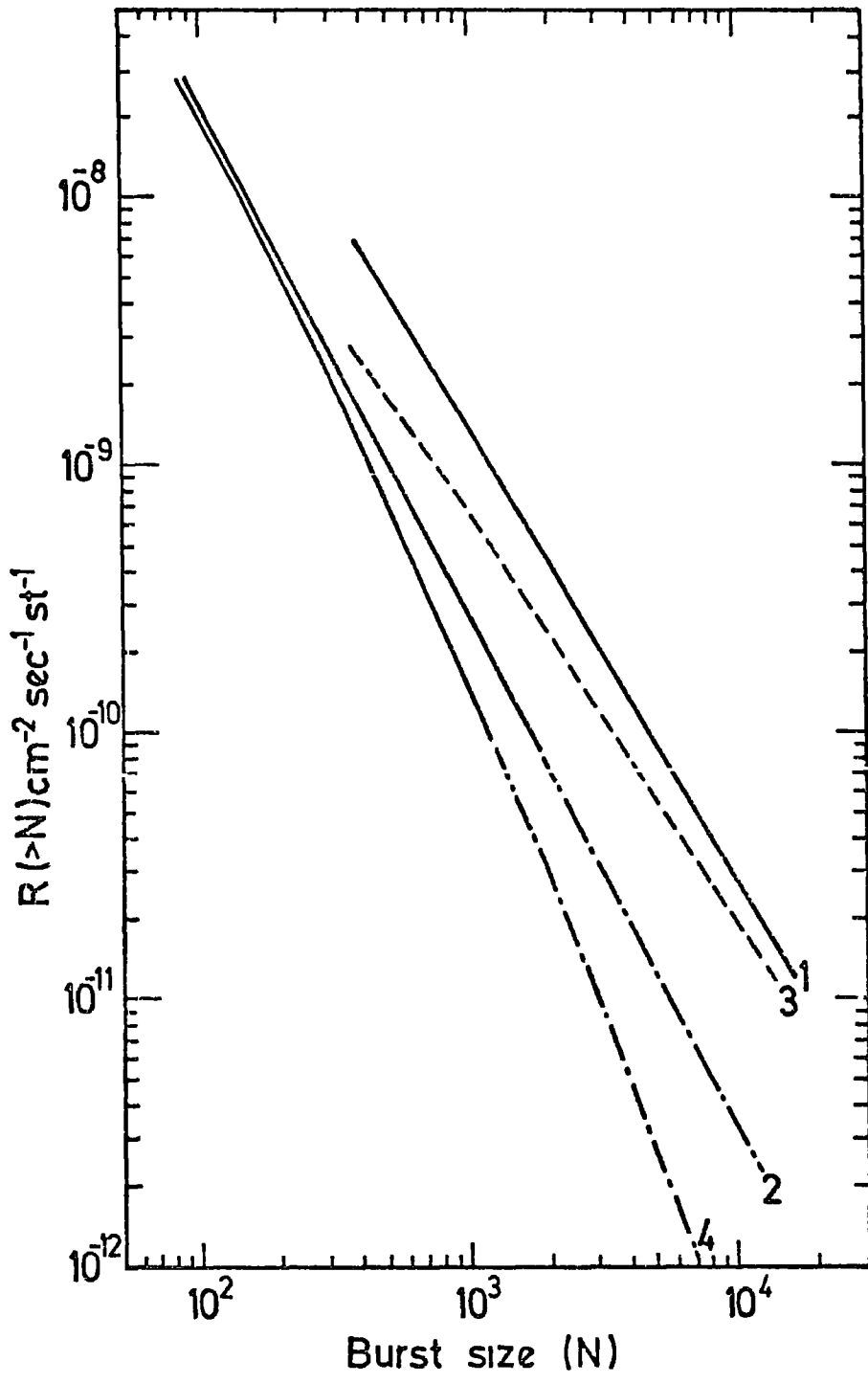


Figure 6.15

The integral burst spectrum of all particles interacted in lead target, data were taken from the 330 μ s run. The relative contributions of the different particles to the total burst spectrum are shown.

- · — · — extrapolation
- 1 - All particles (p, n, π^{\pm} and μ^{\pm})
- 2 - neutrons
- 3 - pions
- 4 - muons

Also at sea level pion flux was determined from the measured rate of the pions interacting in lead as follows:

Rate of incident pions (π^\pm) at sea level ($\text{cm}^{-2} \text{sec}^{-1} \text{st}^{-1}$) = rate of pions observed in pb divided by the probability of pions interacting in lead

$$R_\pi (\text{at S/L}) = R_\pi (\text{measured}) / (1 - e^{-X_{\text{pb}}/\lambda_\pi})$$

As mentioned above the vertical integral burst spectra produced by π^\pm in the lead and iron targets have been used to give two independent measurements of the pion energy spectrum incident on the chamber from the air.

The two spectra were compatible and have the same slope. Averaging those two spectra gives the final result which is shown in figure 6.16. This spectrum shows over the energy range 40 GeV to 7 TeV the differential ($\pi^+ + \pi^-$) vertical flux decreases with increasing energy as $E^{-2.55 \pm 0.10}$.

A comparison between the present charged pion (π^\pm) spectrum and the neutron spectrum has been made, it was found that the flux of energy $> 200 \text{ GeV}$ is greater than that of the neutrons of the same energy. The neutron spectrum was extrapolated after 2 TeV with the same slope $E^{-2.97 \pm 0.1}$ up to 10 TeV, this is shown with a dotted line.

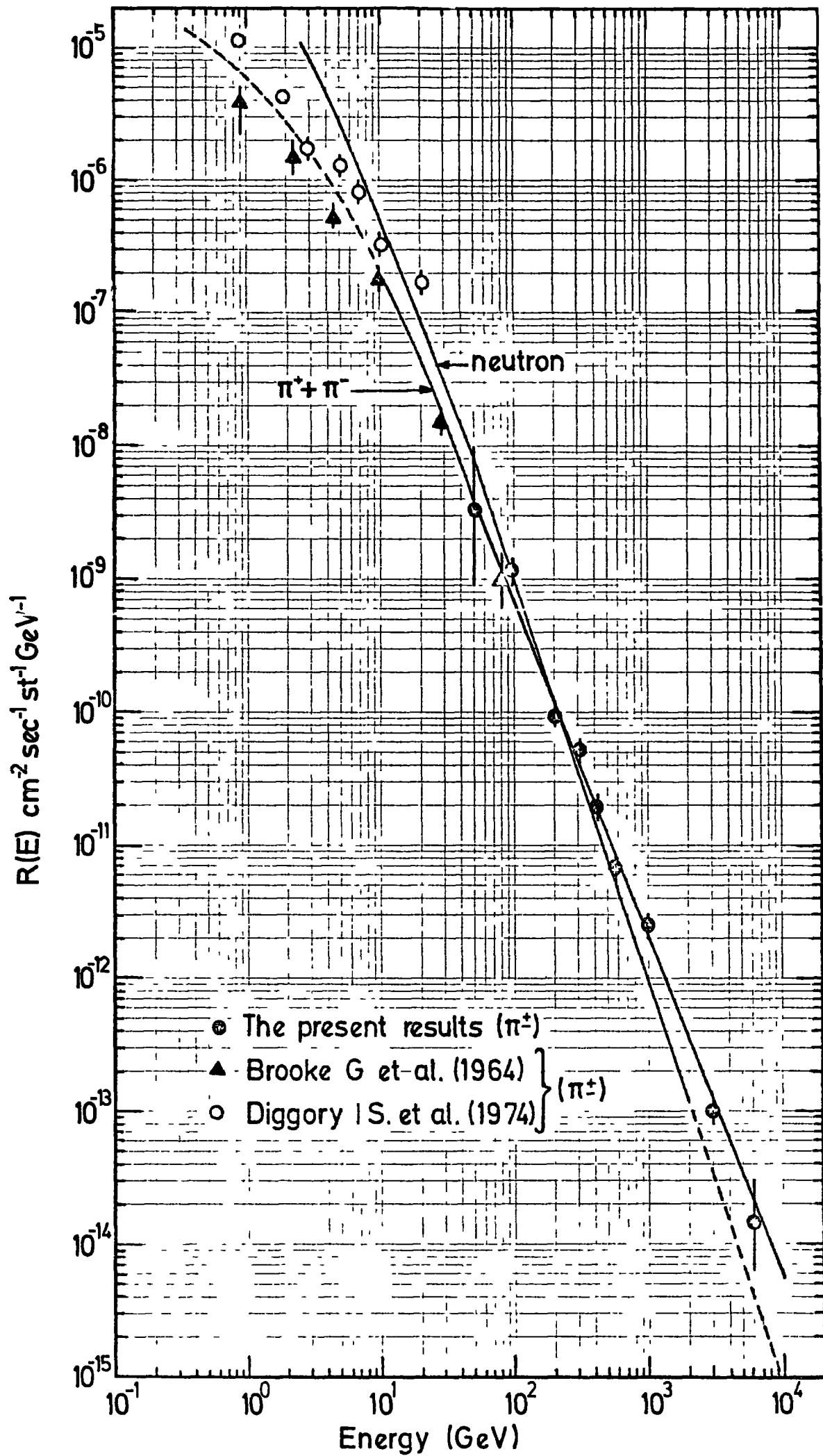
At low energies ($< 100 \text{ GeV}$) a comparison has also been made with the previous pions direct measurement given by Brooke et al. (1964) and Diggory et al. (1974). They obtained measurements of the pion spectrum up to energies of 80 GeV and 20 GeV respectively using magnetic spectrometers in conjunction with neutron monitors (see sections 2.32 and 2.33).

The present measurements are consistent in terms of absolute rate with the measurement of Brooke et al. but not with those of Diggory et al. which are larger by a factor of about 2.

Figure 6.16

The differential energy spectrum of charged pions ($\pi^+ + \pi^-$) in cosmic rays at sea level. The neutron measurements are from the best line through the summary given in figure 6.3.

At low energy (< 100 GeV) the present measurement is consistent in terms of absolute rate with the measurements of Brooke et al. (1964) but not with those of Diggory et al. (1974) which are larger by a factor of about 2. The pion and neutron intensities decrease with increasing energy as $E^{-2.55 \pm 0.1}$ and $E^{-2.97 \pm 0.1}$ respectively.



6.4 Charge to neutral ratio

In this experiment the charge to neutral ratio could be estimated from the measured number of bursts observed in the flash tube chamber by charged and neutral particles interacting in the iron target. Figure 6.17 shows the measured differential burst spectrum of the charged and neutral particles, the best line through the charged and neutral points was drawn and the c/n ratio for two values of energy was given here $c/n = 4.4$ at 100 GeV and $c/n = 9.0$ at 400 GeV. The excess of charged over neutral particles is interpreted usually as the presence of pions, since the ratio of the number of proton to the number of neutrons is close to unity.

Shestoperov (1974) has summarised the experimental data on the ratio of the charge and neutral hadrons with energy $\geq 10^{10}$ eV at mountain altitudes, table 6.1 shows this summary. In the last column he has listed the particles which have been selected to determine the c/n ratio. Some authors used a fraction of the hadrons for their analysis and this is given in the table as a per cent. Other authors selected individual hadrons to obtain the c/n ratio. A recent measurement by Ellsworth et al. (1975) on the charge to neutral ratio of unaccompanied hadrons over 3.3 m^2 and at mountain altitude 730 gm cm^{-2} are shown in table 6.1 also. More charged hadrons than neutral were found as the energy of the particles increases.

So, if the ratio of the number of protons to the number of neutrons at a given depth in the atmosphere is known, then it would be possible to determine the fraction of π^+ in cosmic radiation.

The π^+/p ratio is summarised in table 6.2. Since there are no measurements on the pion spectrum at mountain altitudes or sea level at high energy, the present calculation on the pions from the measured all hadrons shows the following. As the pion energy increases the percentage of

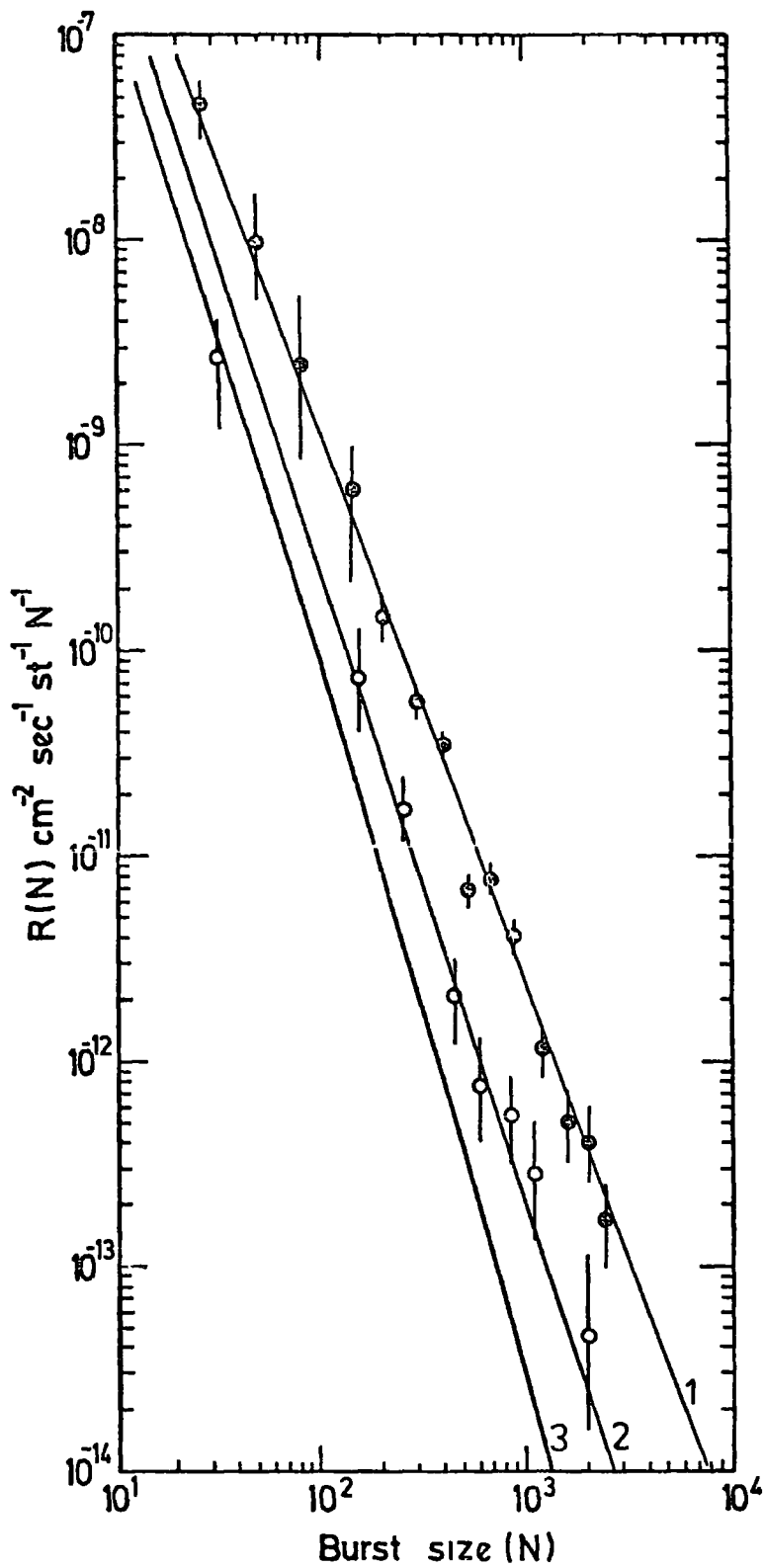


Figure 6.17

A comparison between the differential burst spectra of the charged and neutral particles interacted in iron target, data were taken from the 20 μ s run.

- 1 - measured charge burst spectrum.
- 2 - measured neutral burst spectrum.
- 3 - calculated muon burst spectrum.

Reference	E(Gev)	Depth, X, gm cm ⁻²	c/n	Selection
Lal et al. (1963)	20 - 40	800	1.5 ± 0.2	Single (1 m ²)
Lal et al. (1963)	60	800	2.5 ± 0.8	Single (1 m ²)
Murzin et al. (1967)	350	700	1.8 ± 0.3	~ 50% of flux
Jones et al. (1970)	100 - 500	700	1.5 ± 0.2	Single (7 m ²)
Erofeeva (1971)	100 - 2000	700	2.0 ± 0.3	~ 60% of flux
Hazen et al. (1971)	70 - 800	300	1.9 ± 0.4	Single (1m ²)
Myalkovskil V.M. (1972)	200 - 1000	700	2.2 ± 0.2	~ 60% of flux
Azaryan et al. (1973)	1000	700	1.06 ± 0.09	Single (10 m ²)
Ellsworth et al. (1975)	~ 150	730	2.94 ± 0.6	Single (3.3 m ²)
	~ 350		2.8 ± 0.23	
	~ 700		3.7 ± 0.57	

Table 6.1 Summary on the ratio of charged and neutral hadrons, at mountain altitudes.

pionic component increases. Garraffo et al. (1973) have predicted the pion to proton ratio as a function of energy for three different atmospheric depths and for a fixed pion attenuation length in air $\lambda = 110 \text{ gm cm}^{-2}$. Their prediction for the ratio was found to be considerably higher than the lower energy data.

However, figure 6.18 shows the Garraffo et al. prediction together with the present work on the π^{\pm}/p ratio. A reasonable agreement between the prediction and the calculation was found. In the same figure the ratio was shown for the low energy pion measurement given by Brocke et al. (1964) and Diggory et al. (1974).

6.5 Conclusion

The energy spectrum of neutrons obtained from the measurement of the neutral burst spectrum observed in iron was found to be in good agreement with the previous measurements (Ashton et al., 1970). In the present investigation, it was assumed that there are equal number of protons and neutrons at sea level.

The result obtained on the pion flux at sea level gives a rapid variation in the ratio of pions to protons as the energy of the particles increased. Since no final conclusion has been reached to explain such behaviour, further experimental work is needed in order to confirm the slope of the pion and the nucleon spectra at sea level at high energy.

The present conclusion could be explained as follows: the rapid increase in the ratio could be explained as due to a change in the characteristics of nucleon - air nucleus interactions such that above some energy limit there are more pions produced in the interaction and a larger fraction of the available energy is given to one of the secondary pions.

An alternative explanation is that, the last interaction of the pions

Reference	E (Gev)	π^+ / P	Depth, x , g cm ⁻²
Ial et al. (1963)	20 - 40	0.48 ± 0.11	800
Brooke et al. (1964)	27	0.57 ± 0.11	Sea Level
Brooke et al. (1964)	~ 2	0.15	Sea Level
Khrimyan et al. (1964)	~ 2	0.06 ± 0.02	700
Cowan and Matthews (1971)	330	2.05	Sea Level

Table 6.2 Summary on the ratio of pions to protons at different depths in the atmosphere. After Murzin et al. (1967).

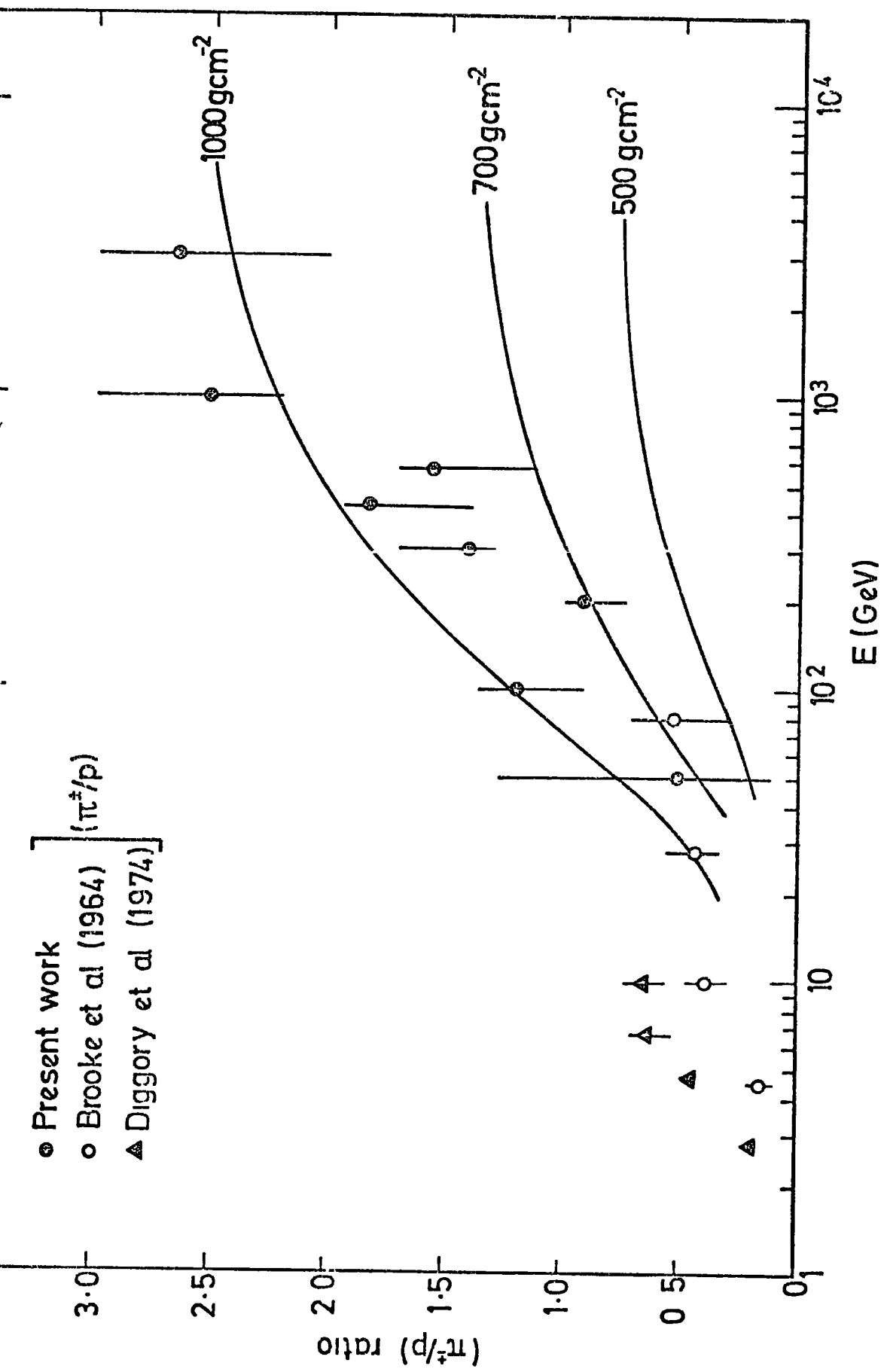


Figure 6.18

Charged pion to proton ratio as a function of particle energy. The sea level measurements are compared with predicted π^+/p ratio for different atmospheric depths (Garraffo et al., 1973).

in the air could be lower on average than that of protons. This gives more chance to the secondary pions to reach ground level.

However, in the low energy regions where the effect of the pion decay becomes important, the π^{\pm}/P ratio decreases rapidly and this has been shown by the results given by other experiments.

CHAPTER 7

QUARK THEORY AND REVIEW ON THE QUARK SEARCHES

7.1 Origin of the concept of quark theory

After the discovery of the π - mesons by Lattes et al. (1947) in nuclear emulsions exposed to cosmic rays at mountain altitudes a large number of particles have been found, and by 1949 the number of particles, so called 'elementary' particles, had grown rapidly. Attempts to understand the known elementary particles in terms of elementary sub-units have been made. Fermi and Yang (1949) discussed the possibility that pions were bound states of nucleon, antinucleon pairs. Subsequently, after the discovery of strange particles it became clear that some sub-unit carrying strangeness was also needed, so the Fermi-Yang suggestion was abandoned.

Sakata (1956) introduced a third symmetry element having spin half, isospin zero, baryon number unity and, in addition, strangeness of minus one. He identified this element with the baryon Λ . Sakata proposed that the sub-units were the triplet of proton, neutron, lambda zero together with their antiparticles. The symmetry underlying the Sakata model is that of $SU(3)$ ($Su(3)$ is the symmetry group which includes isospin and strangeness). The model works rather well in giving qualitative features of the octet and singlet meson multiplets, but it failed to be consistent with the observed octet and decimet multiplets of baryons.

In the Sakata model mesons are formed by particle - antiparticle pairs,

and according to group theory the direct product of triplets forming mesons is: $3 \otimes \bar{3} = 8 \oplus 1$ (where \otimes means direct product, \oplus means direct sum and a bar indicates antiparticle) i.e. singlet and octet states are formed, as had been found experimentally. However, in the case of baryons the theory failed to be consistent with the observed octet and decimet multiplets of baryons when these multiplets of baryons become firmly observed experimentally.

In the Sakata model baryons should be constructed from two particles and an antiparticle to conserve baryon number, and the direct product of triplets forming baryons is: $3 \otimes \bar{3} \otimes 3 = 15 \oplus 6 \oplus 3 \oplus 3$. It was first noticed by Gell-Mann (1964) and Zweig (1964, 1965) that although the Sakata model $3 \otimes \bar{3} \otimes 3$ predicted the wrong multiplet structure for the baryons the alternative reduction $3 \otimes 3 \otimes 3 = 10 \oplus 8 \oplus 8 \oplus 1$ gave the required result. This reduction thus indicated that baryons were composed of 3 sub-units and each sub-unit should carry baryon number $\frac{1}{3}$ so as to be consistent with the law of conservation of baryon number.

Gell-Mann, however, gave the triplet particles the name 'Quarks', and from the Gell-Mann, Nishijima relation given below the charge carried by these hypothetical particles (Quarks) is deduced;

$$Q = T_3 + \frac{B + S}{2} = T_3 + \frac{Y}{2}$$

Where: T_3 is the third component of isospin

B is the baryon number

S is the strangeness

Y is the nypercharge

Q is the electric charge.

The quantum numbers and the basic properties of quarks are given in table 7.1 (To obtain the quantum numbers of antiquarks, reverse all signs in the table). One way of representing quarks is shown in figure 7.1, in this figure the three kinds of quarks p, n, λ each with charge of $1/3$ or $2/3$ can build all known mesons and baryons.

Figure 7.2 shows how mesons can be built up from the quark triplet, and in figure 7.3 the construction of the baryon octet and decuplet states can be seen (all the particles shown in the figures have been established experimentally as given by the Particle Data Group, 1972).

7.2 The predicted properties of free quark

Since the prediction of the quark model and the success which followed it, it is still not clear whether quarks have physical existence or are purely mathematical entities.

However some predicted properties of quarks are: (a) the decay schemes of the quarks (b) the mass of the quark (c) the cross-section for quarks production in nucleon - nucleon collisions (d) the quark - nucleon inelastic cross section and inelasticity.

(a) The decay schemes:

The value of the charge of the three quarks p, n and λ are $+2e/3$, $-e/3$ and $-e/3$. Of these, the $+2e/3$ is expected to be stable while the $-e/3$ components are expected to have lifetimes of the order of seconds and about 10^{-10} second respectively again decay into the stable quark.

According to Adair et al. (1964) the expected decay schemes are shown in table 7.2.

(b) The mass of the quark:

Morpurgo (1967) has obtained a rough estimate of the quark mass assuming mesons are quark - antiquark, states, bound in a square potential

<u>Triplet particle</u>	<u>T₃</u>	<u>B</u>	<u>S</u>	<u>Y</u>	<u>Q</u>	<u>Spin</u>	<u>Mass</u>
p (proton)	1/2	1/3	0	1/3	+2e/3	1/2 ħ	M
n (neutron)	-1/2	1/3	0	1/3	-e/3	1/2 ħ	M
λ (hyperon)	0	1/3	-1	-2/3	-e/3	1/2 ħ	M + 116 MeV.

Table 7.1 The quantum numbers of the three quarks.

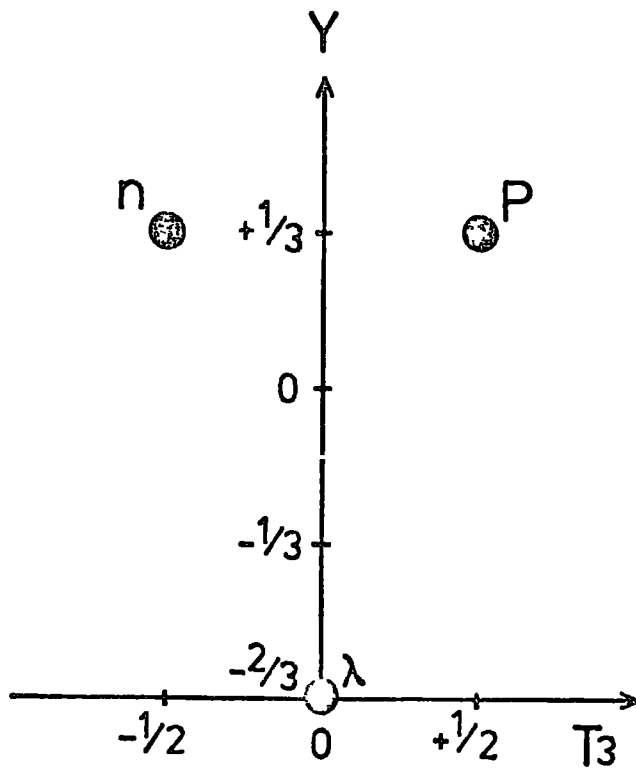


Figure 7.1

The three quarks (p, n and λ) of the quark model.

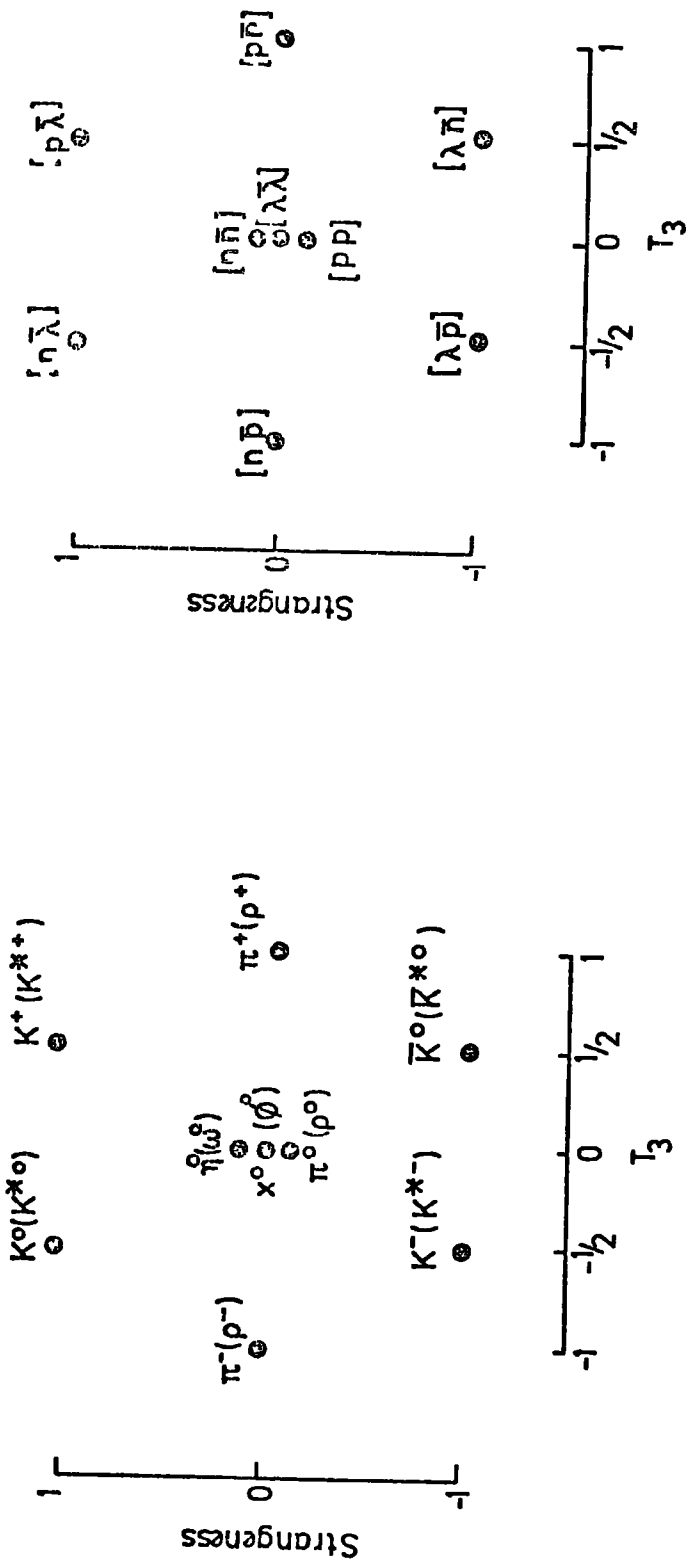


Figure 7.2 The construction of mesons in the quark model.

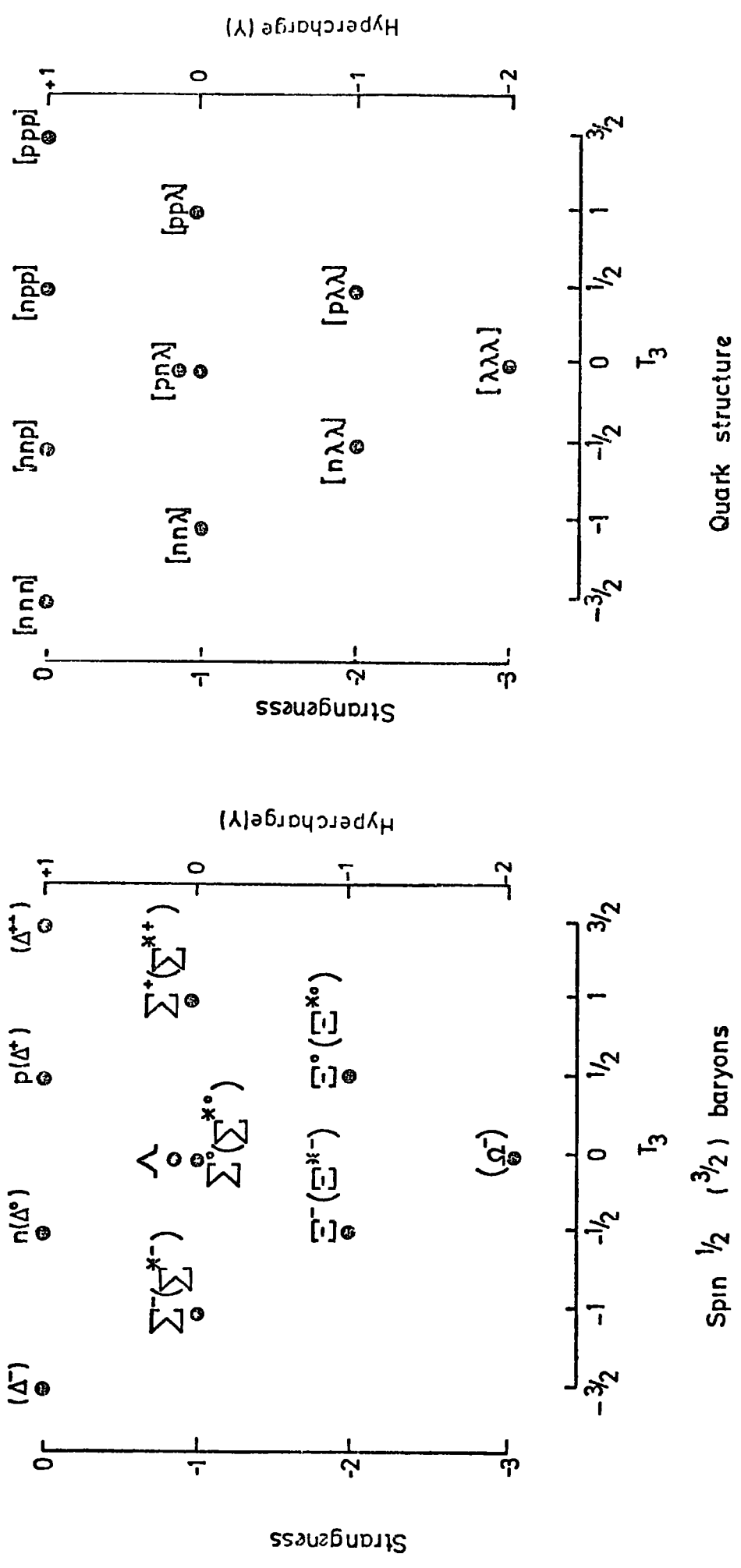


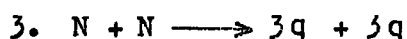
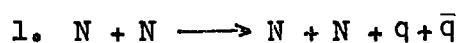
Figure 7.3 The construction of baryons in the quark model.
 Baryons: Octet spin ($1/2$)
 Decuplet spin ($3/2$)

well of radius r . Considering vector mesons with $r = (5 m_\pi)^{-1}$ as providing the binding force between the quark - antiquark pairs ($q \bar{q}$), then the lowest bound state has the mass of the pion.

The value obtained for the quark mass depends on the square of the assumed range of the $q \bar{q}$ potential, and due to the different assumptions the free quark mass has a value in the range $5 \text{ GeV}/c^2$ to several tens of GeV/c^2 .

(c) The cross section of quarks in nucleon - nucleon collision:

If the quarks do exist as free particles, then they can possibly be produced in high energy nucleon-nucleon collisions. The possible production interactions are shown below (Ashton, 1973):



In the first three types of interaction the total kinetic energy of both incident nucleons in the centre of momentum system is available for quark production while in the last two interactions a fraction $\frac{M_\pi}{M_N} = 0.15$ of the total kinetic energy is available for quark production. Figure 7.4 shows the incident nucleon kinetic energy threshold for the above interactions as a function of quark mass (Ashton, 1973).

However, since the quark pair ($q \bar{q}$) are produced in virtual $\pi - \pi$ collision, similar to that in $p \bar{p}$ production, see figure 7.5, the energy threshold of the incident nucleon in the laboratory system for the quark pair to be produced, is $2 \left[\left(\frac{M_q}{M_\pi} \right)^2 - 1 \right] \text{ GeV}$ (Ashton, 1973). So, in order

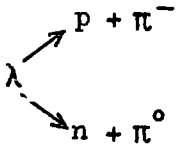
<u>Quark</u>	<u>Decay scheme</u>	<u>Life time</u>
P	Stable	infinite
n	$n \rightarrow p + \bar{e} + \bar{\nu}$	$\sim \text{sec.}$
λ		$\sim 10^{-10} \text{ sec.}$

Table 7.2

Possible decay schemes of quarks.

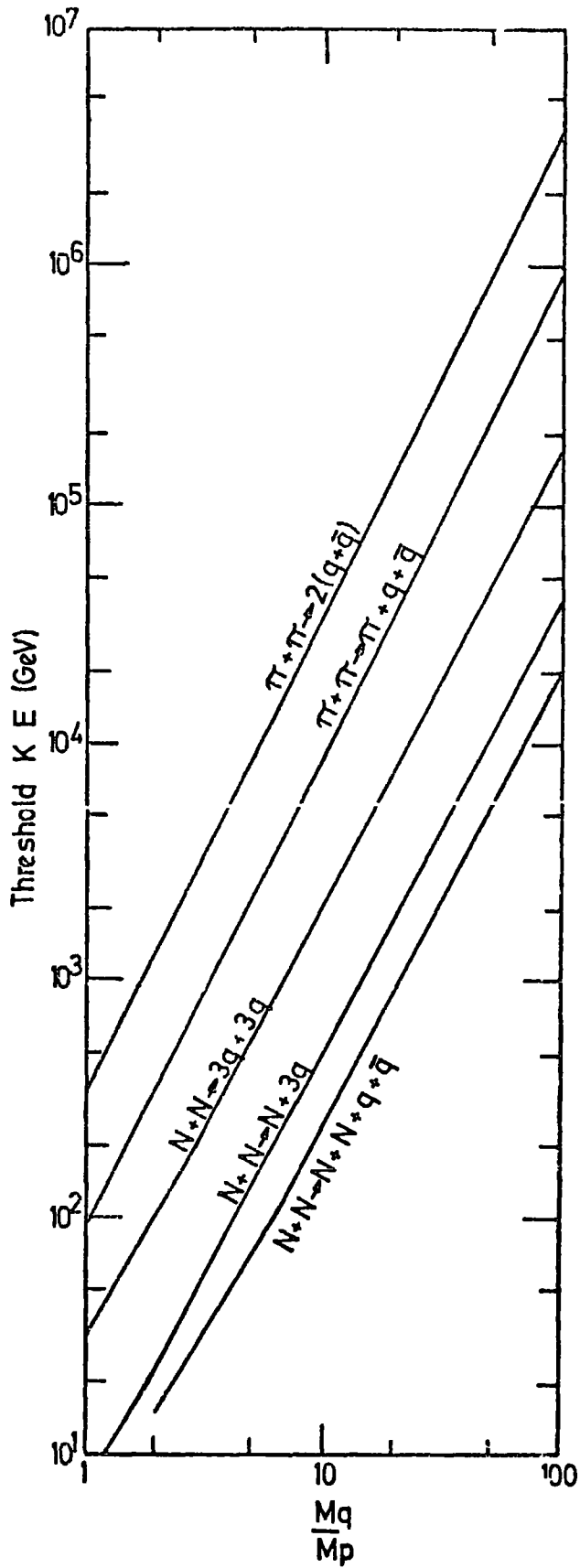


Figure 7.4.

The relation between the quark mass and the threshold kinetic energy for quark production in the nucleon - nucleon collisions. After Ashton, (1973).

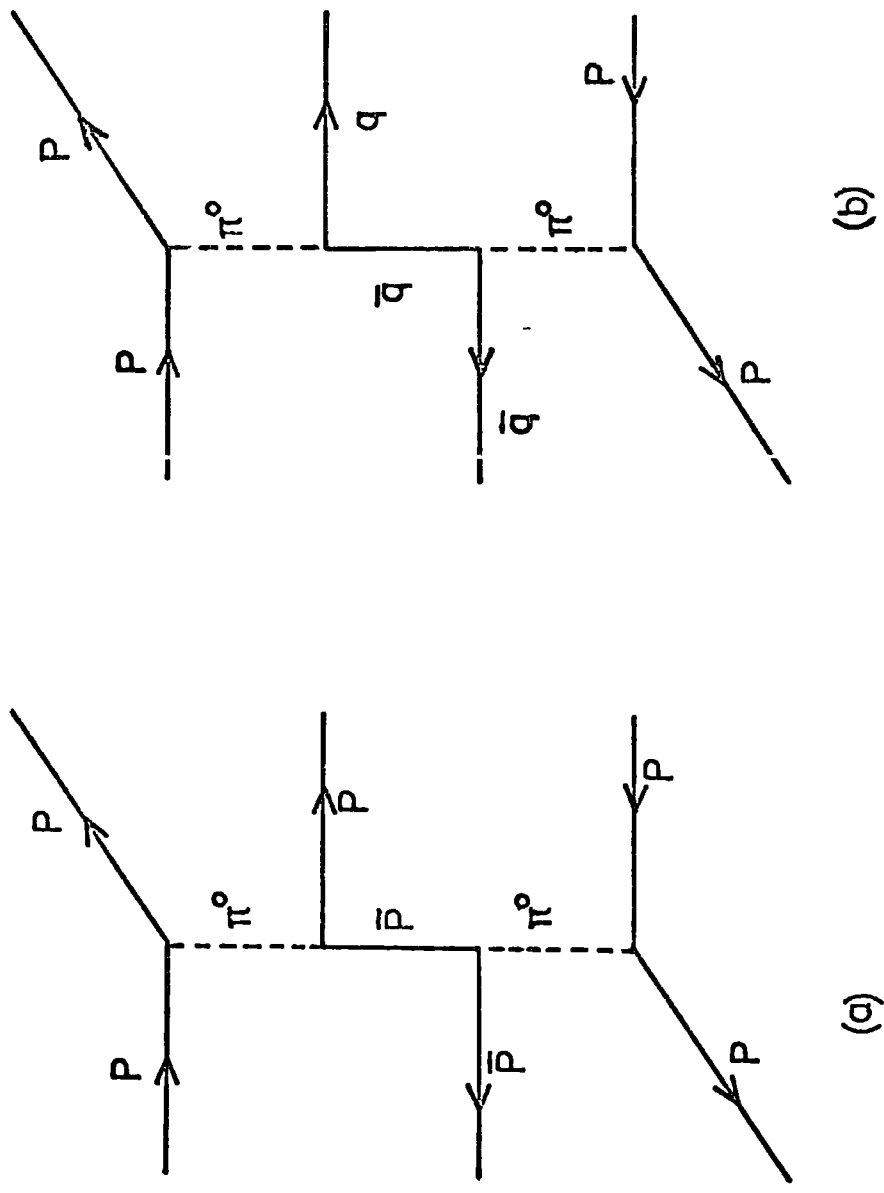


Figure 7.5 (a) Proton - antiproton pair production.
 (b) Quark - antiquark pair production.

to obtain the threshold energy for quark production by way of this mechanism, the mass of the free quark should be estimated.

(d) The quark - nucleon inelastic cross section and inelasticity:

Experimentally it was found that the nucleon - nucleon (NN) inelastic cross section and the pion - proton (πp) inelastic cross section is equal to 33 mb and 22 mb respectively. Since the pion contains two quarks and the nucleon contains three, then the expected ratio of inelastic πp to the inelastic NN cross section is $2/3$. Levin and Frankfurt (1968) have determined the magnitudes of the scattering of a pion on any target and they found it should be two-thirds that of a nucleon on the same target.

However, this agrees with the expected ratio and leads to the conclusion that the quark-nucleon inelastic cross section is ~ 11 mb. From the fact that the measured attenuation length of cosmic ray nucleons in air is larger than their interaction mean free path, it can be shown that on average nucleons lose approximately $30\% = \frac{2 M_{\pi}}{M_N}$ of their energy in nucleon - nucleon collision.

Supposing quarks are surrounded by a mesonic field, the relative energy loss of a quark - nucleon interaction is $\frac{\Delta E}{E} \approx 2 \frac{M_{\pi}}{M_q} \sim 0.3 \frac{M_N}{M_q}$

(Ashton, 1973). It follows from this that the larger the quark mass the more material it is likely to penetrate before being reduced to a non-relativistic velocity.

7.3 Some successes and difficulties arising in the quark model

The simple non relativistic quark model has been used successfully to describe a large variety of phenomena in hadron physics, especially the structure of meson and baryon multiplets. From the quark model the magnetic moments of quarks is found to be proportional to their charges such that

$$\mu_p = \frac{2}{3} \mu_1, \quad \mu_n = -\frac{1}{3} \mu_1, \quad \text{and} \quad \mu_{\lambda} = -\frac{1}{3} \mu_1, \quad (\mu_1 \text{ is unknown}).$$

So, the ratio of the average magnetic moments of neutron (μ_n) to proton (μ_p) is given by $\mu_n/\mu_p = -0.667$. The magnetic moment ratio of neutron to proton measured experimentally is -0.685 , a reasonable agreement between the prediction and experiment.

The quark model makes it possible to derive a large number of relations among the cross sections for strong interactions, for example, the ratio between the inelastic cross sections of πp interaction and pp interaction was predicted to be $2/3$ and this value confirmed by experiments with a satisfactory accuracy. The quark model, however, makes it possible to give a good explanation of a large number of existing experimental data. But, there are still several questions or difficulties which are still unsolved and need to be answered in the quark model, such as whether quarks are real particles which can exist in the free state or whether they are merely of mathematical abstraction. The main difficulty in the quark model is the quarks themselves have not been seen and there is no satisfactory explanation for their failure to be observed. Many explanations can be given, the most popular being that their mass is too high to be within range of all experiments performed to date.

If fractionally charged quarks are the fundamental components from which the hadrons are constructed, then why the fundamental baryons have fractional charge, while the leptons (electron etc) have integral charge. So if the unit of charge is $e/3$ then it is difficult to explain how the electron has unit charge, since the predicted value of magnetic moment of the electron agrees with the experiment under the assumption that the electron is a point particle. However, it has been suggested by Massam and Zichichi (1966) that perhaps the leptons are also constructed from 'leptonic quarks' with fractional charge. This hypothesis that leptonic quarks exist is rather arbitrary in character.

If the quarks are fermions (particles having half integral spin angular momentum), then the following difficulty is coming from the Δ^{++} which consists of three p quarks in the same state. The total wave function of Δ^{++} is symmetric which is not consistent with the Pauli Exclusion Principle state that the total wave function must be antisymmetric for systems of fermions.

It is very important to find out whether, in addition to systems consisting of three quarks (baryon) or quark and antiquark (mesons), whether there is another type of hadron existing having charges $4e/3, 5e/3$ etc.

7.4 Other quark models

Other models have been established to explain the difficulties which have been found with the Gell-Mann-Zweig quark model.

In the first model the idea of coloured quark has been given, in which quarks have different colours, e.g. red, yellow and blue. In this model quarks of different colours have different properties so e.g. 3 p type quarks each with a different colour could bind to form a hadron without violating the Pauli Exclusion Principle.

However, although the simplest interpretation of SU3 symmetry is that the fundamental triplet particles should carry fractional charge it is possible that the basic triplet particles could have integral charge. The concept of integral charged quarks follows the coloured model which was the same as the earlier model proposed by Bacry et al. (1964) and Lee (1965). However, in both models the triplet particles are distinguished by a new

additive quantum number C and the Gell-Mann-Nishijima relation is modified to:

$$Q = T_3 + \frac{Y}{2} + \frac{C}{3}$$

The same modification which has been given above was also required by Bjorken and Glashow (1964). In their theory 'charmed' quarks with this new conserved quantity charm C are different from the basic quark triplet.

Charmed quarks with integral charge are assumed to have a much higher mass than the three basic quarks.

Another model has been proposed by Feynman (1969). In this model Feynman concludes that the nucleons and other hadrons are composed of partons. This model has been used extensively and met some success in deep lepton-hadron inelastic scattering. All of these models, however, have been examined experimentally and each model has its own difficulty.

7.5 Review of quark searches

7.5.1 Introduction

Since Gell-Mann and Zweig predicted the existence of fractionally charged particles, i.e., quarks, in 1964 many experiments using high energy accelerators and cosmic rays have been made to search for these particles using different methods and techniques. In spite of all the efforts, however, these particles have not yet been found in the experiments performed by cosmic rays. Late in 1974, a report from Brookhaven National Laboratory described the observation of a heavy mass particle $M = 3.1 \text{ GeV}/c^2$ and decay width approximately zero. The observation was made from the

reaction $P + Be \longrightarrow e^+ + e^- + X$, where X is anything. In this section the review of the quarks searches at accelerator, in cosmic rays and in different physical branches will be discussed.

7.5.2 Searches at accelerators

In experiments with modern large accelerators, quarks and other fundamental particles could be produced when a target is bombarded by a primary high energy proton beam. So, the searches for the new particles have been carried out in the secondary beams with a given momentum emerging at a definite angle with respect to the direction of motion of the primary protons. The experimental methods have been used to identify these particles were based on determining the charge of the particles or the mass. In the first type the idea of the energy loss was used in determining the charge of the particles. So, for this purpose a scintillation counter or a visible detector like a bubble chamber or steamer chamber have been used to measure the total ionization lost which is a function of the charge z . The second type was to determine the mass of the particles independent of their charge (both integral or fractional charge), the mass was determined by measuring the velocity (at a fixed momentum) by means of Cerenkov counters and by the time of flight. A large number of counters are needed in order to minimise fluctuation effects which could make a charge e particle appear to be fractionally charged. For accelerators using protons as a primary beam the upper limits on the differential cross sections for quark production obtained from these experiments are given in table 7.3.

In all cases the quark - antiquark produced, and the limit refer to the reactions:



As shown in table 7.3 the quarks have not been seen in any of these

experiments.

In the reaction $P + Be \longrightarrow e^+ + e^- + X$, Lubert et al. (1974) have observed a sharp enhancement at $M(e^+e^-) = 3.1 \text{ GeV}/c^2$. The experiment used Cerenkov counters and proportional chambers and was performed at the Brookhaven 30 GeV alternating gradient synchrotron. Figure 7.6 shows the mass spectrum of the new particle at mass $3.1 \text{ GeV}/c^2$.

At the same time a group at the Stanford Linear Accelerator Center (SLAC) observed a sharp peak around $3.1 \text{ GeV}/c^2$ in colliding beam processes $e^+ + e^- \longrightarrow \text{hadrons}$ or $\mu^+ + \mu^-$ or $e^+ + e^-$. The same group have found another particle in the process $e^+ + e^- \longrightarrow \text{hadrons}$. The second particle is quoted to have a mass $3.7 \text{ GeV}/c^2$.

With this discovery, a new kind of quark, the C quark, is postulated to have charge $+2e/3$, strangeness 0, charm + 1 where the P, n, λ quarks all have charm 0 (Jacob, 1975).

7.5.3 Search in cosmic rays

At very high energies, cosmic ray particles interacting in the atmosphere could produce quarks or fundamental particles with masses greater than what is possible with existing accelerators. However, a large number of experiments with different experimental techniques have been performed to search for quarks in cosmic rays at sea level, mountain altitude and underground since the idea of the quark introduced by Gell-Mann (1964).

Quarks searches in cosmic rays have been classified as follows:

- (a) Search for relativistic quarks in unaccompanied cosmic rays.
- (b) Search for non-relativistic heavy mass particles.
- (c) Search for quarks in EAS.
- (d) Delayed particles in EAS.

Reference and method of detection	Target	Proton energy (GeV)	Quark momentum GeV/c	$d^2 \delta_Q / dP d\Omega$	
				$1Q1 = 1/3$ $cm^2/GeV st$	$1Q1 = 2/3$ $cm^2/GeV st$
Hagopian et al.(1964) 'Bubble chamber'	W	31	2.83 5.7	$nQ/n_{\pi} \leq 4 \cdot 10^{-6}$	$nQ/n_{\pi} \leq 8 \cdot 10^{-6}$
Blum et al. (1964) 'Bubble chamber'	CU	27.5	6.7 13.4	$2.2 \cdot 10^{-36}$	$\sim 1.110^{-35}$
Bingham et al.(1964) 'Bubble chamber'	CU	21	5.3 10.6	$10^{-35} - 10^{-36}$	$(2-5)10^{-36}$
Antipov et al.(1969) 'scintillation counter'	Al	70	16.7 33.3 26.7 53.3	$1.4 \cdot 10^{-35}$ $7.1 \cdot 10^{-38}$	7.710^{-36} $4.1 \cdot 10^{-38}$
Allaby et al. (1969) 'scintillation counter'	Be	27	10.9 14.7	$7.2 \cdot 10^{-39}$	$5.2 \cdot 10^{-38}$
Leipuner et al. (1973) 'scintillation counter'	Be	300		$1.0 \cdot 10^{-35}$	$1.0 \cdot 10^{-35}$
Nash et al. (1974) 'scintillation counter'	Be	200 300	150 270	$8.0 \cdot 10^{-35}$ $5.1 \cdot 10^{-34}$	$4.0 \cdot 10^{-35}$ $2.5 \cdot 10^{-34}$

Table 7.3

The upper limits with 90% confidence level on the differential cross sections for quark production with proton accelerators.

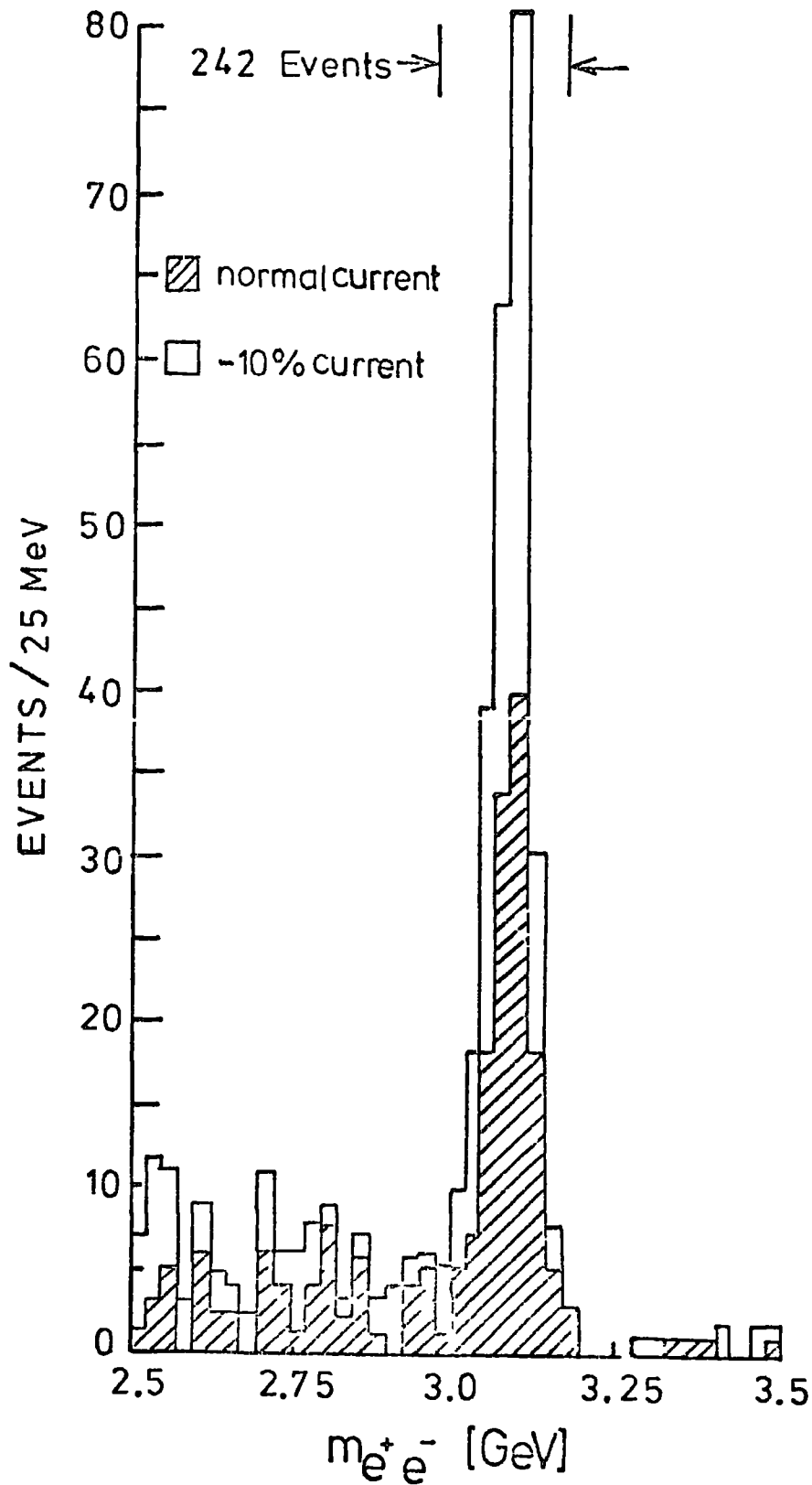


Figure 7.6

Mass spectrum showing the existence of the new particle 'Charm' with a mass $3.1 \text{ GeV}/c^2$. The results from the two spectrometer settings were plotted showing that the peak is independent of spectrometer currents. After Aubert et al. (1974).

(a) Search for relativistic quarks in unaccompanied cosmic rays:-

Search for single (without shower accompaniment, ≤ 1 particle m^{-2}) fractionally charged particles in cosmic rays have been made in most experiments, which are rather similar in their technique. In all these experiments measurements of the ionization of the particles passing through scintillation or proportional counters were made in order to distinguish quarks. Since the ionization loss of particles with charge Ze is proportional to $Z^2 e^2 / \beta^2$, $\beta = 1$ for relativistic particles. If K represents the amount of ionization produced by a charge e particle, then for fractionally charged particle the amount of ionization is proportional to $0.11 K$ and $0.44 K$ for quarks with charge $e/3$ and $2e/3$ respectively. Ashton et al. (1968b) used 6 scintillation counters to search for $e/3$ and $2e/3$ in conjunction with flash tubes as visual detectors. They demanded a coincidence between all 6 counters when the amount of ionization in range $0.05 K - 0.30 K$ and in range $0.3 K - 0.85 K$ for $e/3$ and $2e/3$ respectively.

The limit obtained on the quark flux is shown in table 7.4. Most experiments have used scintillation counters, spark chambers or proportional chambers. The limit given by all these experiments shows a value less than $10^{-10} \text{ cm}^{-2} \text{ sec}^{-1} \text{ st}^{-1}$ and no quark has been found. The lowest limits for the quark flux so far are:

<u>Charge</u>	<u>Limit</u>	<u>Reference</u>
$e/3$	$< 0.57 \cdot 10^{-10} \text{ cm}^{-2} \text{ sec}^{-1} \text{ st}^{-1}$	Chin et al. (1971)
$2e/3$	$< 0.5 \cdot 10^{-10} \text{ cm}^{-2} \text{ sec}^{-1} \text{ st}^{-1}$	Krisor (1975)

(b) Search for non-relativistic heavy mass particles:-

Searches for heavy mass particle have been made in cosmic rays

Reference	Depth in gm/cm ²	Flux limit in units of 10 ⁻¹⁰ cm ⁻² sec ⁻¹ st ⁻¹	
		e/3	2e/3
Grigorov et al. (1970)	Satellite	< 20	< 200
Cox et al. (1971)	2,750 metres	< 0.83	< 0.96
Chin et al. (1971)	2,750 metres	< 0.57	-
Buhler-Broglin et al. (1967)	450 metres	< 4.5	< 1.7
Gomez et al. (1967)	Sea Level	< 1.7	< 3.4
Ashton et al. (1968b)	Sea Level	< 1.15	< 0.8
Kasha et al. (1968)	Sea Level	-	< 2.7
Garmire et al. (1968)	Sea Level	< 0.66	< 0.88
Faissner et al. (1970)	Sea Level	< 1.9	-
Chin et al. (1971)	Sea Level	< 1.3	-
Crouch et al. (1971)	Sea Level	-	< 2.6
Krisor (1975)	Sea Level	< 0.7	< 0.5
Barton (1967)	60 m.w.e. underground	-	< 1.4
Barton et al. (1966)	2,200 m.w.e. underground	-	< 1.4

Table 7.4 Summary of the upper limits on the flux of unaccompanied (≤ 1 particle m⁻²) relativistic e/3 and 2e/3 charge quarks at different depths in the atmosphere.

independent of the charge of the particles. The experiments were constructed to measure the time of flight and range of particles. Franzini et al. (1968) operated this type of detector at sea level and at a large zenith angle of 84° . No events were found and the upper flux limit was $\leq 5 \cdot 10^{-8} \text{ cm}^{-2} \text{ sec}^{-1} \text{ st}^{-1}$. A similar experiment at large zenith angle (75°) has been made by Kasha and Stefanski (1968). This experiment used a magnet for determination of the particle momentum. No positive result was found and the upper limit to the flux was quoted as $< 2.4 \cdot 10^{-8} \text{ cm}^{-2} \text{ sec}^{-1} \text{ st}^{-1}$. Ashton et al. (1969) used a telescope containing six scintillation counters of 1 m^2 area and two water Cerenkov selectors at sea level. They used a velocity/range technique, and found an upper limit to the flux of $< 4.9 \cdot 10^{-10} \text{ cm}^{-2} \text{ sec}^{-1} \text{ st}^{-1}$.

Galper et al. (1970) experimented under 80 cms concrete at sea level, and obtained an upper limit of $< 3.4 \cdot 10^{-8} \text{ cm}^{-2} \text{ sec}^{-1} \text{ st}^{-1}$.

More recently a search for heavy long lived particles has been made by Yock (1974). The telescope used was designed basically to be sensitive to slow particles with high mass. The telescope was constructed from scintillation counters and spark chambers and was situated under 600 gm/cm^2 concrete. The result obtained can be summarised as follows: the flux of singly charged particles having mass $\geq 6M_p$ is $\leq 6 \cdot 10^{-9} \text{ cm}^{-2} \text{ sec}^{-1} \text{ st}^{-1}$.

(c) Search for quark accompanied by EAS:-

Since primary cosmic rays with energy $\sim 10^{14} \text{ eV}$ can produce extensive air shower (EAS) as a result of their interaction with air nuclei, then it is possible that quarks exist in EAS as secondary particles.

Extensive searches have been made in EAS to look for quarks near the core using different techniques. Most of the experiments searching for quarks in EAS used visual detectors, like cloud chambers. A summary of the flux limit for quarks in EAS obtained by different groups is shown in

Reference and Technique	Electron density threshold (Δe)	Flux in units of $10^{-10} \text{ cm}^{-2} \text{ sec}^{-1} \text{ st}^{-1}$	
		$e/3$	$2e/3$
Cairns et al. (1969) 'cloud chamber'	$> 154 \text{ m}^{-2}$	-	~ 5
Hazen (1971) 'cloud chamber'	$\geq 150 \text{ m}^{-2}$	< 1	< 1
Clark et al. (1971) 'cloud chamber'	$> 86 \text{ m}^{-2}$	< 3	< 0.3
Ashton et al. (1971c) 'Flash tube chamber'	$> 40 \text{ m}^{-2}$	< 0.3	-
Evans et al. (1971/1972) 'High pressure cloud chamber'	$> 60 \text{ m}^{-2}$	< 40	-
Hazen et al. (1973) 'cloud chamber'	$> 80 \text{ m}^{-2}$	< 0.4	-
Ashton et al. (1973 a,b) 'Flash tube chamber'	> 40 > 160	< 0.8 < 0.55	-
Hazen et al. (1975) 'cloud chamber'	not given	< 0.12	-

Table 7.5

Summary of the flux limits for quarks in extensive air showers. Δe is the minimum electron density used as a master trigger.

table 7.5.

Only the Sydney group has reported a positive result, and five events were classified as quarks. The claim of the Sydney group that the observed events were genuine quarks was criticised by a number of groups (Adair and Kasha 1969, Rahm and Sternheimer 1969, Wilson 1970, Kiraly and Wolfendale 1970, Rahm and Louttit 1970, Frauenfelder et al. 1970). The main point of the criticism was that the Sydney group do not adequately demonstrate that the five events (quark candidates) were well separated in ionization density from the distribution due to plateau or minimum ionizing charge e particles.

However, there is no strong evidence up to now that show that quarks exist, and all the experiments searching for the fractional charged quarks give negative results - see table 7.5.

The flash tube chamber used by Ashton et al. (1971c, 1973a) was one of the powerful techniques to search for ($e/3$) quarks in EAS. The result of this search will be discussed in the next chapter.

(d) Delayed particles in EAS:-

If quarks are massive particles and produced in high energy interactions of primary protons with air nuclei, then they will be delayed behind the shower front. Consider a detector situated at a distance H from the point of interaction in which quarks and other secondary particles are produced. If the quarks are delayed the time Δt between the arrival of the shower front and the arrival of the quark produced at a height H is

$$\Delta t = \frac{H}{\beta_q c} - \frac{H}{c} \approx \frac{H}{c} \cdot \frac{1}{2 \gamma_q^2}$$

where $\gamma_q = \frac{1}{\sqrt{1 - \beta_q^2}}$

If the quarks are produced at rest in the c.m.s. then their Lorentz factor in the laboratory system is given by $\gamma_q = \gamma_c$, where $\gamma_c = \frac{7 M_q}{M_N}$.

Taking $H = 16.8$ Km above sea level, the value of Δt is

$$\Delta t = \frac{570}{M_q^2} \text{ nano second.}$$

A positive result from some experiments claimed at least they have found one event in which it could be a quark, the limits quoted by each experiment have been summarized in table 7.6.

Only Dardo et al. (1972) working at 70 m.w.e. underground and Tonwar et al. (1971) working at 2,150 metres above sea level have claimed a definite signal at flux levels of 10^{-8} and $10^{-9} \text{ cm}^{-2} \text{ sec}^{-1} \text{ st}^{-1}$ respectively.

7.5.4 Other quark searches

The search for quarks has involved not only particle physics but also some other fields in physics, e.g. cosmology, astrophysics, geophysics, spectroscopy, chemistry and biology.

Astronomical methods have been used in order to study the emission line spectrum from the solar chromosphere, where C, N, O are the most abundant elements next to H and He.

Sinanoglu et al. (1966) have predicted a number of transition wavelengths from C, N and O in various states of ionization. They claim to have identified three lines in the emission spectrum of C and N due to $^{-e}/3$ quark bound to the nucleus. It has been shown later by Bennett (1966) that the lines are most likely due to weak dipole transitions of normal atoms.

Searches for quarks have been made also in stable matter, and recent experimental searches for quarks stopped in terrestrial matter are reviewed and summarized by Kim (1973). The summary given by Kim is shown in table 7.7.

According to Cook et al. (1969), a quark concentration of the order of $10^{-20} - 10^{-23}$ quark/nucleon in sea water corresponds to an unchanging sea level intensity over the last $5 \cdot 10^9$ years of about $10^{-9} \text{ cm}^{-2} \text{ sec}^{-1} \text{ st}^{-1}$. This assumes that a quark mass of the order of $5 \text{ GeV}/c^2$.

Reference	Depth in gm/cm^2	Flux limit in units of $10^{-10} \text{ cm}^{-2} \text{ sec}^{-1} \text{ st}^{-1}$
Jones et al. (1967)	3,230 metres above sea level	< 1
Bjornboe et al. (1968)	16 to 36 m.w.e. underground	< 3
White et al. (1970)	Sea level	< 4
Dardo et al. (1972)	70 m.w.e. underground	~ 100
Tonwar et al. (1971)	2,150 metres above sea level	~ 10
Briatore et al. (1973)	40 m.w.e. underground	~ 20
Briatore et al. (1975)	40 m.w.e. underground	~ 12.5

Table 7.6

Summary of the flux of heavy mass delayed particles in extensive air showers.

Reference	Technique	Sample	Concentration limit (quarks/nucleon)
Chukpa et al. (1966)	Surface evaporation	Air	$< 5 \cdot 10^{-27}$
		Sea water	$< 3 \cdot 10^{-29}$
		Meteorite	$< 1 \cdot 10^{-16}$
Stover et al. (1967)	Magnetic levitation	Iron	$< 4 \cdot 10^{-19}$
Rank (1968)	Oil drop ultraviolet spectroscopy	Sea water	$< 1 \cdot 10^{-18}$
		oysters and plankton	$< 1 \cdot 10^{-17}$
Braginski et al. (1968)	Magnetic levitation	Graphite	$< 1 \cdot 10^{-17}$
Cook et al. (1969)	Surface evaporation	Air	$< 1 \cdot 10^{-24}$
		Rock	$< 1 \cdot 10^{-23}$
Johnson (1969)	Magnetic levitation	Niobium	$< 1 \cdot 10^{-19}$
Morpurgo et al. (1970)	Magnetic levitation	Graphite	$< 2 \cdot 10^{-18}$
Hebard et al. (1970)	Magnetic levitation	Niobium	$< 2 \cdot 10^{-20}$

Table 7.7

Summary of the experimental limits on the concentration of quarks in stable matter.

CHAPTER 8

SEARCH FOR $e/3$ QUARKS IN EXTENSIVE AIR SHOWERS

8.1 Introduction

A search for quarks in the cosmic radiation has been conducted at Durham since 1966. The experiments already completed (Ashton et al. 1968b, Ashton et al. 1969a and Ashton and King 1971) gave a negative result and the limits given by these experiments refer to quarks arriving at sea level with an accompaniment of ≤ 1 particle/m².

Since 1969 attention was turned to a search for quarks in extensive air showers (EAS) as a result of the work of McCusker and Cairns (1969) and Cairns et al. (1969) who presented evidence for the existence of quarks with $2e/3$ charge.

A flash tube chamber was constructed as a visual detector using a neon tube, Ashton et al. (1971c) to search for the fractionally charged particles in EAS. Later, the chamber was reconstructed by increasing the sensitive volume and also it was found that it is important to use the defining layers of flash tubes at the top and bottom of the chamber in order to eliminate the edge effect in which a particle with a charge e could simulate quarks. The details about the construction of the chamber and the characteristics of the neon flash tubes have been given in chapter 4.

From the measurement of the efficiency - time delay (see section 4.2.4) it was found that the flash tube chamber is sensitive to particles of charge $e/3$ but not to charge $2e/3$, since these can not be resolved from the distribution of charge e particles.

The 20 μ s time delay T_D (the time between the passage of the particle through the chamber and the application of the high voltage) was chosen to

operate the chamber, because it gave a wide separation between the distribution of the number of flashes on a track for e and $e/3$ particle respectively, so this time delay is considered to be optimum time, see figure 4.8.

Briefly, the aim of the present technique was to look for a track produced by the passage of a fractionally charged $e/3$ particle in which it has significantly fewer flashes along its track than a charge e particle.

The chamber has been operated to look for these particles in regions of EAS of local electron density $\geq \Delta e \text{ m}^{-2}$, the electron density being selected by three liquid scintillators.

The first search for $e/3$ quarks was made in EAS using a local electron density $\geq 40 \text{ m}^{-2}$ (Ashton et al. 1973a). The result shows that with a running time of 2,750 hours, 20 tracks were observed which resembled $e/3$ quarks. All but 2 of them were explicable in terms of background muons traversing the chamber in the 103 - 144 μs period before the application of the high voltage pulse to the chamber. The details and the scale diagrams of these 20 tracks (quark candidates) have been given by Saleh (1973). To eliminate the background effect it was suggested that the sensitive area of the chamber must be covered with plastic scintillators, but as the chamber was new and it was apparent from the photographs obtained that many other aspect of EAS could be studied with it, for example, the energy spectra of charged and neutral hadrons in EAS (this will be discussed in the next chapter), muon groups etc. it was decided that rather than to dismantle the chamber and redesign it to overcome the effect of the background muons, the chamber should be carried on running to obtain more data using higher local electron densities. It was hoped that higher shower energies (i.e. higher electron densities selected) may increase the number of genuine events to the number of background events simulating quarks. Subsequent work using local electron density $\Delta e \geq 160 \text{ m}^{-2}$

has been made, no positive events having been observed, Ashton et al. (1973b).

The present measurements are a continuation of this work and the search for $e/3$ quarks has been made near the core of EAS using a local electron density $\Delta e \geq 500 \text{ m}^{-2}$.

8.2 Distribution of the core distance and shower size of EAS given by a local electron density trigger

Parvaresh (1975) has performed a calculation to determine the mean shower size and the mean core distance of showers selected by the detector. The calculations were carried out numerically taking the sea level number spectrum given by Hillas (1970) and the lateral structure function for electrons and muons at sea level given by Greison (1960). Namely, for electrons:

$$f(N_e, r) = \frac{0.4 N_e}{r_1^2} \left(\frac{r}{r_1} \right)^{0.75} \left(\frac{r_1}{r + r_1} \right)^{3.25} \left(1 + \frac{r}{11.4 r_1} \right) \text{ m}^{-2}$$

where r_1 is the cascade length in air (= 79 metres), and for muons:

$$g(N_e, r) = 18 \left(\frac{N_e}{10^6} \right)^{0.75} r^{-0.75} \left(1 + \frac{r}{320} \right)^{-2.5} \text{ m}^{-2}$$

Where N_e is the electron shower size and r is the radial distance from the core in metres.

The rate of triggers with local electron density $\geq \Delta e \text{ m}^{-2}$ and considering the muon density $\Delta \mu \geq 0 \text{ m}^{-2}$ is given by:

$$R(>r, \geq \Delta e) = \int_r^{r_{\max}} 2\pi r R \left[\geq N_e = \frac{\Delta e}{f(r)} \right] dr \quad \text{sec}^{-1}$$

$$R(>N_e, \geq \Delta e) = \int_{r_{\min}}^{r_{\max}} 2\pi r R \left[\geq N_e = \frac{\Delta e}{f(r)} \right] dr \quad \text{sec}^{-1}$$

where $R(> r, \geq \Delta_e)$ is the rate of triggers produced by showers falling at the distance $> r$ from the core and $R(> Ne, \geq \Delta_e)$ is the rate of triggers produced by showers of size $> Ne$.

where $Ne = \frac{\Delta_e}{f(r)}$, $f(r)$ is the lateral structure function for electrons given by Greisen.

The above integral was evaluated numerically for different values of Δ_e , and for each value of Δ_e the muon density was considered to be $\Delta\mu \geq C \text{ m}^{-2}$.

However, for the present information the calculation on the rate of the EAS as a function of shower size and core distance producing a local electron density $\Delta_e \text{ m}^{-2}$ have been shown in figures 8.1 and 8.2.

From these figures it can be seen that the shower size selected by the trigger $\geq 500 \text{ m}^{-2}$ is $\sim 1.3 \cdot 10^6$ and the core distance is ~ 5.5 metres.

Table 8.1 shows the characteristics of EAS selected by a local density detector (see figures 8.1 and 8.2).

8.3 The EAS experiment

8.3.1 Calibration of the chamber

The response of the flash tube chamber to single particles (muons) has been measured using the coincidence between the two plastic scintillators A and B. (see figures 4.1 and 4.6).

The $20 \mu\text{s}$ time delay was used to measure the efficiency distribution of the number of tubes along the track using the same method which has been described in section 4.2.4.

1,046 single tracks were obtained and their photographs were scanned. The distribution of the number of flashes in F2 + F3 was shown in figure 8.3, no low efficiency track was found (if any) in the region of $e/3$ quarks. The mean number of flashed tubes along the track of a single particle (muon) passing through the chamber is $74 \pm .14$ with standard deviation of distribu-

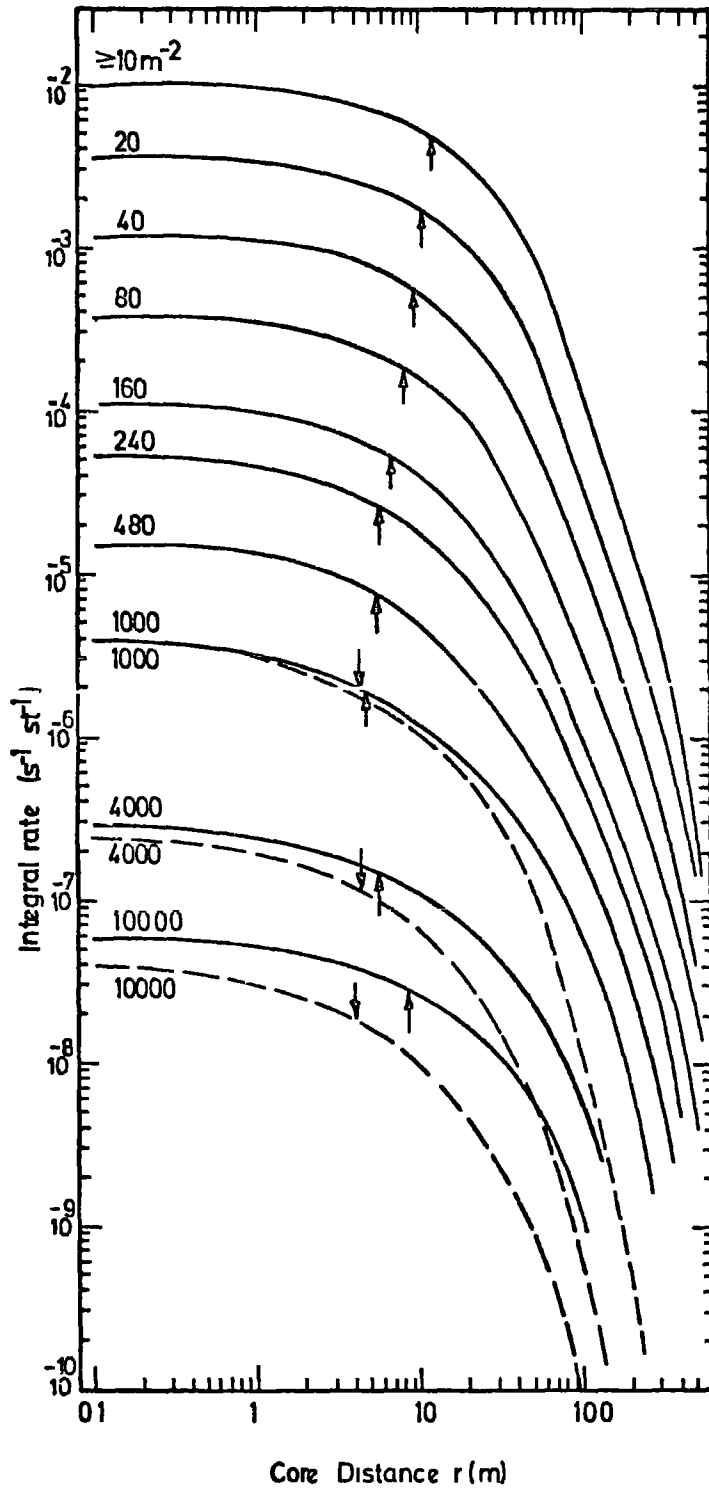


Figure 8.1

The predicted rate of EAS which produce a local electron density trigger $> \Delta e m^{-2}$, as indicated on each curve, whose core falls at distance $> r$ metres from the detector. Median core distances are shown by arrows. After Parvaresh, (1975).

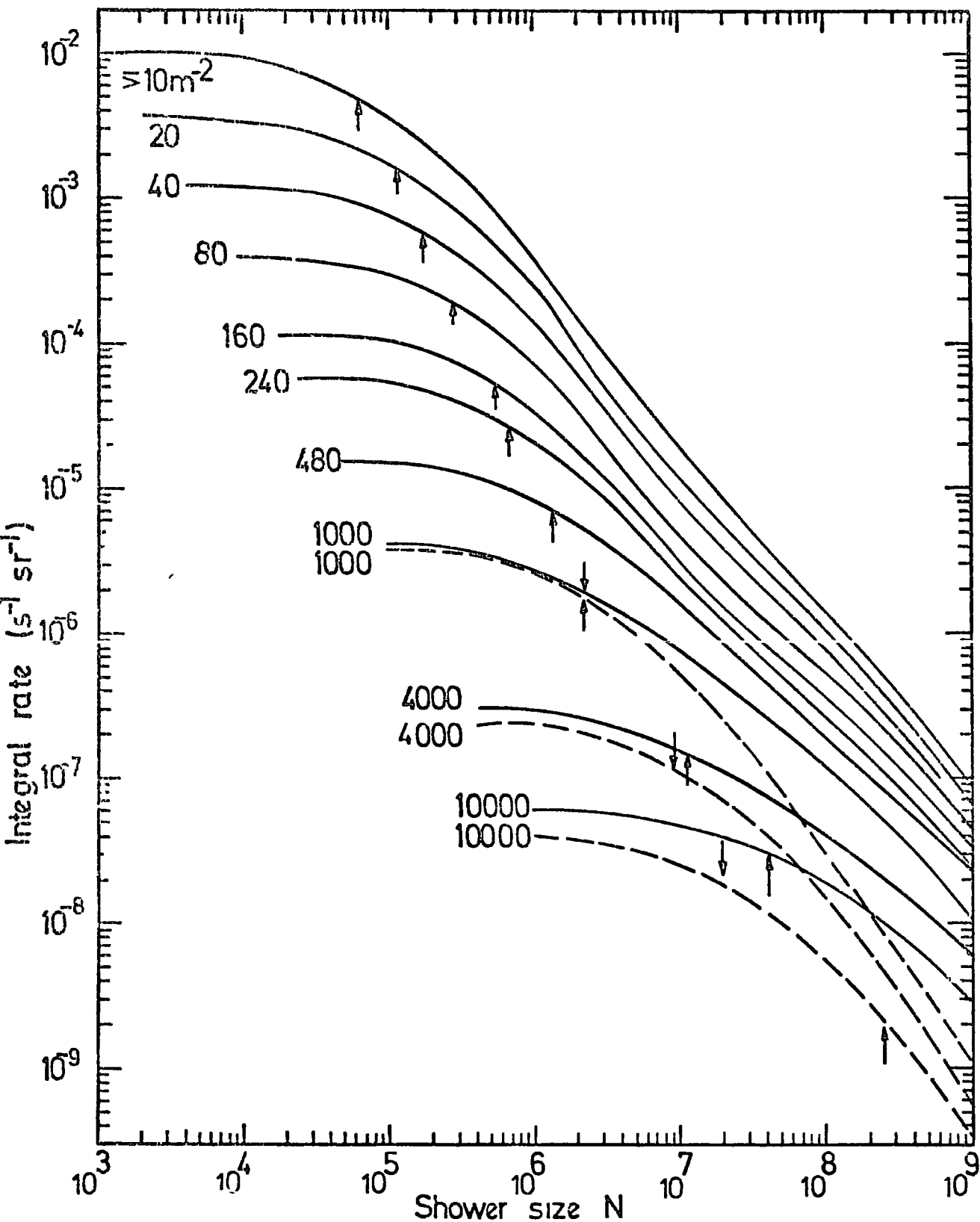


Figure 8.2.

The predicted rate of EAS of size $> N_e$ producing a local electron density trigger $\Delta e m^{-2}$ as indicated on each curve. Median shower sizes are shown by arrows. After Parvaresh, (1975).

<u>Electron density</u> <u>$\geq \Delta e \text{ m}^{-2}$</u>	<u>Minimum</u> <u>shower</u> <u>size</u>	<u>Median</u> <u>shower</u> <u>size</u>	<u>Median</u> <u>core distance</u> <u>(metres)</u>
≈ 10	$1.1 \cdot 10^3$	$6.0 \cdot 10^4$	12
≈ 20	$2.1 \cdot 10^3$	$1.2 \cdot 10^5$	10.5
≈ 40	$4.3 \cdot 10^3$	$1.8 \cdot 10^5$	9.5
≈ 80	$8.6 \cdot 10^3$	$2.7 \cdot 10^5$	8.0
≈ 160	$1.7 \cdot 10^4$	$5.01 \cdot 10^5$	6.5
≈ 240	$2.3 \cdot 10^4$	$6.5 \cdot 10^5$	5.8
≈ 480	$5.1 \cdot 10^4$	$1.3 \cdot 10^5$	5.5
$\approx 1,000$	$1.0 \cdot 10^5$	$2.3 \cdot 10^6$	4.5

Table 8.1

Characteristics of extensive air showers selected by a local electron density detector (Parvaresh, 1975).

tion of $\sigma = 4.6$.

8.3.2 Setting up the trigger

Figure 8.4 shows the block diagram of the extensive air shower (EAS) trigger system. Three liquid scintillation counters North, Middle and South (each of area 1.24 m^2) placed close to each other on top of the chamber (see figure 4.1) were used to select the EAS trigger by a coincidence between the scintillators. The single particle pulse height for each scintillator was measured using a small geiger telescope, and for all the running time the discrimination level on each scintillator was set so as to accept a minimum of about 620 particles through it (i.e. about $500 \text{ particles/m}^2$ in each scintillator) and the average rate of coincidences was 4 per day.

8.3.3 Running the experiment

With this master trigger $\geq 500 \text{ m}^{-2}$, the chamber was operated in this mode from March 1973 to January 1974 for a total running time of 7,009 hours. The whole of the run was recorded on a series of films called 'G- series' and the number of films taken in this series are 21.

The procedure of scanning the films and the basic data will be discussed in the next section.

8.4 Analysis of the data

8.4.1 The procedure of the analysis

In 7,009 hours, only 1,217 air shower triggers were recorded with the electron density threshold set at $\Delta a \geq 500 \text{ m}^{-2}$. The events were recorded on films taken by a front camera. The analysis procedure for individual events was achieved by projection of the negative obtained onto a scanning table, where each event could be examined in detail. The events were projected on a scale diagram showing the front view of the chamber, scale

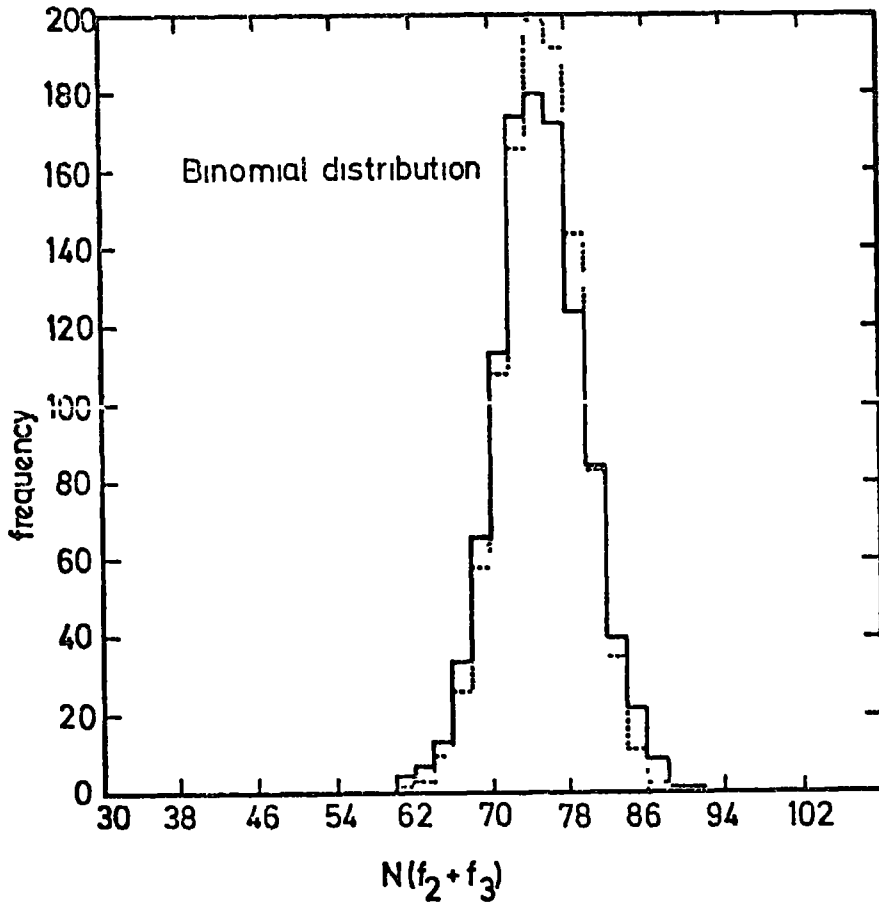
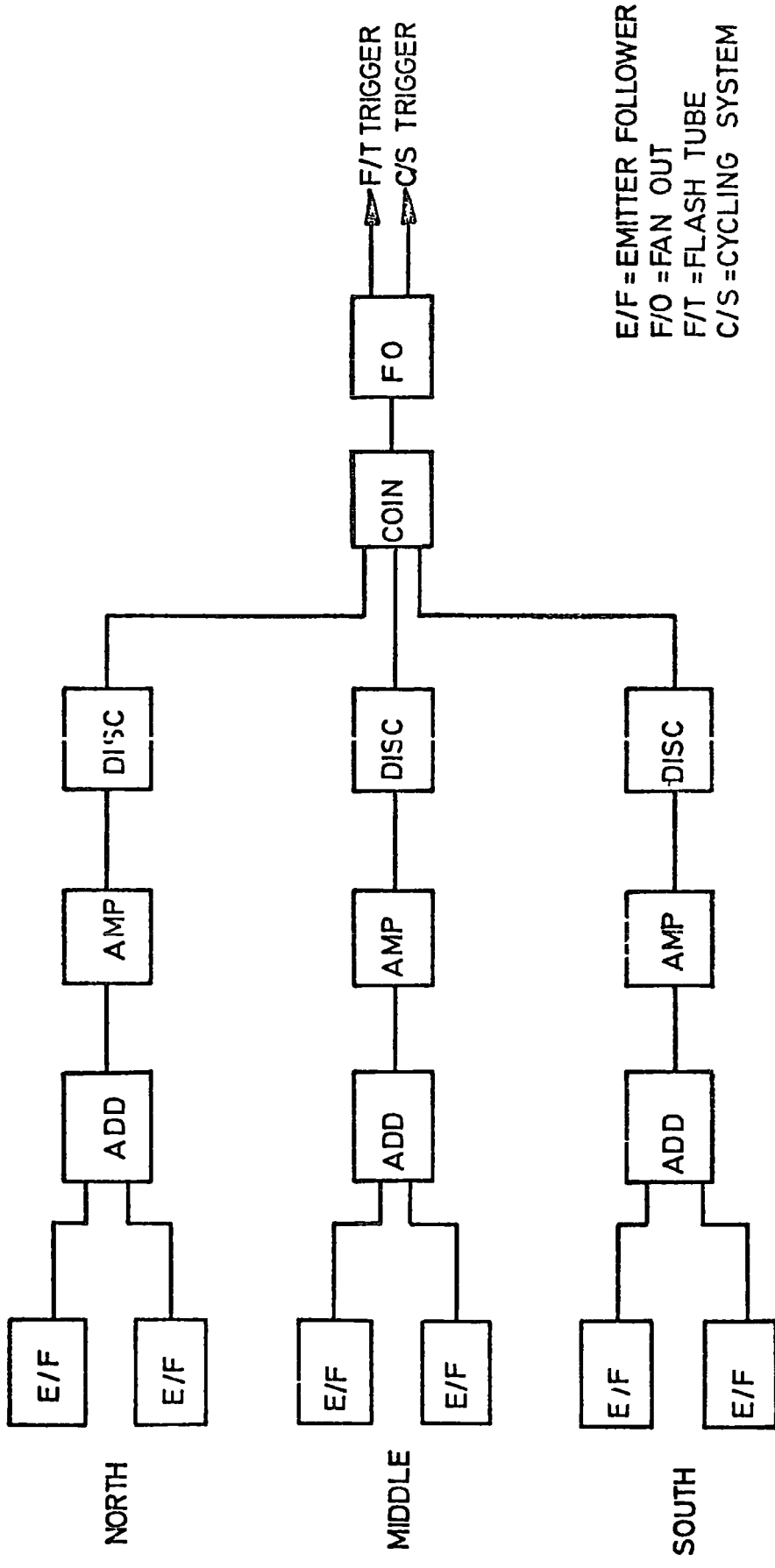


Figure 8.3

The frequency distribution of the number of flashes along the track in F2 and F3 for 1,046 single muons. (The dotted curve represents a binomial fit).



E/F = EMITTER FOLLOWER
 F/O = FAN OUT
 F/T = FLASH TUBE
 C/S = CYCLING SYSTEM

Figure 8.4 Block diagram of the electronics used in the extensive air shower experiment.

1 : 4.5 to real space.

In the analysis the definition of a measurable track was one which passed through F2 + F3 layers and produce at least one flash in the defining layers F1 and F4. Since the defining layers are shorter than the measuring layers F2 and F3 then this ensures that the track has passed the sensitive volume of the chamber (the sensitive volume could be defined as the volume covered by the electrodes) and this could eliminate the background muons due to the edge effect (Ashton et al. 1971c).

A measurable track with F2 + F3 > 60 flashed tubes also must be accompanied by at least one shower track in the chamber of length greater than 60 cms parallel to it or within $\pm 5^\circ$ in the projected plane.

All the tracks with F2 + F3 in range 20 - 60 were measured irrespective of the angle they made to shower tracks in a picture. However, all the events observed in the chamber were drawn and studied carefully.

8.4.2 Basic quark data

The basic data from the quark searches are summarized and shown in table 8.2. All the data were obtained using a local electron density $\geq 500 \text{ m}^{-2}$ as a master trigger.

The frequency distribution of the number of measurable tracks per photograph is shown in table 8.3, and the frequency distribution of the sum (F2 + F3) of the number of flashes on each track in the 96 measuring layers for the 452 measured tracks is shown in figure 8.5. The mean number of flashes along the track in F2 + F3 layers for shower particles passing through the chamber is 77.88 ± 0.22 and the standard deviation of the distribution is 4.67.

In figure 8.5 the arrows represented the expected number of flashes for minimum and plateau ionising charge e particles and quarks of charge $e/3$ and

<u>Film No.</u>	<u>EAS Selection</u>	<u>Running Time (hrs)</u>	<u>Total No. of triggers</u>	<u>Total No. of measurable triggers.</u>	<u>% of triggers that give at least one measurable track</u>	<u>Total No. of measurable tracks</u>
G1-G21	$\Delta e \geq 500 \text{ m}^{-2}$	7,009	1,217	207	(17.1 ± 1.1)%	452

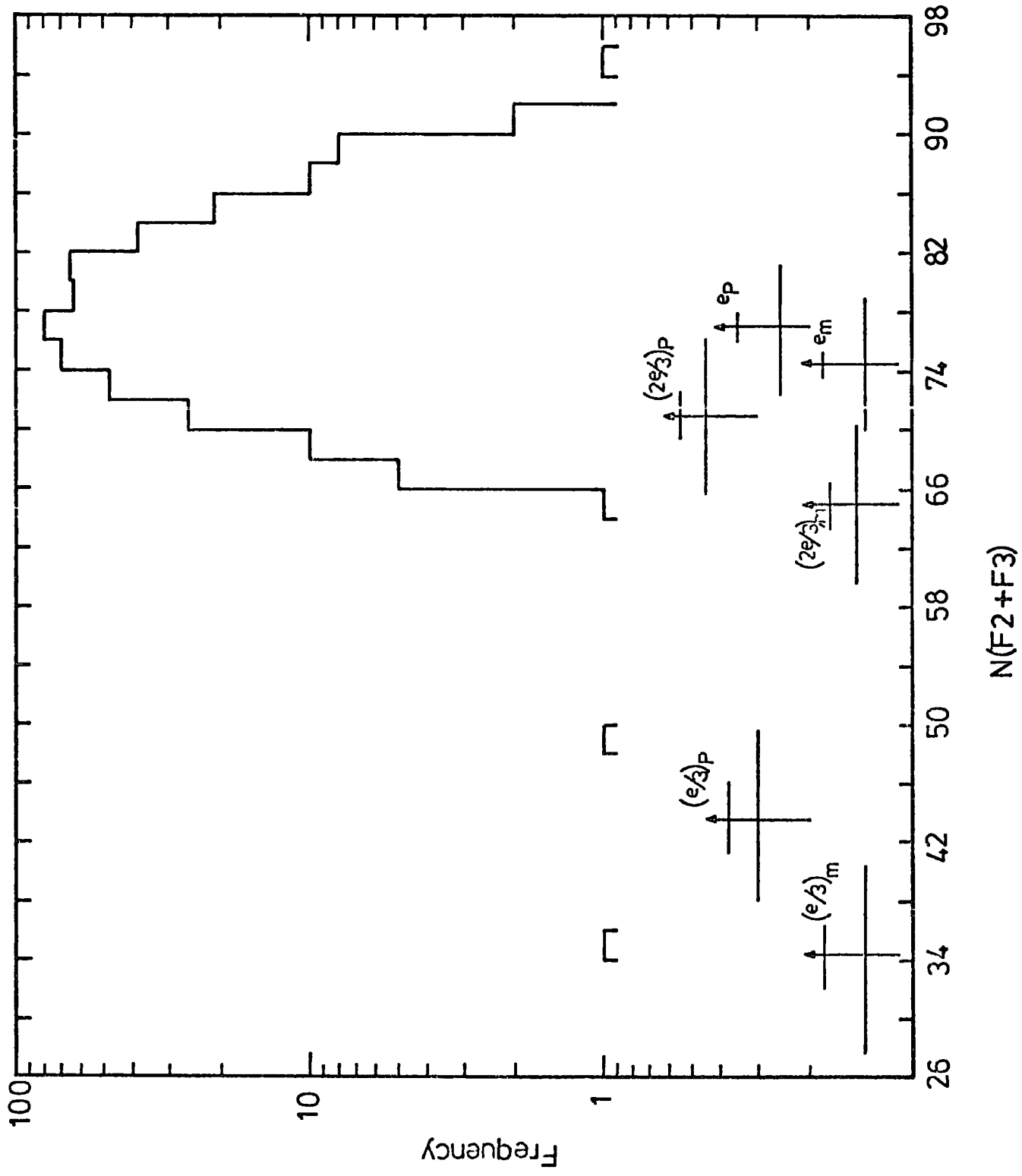
Table 8.2 The basic data obtained in the G-series (March 1973 - January 1974)

<u>No. of measurable tracks, n, per event</u>	<u>No. of events, N, showing, n, measurable tracks</u>	<u>N x n</u>
1	84	84
2	57	114
3	33	99
4	21	84
5	6	30
6	2	12
7	3	21
8	1	8
<u>Total</u>	<u>207</u>	<u>452</u>

Table 8.3 The frequency distribution of the number of triggers N having n measurable tracks.

Figure 8.5

Basic experimental data. The frequency distribution of the sum of the number of flashes in the measuring layer F2 + F3. The arrows indicate the expected number of flashes for minimum and plateau ionising charge e , $e/3$ and $2e/3$, (see table 8.5).



$2e/3$. The position of the arrows are calculated as follows:

(a) Assume the median momentum of muons at the centre of F2 + F3 producing coincidences between the plastic scintillators A and B is 2.1 GeV/c.

This was calculated from the spectrum given by Hayman and Wolfendale (1962),

and (b) using the curve of most probably^e ionisation loss in neon as a function of muon momentum given by Crispin and Fowler (1970). According to this curve the ratio between I/I_M and I_P/I_M for muons with $p_\mu = 2.1$ GeV/c is 1.14 and 1.43 respectively, where I is the most probable ionisation loss, I_M and I_P is the minimum and Plateau ionisation losses. From the efficiency - time delay measurements the overall best fit to the experimental points using Lloyd parameters af_1Q_1 was 9 ± 1 (see figure 4.8). Now, since the ratio of amount of ionisation produced by these muons to that of plateau and minimum ionising muons was known (Crispin and Fowler), the Lloyd parameter (af_1Q_1) suitable to these cases could be calculated. The expected value of the af_1Q_1 for charge e particles in I_M and I_P cases are $(\frac{9 \pm 1}{1.14}) = 7.9 \pm 0.9$ and $(7.9 \pm 0.9) \times 1.43 = 11.3 \pm 1.3$ respectively. The expected position for $e/3$ and $2e/3$ quarks are obtained by dividing the Lloyd parameter calculated for charge e particles by $1/9$ th and $4/9$ ths respectively, since the value of af_1Q_1 is proportional to the charge squared of the traversing particle. Table 8.4 shows the expected number of flashes produced by charge e particles and the $e/3$ and $2e/3$ quarks in the minimum and plateau ionisation regions. The values of the internal efficiency shown in table 8.4 were calculated from the af_1Q_1 values, using the relation between the internal efficiency and af_1Q_1 for a fixed time delay of $20 \mu s$ which has been calculated from Lloyd theory (see section 4.2.3 and figure 4.5).

In figure 8.5, the small bars shown on the arrows indicate the uncertainty in the position of the arrow and the large bars are the expected standard deviation of the distribution. At one standard deviation level, the $e/3$

Charge	Ionisation Loss	$af_1 Q_1$	Internal efficiency(%) η_I (for $T_D = 20\mu s$)	Layer efficiency(%) $\eta_L = 0.873 \eta_I$	Expected No. of flashes in F2+F3(96 layers)	Expected standard deviation of the distribu- tion of number of flashes about mean = $96\eta_L$
e	I_p	11.3 ± 1.3	92 ± 1	80.0 ± 0.9	77.1 ± 0.9	± 4.5
e	I_m	7.9 ± 0.9	89 ± 1	77.6 ± 0.9	74.5 ± 0.9	± 4.7
$e/3$	I_p	1.26 ± 0.15	52 ± 3	45.4 ± 2.6	43.5 ± 2.6	± 5.9
$e/3$	I_m	0.88 ± 0.1	41 ± 3	35.8 ± 2.6	34.4 ± 2.5	± 5.8
$2e/3$	I_p	5.04 ± 0.6	84.5 ± 1.8	73.7 ± 1.6	70.9 ± 1.5	± 4.9
$2e/3$	I_m	3.52 ± 0.4	78 ± 2	68.0 ± 1.7	65.2 ± 1.6	± 5.3

Table 8.4 The expected number of flashes produced by plateau and minimum ionising (I_p and I_m) e particles, $e/3$ and $2e/3$ quarks in F2 + F3 layers for time delay $T_D = 20 \mu s$.

quark track efficiency was considered to be between 28 to 50 flashes in $F2 + F3$, since it was estimated the lowest number of flashes along track in $F2 + F3$ was 20 flashes.

It can be seen from figure 8.5 that the chamber could not resolve $2e/3$ quarks, because it cannot be distinguished from charge e particle, but it could resolve $e/3$ quarks (if any). Only two events (G15 - 59) and (G17 - 42) were observed showing low efficiency tracks with number of flashes in $F2 + F3$ falling in the $e/3$ quark region. The 2 quark candidates were examined in detail in order to prove whether they are background produced by a muon or they are genuine quarks.

8.4.3 Details of the two quark candidates

As mentioned in the previous section only two candidates were observed in this run and according to their efficiencies the two candidates could be classified as $e/3$ quarks.

Table 8.5 shows the full details of the two quark candidate tracks which appeared in the tail of the observed $F2 + F3$ distribution (see figure 8.5).

Plate 8.1 shows the event G15 - 59 with a possible $e/3$ quark track indicated.

To prove whether these two tracks are genuine quarks or a background, an examination has been made on these two tracks and this will be discussed in the next section.

8.5 The background effects

8.5.1 The expected number of background muon tracks

Incoherent muons could simulate $e/3$ quarks if they traverse the sensitive volume of the chamber immediately before the chamber trigger by EAS. From the efficiency time delay measurements (see figure 4.8) the

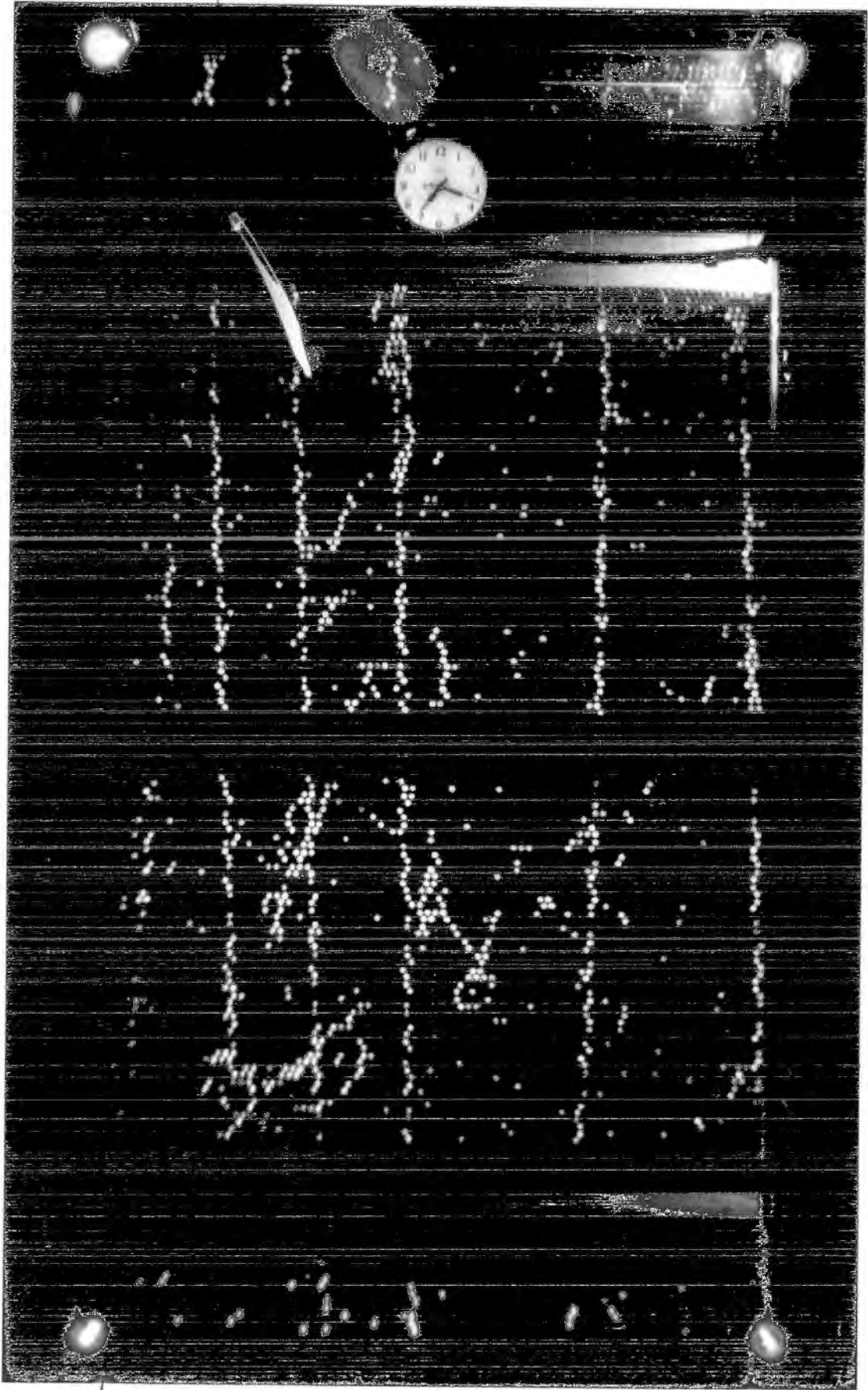
Event	No. of flashes in F2 and F3 for quark candidate	Angle of quark candidate tracks to other shower tracks	No. of shower tracks in the picture excluding the quark candidate	No. of knock-on flashes (side by side adjacent flashes) on the quark track	No. of singles random background flashes in (F2 + F3)
G15 - 59	35	2°	5	4	162
G17 - 42	48	5°	14	3	70

Table 8.5 Details of the two quark candidate tracks observed in this run (G - series)

Plate 8.1

Event G15 - 59

A possible quark track is indicated



track with F2 + F3 in the range 28 - 50 (as expected for $e/3$ quarks) could be produced by incoherent muons which traversed the chamber in the time domain 103 - 144 μ s preceding the E+S trigger.

However, it is important to calculate the expected number of background muon tracks traversing the chamber in this period.

From the sea level vertical muon momentum spectrum given by Hayman and Wolfendale (1962), the rate of muons with momentum > 0.78 GeV/c (this momentum corresponds to the minimum energy of muons traversing the flash tube chamber) is equal to $6.3 \cdot 10^{-3} \text{ cm}^{-2} \text{ sec}^{-1} \text{ st}^{-1}$.

The rate of muons traversing the chamber within the acceptance geometry was calculated to be 104.2 sec^{-1} . This was calculated taking the rate of muons at sea level with momentum 0.78 GeV/c multiplied by the sensitive aperture of the chamber.

The rate of the incoherent muons simulating $e/3$ quarks in the sample of 207 measured photographs could be calculated as follows: $207 \times 41.10^{-6} \text{ sec} \times 104.2 \text{ sec}^{-1} = 0.9$, where 41.10^{-6} sec is the time domain in which the muon could simulate quarks. This result is sufficiently close to the observed number 2 to suggest that both the observed events (G15 - 59) and (G17 - 42) are background muons.

8.5.2 The expected number of knock-on electrons

A further experimental test could be applied to examine the number of knock-on electrons (5 rays) observed on each quark candidate track. From knock-on electron (K.O's) theory one can conclude that the probability of production of K.O's is proportional to the square of the charge (Z^2) of the particle, so it was expected to find lower number of flashes on $e/3$ quark tracks than the tracks of particles with charge e .

A knock-on electron was defined as two adjacent flashes (side by side)

occurring in one layer of flash tubes. The number of K.O's on the two observed candidates has been given in table 8.5.

There is the possibility that these K.O's are not genuine, but it could be presented by chance as K.O's due to the finite number of single random background flashes that appear in each picture. These spurious flashes are mainly due to radio activity produced in the glass. Ashton et al. (1973c) have measured the relation between the average number of knock-on electrons on a track as a function of time delay T_D . They found for the time delay of $20 \mu s$ between the passage of a relativistic charge e particle (muon) and the application of the high voltage pulse to the chamber the measured number of side by side flashes in 96 layers ($F_2 + F_3$) of tubes corrected for the spurious background flashes to be 1.6. Therefore the expected number of K.O's/track for a quark of charge $e/3$ is $\frac{1.6}{9} = 0.18$.

This result is sufficiently close to zero to suggest that there should be no knock-on electrons expected on the quark track.

On the other hand one can calculate the side by side flashes expected due to the background on each quark track. For event G15 - 19 (see table 8.5) the number of side by side flashes expected due to background = $2/84.5 \times 35/96 \times 162 = 1.4$, where alternate layers of the 96 layers of measuring tubes contain 84 and 85 flash tubes respectively. The number 162 represents the number of single random background flashes in $F_2 + F_3$ and the number 35 represents the number of flashes on the quark track in the $F_2 + F_3$ measuring layers. Comparing the expected number of side by side flashes due to background (1.4) with the observed number of 4 it is concluded that this event is not a genuine $e/3$ quark as there is evidence for $4 - 1.4 = 2.6$ knock-on flashes.

Similarly for event G17 - 42 the expected and observed numbers of side by side flashes are 0.8 and 3 respectively. Therefore, again there is

evidence here for genuine knock-on electrons, and this shows that the track observed in this event is also not a genuine quark track.

8.6 Quark flux limit

No genuine $u/3$ quark tracks have been found in the running time of 7,009 hours, when a local electron density greater than 500 m^{-2} used as a master trigger. The flux obtained at 90% confidence level is $< 4.3 \cdot 10^{-11} \text{ cm}^{-2} \text{ sec}^{-1} \text{ st}^{-1}$.

This limit refers to $u/3$ quarks incident on the top of the chamber from the atmosphere. In obtaining the above limit, account was taken of (a) the $16\% = (1 - e^{-0.18}) \cdot 100$ loss of genuine quark tracks which would produce side by side flashes on their tracks after correction for random background, and (b) due to their interaction with chamber material, assuming $(\sigma_{qN})_{\text{inelastic}} = \frac{1}{3} (\sigma_{pp})_{\text{inelastic}} = 11 \text{ m b}$.

The correction factor for the interaction effect was calculated to be 6.1.

8.7 Summary of the flash tube chamber results

Since the new arrangement of the flash tubes was completed in 1971 three experimental runs E, F and this experiment G series with different triggering threshold have been made to look for $u/3$ quarks. Each run has quoted an upper limit for $u/3$ quarks at sea level. However, the comparison of the basic experimental data for the three runs are given in table 8.6.

As can be seen from the table the percentage of triggers that gave at least one measurable track decreases as the minimum density trigger requirement increases. This is because the probability of observing clean measurable tracks in the events decreases. This effect can be seen through figure 8.6 which shows the frequency distribution of the observed tracks in the chamber for the three runs.

Film No.	Running time (hours)	Total No. of triggers	Total No. of measurable triggers	% of triggers that gives at least one measurable track	Total No. of measurable tracks	The electron density on the top of the chamber (EAS selection)	Reference
E1 - E69	2,570	12,057	2,753	23	4,501	$\Delta e \geq 40 \text{ m}^{-2}$	Ashton et al. (1973a)
F1 - F40	5,420	4,516	1,116	25	2,077	$\Delta e \geq 160 \text{ m}^{-2}$	Ashton et al. (1973b)
G1 - G21	7,009	1,217	207	17	452	$\Delta e \geq 500 \text{ m}^{-2}$	present work

Table 8.6 Comparison of the basic experimental data obtained with different EAS selections.

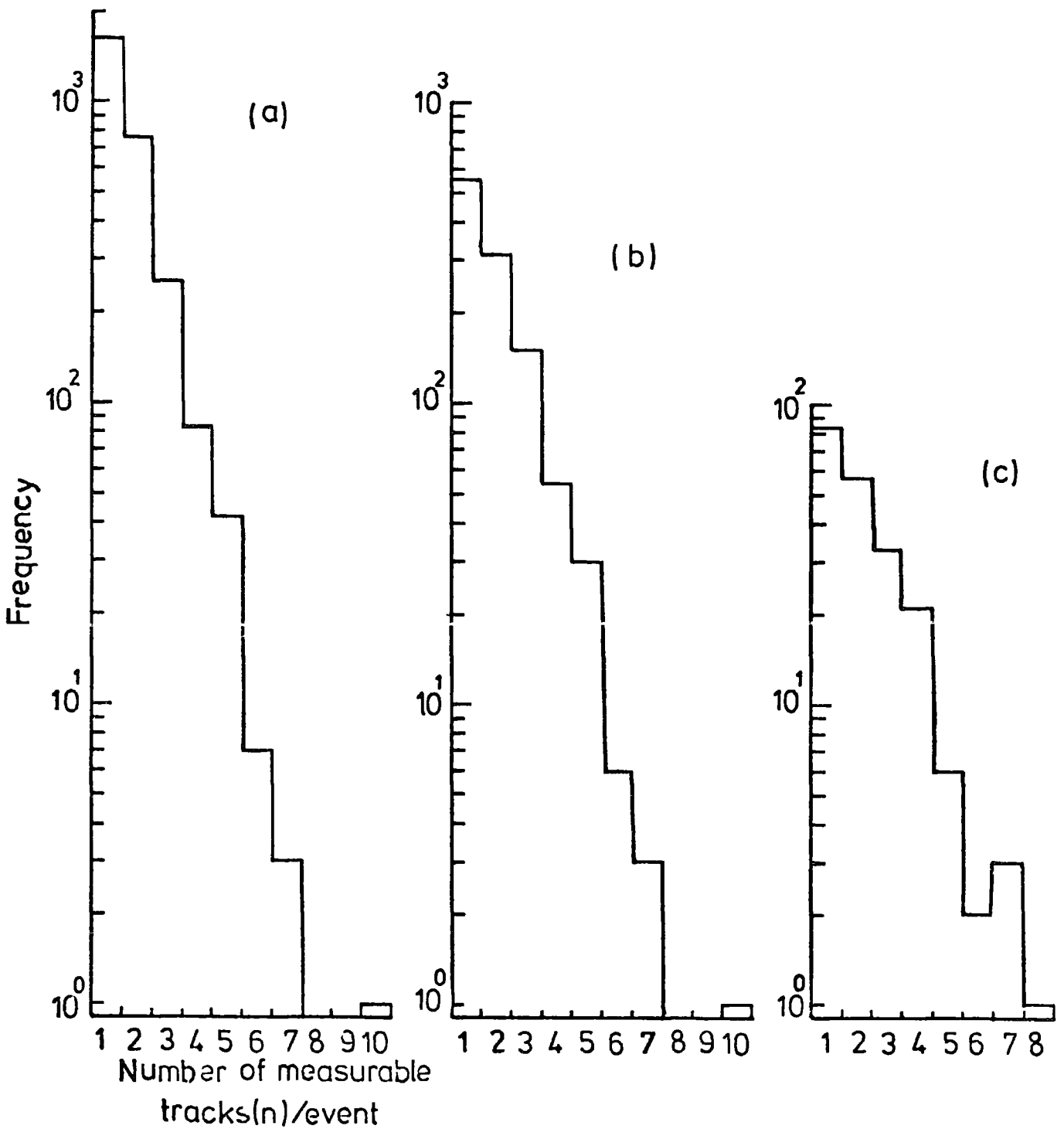


Figure 8.6

The frequency distributions of the number of events having n measurable tracks.

- (a) E - series (Ashton et al., 1973a)
- (b) F - series (Ashton et al., 1973b)
- (c) G - series (This work).

EAS selection		No. of photos scanned	Total no. of quark candidates including background muons (F2+F3 in the range 28-50)	No. of quark candidates with shower track of length > 60 cm and parallel to it to $\pm 5^\circ$, F2+F3 in the range 28-50	No. of quark candidates after applying no genuine side by side flashes criterion	Quark flux $\text{cm}^{-2} \text{sec}^{-1} \text{st}^{-1}$	Reference
Δ (scint.)	Δ (true)						
$> 40 \text{ m}^{-2}$	$> 20 \text{ m}^{-2}$	12,057	20	6	2	$< 8.0 \cdot 10^{-11}$ based on ? possible events	Ashton et al. (1973a)
$> 160 \text{ m}^{-2}$	$> 80 \text{ m}^{-2}$	4,516	3	0	0	$< 5.5 \cdot 10^{-11}$ at 90% confidence level	Ashton et al. (1973b)
$> 500 \text{ m}^{-2}$	$> 250 \text{ m}^{-2}$	1,217	2	2	0	$< 4.3 \cdot 10^{-11}$ at 90% confidence level	Present work

Table 8.7 Summary of the flash tube chamber results during November 1972 - January 1974.

Table 8.7 shows the limits given by each run. It can be noted from this table that when the selection triggers was set on $\Delta e \geq 40 \text{ m}^{-2}$ only 2 events satisfy all the conditions as $e/3$ quarks and the limit given in the table is based on these two events. For $\Delta e \geq 160 \text{ m}^{-2}$ and $\Delta e \geq 500 \text{ m}^{-2}$ the limit is calculated at the 90% confidence level (i.e. no events observed).

It can be seen also from table 8.7, that two values for the scintillator trigger threshold are given. Initially the three liquid scintillators used to select EAS were calibrated using a two fold coincidence geiger telescope using muons. Their trigger thresholds Δ (scint.) were set according to this calibration.

Farvaresn (1975) in his work using a proportional counter in connection with the three scintillators has revealed that the density measured by scintillator is too large by a factor of 2 (see table 8.7). The reason for this is believed to be due to electron-photon cascade development in the comparatively thick liquid scintillations (phosphor thickness 17.5 cms). The same effect has also been observed by Katsumata (1964). Δ (true) shown in table 8.7 is believed to refer to particle density as measured by a proportional counter or a scintillation counter with a phosphor thickness < 5 cms.

8.8 Conclusion

Using the neon flash tube technique the flash tube chamber shows the capability of detecting fractional charged particles and $e/3$ charge particle was most likely to be detected rather than $2e/3$ charge particle.

In a running time of 7,009 hours two tracks were observed in the expected quark region and both were explained as due to background incoherent muons.

The upper limit for $e/3$ quarks in EAS of a median shower size $6.5 \cdot 10^5$

26 17
LIBRARY

(assuming Δe (true) = 250 m^{-2}) is found to be $< 4.3 \cdot 10^{-11} \text{ cm}^{-2} \text{ sec}^{-1} \text{ st}^{-1}$ at the 90% confidence level.

In future work to search for quarks, the chamber needs to be modified such that the effect of the background will be eliminated (or minimised). The plan is to increase the number of plastic scintillators (in positions A and B, see figure 4.1) so as to cover the whole sensitive area of the flash tube. The coincidence from A and B indicates the passage of single particles (muons) through the chamber in the time period 0 - $200 \mu\text{s}$ preceding the EAS trigger.

The background muon will be indicated through a system called a 'previous particle indicator' and with this system the background problem should be eliminated.

However, the results shown in table 8.7 suggest also that with the above modification the search for $e/3$ quark in EAS should be undertaken using a local electron density Δe (true) of $\geq 20 \text{ m}^{-2}$.

CHAPTER 9

THE ENERGY SPECTRA OF HADRONS

IN EXTENSIVE AIR SHOWERS

9.1 Introduction

While the chamber was running to search for quarks in regions of EAS of local electron density $\geq 250 \text{ m}^{-2}$, many examples of high energy hadrons interacting in a 15 cm lead absorber above the chamber and a 15 cm iron target situated in the chamber were observed. This could be explained as due to the existence of high energy hadrons in the core of EAS.

Experimentally only the width of the burst emerging from the target can be measured. Later, the chamber has been modified and a calibration of the relationship between the average burst width and burst size was obtained experimentally for both lead and iron targets (see section 4.4).

However, in this chapter the measurements of the hadron energy spectrum from the iron and lead targets will be discussed. The reason for studying hadrons in EAS was to relate the measurement to general shower characteristics which is still not fully understandable.

9.2 Analysis of the data

9.2.1 Scanning technique

The technique used in scanning the films was based on projecting the negative onto a scanning table. The reduction in scale being 20 : 1 to the real space. The same methods discussed in chapter 4 were used to measure the width of the burst in the flash tube layers directly below the iron and lead absorbers. An event was accepted when the whole width of the burst fell on the flash tube chamber and it has a definable width.

For bursts occurring in iron charge identification was possible in the flash tubes Fla (8 layers) situated directly above the iron. The definition adopted for a burst produced by a charged particle was that it must have an observable track in Fla parallel to the burst direction inside the chamber and be coincident with the middle of the burst. A neutral particle burst was defined as one for which the above definition of a charged particle was not satisfied.

The bursts observed in the lead could be explained due to charge and neutral particles together, since there is no flash tube located above the lead to identify the incoming particle.

In this run it was difficult to identify the neutral particles producing bursts in iron, because with the high electron density trigger ($\Delta e \geq 250 \text{m}^{-2}$) the probability to get more tracks in Fla within the width of the burst is high, so only 4 events were classified as neutral events in this run.

Since the defining layer Fla does not cover all the area of the iron absorber, some observed bursts produced in iron in which the track showing the incoming particle has missed the top flash tube layer Fla and simulates a neutral particle burst by entering the iron either at the back or the front of the chamber where the iron was not covered completely by the flash tubes (see figure 4.1). This type of event could be recognised by the strange shape they made on the layer F2. Plate 9.1 shows an example for this effect. However, this type of event (edge effect) does not count for neutral or charged particles.

9.2.2 Basic data

In 7,009 hours 407 bursts in lead and iron have been observed from 1,217 total triggers. The run was in regions of EAS of a local electron density $\geq 250 \text{m}^{-2}$ (G-series). Plates 9.2 to 9.4 show some typical interaction events observed in the chamber.

Plate 9.1

Event G18 - 39

An edge effect event simulating a neutral particle burst. The width of the burst increases immediately on passing from F1b to F2.

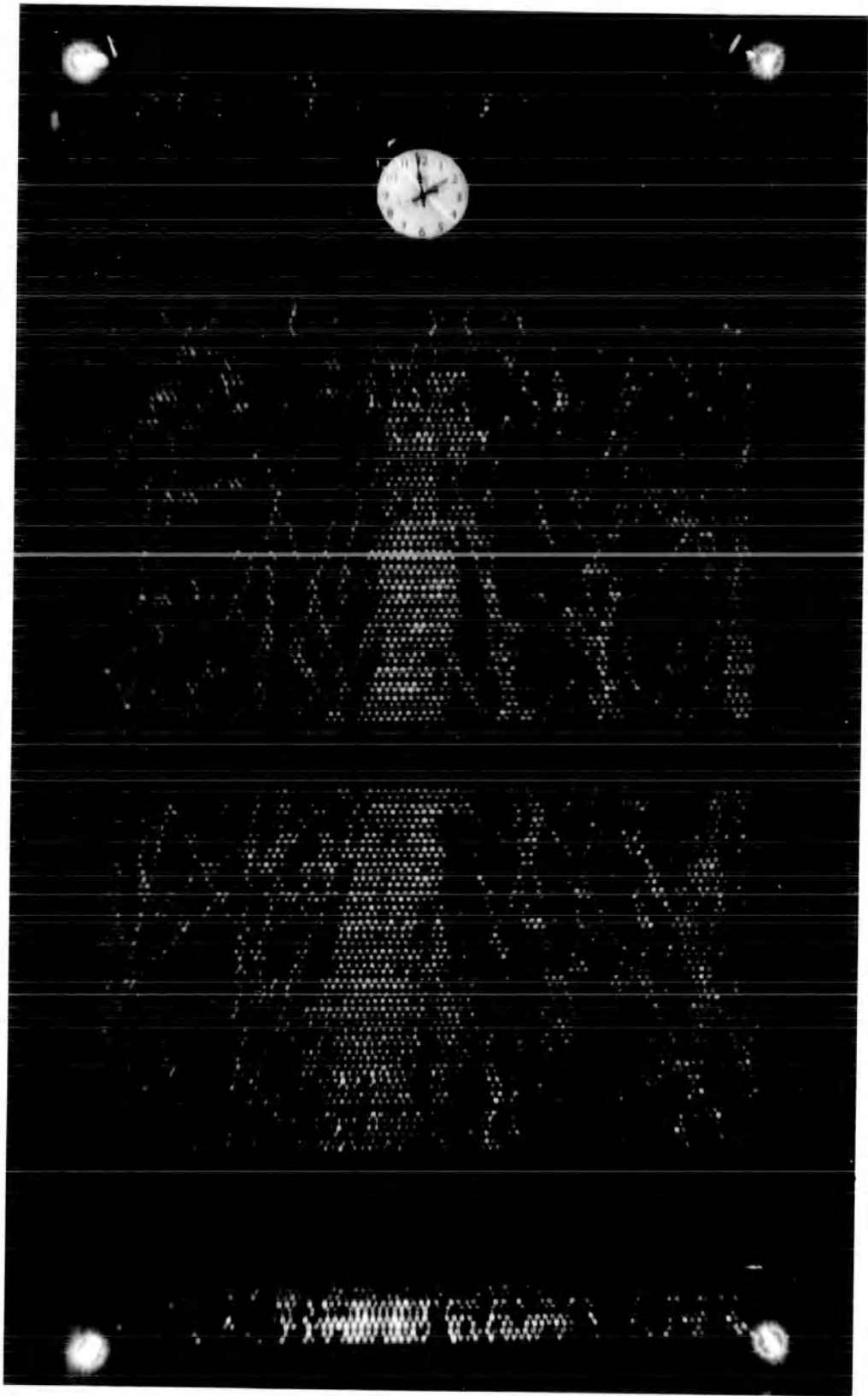


Plate 9.2

Event G19 - 52

A charge particle burst produced in the iron.

$N = 215$ particles

$E_{\pi} = 143$ GeV.

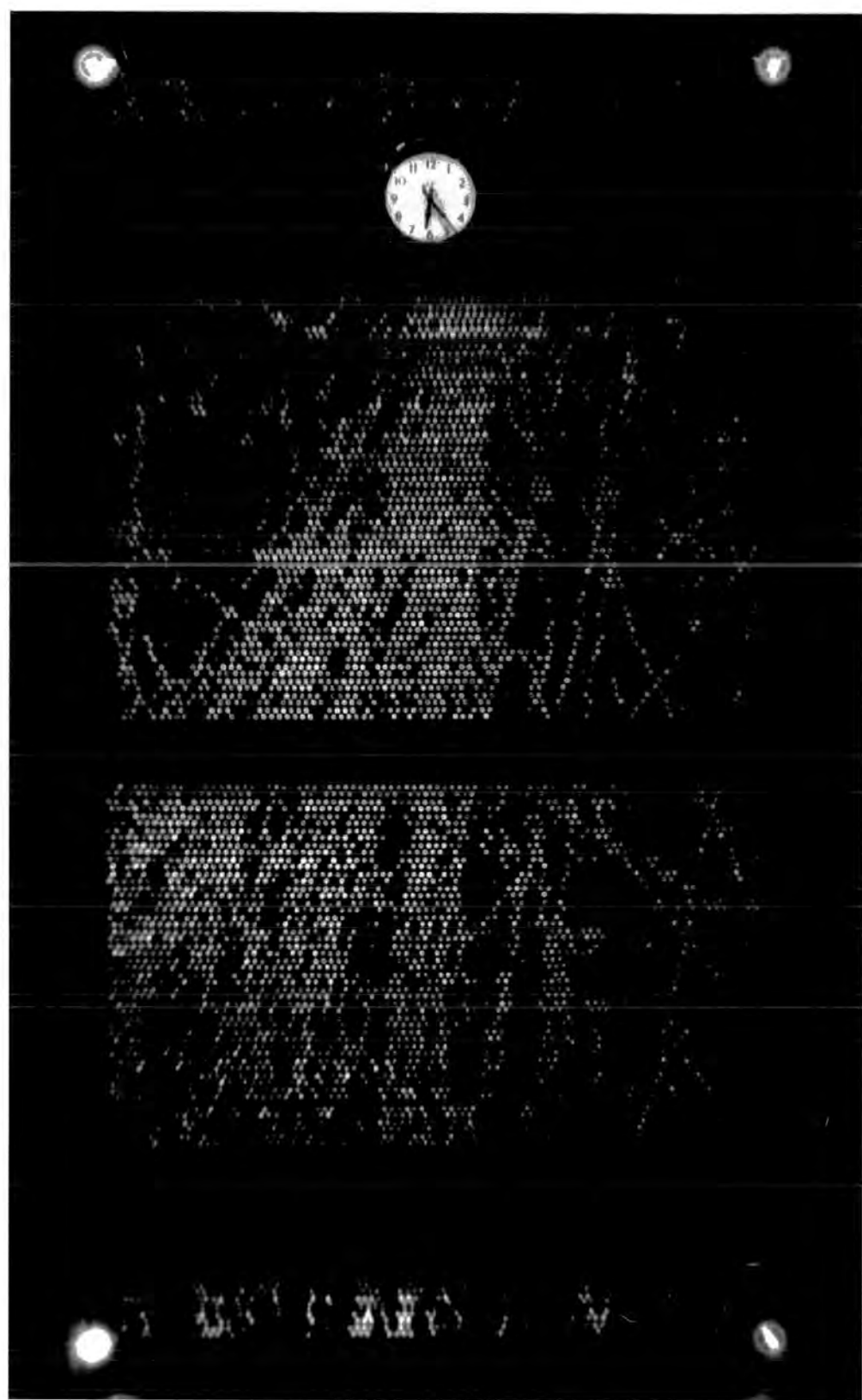


Plate 9.3

Event G21 - 8

A burst produced in the lead and penetrating
the iron.

$N = 1,350$ particles

$E_{\pi} = 1,000$ GeV.

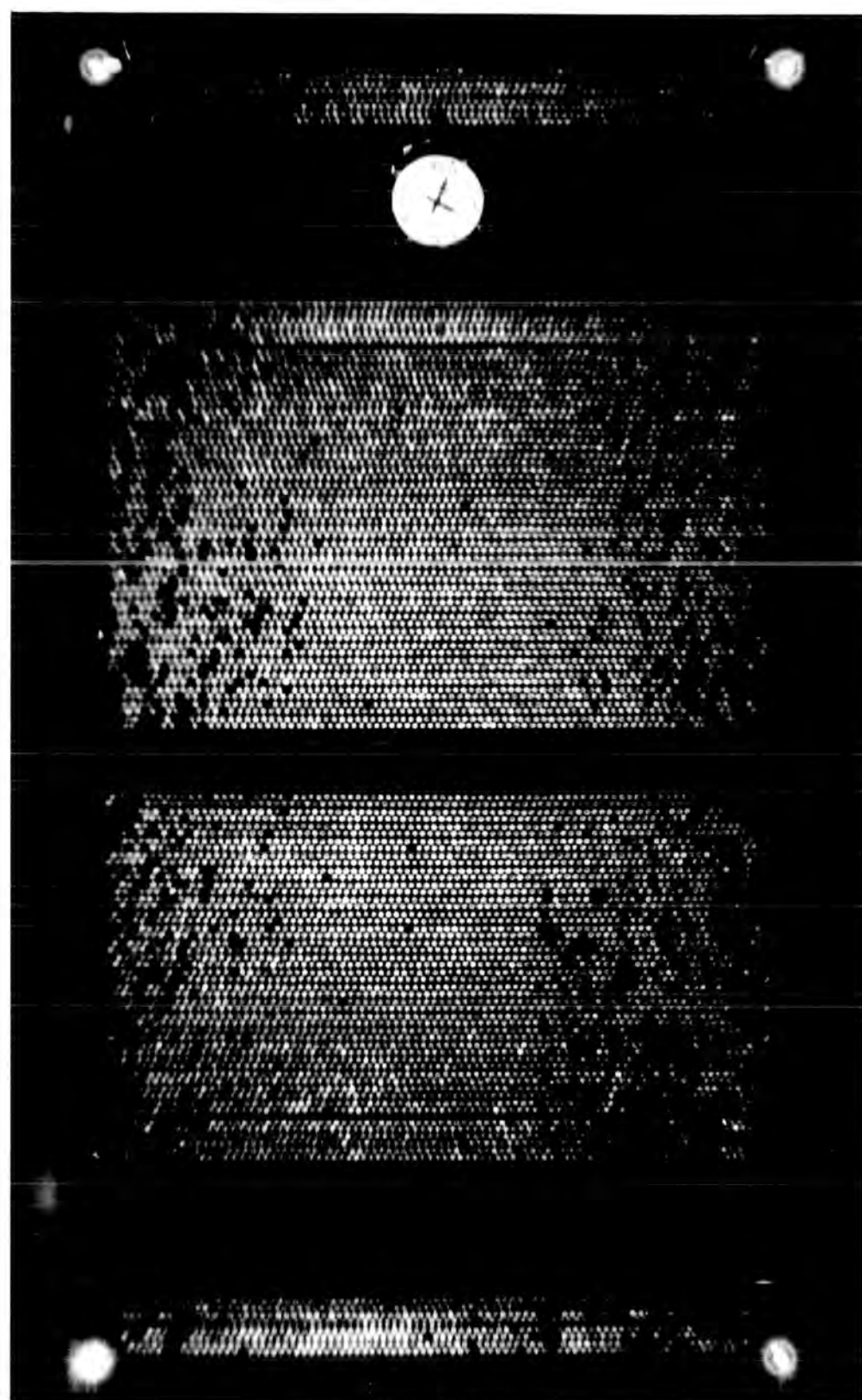
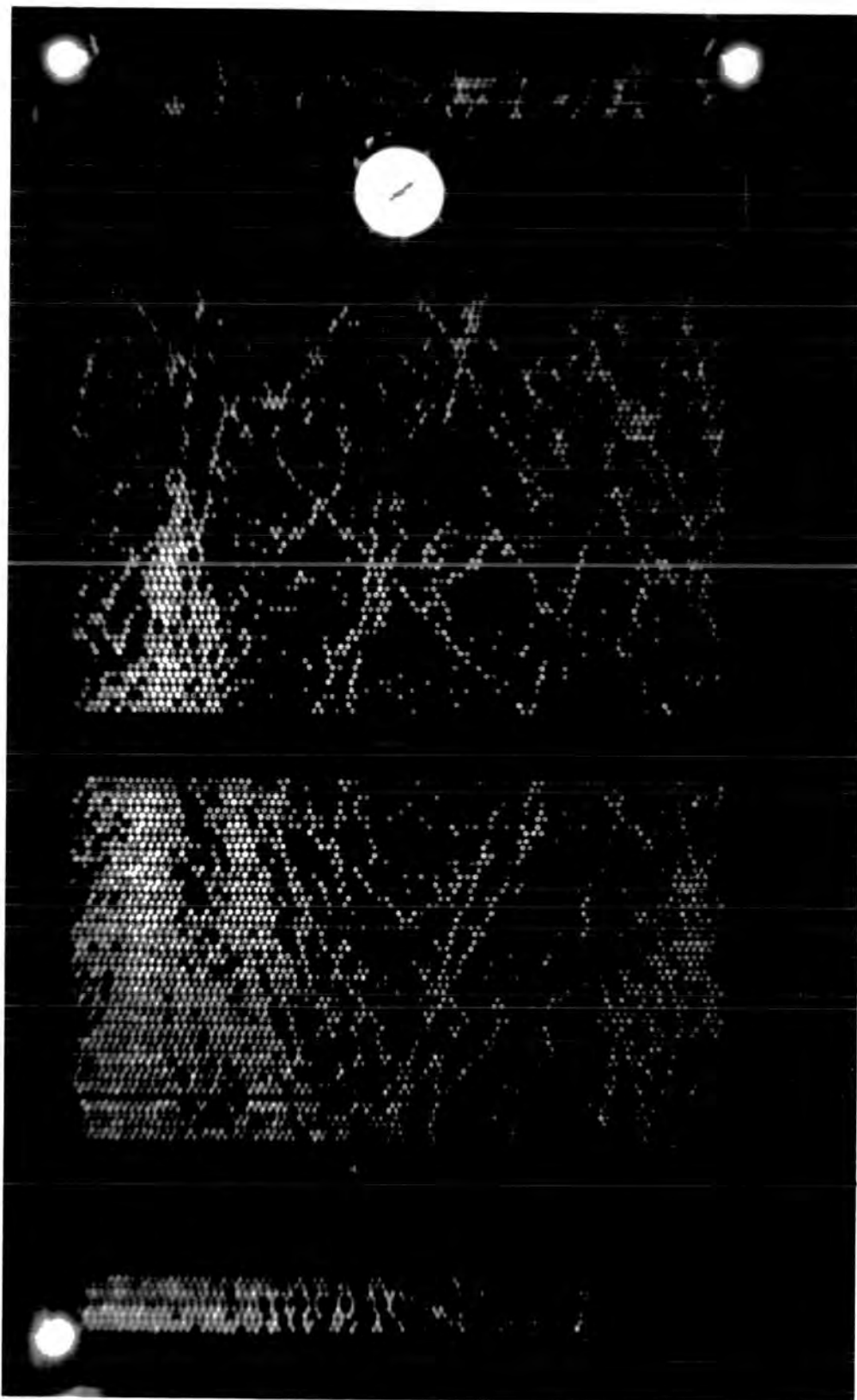


Plate 9.4

Event G19 - 49

A burst produced in the chamber as a result
of the interaction of a charged particle
with the glass of a flash tube.



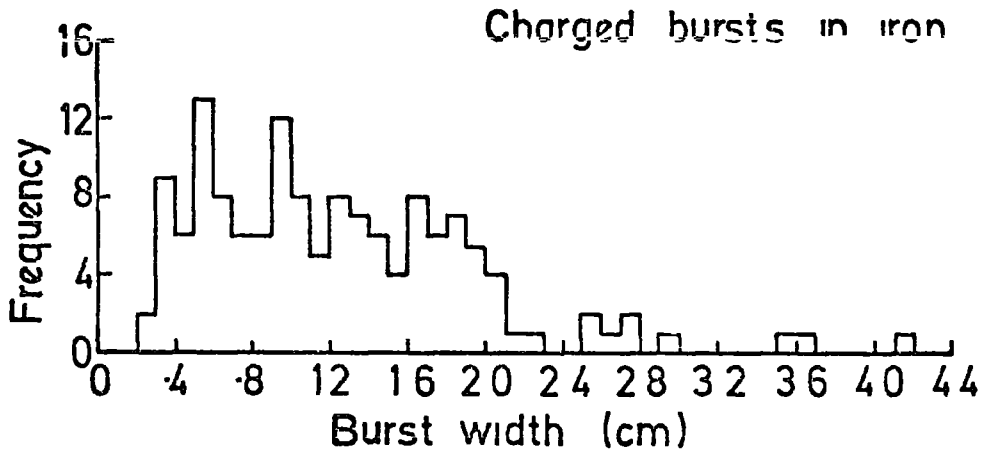
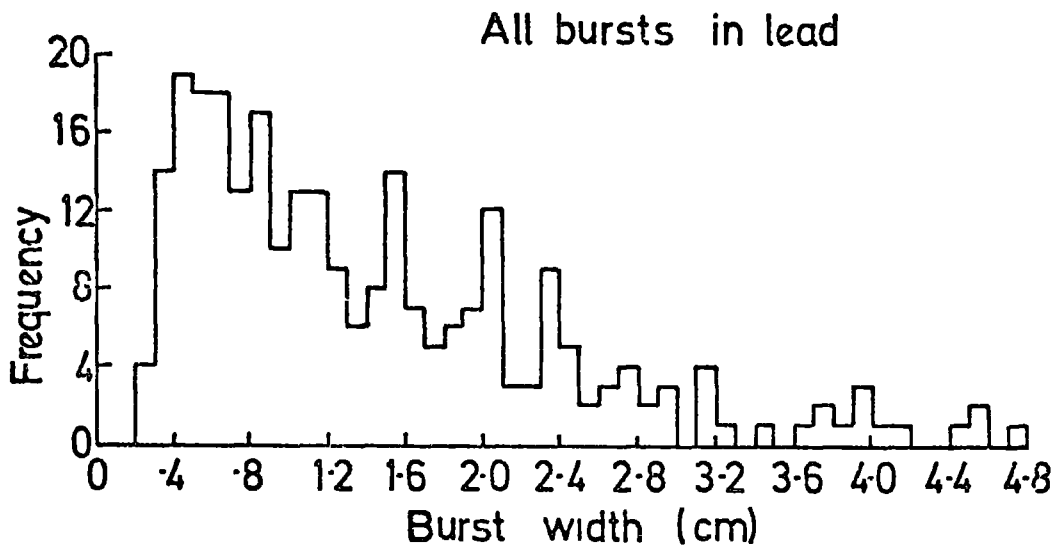


Figure 9.1

The distribution of the measured burst width obtained below the lead and iron absorbers, (see table 9.1). The burst widths were measured on the scanning sheets (scale 1:20 in real space).

Total No. of triggers	Running time (hours)	No. of bursts observed in the lead with $E > 16$ GeV assuming produced by π^+	No. of charged bursts observed in iron with energy $E > 12$ GeV assuming produced by π^+	No. of neutral bursts observed in iron.
1,217 (G-series, G1 - G21)	7,009	266	141	4

Table 9.1 Basic experimental data obtained from the G - series run in region of EAS of local electron density trigger $\geq 2.0 \pi^{-2}$.

The results of the measured burst width distributions obtained from the bursts observed in the lead and iron absorbers are shown in figure 9.1. Table 9.1 shows also the number of the bursts observed in the lead and iron absorber.

9.3 The energy spectra

The measured burst widths below the lead and iron target were converted into number of particles (burst size) using the measured relationship between the burst width and the burst size measured in the vertical burst experiment for a single unaccompanied hadron (see figures 4.22 and 4.23). For the energy conversion it was assumed that the bursts observed in the lead target have been produced by π^+ , and for the iron target bursts with charged primary particle are assumed to be produced by π^+ and those with a neutral primary by neutrons or antineutrons, although it is possible that some of these events could be produced by K^0 , K^{*0} mesons.

The measured energy spectra of hadrons observed to interact in the lead and iron targets were calculated using the burst size - energy relationship for pion induced bursts in the lead and iron (see figures 3.6 and 3.7). Figures 9.2 and 9.3 show respectively the differential and the integral energy spectra obtained from the present experiment.

In both figures the energy spectrum measured from bursts observed in lead refer to the all particles and the energy spectrum measured from bursts observed in iron refer to charged particles only. Both spectra have been corrected for the aperture effect in which the probability will be reduced for an event being accepted as the burst width increases. The spectra represented the total number of hadrons falling on the chamber, and the integral exponent from both the iron and lead spectra shows $\gamma = 1.07 \pm 0.09$ for energy $E \geq 200$ GeV.

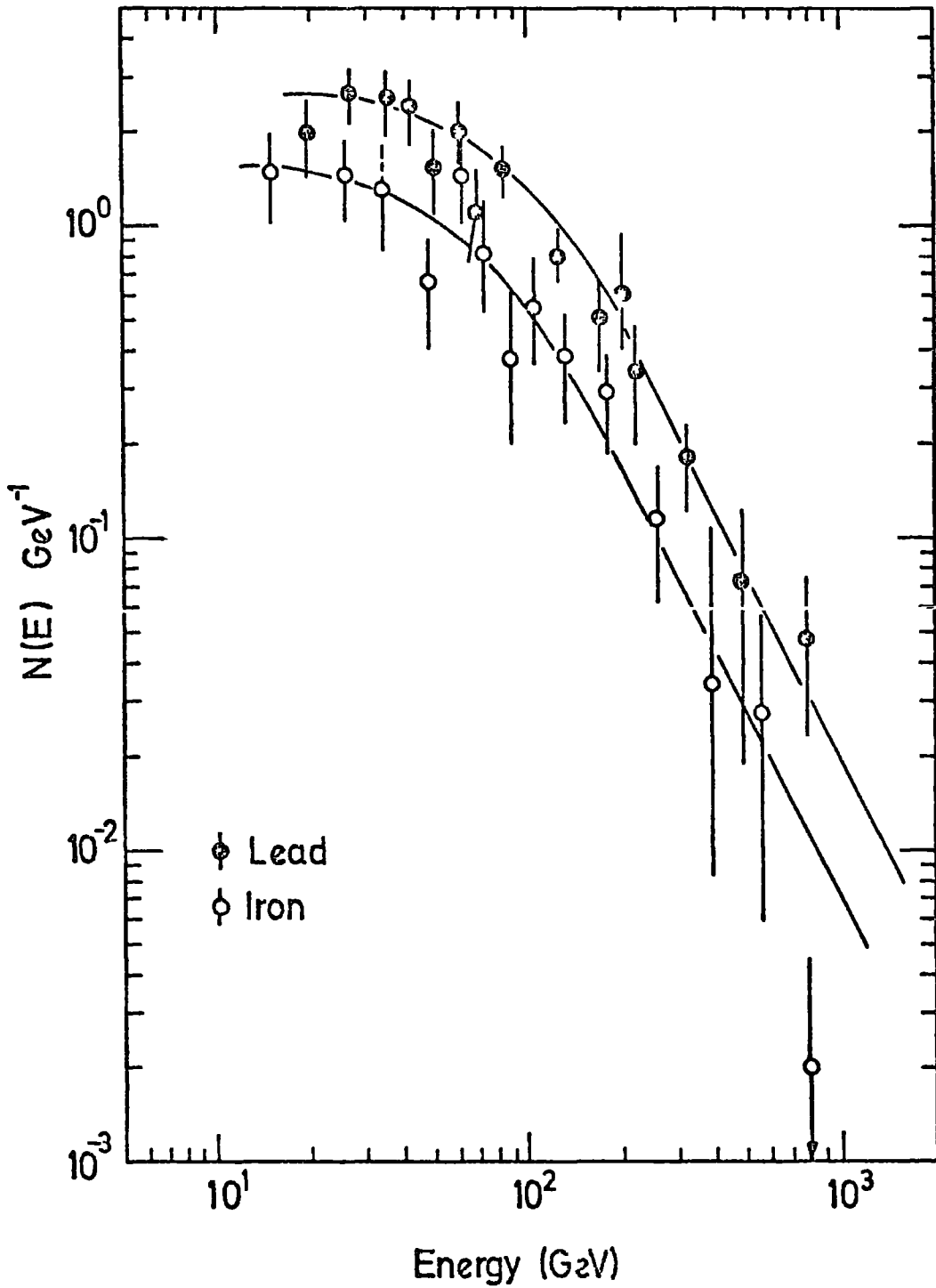


Figure 9.2

Differential energy spectra of all hadrons and charged hadrons in EAS with $\Delta e \geq 250 \text{ m}^{-2}$ measured below the lead and iron absorber respectively.

\bullet From all measured bursts in lead.

\circ From measured charged bursts in iron.

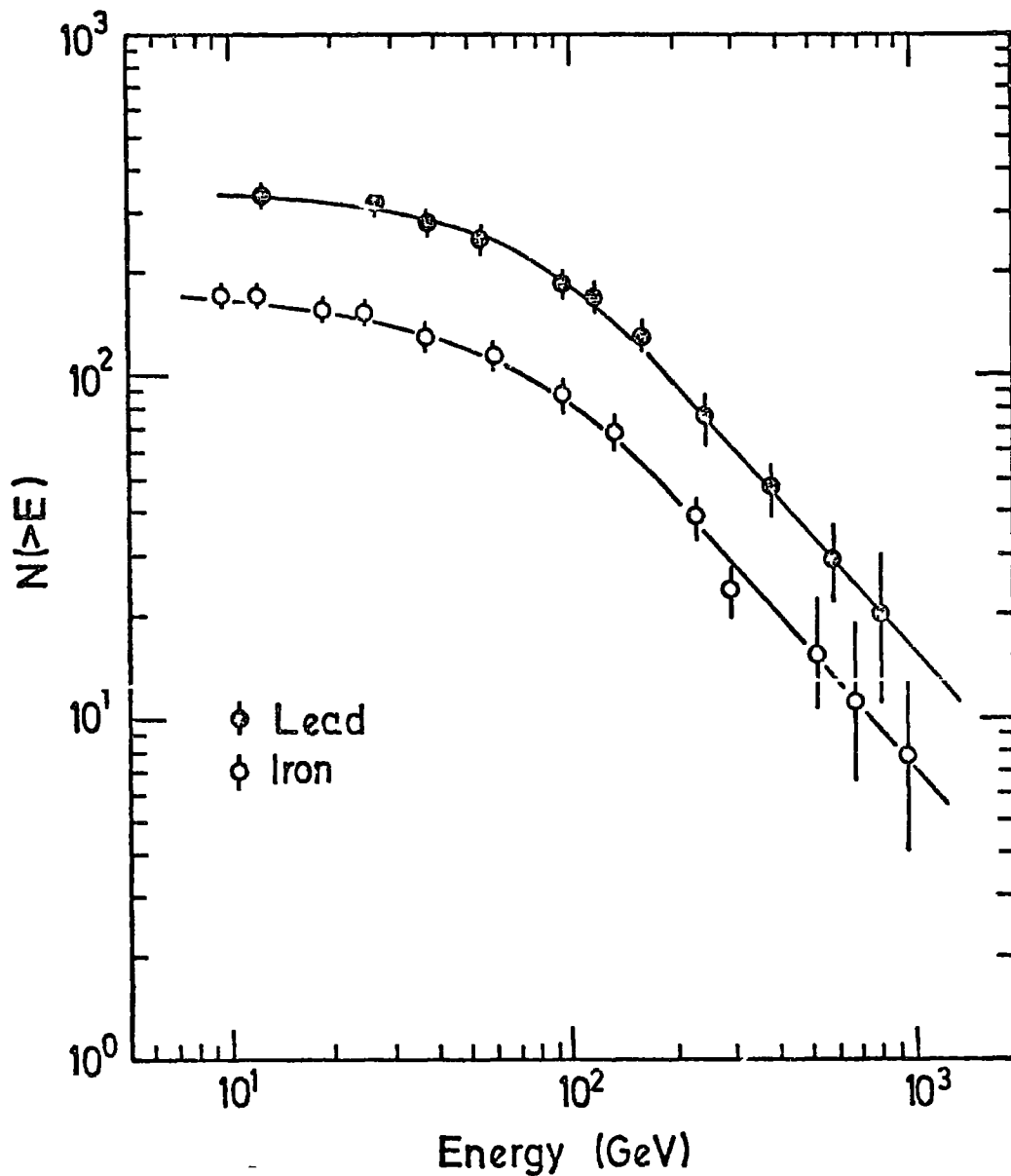


Figure 9.3

Integral energy spectra of all hadrons and charged hadrons in EAS with $\Delta e \geq 250 \text{ m}^{-2}$ measured below the lead and iron absorber respectively.

- ◆ From all measured bursts in lead.
- From measured charged bursts in iron.

9.4 Study of the muon contamination

9.4.1 General remarks

In section 9.2 it was assumed that all the bursts observed in lead and the charged bursts in iron are produced by pions and according to this assumption the energy spectra were evaluated (see figures 9.2 and 9.3). But as in every problem which deals with nuclear interaction studies the muons contribution to the measured burst spectrum must be known. In this section a prediction for the muon burst spectrum in iron and lead is made and compared with the measured burst spectrum.

9.4.2 Ratio of rate of bursts produced in lead and iron absorber

The ratio of measured bursts in lead and iron absorbers could lead to information about the contribution of muons to the measured spectra.

The ratio of the number of bursts in iron to the number of burst in lead was taken to be 0.45. This has been calculated using the constant values for the interaction length of pions in the lead and iron (see table 3.1a).

However, Figure 9.4 shows this ratio as a function of energy. The points represent the measured ratio, and it can be seen that there is good agreement between the measured and the predicted ratio (dash line). This suggests that there is no evidence for a significant muon contribution to the measured spectra.

9.4.3 Bursts produced in the flash tubes

A total of 34 events observed during this run show interactions inside the chamber with the glass of the flash tubes and the aluminium electrodes.

The interaction length of these particles interacting in the chamber could be estimated in order to produce evidence that the observed bursts are due to pions interacting rather than muons. For this purpose all the measured

charged particles producing bursts in F2 and F3 should have a track appearing in Fla and Flb, i.e. that the particle had passed through the lead and iron absorber. Each event was drawn on a small scale diagram (scale 20 : 1) and the distance from the top of F2 to the point of interaction was measured. A correction has been made to the observed frequency for the aperture of the chamber, based on the measured angular distribution of charged particle produced bursts in iron (G - series) and using the method of Lovati et al. (1954). From the angular distribution the value of n found was 8 ± 2 , where n is the exponent in the $\cos^n \theta$ angular distribution assumed.

Figure 9.5 shows this result. The best line through the corrected points has been drawn and the interaction length of particles producing bursts in the chamber was found to be $\lambda = 110 \pm 45 \text{ g cm}^{-2}$. This is consistent with the value of 130 g cm^{-2} found using Alexander and Yekutieli (1961). The above value of λ shows that bursts in glass are produced by hadrons and the contribution of muons to the bursts is not significant. Since the muon probability to produce bursts depends on the material (Z and A), so one can expect greater relative contribution in the lead and iron absorber, more than in the glass (91.5 g cm^{-2} in F2 + F3). But since the probability of hadrons traversing the lead and iron and interacting in the chamber is only 25% (see table 5.3) then one could expect that the measurement of the interaction length in the flash tubes is relevant to the consideration of the muon burst contribution in both absorbers. Plate 9.4 shows an example of a burst in the glass

9.4.4 Predicted muon burst spectrum

A calculation has been made to predict the rate of muons producing bursts in the lead and iron absorbers as another test to show the contribution of muons to the total observed bursts.

In this case the integral muon energy spectrum in extensive air showers

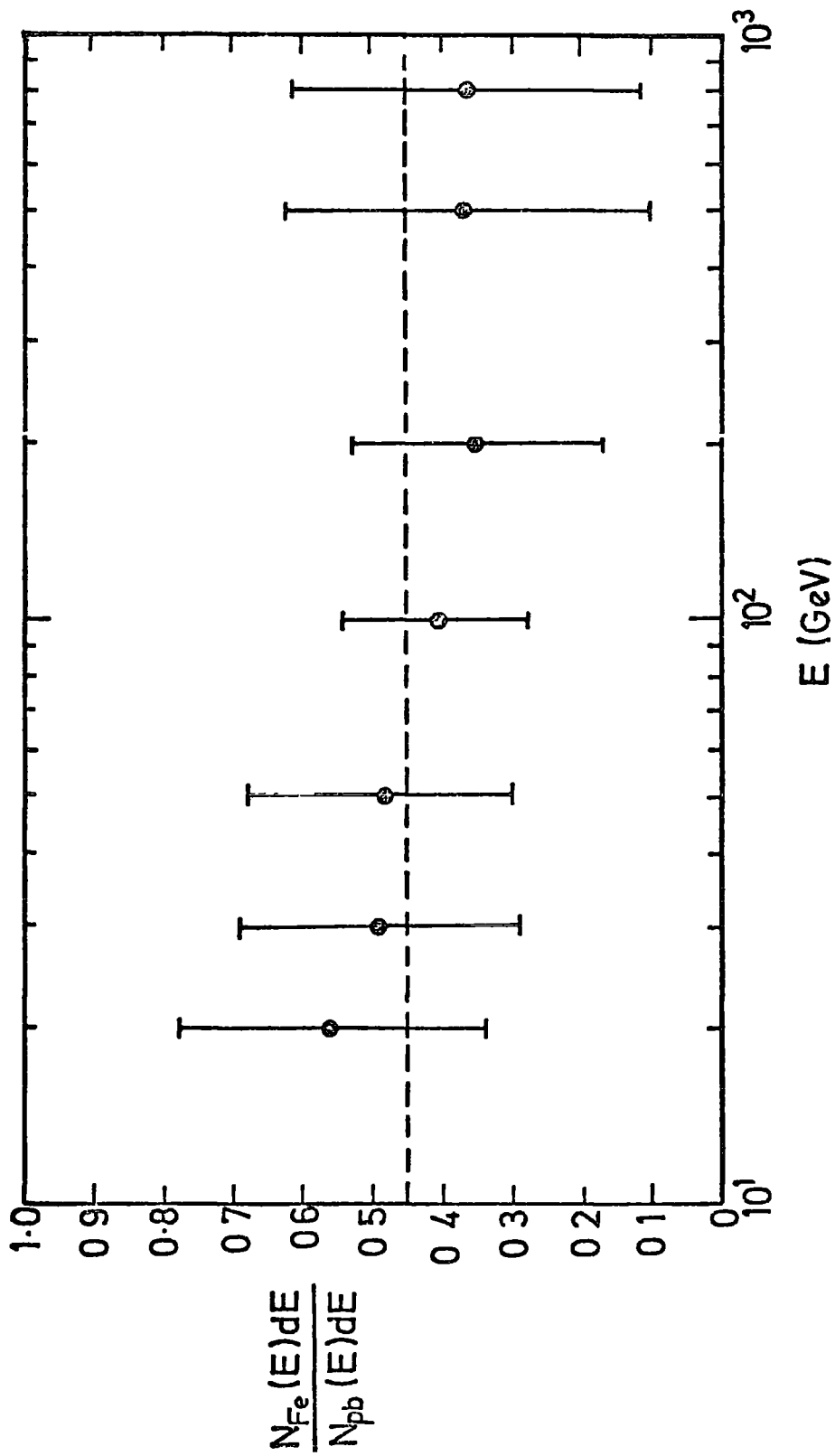


Figure 9.4.

Ratio of rate of events in the lead and iron absorber as a function of hadrons energy. The dashed line shows the predicted ratio.

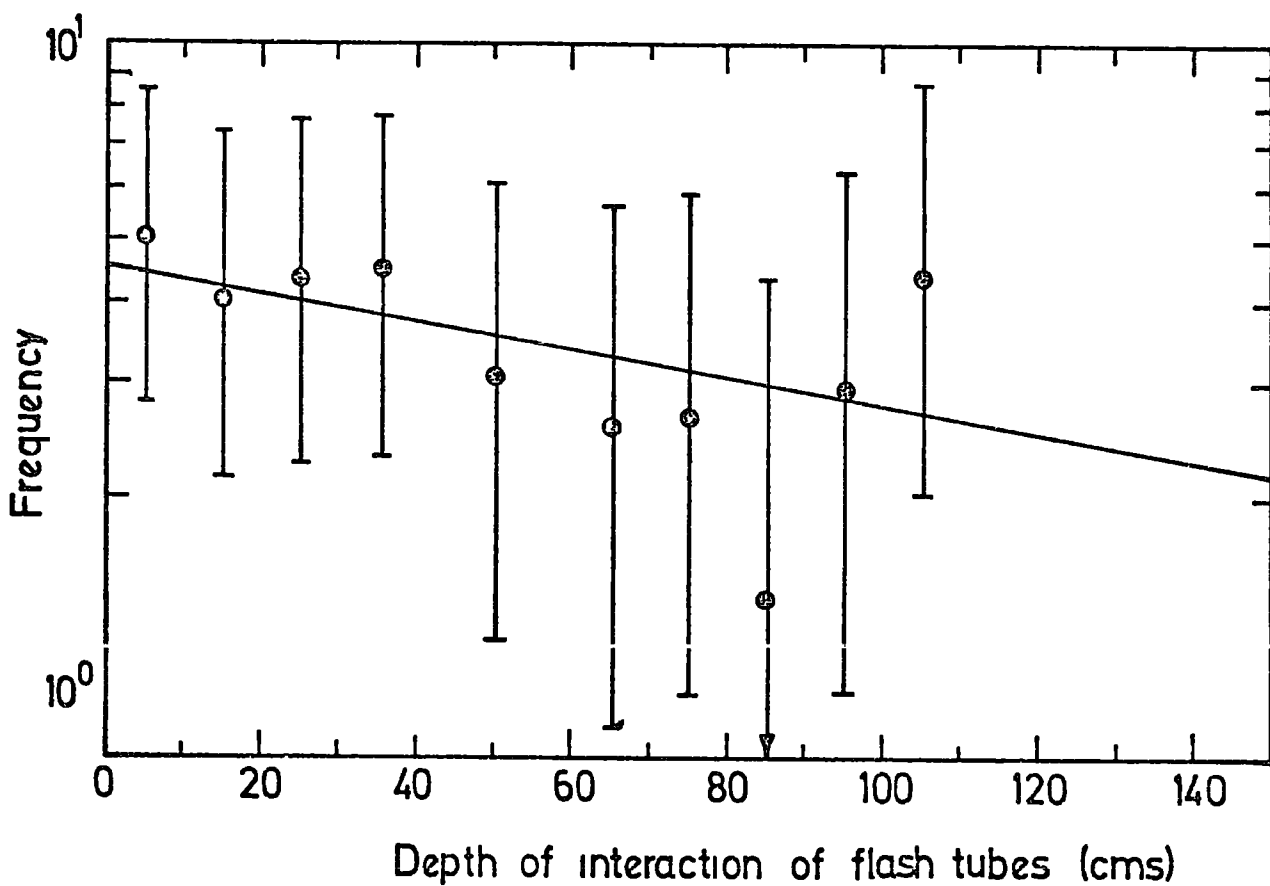


Figure 9.5

The relation between the number of bursts observed in F2 and F3 as a function of the depth of interaction measured from the top of F2. From the best line through the experimental points one can calculate the interaction length of the charged particles,
 $\lambda = 110 \pm 45 \text{ g cm}^{-2}$.

above the flash tube chamber with local electron density of $\Delta e \geq 250 \text{ m}^{-2}$ was calculated. The calculation was carried out by Parvaresh (1975, private communication). In this calculation the number spectrum given by Hillas (1970), the lateral electron density and the lateral muon density of energy $\geq E_\mu$ given by Greisen (1960) were taken. Then the integral rate of muons of energy $\geq E_\mu$ could be written as follows:

$$R(\geq E_\mu, \geq 250) = \int_{r=0.1}^{r_{\max}} \int_{N_{\min}}^{N_{\max}} 2\pi r \Delta\mu(\geq E_\mu, r, N) R(N) dN dr$$

where $R(N) dN$ is the differential number spectrum, $\Delta\mu(\geq E_\mu, r, N)$ is the lateral density of muons of energy $\geq E_\mu$ at core distance r and in a shower of size N . N_{\max} was taken to be 510^9 , N_{\min} the minimum size capable of producing a density of 250 m^{-2} at the core distance r , calculated from the electron structure function, and r_{\max} is the maximum core distance for a shower of size 510^9 .

However, to calculate the muon burst spectrum one has to take the calculated muon cross sections given in section 6.2 and fold in the above calculated muon energy spectrum. The result for the predicted muon burst spectrum in the iron and lead absorbers is shown in figures 9.6 and 9.7 respectively. Figure 9.6 shows the comparison between the predicted differential burst and energy spectra for muons and the measured hadron burst and energy spectra in iron. Similarly figure 9.7 shows this comparison in lead.

The dotted curve on the measured hadron burst spectrum shows the shape of the spectrum after subtracting the muon contribution, the contribution at larger burst sizes was very small.

From the comparison between both figures one can see that more muons

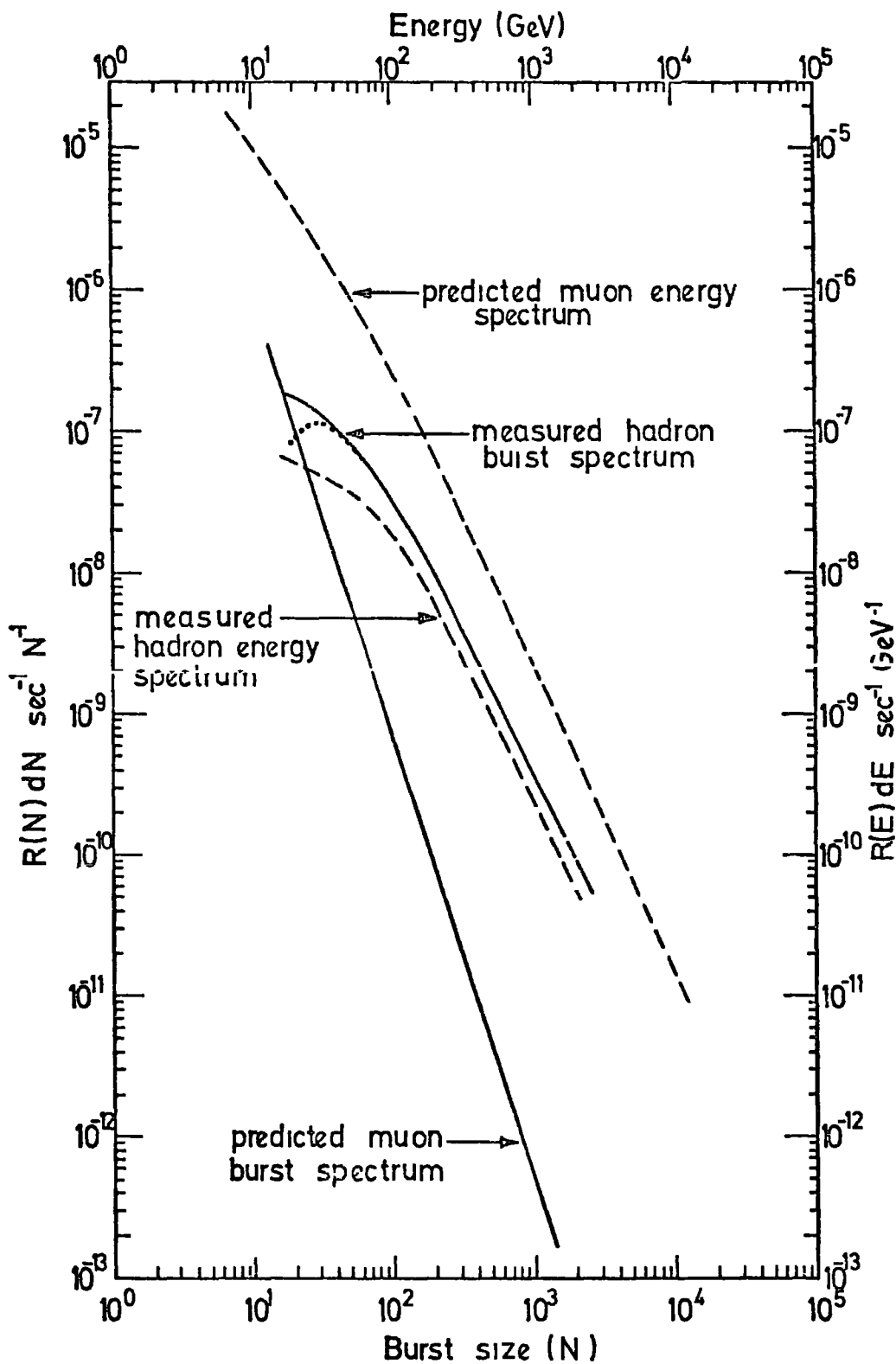


Figure 9.6

A comparison between the total burst spectrum measured below 15 cms of iron with the predicted contribution for muon induced bursts in iron. The dashed lines refer to the respective energy spectra.

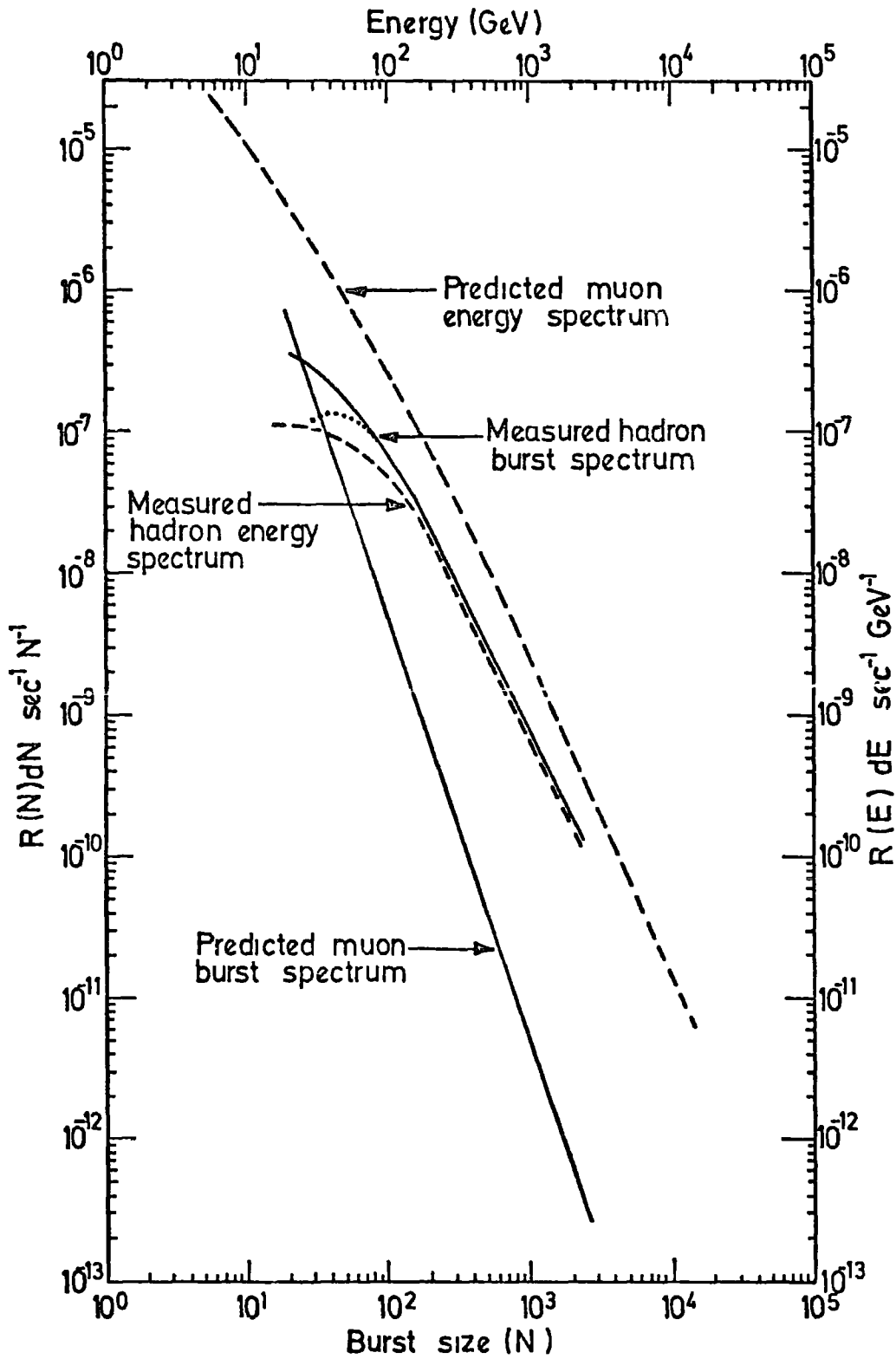


Figure 9.7

A comparison between the total burst spectrum measured below 15 cms of lead with the predicted contribution from muon induced bursts in lead. The dashed lines refer to the respective energy spectra.

could be expected in lead absorber than iron. With this prediction one could give the percentage of the contribution of muons to the measured burst at 100 GeV in iron and lead as 2% and 7% respectively.

9.5 Characteristics of hadrons in EAS

To relate the present measurement to the characteristic of hadrons in a shower of a given size, an expression is required for the density of hadrons of energy E per unit E at core distance r in a shower size N . For this purpose the results of Kameda et al. (1965) were used. They studied the density of the hadrons of energy > 100 GeV in EAS of size $4 \cdot 10^4 - 4 \cdot 10^6$, using a multiplate cloud chamber situated in the EAS array.

The expression they give for the lateral density of hadrons of energy $(E, E + dE)$ at a core distance $(r, r + dr)$ from the axis of shower size $N/10^5$ particles, and they expressed their results as:

$$n(E, r, N) dE dr = 0.35 N^{0.35} E^{-1.2} \exp\left(-\frac{r}{r_0}\right) dE dr$$

where $r_0 = 2.4 n^{0.32} E^{-0.25}$, E is in units of 100 GeV, and r in metres.

By integrating the above expression over all core distance, one obtains the number of hadrons of energy ≥ 100 GeV in a shower of size N not consistent with a following expression given in their paper. They found the number of hadrons of energy ≥ 100 GeV in a shower of size N particles is:

$$n(N, \geq 100 \text{ GeV}) = C \left(\frac{N}{10^5}\right)^{1.0 \pm 0.15}$$

where $C = 7.2 \pm 1.5$

It is, however, necessary to modify the lateral density of hadrons given by Kameda et al. in which it gives 7.2 hadrons of energy ≥ 100 GeV in 10^5 shower size.

The modified expression for the above lateral density has been calculated

and the result is shown below:

$$n(E,r,N) dE dr = 6.23 \cdot 10^{-3} N^{0.35} E^{-1.2} \exp\left(-\frac{r}{r_0}\right) dE dr \text{ m}^{-2} \text{ GeV}^{-1}$$

$$\text{where } r_0 = 0.19 N^{0.32} r^{-0.25}$$

The energy spectrum of hadrons in showers could be obtained by integrating the above expression over all core distances. Kameda et al. found that the slope of their energy spectrum to be -0.75 , while other workers (for example, Bradt and Rappaport, 1967 and Grieder, 1972 from their Monte Carlo simulations) found different slopes varying between $-(1.0 \text{ to } 1.2)$.

Since with the present experiment the N - dependence and the value of the parameter r_0 can not be checked, it was assumed that the expression given by Kameda et al. for r_0 and the size dependence are correct and a new lateral density of hadrons was assumed for the present experiment to fit the data.

This was as follows:

$$n(E,r,N) dE dr = A N^{0.35} E^{-\alpha} \exp\left(-\frac{r}{r_0}\right) dE dr \text{ m}^{-2} \text{ GeV}^{-1}$$

where $r_0 = 0.19 N^{0.32} E^{-0.25}$, with r in metres, N in unit of single particles and E in GeV.

To derive the differential energy spectrum of hadrons associated with a minimum local electron density Δe , it is necessary to evaluate numerically the following integral:

$$R(E, > \Delta e) = \int_{r=0}^{r_{\max}} \int_{N_{\min}}^{N_{\max}} 2\pi r n(E,r,N) R(N) dE dN dr$$

where N_{\min} is the minimum shower size that falls at core distance r which can produce a local electron density $> \Delta e$, $R(N) dN$ is the differential number spectrum, r_{\max} is taken to be 100 metres and N_{\max} was assumed to be $5 \cdot 10^9$.

The procedure of calculation was to find the best value of A and which fit the present measurements. To do this α was allowed to vary between 1.5 and 2.2 and for each value of α the constant A was normalised such that it gives 7.2 hadrons of energy > 100 GeV in showers of size $N = 10^5$.

The result of the calculation which shows the predicted rates of hadrons $R(> E, > \Delta e)$ for different values of local electron density trigger and $\alpha = 1.75$ are presented in figure 9.8. (Parvaresh, 1975 private communication). It was found that $\alpha = 1.75$ gives the best fit to the measured slope ($\gamma = 1.07 \pm 0.09$) of the integral spectrum of hadrons for $E \geq 200$ GeV. It should be noted that the calculations shown in figure 9.8 have been performed using the number spectrum given by Ashton and Parvaresh(1975).

The predicted spectra for $100 > E > 1,000$ GeV have been shown as dashed lines in figure 9.8 because the function which is given by Kameda et al. is valid for the energy range $100 < E < 1,000$ GeV.

The integral rates of extensive air showers producing hadrons of energy $\geq E$ GeV, when the local electron density $\Delta e \geq 250 \text{ m}^{-2}$ have been calculated as a function of shower sizes and core distances. The results are shown in figure 9.9 and 9.10 respectively.

9.6 Comparison between the measured and predicted hadron number

Using figure 9.3 the total number of hadrons of energy > 200 GeV incident from the atmosphere on the sensitive area of the chamber $1.51 \times 1.70 \text{ m}^2$ in a running time of 7,009 hours is found to be 180. This figure is calculated by adding the number of observed hadrons interacting in lead and iron and correcting this number due to the probability of interaction (see table 5.3).

Measurements on the angular distribution of hadrons about the zenith using the G - series data shows that their spatial angular distribution can be represented by $I(\theta) = I(0) \cos^n \theta$, where $n = 8 \pm 2$.

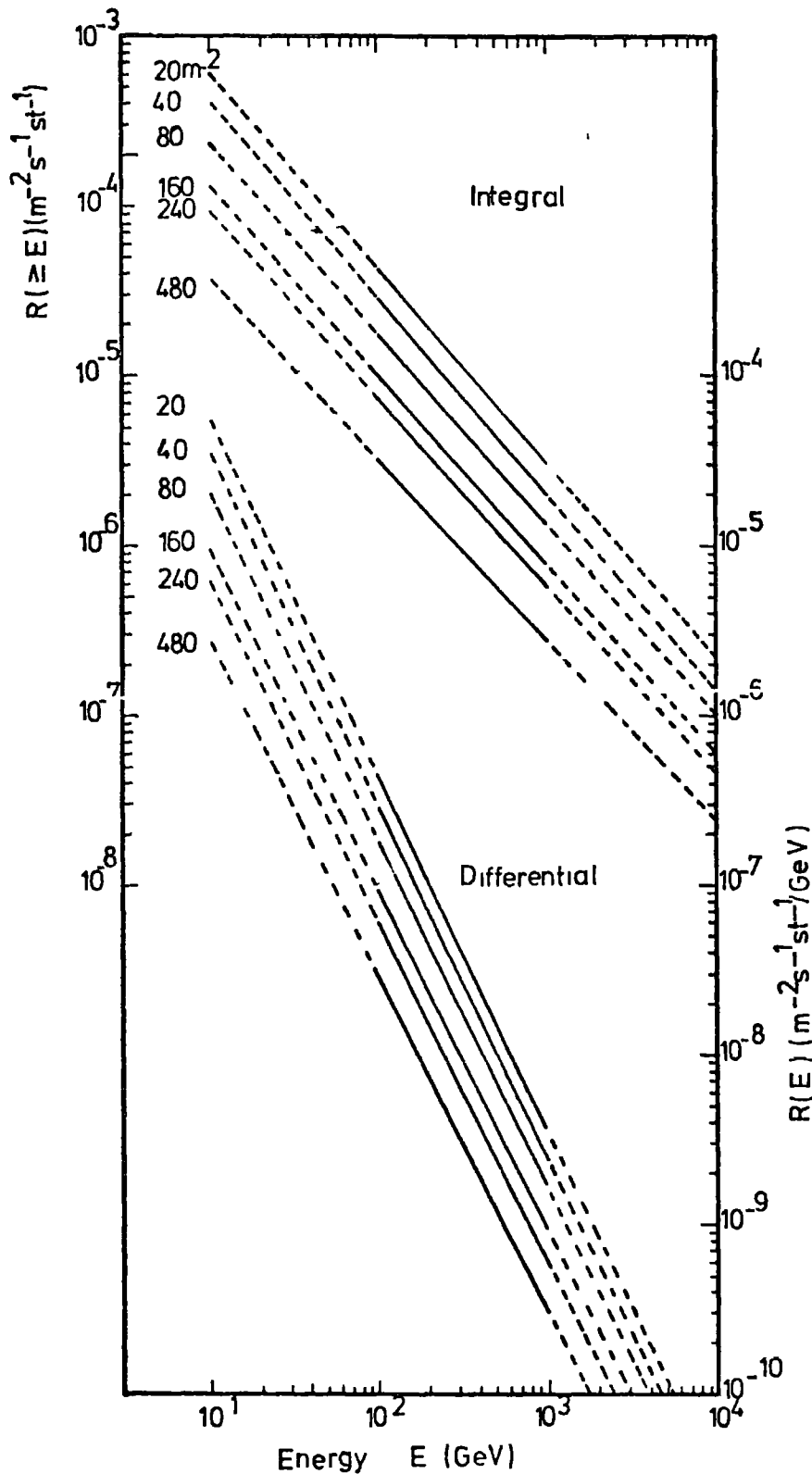


Figure 9.8

The predicted integral and differential spectra of hadrons for different values of electron density trigger $\geq \Delta e$ indicated for each spectrum. The procedure of calculating these curves is given in the text. After Parvaresh (1975).

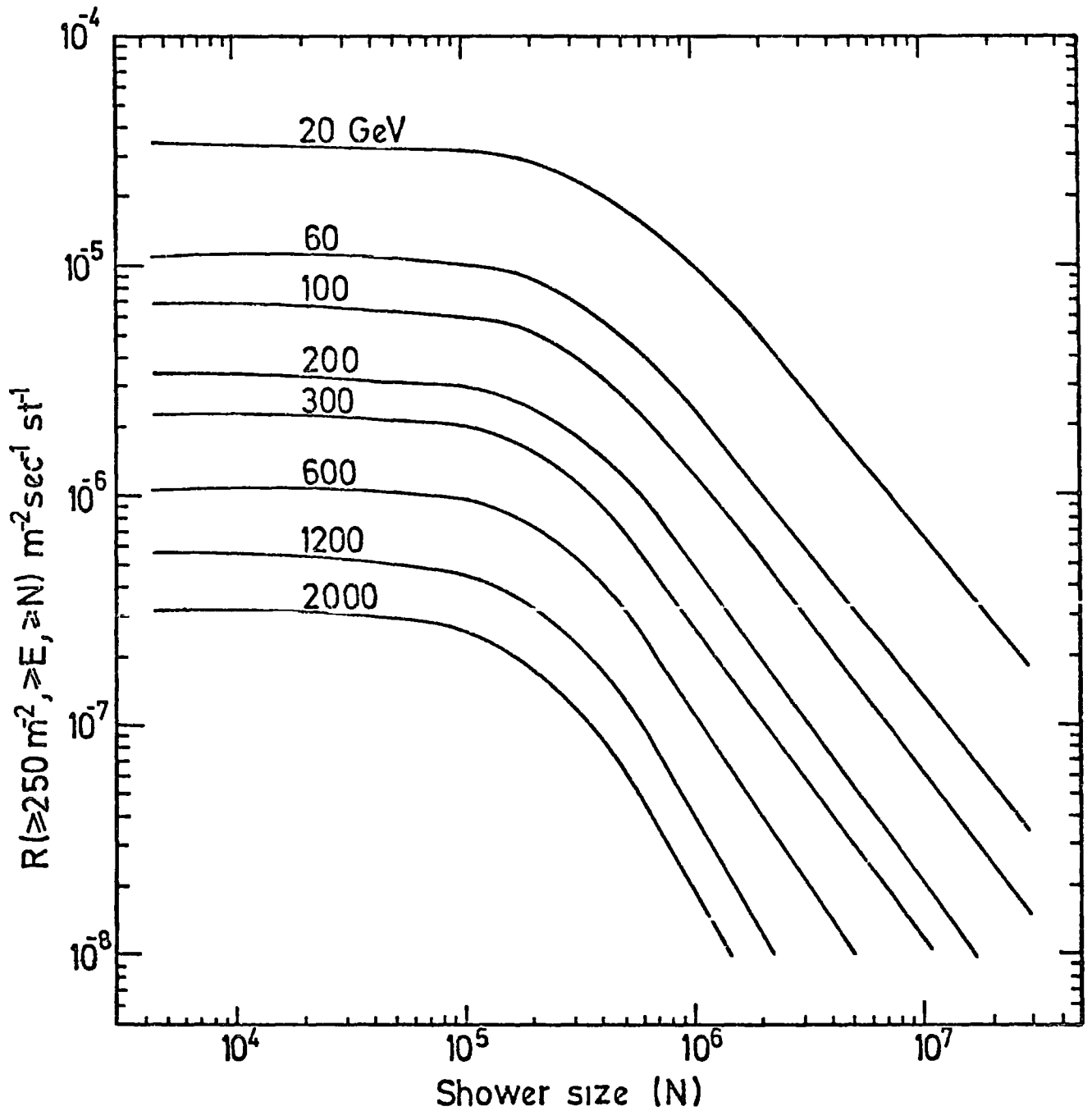


Figure 9.9

The calculated integral rate of hadrons of energy $\geq E$ produced in shower or size $\geq N$ in a detector. The number attached to each curve represents the hadron energy in GeV. (see text for more details).

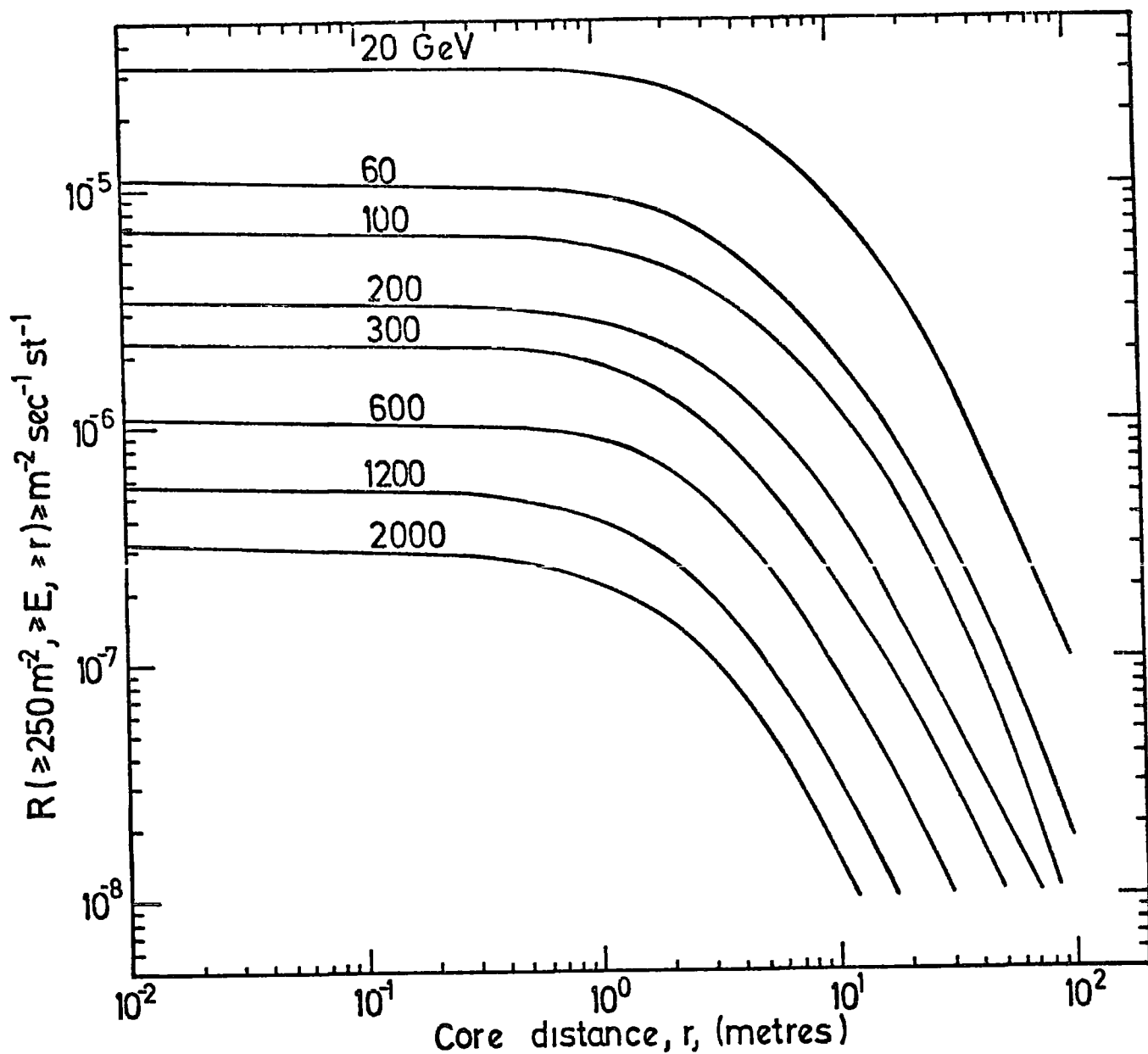


Figure 9.10

The calculated integral rate of EAS falling at core distances $\geq r$ metres in a detector producing hadrons of energy $\geq E$. The numbers attached to each curve represents the hadron energy in GeV. (see text for more details).

The total intensity $I(T)$ of hadrons per unit area is therefore related to their vertical intensity $I(0)$ by:

$$I(T) = I(0) \cdot \frac{2\pi}{n+2}, \text{ where } \frac{2\pi}{n+2} \text{ (Solid angle factor)} = 0.57 \pm 0.11 \text{ st.}$$

Taking the above figures the rate of measured hadrons of energy $E \geq 200 \text{ GeV}$ is $4.8 \cdot 10^{-6} \text{ sec}^{-1} \text{ st}^{-1} \text{ m}^{-2}$.

This can be compared with the predicted rate of hadrons of energy $\geq 200 \text{ GeV}$ and associated with vertical showers giving a local electron density $\geq 250 \text{ m}^{-2}$ of $3.5 \cdot 10^{-6} \text{ sec}^{-1} \text{ st}^{-1} \text{ m}^{-2}$. There is reasonable agreement between the predicted and measured rate of hadrons.

However, the present measurements suggest that for hadrons of energy E in the range $200 < E < 1,000 \text{ GeV}$ the lateral density of hadrons could be represented as follows:

$$n(E, r, N) dE dr = 0.26 N^{0.35} E^{-1.75} \exp\left(-\frac{r}{r_0}\right) dE dr \text{ m}^{-2} \text{ GeV}^{-1}$$

where $r_0 = 0.19 N^{0.32} E^{-0.25}$ with E in GeV and N in units of single particles.

Integrating the above expression over core distance and hadron energy gives the total number of hadrons of energy $\geq E \text{ GeV}$ in shower of size N .

$$N(\geq E, N) = \int_E^\infty \int_{r=0}^\infty 2\pi r n(E, r, N) dr dE$$

$$= 0.045 N^{0.99} E^{-1.25} \text{ where } N \text{ is in units of single particles}$$

and E in GeV.

The present calculation shows that 80% of the hadrons of energy ≥ 200 GeV measured in this experiment are produced by showers in the size range $1.3 \cdot 10^5 - 8.0 \cdot 10^5$. This was calculated using figure 9.9 which shows that in regions of EAS of local density $\geq 250 \text{ m}^{-2}$, hadrons of this energy accompanied the shower in 80% of the triggers.

Table 9.2 shows a summary of the two previous experiments and the present experiment which have been made with the flash tube chamber to study the number of hadrons in EAS. In this table the shower size range for each run is given with the expressions showing the number of hadrons of energy $\geq E$ in showers of size N . It should be noted that in both previous measurements the same technique was used to evaluate the number of hadrons $\geq T$ GeV.

Figure 9.11 shows the number spectrum of hadrons of energy ≥ 200 GeV per shower as a function of shower size for the three results. Good agreement between the three results is obtained.

Figure 9.12 shows also the comparison of the number of hadrons per shower obtained from different experiments at sea level and different theoretical predictions. In this figure the experimental results of Kameda et al. (1965) and Tanahashi (1965) were compared with the present results and it was found that the Kameda et al. results are in good agreement with the present results but there is some inconsistency for shower sizes less than 10^5 particles between the present results and those of Tanahashi. This discrepancy could be due to the lateral density expression of hadrons given by Kameda et al. which is not corrected for the smaller shower size.

The theoretical calculations (Monte Carlo) also were shown with two different models. Greider (1970) has produced two models so called IDFB* and SFB*. In both models the assumption has been made that $N\bar{N}$ are produced in high energy interactions. Both models have a different multiplicity

Trigger electron density, $\geq \Delta e$	Shower size, N range	Number of hadron ($\geq E, N$) =	Reference
20 m^{-2}	$7 \cdot 10^3 - 8 \cdot 10^4$	$0.047 N^{0.99} E^{-1.2}$	Ahston et al. (1975)
80 m^{-2}	$2 \cdot 10^4 - 4 \cdot 10^5$	$0.040 N^{0.99} E^{-1.25}$	Parvaresh (1975)
250 m^{-2}	$1.3 \cdot 10^5 - 8 \cdot 10^5$	$0.045 N^{0.99} E^{-1.25}$	Present result

Table 9.2 Summary of the flash tube clamper results on the number of hadrons per shower as a function of shower size.

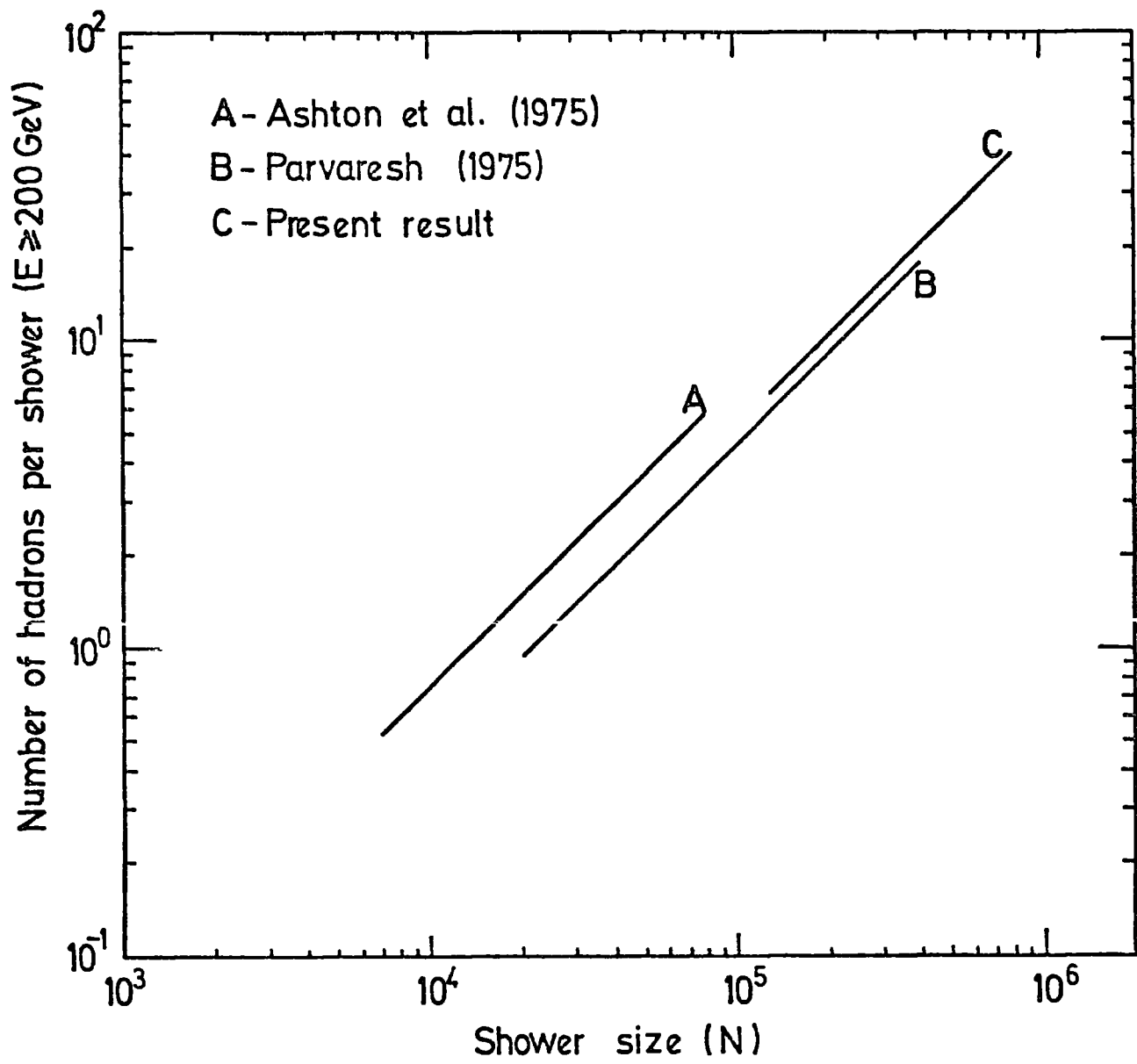


Figure 9.11

Variation of the total number of hadrons of energy ≥ 200 GeV with shower size. (see table 9.2 for more details).

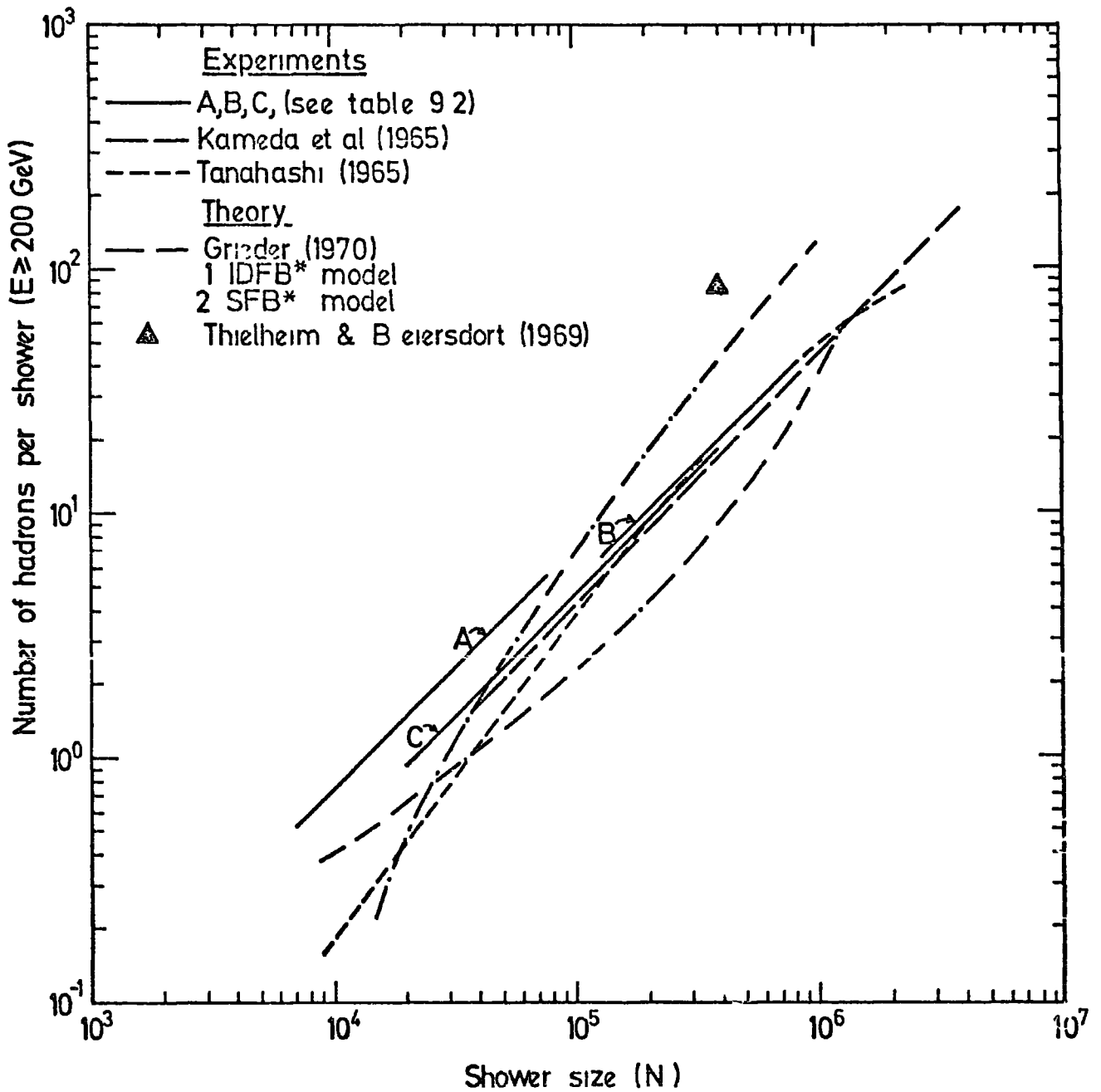


Figure 9.12

Comparison between the measured and predicted number of hadrons of energy $E \geq 200$ GeV at sea level as a function of shower size. The flash tube chamber results are shown as curves A, B and C.

form, so for IDFB* the multiplicity was $n_s \propto E^{3/8}$ and for SFB* was $n_s \propto E^{1/2}$. No agreement was found with the experimental data.

9.7 Conclusion

The energy spectra of hadrons in extensive air showers at sea level has been obtained from measuring the burst width in the flash tubes.

In converting from burst width, to burst size, to energy all the bursts observed in lead have been assumed to be produced by π^\pm , and for iron the charged bursts are assumed also to be produced by π^\pm .

The energy spectra have been measured in the energy range $10 < E < 1,000$ GeV, and a slope of $\gamma = 1.07 \pm 0.9$ has been found for the integral spectra of energy > 200 GeV.

Investigations have been made to study the muon contribution to the measured burst spectrum. The rate of muon induced bursts in the iron and lead absorbers was calculated and it was found that only 2% and 7% of the muons contribute to the measured bursts at energy 100 GeV in iron and lead respectively. So it was suggested that the contribution of muon bursts to the total measured bursts was small and neglected. The energy spectrum was related to shower characteristics by adopting a parameterisation of the form obtained by Kameda et al. (1965). The results of the number of hadrons of energy ≥ 200 GeV in showers of size $1.3 \cdot 10^5 - 8.0 \cdot 10^5$ was determined and compared with different results. Good agreement was found with other experimental results but not with the prediction.

From the charge to neutral ratio one could explain the behaviour of high energy collision, but since only 4 events were observed as bursts produced by neutral particles (the loss of neutral particle bursts could be due to the effects explained in the text) the ratio can not be given accurately.

CHAPTER 10SUMMARY

The study of the strongly interacting particles in cosmic rays has been carried out using a flash tube chamber in an attempt to understand the nature of these particles.

A vertical burst experiment has been performed with the flash tube chamber and a measurement of the hadron energy spectrum has been made in the energy range 10 GeV - 10 TeV. According to the Baruch et al. (1973) measurements the spectrum has a step in the region of 2 - 8 TeV. They explained such an effect is due to the existence of a new particle of rest mass in the range 40 - 70 GeV/c², mean life time $> 2 \cdot 10^7$ second and interaction length of $1,000 \pm \frac{1,000}{700}$ g cm⁻². The present result on the energy spectrum shows a constant slope of $E^{-2.7 \pm 0.1}$ over the energy range 10 GeV to 10 TeV and does not support the observation made by Baruch et al. However, it is concluded that if such a step exists as a real effect and has been observed by Baruch et al. then it must be seen in the present experiment.

More recently, a paper by Baruch et al. (1975) states:

"The argument for the existence of the Mandela, given by Baruch et al. (1973) was based mainly on the observation 'step' in the sea level hadron spectrum. We now know that this step was due to a fault in the initial storage of the signals from the proportional counter."

However, according to this paper the electronic fault now has been corrected and the apparatus modified by adding neon flash tubes to measure the zenith angle distribution and to identify the incoming particles. The hadron spectrum measured in 26 days with the new arrangement is shown in figure 10.1. Their new measurements are in good agreement with the present

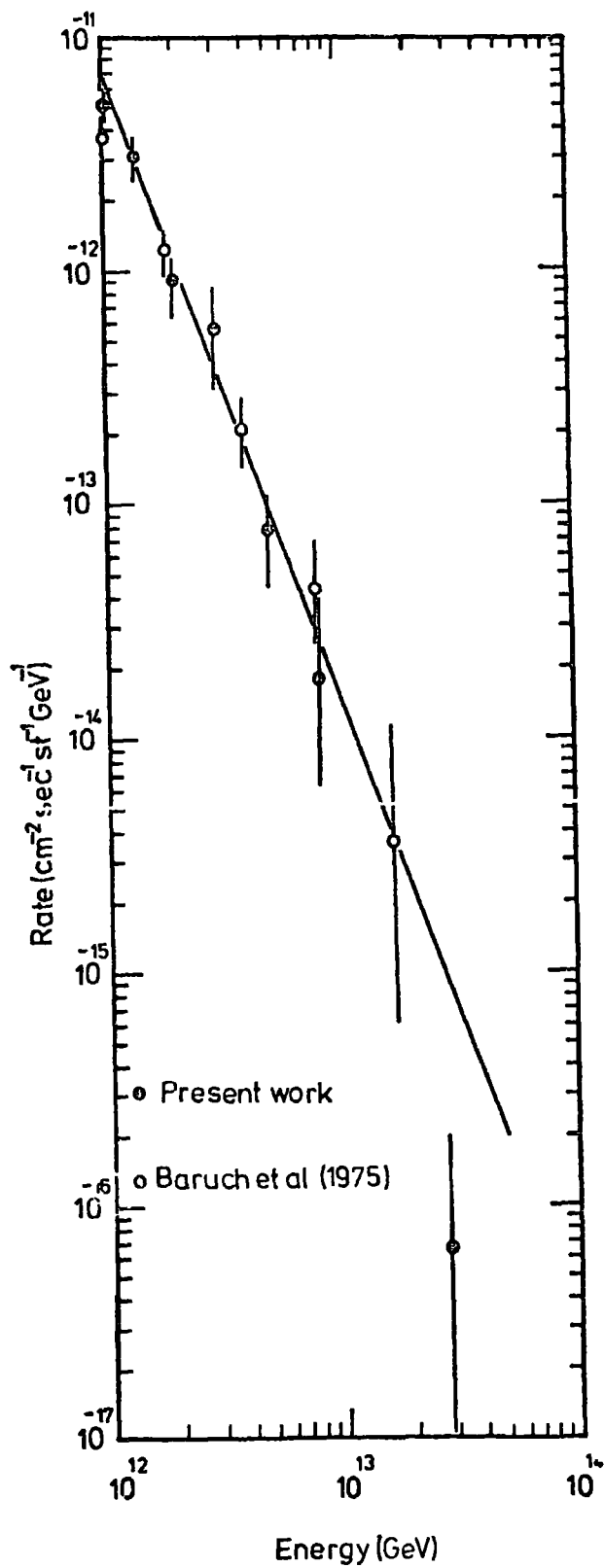


Figure 10.1

The vertical differential energy spectrum of hadron at sea level. A comparison is made between the present results for energies > 1 TeV and the more recent results given by Baruch et al. (1975). The spectrum can be represented by the form $R(E) = AE^{-2.7}$.

work and a slope of $\gamma = 2.7$ for the differential spectrum is found.

A measurement of the sea level neutron energy spectrum has been made with the present experiment in the energy range 30 - 1,000 GeV. The spectrum was found to be in good agreement with the neutron measurements summarised by Ahston et al. (1970). At lower energy the spectrum is also found to be in good agreement with proton measurements of Brooke and Wolfendale (1964) and Diggory et al. (1974). The measured spectrum has been represented by a power law of the form $E^{-2.9 \pm 0.1}$ in the energy range 50 - 1,000 GeV.

The pion energy spectrum has been derived from the total burst spectrum measured in the chamber after subtracting the nucleon burst spectrum and the muon contamination. The results obtained on the pion spectrum gave a rapid variation in the ratio of pions to proton as the energy increases. In the lower energy region the results of Brooke et al. (1964) and Diggory et al. (1974) have been found to be in good agreement with the present results.

An extensive air shower experiment has been set up to search for quarks near the core of EAS using the flash tube chamber as a visual detector.

Although the quark model has provided useful information to understand the observed multiplet structure of elementary particles, there is as yet no strong evidence of the existence of the quarks. In this experiment the chamber was run for 7,009 hours using a master trigger EAS producing a local electron density $\geq 250 \text{ m}^{-2}$. Two events observed were explained later as due to background incoherent muons traversing the chamber in the time period 103 - 144 μs before the EAS trigger. An upper limit was given on the flux of $\frac{e}{3}$ quarks at sea level of $< 4.3 \cdot 10^{-11} \text{ cm}^{-2} \text{ sec}^{-1} \text{ st}^{-1}$. Possible modifications to the flash tube chamber to improve the technique were suggested in section 8.8.

It has been shown that the technique of measuring cascade widths below thick absorbers is a valid method of measuring the energy spectra of hadrons. The integral spectra which have been measured in lead and iron absorber show a slope of 1.07 ± 0.09 for energy > 200 GeV. The number of hadrons with energy > 200 GeV have been evaluated and compared with other experimental results and theoretical predictions.

At present, a small air shower array has been constructed around the flash tube chamber in order to give information on the shower size and the core distance for each event accompanied by a shower. With this arrangement, hadrons in air showers will be studied in more detail.

Finally, one of the results provided by this experiment is the detection of highly ionising particles as magnetic monopoles. Briefly a high ionising track should be observed at these long time delays, whereas normal tracks due to charge e particles will not be seen. This will be discussed in Appendix B.

APPENDIX ADERIVATION OF A HADRON BURST SPECTRUM IN 15 CM OF LEAD

A hadron burst spectrum was derived in a 15 cm of lead absorber using the results of the calculations introduced in Chapter 3 and the assumed sea level differential hadron energy spectrum.

The procedure in the calculations to derive this spectrum was the same as the one discussed in section 5.8. The aim of these calculations was made in order to re-examine the effect of fluctuations on the measured burst size spectrum.

In section 5.8 this was discussed using the sea level hadrons energy spectrum given by Baruch et al. (1973) with a step in the spectrum in the region of 2 - 8 TeV. (see section 5.8 for more details).

In this appendix another case was taken where the spectrum has a constant slope, $\gamma = 2.8$. However, one can briefly discuss the procedure of this calculation again as follows:

The differential spectrum was divided into many cells and for each cell the number of events in units of $\text{cm}^{-2} \text{sec}^{-1} \text{sr}^{-1}$ was calculated. The burst size distributions (N_e) as a function of the depth of interaction in the lead absorber was used. These distributions have been calculated for different primary particles (protons), (see figure 3.11).

From the above distributions the probability that a primary proton incident on the lead absorber produces a burst size N per unit N was calculated.

Now the above probabilities were folded into the frequency of each cell and the expected shape of the burst spectrum observed in the lead is shown in figure A.1. The predicted burst spectrum shows a slope of $\gamma = 2.8$ also. To derive the energy spectrum from the above predicted burst spectrum the burst size - energy relationship was used assuming the incident primary particles to be protons (see figure 3.7). The spectrum was corrected for

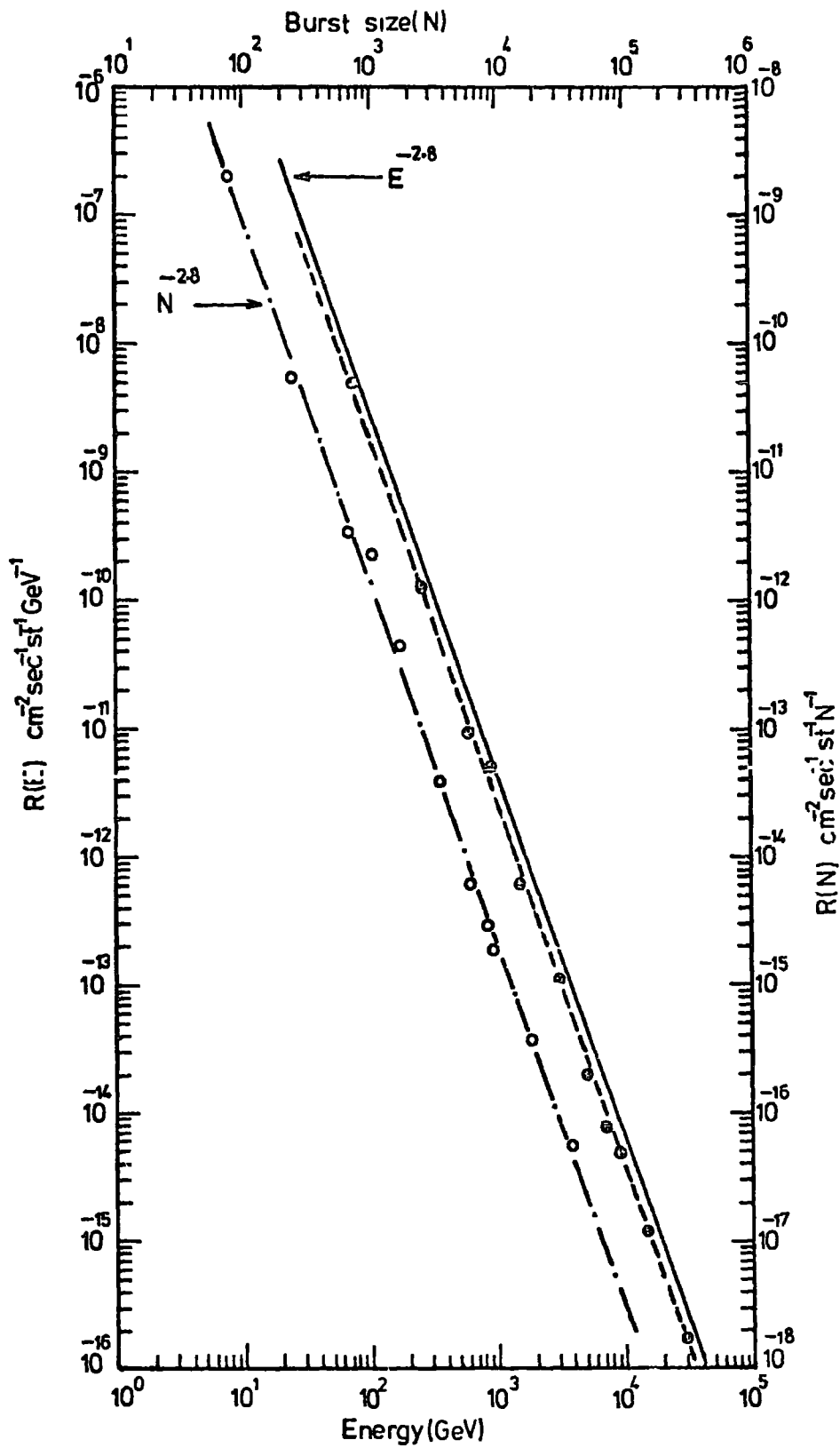


Figure A.1.

Predicted hadron burst spectrum under 15 cm of lead. The solid line with $E^{-2.8}$ represents the selected differential energy spectrum. The open circles show the predicted burst spectrum derived from the above energy spectrum, $N^{-2.8}$. The solid circles show the energy spectrum derived from the predicted burst spectrum using the average relation between burst size and primary energy.

the probability of protons which did not interact in lead. The derived energy spectrum is also shown in the same figure A.1. The energy spectrum shows a slope of $\gamma = 2.8$ also.

Although there is a factor of about 1.5 difference in the intensity between the two energy spectra the slopes of the two spectra are the same.

APPENDIX BSEARCH FOR THE MAGNETIC MONOPOLEB.1 Introduction

In 1931 Dirac introduced a mathematical prediction for the existence of magnetic monopoles. These monopoles are interesting as they appear to be the only way of explaining the quantization of electric charge. However, according to Dirac (1931, 1948), if the fundamental electric charge is e then the monopoles of fundamental strength $g = n \frac{\hbar c}{2e}$, $n = 1, 2, 3, \dots$ should exist, where $\frac{\hbar c}{e^2}$ is the reciprocal of the fine structure constant = 137.

Schwinger (1966) predicts that the monopole's charge is twice that Dirac deduced, i.e. $g = n \frac{\hbar c}{e}$, $n = 1, 2, 3, \dots$. So, if the quarks with $e/3$ charge exist then the values of g becomes $\frac{3\hbar c}{2e}$ and $\frac{3\hbar c}{e}$ respectively. Thus, the detection of monopoles with $g = \frac{\hbar c}{2e}$ or $\frac{\hbar c}{e}$ would indicate that the quarks with fractional charge do not exist. The main characteristic of monopoles is their very large rate of ionization loss in matter (Bauer 1951, Cole 1951). So, for relativistic monopoles the track they produce in any visual detector shows a similar structure to those produced by high Z nuclei. Table B.1 shows a summary of some expected properties of monopoles. The production of monopoles is expected to be similar to those producing electron - positron pairs and the following process shows this: Ashton (1973).

$$\gamma + P \longrightarrow P + g + \bar{g}$$

$$P + P \longrightarrow P + P + g + \bar{g}$$

Author	Fundamental electric charge	Fundamental monopole strength, g .	$\frac{dE}{dx}$ GeV cm^{-1} cm^{-2}	Z of nucleus with same $\frac{dE}{dx}$	Ionisation loss in penetrating the atmosphere to sea level
Dirac	e	$\frac{hc}{2e}$	9.4	68.5	$9.4 \cdot 10^{12}$ eV
Dirac	$e/3$	$\frac{3hc}{2e}$	24.6	205.5	$8.5 \cdot 10^{13}$ eV
Schwinger	e	$\frac{hc}{e}$	36.6	137	$3.8 \cdot 10^{13}$ eV
Schwinger	$e/3$	$\frac{3hc}{e}$	329.4	411	$3.4 \cdot 10^{14}$ eV

Table B.1. Expected properties of magnetic monopoles corresponding to fundamental electric charges e and $e/3$. After Ashton, (1973).

B.2 Previous monopole searches

Cosmic ray searches for monopoles have been performed by many groups: Ashton et al. (1969b) searched at sea level for monopoles using scintillation counters and flash tubes. They demanded a pulse produced by monopoles of greater than 4,000 times the pulse height produced by single particle muons. No events were observed and a flux limit of less than $1.3 \cdot 10^{-10} \text{ cm}^{-2} \text{ sec}^{-1} \text{ st}^{-1}$ was given. Erlykin and Yakovlev (1969) have used ionisation calorimeter to search for monopoles with $g = \frac{\hbar c}{2e}$ and the flux limit they produced is $< 2.5 \cdot 10^{-12} \text{ cm}^{-2} \text{ sec}^{-1} \text{ st}^{-1}$ for energy $E > 10^{13} \text{ eV}$ and less than $7 \cdot 10^{-13} \text{ cm}^{-2} \text{ sec}^{-1} \text{ st}^{-1}$ for $E > 3 \cdot 10^{13} \text{ eV}$.

Fleischer et al. (1971) have produced a negative result using an 18 m^2 area lexan polycarbonate array exposed at sea level and the flux at sea level they found to be $< 1.5 \cdot 10^{-13} \text{ cm}^{-2} \text{ sec}^{-1} \text{ st}^{-1}$.

Yock (1975) searched for the heavy mass highly charged particles in cosmic rays, no candidates were detected and an upper limit of $7 \cdot 10^{-10} \text{ cm}^{-2} \text{ sec}^{-1} \text{ st}^{-1}$ at sea level under 600 gm/cm^2 concrete was obtained with 90% confidence level.

In accelerator work searches also have been made for monopoles and a 30 GeV proton accelerator experiment of Amaldi et al. (1963) and Purcell et al. (1963) show that the monopoles mass is greater than $2.8 \text{ GeV}/c^2$ if they exist.

Gurevich et al. (1972) used a 70 GeV proton accelerator and they have given the production cross section $\sigma < 1.4 \cdot 10^{-43} \text{ cm}^2$ for $Mg < 4.9 \text{ GeV}/c^2$.

A search for monopoles in p-p collision was performed at CERN - ISR by Giacomelli (1975). The experiment was sensitive for monopoles of mass $Mg < 30 \text{ GeV}$. The search yielded an upper limit on the production cross-section of $\sigma < 2 \cdot 10^{-36} \text{ cm}^2$ at 90% confidence level.

B.3 Present search

The advantage of the technique performed in the vertical burst experiment as described in chapter 4 has been used to search for monopoles in cosmic rays. This search was made while the chamber was run on a long time delay of $330 \mu s$. In this time delay, if a burst occurred in the iron absorber the track which indicated the incoming particle can not be seen in Fla. Therefore, it was suggested that if monopoles exist then they could be seen in the chamber and their detection will be by pulses recorded from scintillators C and A due to bursts produced in lead and iron (see figure 4.9) and the appearance of an efficient track in the chamber associated with bursts. However, in scanning a definition was assumed to look for these high efficiency tracks.

Two types of events were observed from the data taken from the H - series, (a) events showing only a single track in the chamber with no burst width observed on the flash tubes and a pulse height corresponding to a burst size N_e either in scintillator A or scintillator B, (b) events showing a single track appearing in the flash tube layer Fla and a burst observed in the chamber under a 15 cm iron absorber.

9 events were observed and classified as type (a) events. Table B.2 shows more details about these events. According to this table no event shows a burst size in both scintillators due to the passage of a single particle. Plate B.1 shows an example of this type of event. Figure B.1 and B.2 show the relationship which has been measured in chapter 4 for the number of flash tubes flashed between ± 0.5 cm on the scanning sheets (scale 1 : 20) from the core of the cascade over the flash tube layer Fla or Flb (Fla and Flb are the flash tube layers under the lead and the iron respectively) and the burst size recorded either in scintillator C or A. The results of those 9 events (see table B.2) are plotted in the figures B.1 and B.2 as crosses.

Event	Burst occurred in	No. of flashes along the track in,		Burst size (N) in scintillator	
		Fla	Flb	A	C
H42-34	Fe	4	3	950	-
H51-13	Fe	5	3	1,500	-
H53-62	Fe	7	6	1,025	-
H55-10	pb	7	5	-	2,600
H55-11	Fe	3	3	675	-
H56-15	Fe	4	3	1,225	-
H56-35	Fe	6	5	675	-
H63-13	pb	4	3	-	1,400
H77-36	Fe	7	6	825	-

Table B.2.

Experimental details about the 9 events observed in the flash tube chamber (type (a) event), these events show only a single track traversing the chamber and a pulse height corresponding to a burst size (N) either in scintillator A or C with no burst width seen in the flash tubes.

(Fla and Flb are the flash tube layers under the lead and iron respectively).

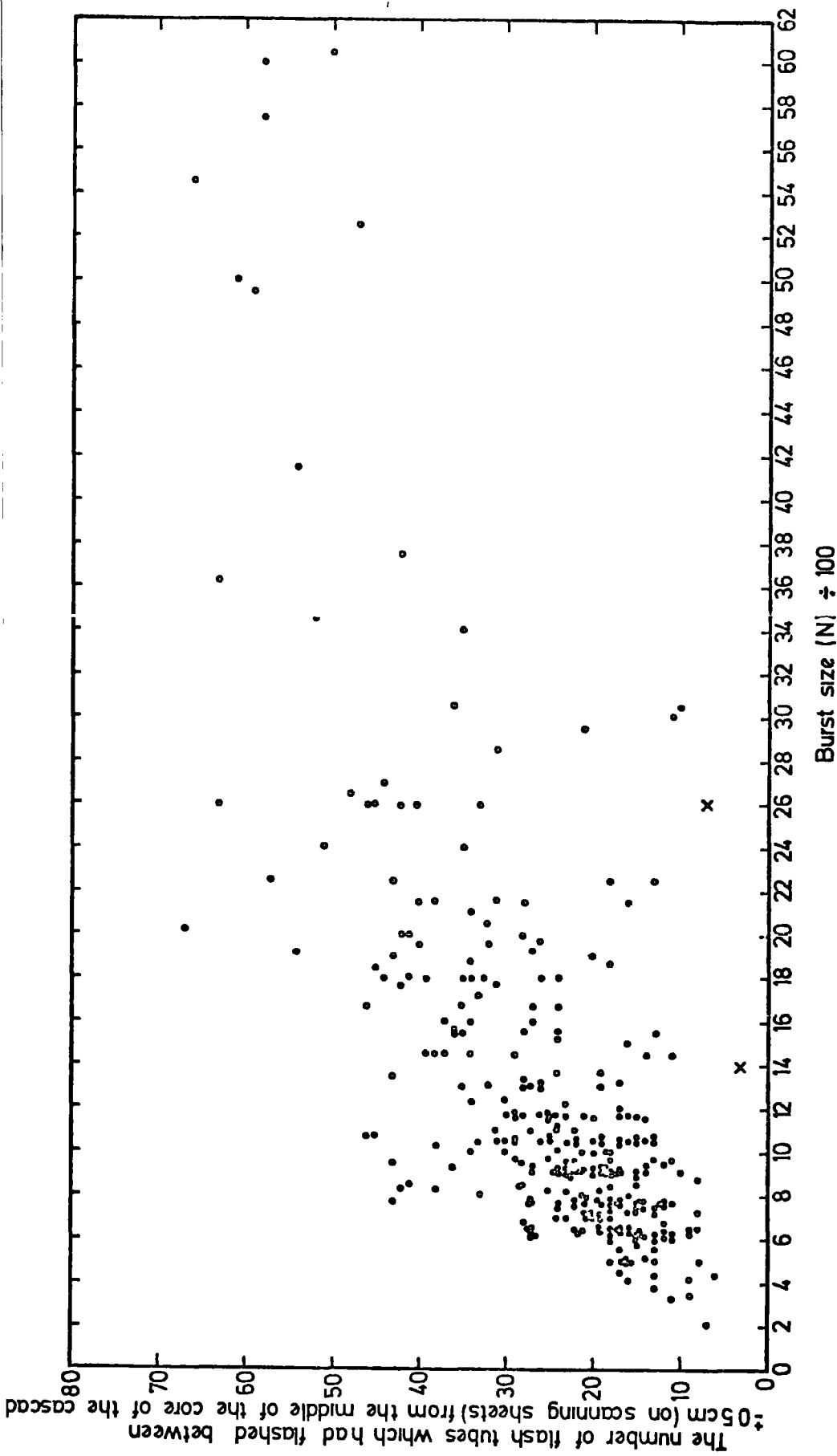


Figure B.1.

Scatter plot showing the relation between burst size (N) measured in scintillator C (burst in lead) and the number of flash tubes which had flashed between ± 0.5 cm from the middle of the core (1 cm full width) on scanning sheets (scale 1:20) (see section 4.4.3 for more details).

The crosses show the two events which were observed as a single track with a burst produced in lead (see table B.2.).

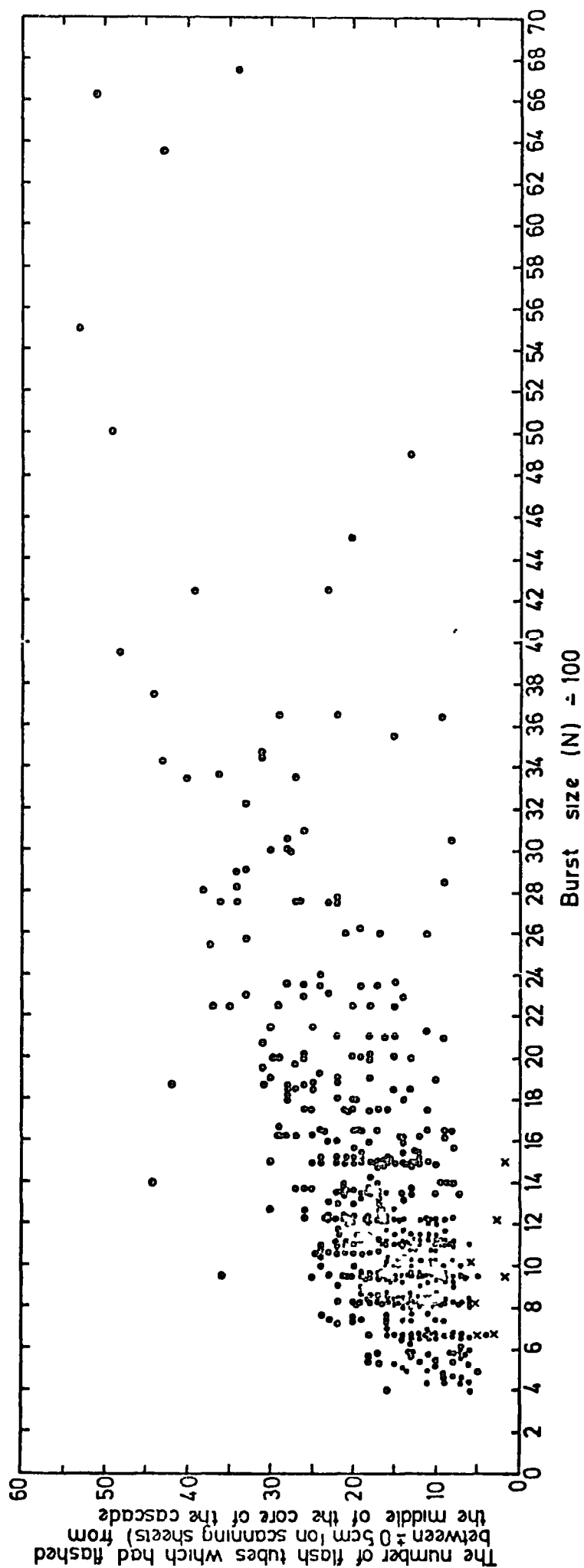


Figure B.2. Scatter plot showing the relation between burst size (N) measured in scintillator A (burst in iron) and the number of flash tubes which had flashed between ± 0.5 cm from the middle of the core (1 cm full width) on the scanning sheets (scale 1:20) (see section 4.4.3 for more details). The crosses show the 7 events which were observed as a single track with a burst produced in iron (see table B.2.).

These type of events can be explained as background muons traversing the chamber within the $350 \mu\text{s}$ time delay. They are probably caused by large angular bursts which trigger the chamber but the core of the cascade missed the flash tubes.

One event was observed of type (b) and this is shown in plate B.2. This type of event is explained by the calculations made by Ward (1975), private communication as being due to a young burst produced in the last few radiation lengths in lead absorber and the secondary pions emerged from the absorber close together fall on the flash tube layer Fla within one tube. So a track could be seen in Fla and a burst in the chamber could be observed due to these pions interacted in iron absorber.

With no genuine events having been detected the upper limit could be set at 90% confidence level for these monopoles as $< 2.5 \cdot 10^{-11} \text{ cm}^{-2} \text{ sec}^{-1} \text{ st}^{-1}$.

B.4. Discussion

It is important to discuss the recent result given by Price et al. (1975) on the detection of a monopole. Price et al. in a balloon flight found a very heavily ionising particle passing through their experiment. The experiment contained a stack of Cherenkov films, emulsion and Lexan sheets. The lexan sheets indicate that the observed track was produced by either a nucleus with $125 \leq Z \leq 137$ and $\beta \leq 0.92$ or a monopole with $g = 137 e$. The result from the emulsion shows that the particle was moving downward with $\beta = 0.5$ and was either a nucleus with $Z \simeq 80$ or a monopole with $g = 137 e$. They concluded that this track was due to a monopole of strength $g = 137 e$ and mass $> 200 m_p$.

However, one can point out here that the search for monopoles at sea level has an important advantage over high altitude searches because at high altitude one can find many high Z particles which could in any

experiment simulate monopoles whereas at sea level the probability is very small to detect high Z.

The origin of the monopole is still unknown but it could be produced in the cosmic rays either in high energy cosmic ray interactions in the atmosphere or in the primary cosmic radiation.

With the present experiment the search for monopoles is not very reliable and a new experimental arrangement is needed to be set up for this purpose.

Plate B.1

Event H53 - 62

An example of a possible monopole
traversing the chamber. The
oscilloscope trace shows a pulse
from scintillator A only. The
event was observed on a run using
a time delay T_D of $530 \mu s$.

A = 1,025 particles

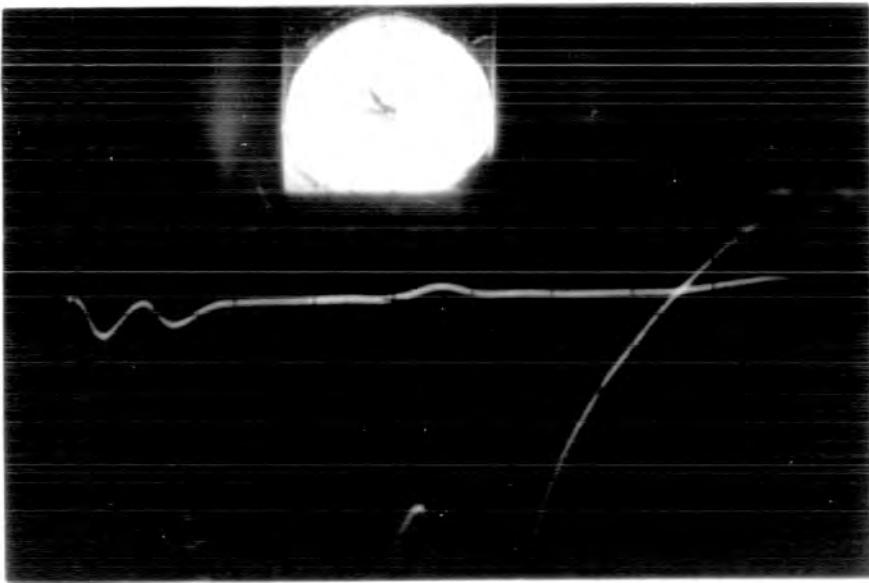
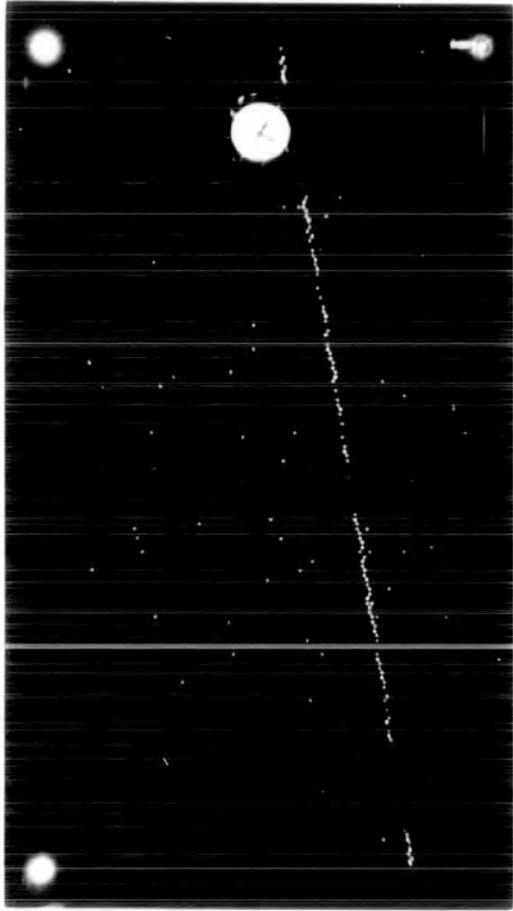


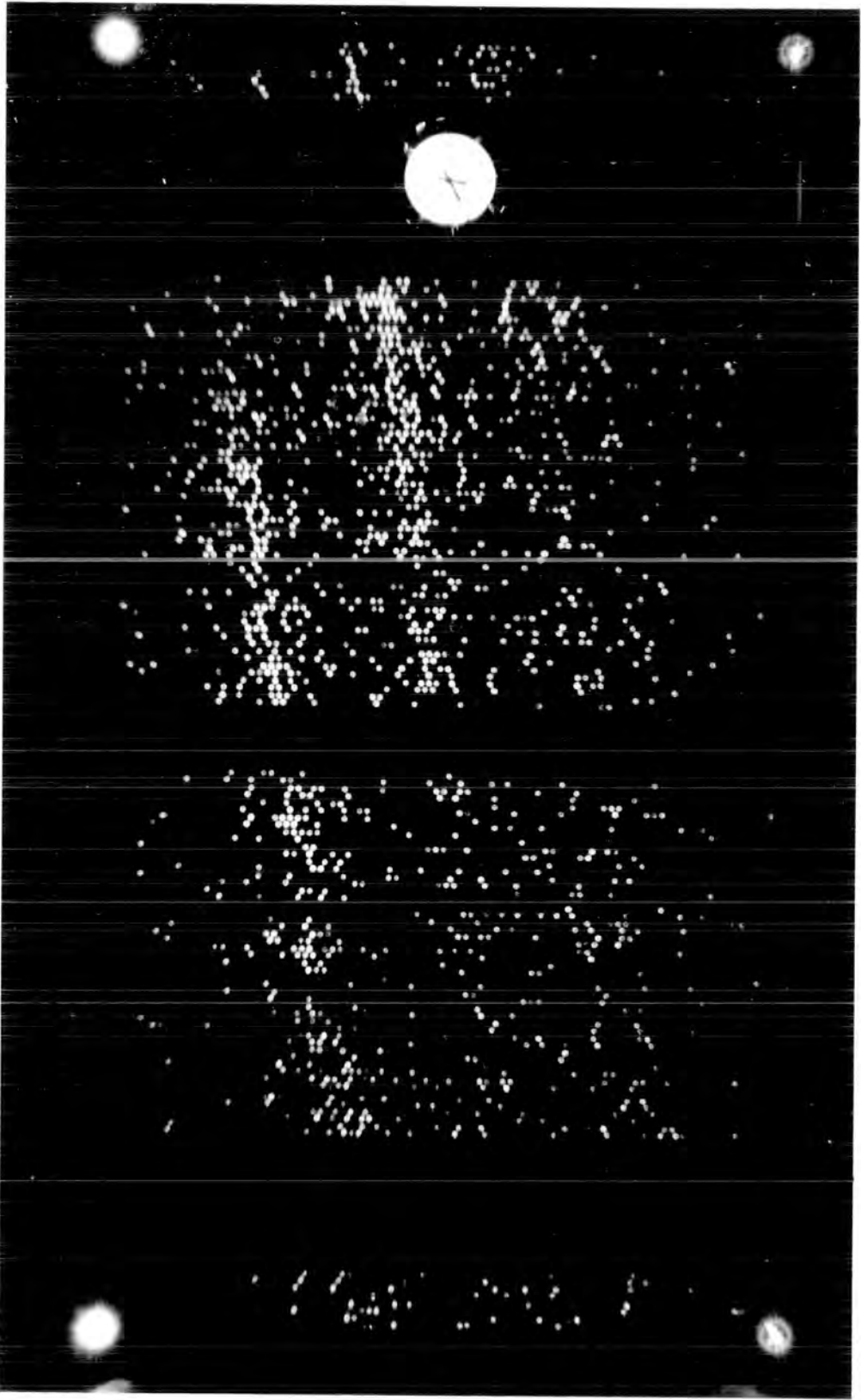
Plate B.2

Event H49 - 1

An example of an event in which three separated bursts can be seen.

The middle shows a burst produced by a possible monopole.

~~The event was observed on a run using~~
a time delay T_D of $330 \mu s$.



ACKNOWLEDGMENTS

The author wishes to thank Professor A.W. Wolfendale for the provision of the facilities for this work and for his interest and support.

He is extremely grateful to his supervisor Dr. P. Ashton for his willing guidance, stimulating suggestions and invaluable help throughout the work.

Many members of the Cosmic Ray Research Group, Staff and Research Students, are thanked for helpful discussions, in particular Dr. D.A. Cooper and Dr. A. Parvaresh for their friendly assistance.

The technical staff of the Physics Department, in particular Mr. W. Leslie, Mr. M. Lee and Mr. E. Lincoln are thanked for their help. The author is grateful to Mrs. A. Gregory for her invaluable help in drawing many of the diagrams for this thesis.

The Durham Computing Unit is thanked for the provision of computing facilities as well as for advice at various times.

The author is grateful to Mrs. J. Lincoln for her careful typing of this thesis.

The author is grateful to the members of his family, in particular to his mother, who has been a great source of help.

He is grateful to the British Council for the grant of a fee award. Finally, the Government of Iraq is thanked for financial assistance.

REFERENCES

P.I.C.C.R. = Proceedings. Int. Conf. Cosmic Rays

- Adair, R.K., Barge, D.A., Chu, T.T. and Leipuner, L.B., (1964),
Proc. Coral. Gables Conf., 36.
- Adair, R.K. and Kasha H., (1969), Phys. Rev. Lett., 23, 1355.
- Alexander, G. and Yekutielli, G., (1961), Nuovo Cim., 19, 103.
- Alkofer, O.C., Carstensen, K. and Dan, V.D., (1971), P.I.C.C.R., Hobart,
4, 1314.
- Allaby, J.V. et al. (1969), Nuovo Cim., 64A, 75.
- Amaldi, E. et al. (1963), Nuovo Cim., 28, 733.
- Anderson, C.D. (1932), Science, 76, 238.
- Anderson, C.D. and Neddermeyer, S.H., (1938), Phys. Rev., 54, 88.
- Antipov, Yu.M. et al. (1969), Phys. Lett., 30B, 576.
- Ashton, F., Coats, R.B., Holyoak, B., Simpson, D.A. and Thompson, M.G.,
(1965), Nucl. Inst. and Methods, 37, 191.
- Ashton, F., Coats, R.B., Kelly, G.M., Simpson, D.A., Smith, N.I. and
Takahashi, T., (1968a), Canadian Journal of Phys., 46, 1125.
- Ashton, F., Coats, R.B., Kelly, G.M., Simpson, D.A., Smith, N.I. and
Takahashi, T., (1968b), J. Phys. A., 1, 569.
- Ashton, F., Edwards, H.J. and Kelly, G.M. (1969a), Phys. Lett., 29B, 249.
- Ashton, F. et al. (1969b), Izvest Akad. Nauk., 33, 1817.
- Ashton, F., Smith, N.I. King, J. and Mamidzhyan, V.A., (1970),
Acta. Phys. Hung., 29, Suppl. 3, 25.
- Ashton, F., Edwards, H.J. and Kelly, G.M., (1971a), J. Phys. A, Gen. Phys.,
4, 352.
- Ashton, F., Breare, J.M., Holroyd, W.W., Tsuji, K. and Wolfendale, A.W., (1971b),
Lett. Nuovo Cim., 2 (14), 707.
- Ashton, F., Coats, R.B., King, J., Tsuji, K. and Wolfendale, A.W., (1971c),
J. Phys. A., 4, 895.
- Ashton, F. and King, J., (1971), J. Phys. A ; Gen. Phys., 4, 431.
- Ashton, F., (1973), 'Cosmic Rays at Ground Level', Edited by A.W. Wolfendale,
Published by the Institute of Phys. (London).
- Ashton, F., Cooper, D.A., Parvaresh, A. and Saleh, A.J. (1973a),
J. Phys. A , 6, 577.
- Ashton, F., Cooper, D.A., Parvaresh, A. and Saleh, A.J.,
(1973b), P.I.C.C.R., Denver, 3, 2096.
(1973c), P.I.C.C.R., Denver, 4, 2997.
- Ashton, F. and Parvaresh, A., (1975), P.I.C.C.R., Munich, 8, 2719.
- Ashton, F., Cooper, D.A., Nasri, A., Parvaresh, A. and Saleh, A.J., (1975),
P.I.C.C.R., Munich, 8, 2980.

- Ashton, F. and Saltch, A.J.,
 (1975a), Nature, 256 (5516), 387.
 (1975b), P.I.C.C.R., Munich, 7, 2507.
 (1975c), P.I.C.C.R., Munich, 7, 2467.
- Aubert, J.J. et al. (1974), Lab. for Nucl. Scie. Technical report
 NC CCO - 3069 - 271.
- Aurela, A. and Wolfendale, A.W., (1967), Ann. Acad. Scie. Fenn., 6A, 226.
- Azaryan, M.C. et al. (1973), Sov. J. Nucl. Phys., 16, 678.
- Azimov, S.A., Abdullaev, A.M., M'yalovsky, V.M. and Yuldashbaev, T.S.,
 (1963), P.I.C.C.R., Jaipure, 5, 69.
- Babecki, J., Buja, Z., Grigorov, N.L., Loskiowacz, J., Massalski, J.,
 Oles, A. and Shestoporov, V. Ya., (1961), Sov. Phys. JETP, 13, 1089.
- Bacry, H., Nuyts, J. and Van Hove, L., (1964), Phys. Lett., 9, 279.
- Barton, J.C., (1967), Proc. Phys. Soc., 90, 87.
- Barton, J.C. and Stockel, C.T., (1966), Phys. Lett., 21, 360.
- Baruch, J.J.F., Brooke, G. and Kellermann, E.W.,
 (1973), Nature, 242 (114), 6.
 (1973), J. Phys. A ; Math. Nucl. Gen., 6, 98.
 (1973), P.I.C.C.R., Denver, 3, 2301.
- Baruch, J.J.F., Brooke, G., Huang, C.H., Kellermann, E.W. and Walster, N.D.,
 (1975), To be published in the final P.I.C.C.R. Volume, Munich.
- Bauer, E., (1951), Proc. Camb. Phil. Soc., 47, 777.
- Becklin, E.E. and Earl, J.A., (1964), Phys. Rev., 136B, 237.
- Belenkij, S.Z. and Landau, L.D., (1956), Nuovo Cim. Suppl., 3, 15.
- Bennett, W.R., (1966), Phys. Rev. Lett., 17, 1196.
- Bhabha, H.J., (1935), Proc. Roy. Soc., 152A, 559.
- Bhabha, H.J., (1938), Proc. Roy. Soc., 164A, 257.
- Bingham et al. (1964), Phys. Rev. Lett., 12, 423.
- Bjornboe, J., Damgard, G., Hansen, K., Chatterjee, B.K., Grieder, P.,
 Klovning, A., Lillethun, E., and Peters, B., (1968), Nuovo Cim., 53B, 241.
- Bjorken, J.D., Glashow, S.L., (1964), Phys. Lett., 11, 255.
- Blackett, P.M.S. and Occhialini, G.P.S., (1932), Nature, 130, 363.
- Blum et al. (1964), *ibid*, page 353a.
- Bothe, W. and Kolhorster, W.Z., (1929), Phys., 56, 751.
- Bradt, V.H., and Rappaport, S.A., (1967), Phys. Rev., 164, 1567.
- Braginskii, V.B., Zel'dovich, Ya. B., Martynov, V.K. and Migulin, V.V.,
 (1968), Sov. Phys., JETP, 27, 51.
- Briatore, L., D'Ettoire Pizzoli, B., Piano, A., Sitte, K., Picchi, P.,
 and Visentin, R., (1973), P.I.C.C.R., Denver, 3, 2101.
- Briatore, L., Dardo, I., D'Ettoire Pizzoli, B., Mannocchi, G., Picchi, P.,
 Sitte, K. and Visentin, R., (1975), P.I.C.C.R., Munich, 7, 2405.
- Brooke, G. and Wolfendale, A.W., (1964), Proc. Phys. Soc., 83, 843.
- Brooke, G., Meyer, M.A. and Wolfendale, A.W., (1964), Proc. Phys. Soc., 83, 871.

- Buhler - Broglin, A., Dalpiaz, P., Massam, T. and Zichichi, A., (1967), Nuovo Cim., 51A, 837.
- Buja, Z., (1963), Acta Phys. Pol., 24, 381.
- Cairns, I., McCusker, C.B.A., Peak, L.S. and Woolcott, R.L.S., (1969), Phys. Rev., 186, 1394.
- Chin, S., Hanayama, Y., Hara, T., Higashi, S. and Tsuji, K., (1971), Nuovo Cim., 2A, 419.
- Christy, R.F. and Kusaka, S., (1941), Phys. Rev., 59, 405.
- Chukpa, W.A., Schiffer, J.P. and Stevens, C.M., (1966), Phys. Rev. Lett., 17, 60.
- Clark, A.F., Ernst, F.D., Flinn, H.F., Graffin, G.G., Hansen, W.F., and Smith D.E., (1971), Phys. Rev. Lett., 27, 51.
- Coats, R.B., (1967), Ph.D. thesis, Durham, Unpublished.
- Cocconi, G., Koester, I.S. and Perkins, D.H., (1961), UCRL High Energy Phys. Study Seminars, 28, (UCID - 1444).
- Cole, H.J.D., (1951), Proc. Camb. Phil. Soc., 47, 196.
- Cook, D.D., De Pasquelli, G., Framfelder, H., Peacock, R.N., Steinrisser, F. and Wattenburg, A., (1969), Phys. Rev., 188, 2092.
- Cowan, E.W. and Matthews, K., (1971), Phys. Rev., 4D, 37.
- Cox, A.J., Beauchamp, W.T., Bowen, T. and Kalbach, R.N., (1971), P.I.C.C.R., Hobert, 2, 1167.
- Crawford, D.F. and Kessel, H., (1965), Nucl. Phys., 61, 145.
- Crispan, A. and Fowler, G.N., (1970), Rev. Mod. Phys., 42, 290.
- Crouch et al. (1971) Preprint.
- Dardo, M., Navarra, G. Penengo, P. and Salte, K., (1972), Nuovo Cim., 9A, 319.
- Diggory, I.S. Hook, J.R., Jenkins, J.A. and Turver, K.E., (1974), J. Phys. A, 7 (6), 741.
- Dirac, P.A.M., (1931), Proc. Roy. Soc., 13A, 60.
- Dirac, P.A.M., (1948), Phys. Rev., 74, 817.
- Dmitriev, V.A., Kulikov, G.V. and Khristiansen, G.B., (1960), Sov. Phys., JETP, 37, 637.
- Dobrotin, N.A. and Salavatinsky, S.A., (1960), Proc. 10th Ann. Rochester Conf. on High Energy Nucl. Phys.
- Ellsworth, R.W. Ito, A., Tonwar, S.C., Streetmatter, R.E., MacFall, J.R., Siohan, F. and Yodh, G.B., (1975), P.I.C.C.R., Munich, 7, 2537.
- Erlykin, A.D. and Yakovlev, V.I., (1969), Sov. Phys., JETP, 29, 922.
- Erofeeva, I.N., Mitschenko, L.G., Murzin, V.S., Rapoport, I.D., Sarichera, L.I., (1965), P.I.C.C.R., London, 2, 833.
- Erofeeva, I.N., (1971), Dissertation, Nucl. Phys. Inst. of the Moscow State University.
- Evans, G. et al. (1971/72), Proc. Roy. Soc. Edinburgh (A), 70, 143.
- Faissner, H., Holder, N., Krasor, K., Mason, G., Sawaf, Z. and Umbach, H., (1970), Phys. Rev. Lett., 24, 1357.

- Fermi, E. and Yang, C.N., (1949), Phys. Rev., 76, 1739.
- Feynman, R.P., (1969), Phys. Rev. Lett., 23, 1415.
- Fleischer, R.L., Hart, H.R., Nichols, G.E. and Price, P.B., (1971), Phys. Rev., 4D, 24.
- Frenzi, P. and Shulman, S., (1968), Phys. Rev. Lett., 21, 1031.
- Freunfelder, H., Kruse, U.E. and Sard, R.D., (1970), Phys. Rev. Lett., 24, 33.
- Galper, A.M., Gomofov, V.A., et al. (1970), Sov. J. Nucl. Phys., 10, 193.
- Garmare, G., Leong, C. and Sreekantan, B.V., (1968), Phys. Rev., 166, 1280.
- Garraffo, Z., Pignotto, A. and Zgrablich, G., (1973), Nucl. Phys., 538, 419.
- Gell-Mann, M., (1964), Phys. Lett., 8, 214.
- Giacomelli, G., Rossi, A. M. and Vannini, G., (1975), Nuovo Cim., 28A, 21.
- Gomcz, R., et al. (1967), Phys. Rev. Lett., 18, 1022.
- Groder, P.K.F., (1970), Inst. Nucl. Study, Tokyo, Pub. INS J 125.
- Groder, P.K.F. (1972), Nuovo Cim., 7A, 867.
- Greisen, K., (1956), Progress in Cosmic Rays Phys., 3, (Amsterdam, North Holland).
- Greisen, K., (1960), Ann. Rev. Nucl. Sci., 10, 63.
- Grigorov, N.L., Murzin, V.S. and Raport, I.D., (1958), Zh. EKSP. Teor. Fiz., 34, 506. Sov. Phys., JETP, 7, 348.
- Grigorov, N.L., Sobnyakov, V.A., Tretyakova, Ch.A., Shestoporov, V. Ya., Babayan, Kn. P. and Dulyan, G.G., (1965), P.I.C.C.R., London, 2, 860.
- Grigorov, N.L. et al. (1970), Acta Phys. Hung., 29, Suppl. 3, 37.
- Gurevich, I.I. et al. (1972), Phys. Lett., 38B, 549.
- Hagopian, V., Sclove, J., Ehrlich, P., Leboy, E., Lanza, R., Rahm, D. and Webster, M., (1964), Phys. Rev. Lett., 13, 280.
- Hayakawa, S., (1969), Cosmic Ray Physics, Published by Wiley, New York.
- Hayman, P.J., and Wolfendale, A.W., (1962), Proc. Phys. Soc., 80, 710.
- Hazen, W.E., Hendel, A.Z. and Weiner, S.R., (1971), P.I.C.C.R., Hobart, 3, 1200.
- Hazen, W.E. (1971), Phys. Rev. Lett., 26, 582.
- Hazen, W.E., Hadson, A.L., Winterstein, D. and Keller, C., (1973), P.I.C.C.R., Denver, 3, 2087.
- Hazen, W.E., Hadson, A.L., Kass, J.R., Green. B.R. and Lloyd, P.G., (1975), P.I.C.C.R., Munich, 7, 2473.
- Hebart et al. (1970), Proc. 12th Int. Conf. on Low Temp. Phys., 855.
- Hess, V.F., (1912), Phys. Z., 13, 1084.
- Heusch, C.A. and Prescott, C.Y., (1964), Phys. Rev., 135B, 772.
- Hillas, A.M., (1970), Acta Phys. Hung., 29, Suppl. 3, 355.
- Hillas, A.M., (1972), Cosmic rays, Pergamon Press.
- Hughes, E.B. and Marsden P.L., (1966), J. Geophys. Res., 71, 1435.
- Ivanenko, I.P. and Samosudov, B.E.,
 (1959), Sov. Phys. JETP, 35 (8), 884.
 (1967a), Bull. Acad. Sci., USSR, 30, 1722.
 (1967b), Sov. J. of Nucl. Phys., 2 (3), 442.

- Jacob, M., (1975), Phys. Bulletin (April), 175.
- Johnson, E.W., (1969), Ph.D. Thesis, Michigan University.
- Jones, L.W. et al. (1967), Phys. Rev., 164, 1584.
- Jones, L.W., Russian, A.F. and Demoester, G.D. et al., (1970), Phys. Rev. Lett., 25, 1679.
- Jones, W.V., (1969a), Phys. Rev., 187, 1868.
- Jones, W.V. (1969b), P.I.C.C.R., Budapest, Acta Phys. Acad. Sci. Hung.(1970), 29, Supp. 4, 513.
- Jones, W.V., Finkau, K., Pollvogt, U., Schmidt, W.K.H. and Huggett R.V., (1969), P.I.C.C.R., Budapest. Acta Phys. Acad. Sci. Hung., 29, Suppl. 4, 521.
- Kameda, T., Maeda, H., Oda, H. and Sugihara, T., (1965), P.I.C.C.R., London, 2, 681.
- Kaneko, T. et al. (1971), P.I.C.C.R., Hobart, 7, 2759.
- Kasha, H. and Stefanski, R.J., (1968), Phys. Rev., 172, 1297.
- Katsumata, I., (1964), J. Phys. Soc. Japan, 19, 800.
- Khrimyan, A.V., Avakyan, V.V., Pleshko, M.P. and Khrimyan, G.V., (1964), Izv. ANSSSR Ser. fiz., 28, 1803.
- Kim, Y.S., (1973), Contemp. Phys., 14 (4), 289.
- Kiraly, P. and Wolfendale, A.W., (1970), Phys. Lett., 31B, 410.
- Kolhorster, W., (1914), Ber deutsch Phys. Ges., 16, 719.
- Krisor, K., (1975), Nuovo Cim., 27A, 132.
- Lal, S., Raghavan, R., Rangaswamy, T.M., Sreekantan, B.V. and Subramanian, (1963), P.I.C.C.R., Jaipur, 5, 260.
- Lattes, C.K.G., Muirhead, H., Occhialini, G.P.S. and Powell, C.F., (1947), Nature, 159, 694.
- Lee, T.D., (1965), Nuovo Cim., 35, 933.
- Leipuner, L., Larsen, R., Sessoms, A., Smith, L. and Williams, H., (1973), P.I.C.C.R., Denver, 3, 2081.
- Levin, T.M. and Frankfurt, L.L., (1968), Sov. Phys. Usp, 2, 106.
- Lloyd, J.L., (1960), Proc. of the Phys. Soc., LXXV, 387.
- Lovati, A., Mura, A., Succì, C. and Tagliaferri, G., (1954), Nuovo Cim., 12, 526.
- Massam, T. and Zichichi, A., (1956), Nuovo Cim., 43, 227.
- McCusker, C.B.A. and Cairns, I., (1969), Phys. Rev. Lett., 23, 658.
- McDiarmid, I.B. and Wilson, M.D., (1962), Can. J. Phys., 40, 698.
- Messel, H. and Crawford, D., (1970), Tables (Oxford, Pergaman).
- Morpurgo, G., (1967), Acta Phys. Hung., 22, 105.
- Morpurgo, G. et al. (1970), Nucl. Ins. and Meth., 79, 95.
- Murzin, V.S., Bashindzhagyan, G.L., Eroffeeva, I.N. Mishchenko, L.G., Ra p o p o r t, I.D. and Sarycheva, L.I., (1967), Sov. J. Nucl. Phys., 5, 435.
- Myalkovskii, V.M., (1972), Dissertation, FTIAN UZBSSR.
- Mylroie, W.G. and Wilson, J.G., (1951), Proc. Phys. Soc. A , 64, 404.

- Nagel, H.H., (1965), *Z. Physik*, 186, 319.
- Nash, T., Yamanouchi, T., Nesse, D. and Scully, J., (1974),
Phys. Rev. Lett., 32 (15), 858.
- Nikolsky, S.I., (1967), *Sov. Phys. JETP*, 24, 535.
- Nishimura, J. and Kamata, K., (1952), *Prog. Theor. Phys.*, 1, 185.
- Nishina, Y., Tomonaga, S. and Kobayashi, M., (1935), *Sci. Pap. Ins. Phys. Chem. Research, Japan*, 27, 137.
- Owen, B.G. and Wilson, J.G., (1955), *Proc. Phys. Soc.*, 68A, 409.
Particle Data Group, (1972), *Phys. Lett.*, 39B (11), 145.
- Parvaresh, A., (1975), Ph.D. Thesis, Durham, Unpublished.
- Pattison, J.B.M., (1965), Ph.D. Thesis, Durham, Unpublished.
- Pinkau, K. and Thompson, K.V., (1966), *The Rev. of the Scientific Inst.*
37 (3), 302.
- Pine, J. Davison, R.J. and Greisen, K., (1959), *Nuovo Cim*, 14, 1181.
- Price, F.B. Shark, E.K., Osborne, W.Z. and Pinsky, L.S., (1975),
Phys. Rev. Lett., 35 (8), 487.
- Purcell et al. (1953), *Phys. Rev.*, 129, 2326.
- Racah, G., (1937), *Nuovo Cim*, 14, 93.
- Rahm, D.C. and Sternheimer, R.M., (1969), Brookhaven preprint BNL 14072.
- Rahm, D.C. and Louttit, R.I., (1970), *Phys. Rev. Lett.*, 24, 279.
- Rank, D.M., (1968), *Phys. Rev.*, 176, 1635.
- Rochester, G.D. and Butler, C.C., (1947), *Nature*, 160, 855.
- Rossi, B., (1932), *Phys. Z.*, 33, 304.
- Rossi, B., (1952), *High Energy Particles*, (Prentice-Hall).
- Ryan, M.J., Crmes, J.F. and Balasubrahmanyam, V.K., (1972),
Phys. Rev. Lett., 28, 985.
- Sakata, S., (1956), *Prog. Theor. Phys.*, 16, 686.
- Saleh, A.J. (1973), M.Sc. Thesis, Durham, Unpublished.
- Schwinger, J., (1966), *Phys. Rev.*, 144, 1087.
- Shestoprov, V. Ya., (1974), *Sov. J. Nuc. Phys.*, 19, 656.
- Sinanoglu, C., Skutnick, B. and Tousey, R., (1966), *Phys. Rev. Lett.*, 17, 795.
- Siohan, F., La Pointe, M., MacFall, J., Stottlemeyer, A., Ellsworth, R.W.,
Yodh, G.B., (1973a), *P.I.C.C.R.*, Denver, 3, 2129.
- Siohan, F., La Pointe, M., MacFall, J., Ito, A., Stottlemeyer, A.,
Tonwar, S.C., Ellsworth, R.W., Yodh, G.B., (1973b), *P.I.C.C.R.*,
Denver, 3, 2135.
- Siohan, F., La Pointe, M., MacFall, J., Stottlemeyer, A., Straitmatter, R.,
Ellsworth, R.W., Yodh, G.B., (1975), *P.I.C.C.R.*, Munich, 7, 2532.
- Stover, R.W., Moran, T.I. and Trischka, J.W., (1967), *Phys. Rev.*, 164, 1599.
- Street, J.C. and Stevenson, E.C., (1937), *Phys. Rev.*, 52, 1003.
- Tanahashi, G., (1965), *Proc. Phys. Soc. Japan*, 20, 883.

- Thielheim, K.O. and Beiersdorf, R., (1969), Acta Phys. Acad. Sci. Hung., 29, Suppl. 3, 519.
- Thielheim, K.O. and Zollner, R., (1972), J. Phys. A, 5, 1054.
- Thom, H., (1964), Phys. Rev., 136, B447.
- Tonwar, S.C. Narayan, S. and Srcekantan, B.V., (1971), P.I.C.C.R., Hobart, 2, 1171.
- Vatch, R.H. et al. (1972), J. Phys. A, 6, 1050.
- Wdowczyk, J., (1973), 'Cosmic Rays at Ground Level', Edited by A.W. Wolfendale, Published by the Institute of Phys. (London).
- Webber, W.R., (1973), P.I.C.C.R., Denver, 5, 3568.
- White, G.M. et al. (1970), Acta Phys. Acad. Sci. Hung., 29, Suppl. 3, 31.
- Wilson, J.G., (1970), Nature, 225, 1238.
- Wolfendale, A.W., (1973), 'Cosmic Rays at Ground Level', Edited by A.W. Wolfendale, Published by the Institute of Phys. (London).
- Yukawa, H., (1935), Proc. Phys. Math. Soc. Japan, 17, 48.
- Yock, P.C.M., (1974), Nucl. Phys., B76, 175.
- Yock, P.C.M., (1975), Nucl. Phys. B86, 216.
- Yodh, G.B., Pal Yash and Trefil, J.S., (1972), Phys. Rev. Lett., 28 (15), 1005.
- Yodh, G.B., (1974), (private communication).
- Zerby, C.D. and Moran, H.S., (1963), J. Appl. Phys., 34, 2443.
- Zweig, G., (1964), CERN Preprints TH401, TH412.
- Zweig, G., (1965), Symmetries in Elementary Particle Physics Ed. A. Zichichi (New York : Acad. Press).

